THE UNIVERSITY OF CALGARY

Dynamics of Bubble Groups

by

Catherine Laureshen

A DISSERTATION

SUBMITTED TO THE FACULTY OF GRADUATE STUDIES

IN PARTIAL FULFILLMENT OF THE REQUIREMENTS FOR THE

DEGREE OF DOCTOR OF PHILOSOPHY

DEPARMENT OF MECHANICAL ENGINEERING

CALGARY, ALBERTA

DECEMBER, 1997

© Catherine Laureshen 1997

National Library of Canada
Acquisitions and Bibliographic Services
395 Wellington Street
Ottawa ON K1A 0N4
Canada

Bibliothèque nationale du Canada
Acquisitions et services bibliographiques
395, rue Wellington
Ottawa ON K1A 0N4
Canada

Your file Votre référence

Our file Notre référence

The author has granted a non-exclusive licence allowing the National Library of Canada to reproduce, loan, distribute or sell copies of this thesis in microform, paper or electronic formats.

The author retains ownership of the copyright in this thesis. Neither the thesis nor substantial extracts from it may be printed or otherwise reproduced without the author's permission.

L'auteur a accordé une licence non exclusive permettant à la Bibliothèque nationale du Canada de reproduire, prêter, distribuer ou vendre des copies de cette thèse sous la forme de microfiche/film, de reproduction sur papier ou sur format électronique.

L'auteur conserve la propriété du droit d'auteur qui protège cette thèse. Ni la thèse ni des extraits substantiels de celle-ci ne doivent être imprimés ou autrement reproduits sans son autorisation.

0-612-31045-0

Canada

ABSTRACT

An experimental program was designed to study the effect of the four major paramenters affecting the behaviour of bubble groups in an unconfined, quiescent fluid: injected gas volume, water depth above the source, surface tension and gravitational acceleration. The dependent parameters for bubble groups were identified and reduced through dimensional analysis, and it was found that the most important of these dimensionless groups was the bubble Reynolds number. Nine scaling parameters were also derived so that experimental results could be applied to a full-scale prototype. Results of the experiments were used to generate a database of bubble group behaviour under specified conditions, and to describe this behaviour qualitatively. Experiments were also carried out to identify the starting conditions for the theoretical model.

A theoretical two-phase model is proposed to describe the behaviour of bubble groups released into a non-stratified quiescent environment. The model assumes a background flow field consisting of a Hill's spherical vortex moving at a uniform speed to describe the flow within the bubble group, and potential flow theory to describe the ambient flow field. The bubble equations account for all of the forces affecting the individual bubbles within the range of the experimental work, including the lift force. Theoretical results are presented, and compared to the results of the laboratory work, with reasonable agreement for the radial distance, and excellent agreement for the velocity terms. Correction factors are proposed to fit the model more closely to the experimental data.

ACKNOWLEDGEMENTS

A doctoral thesis is never entirely the work of the author, and I would like to acknowledge the contributions which have made this work possible. Many of these thanks are long overdue, as it took me 14 years from the inception of this project to finally put these words to paper. Therefore, my first acknowledgement must be to all of the members of the Faculty of Engineering for their encouragement and support throughout this extended period of time, and especially to Dr. Chan Wirasinghe, the current Dean of Engineering, who provided the final impetus for me to finish this work by requesting me to become a part of this Faculty as an instructor with the Common Core program. I would also like to extend my thanks to the Department of Mechanical Engineering, the Department of Chemical and Petroleum Engineering, and the Undergraduate Studies Program for providing the funding for this joint position. I must also give credit to the students that I have taught over the past 12 years; without them, I never would have realized that I had a vocation as a teacher.

My initial supervisor, Dr. Richard Rowe, provided the encouragement to explore new ideas and the freedom to learn from my own mistakes. My current supervisor, Dr. Graham Reader, very kindly agreed to take his place when Dr. Rowe retired, and despite his major commitments elsewhere, Dr. Reader has always found time to give me advice and encouragement when it was necessary.

I would like to thank the other members of my supervisory committe, Dr. John A.C. Kentfield and Dr. Ida Wierzba, for continuing with me for so long. Dr. Kentfield, especially, contributed much of his valuable time towards reading the early draft of this dissertation and

giving me advice on grammar and concepts. He also advised me as to the correct procedures to follow with regards to my defense, and offered me moral support when I needed it most.

Much of the credit for this work also belongs to Dr. David Topham. It was his Co-op student's work that initially showed that bubble groups would be a promising line of research to pursue. In addition to providing funding for this project, Dr. Topham was always generous with his ideas and advice, both to Dr. Rowe and myself.

I am indebted to Dr. Gordon Moore of the Department of Chemical and Petroleum Engineering for his advice on equipment design, the pressure testing of the apparatus used for microgravity tests carried out on board a Boeing KC-135 aircraft, and for his generous donations of time, moral support and Glenlivet during the experimental phases of this work. In addition, I have worked with the In Situ Combustion Research Group, of which he is the head, for the past seven years. Although my work with the group may have delayed the final writing of this thesis, I believe that this time was wisely spent, as it honed my skills as a writer, editor and researcher. Words cannot express what I owe to Dr. Moore for being both friend and mentor to me over the years, and I only hope that I can continue to live up to his high expectations of me in the years to come.

Dr. Raj Mehta is another person who has provided assistance to me above and beyond the normal call of friendship over the past 14 years. His help with my experimental photography and equipment on many nights and weekends, his insightful ideas and the (purely medicinal) doses of coffee and beer that he fed me to wake me up and calm me down will not be forgotten. Working with him as part of the In Situ Combustion Research Group

has been both a blessing and a curse over the years, but it has never been boring. Hopefully, our association will continue for a long time to come, so I can repay him.

Matthew Ursenbach sacrificed precious time away from his family to help me with my plots and with proof-reading the text of this dissertation. His friendship and encouragement over the years has meant a lot to me, and I would like to also thank his family, especially his wife Lynn, for allowing him to assist me.

Special thanks are also due to Dr. Jana Simandl, Dr. T.J. Al-Himyary, Ms. Heloisa Mello, Mr. Vladimir Bakalchuk, Ms. Dorothy MacDiarmid, Ms. Jackie Staples and Ms. Wendy Reid for their friendship and belief in me during the many years of my doctoral program.

Dr. Ayo Jeje, of the Department of Chemical and Petroleum Engineering, allowed me the use of his Hycam camera, and I would also like to thank him for the time that he spent helping me to set up the initial high-speed film sessions. In addition, I would like to thank him for encouraging me to finish this dissertation.

The technicians in the Mechanical Engineering shop deserve a special vote of thanks for building my experimental equipment: Mr. Bill Crewes, who was responsible for assembling the large and the small tanks; Mr. Rob Scorey, who built the majority of the KC-135 apparatus; and Mr. Ben Sanders, who designed the electronic controls. Mr. Mike Johnson and Mr. Greg East also helped to make this work possible. I would like to express my gratitude to Mr. Art Moehrle, who helped me to set up the laser-Doppler anemometer and gave me invaluable assistance with my photographic lighting.

Mr. Bert Unterberger processed and printed all of my black-and-white photographs, and I would like to thank him for all of the long and tedious hours which he spent on my behalf.

Mr. Terry Nail of the Department of Civil Engineering also gave generously of his time and equipment in the structural testing of the KC-135 apparatus.

I would also like to gratefully acknowledge the people of Canada, who supported this work through the financial contributions of the Department of Mechanical Engineering at the University of Calgary, the Natural Sciences and Engineering Research Council of Canada, the Department of Fisheries and Oceans Science Subvention Program and the Space Division of the National Research Council.

Most of all, I would like to thank my family, whose love and support made all of this possible. My daughter Sarah, especially, was forced to tolerate a mother who was absent both in mind and body for most of her formative years, and I only hope that I can make it up to her in the years to come.

TABLE OF CONTENTS

Page

APPROVAL PAGE ..... *ii*

ABSTRACT ..... *iii*

ACKNOWLEDGEMENTS ..... *iv*

TABLE OF CONTENTS ..... *viii*

LIST OF TABLES ..... *xiii*

LIST OF FIGURES ..... *xiv*

NOMENCLATURE ..... *xxi*

CHAPTER 1 INTRODUCTION 1

1.1 Problem 1

1.2 Background 3

1.3 Objectives 5

CHAPTER 2 A REVIEW OF THERMALS AND VORTEX RINGS 6

2.1 Introduction 6

2.2 Vortex Rings 6

2.3 Buoyant Vortex Rings 12

2.4 Thermals 14

2.4.1 Single-Phase Thermals 14

2.4.2 Entrainment 20

2.4.3 Virtual or Added Mass 22

TABLE OF CONTENTS (Cont'd)

Page

2.4.4 Solid-Particle Two-Phase Thermals 23

2.4.5 Gas-Liquid Two-Phase Thermals 26

CHAPTER 3 DIMENSIONAL ANALYSIS AND SCALING PARAMETERS . 32

3.1 Model Theory 32

3.2 Dimensional Considerations 34

3.2.1 Bubble Size 35

3.2.2 Terminal Bubble Velocity 37

3.3 Dimensional Analysis for a Bubble Group 39

3.4 Scaling Parameters and Physical Constraints 44

CHAPTER 4 EXPERIMENTAL EQUIPMENT AND PROCEDURES 50

4.1 Description of the Research Program 50

4.2 Experimental Apparatus 51

4.2.1 Small Tank 51

4.2.2 Large Tank 55

4.2.3 KC-135 Zero-Gravity Apparatus 60

4.3 Experimental Procedures 67

4.3.1 Experiments to Test Water Depth and Air Volume Effects 67

4.3.2 Experiments to Test Surface Tension Effects 72

TABLE OF CONTENTS (Cont'd)

Page

4.3.3 Experiments to Test the Effect of Gravity 74

4.3.4 Dye Injection Experiments 78

4.3.5 Experiments Using High-Speed Photography 85

CHAPTER 5 EXPERIMENTAL RESULTS 87

5.1 Introduction 87

5.2 Growth Patterns of Bubble Groups 88

5.3 Bubble Group Database 95

5.4 Effects of Varying Experimental Parameters 98

5.4.1 Effect of Water Depth 98

5.4.2 Effect of Injected Air Volume 100

5.4.3 Effect of Surface Tension 102

5.4.4 Effect of Gravitational Acceleration 103

5.4.5 Effect of Tank Size 112

5.5 Results of Dye Injection and HYCAM Experiments 114

CHAPTER 6 PREDICTIVE MODEL FOR BUBBLE PATHS 128

6.1 Modelling of Bubble Transport in Vortex Flows 128

6.2 Basis of Curent Model 129

6.3 Bubble Equation of Motion 131

6.3.1 Buoyancy Force 131

TABLE OF CONTENTS (Cont'd)

Page

6.3.2 Drag Force 132

6.3.3 Lift Force 133

6.3.4 Added Mass Force 134

6.3.5 Pressure Gradient Force 136

6.3.6 Basset History Term 136

6.3.7 Equation of Motion for a Bubble 137

6.4 Equations of Motion for the Background Fluid Flow 139

6.4.1 Flow Outside the Vortex 140

6.4.2 Flow Inside the Vortex 141

6.4.3 Vortex Expansion 141

6.4.4 Velocity Equations for the Background Fluid Flow 142

6.4.5 Assumptions Underlying the Fluid Flow Equations 145

CHAPTER 7 A COMPARISON OF THE RESULTS OF THEORY AND EXPERIMENT 147

7.1 Introduction 147

7.2 Comparison of Bubble Path Predictive Model with Early Published Version 152

7.3 Effect of Altering Bubble Model Parameters 158

7.4 Comparison of Simulations with Experimental Results 164

7.5 Correction of the Bubble Group Simulation Model 168

TABLE OF CONTENTS (Cont'd)

Page

7.6 Relevance of Scaling Parameters for the Theoretical Model ... 177

CHAPTER 8 CONCLUSIONS AND RECOMMENDATIONS 182

8.1 Conclusions 182

8.1.1 Conclusions From Experimental Portion of the Study ... 186

8.1.2 Conclusions From the Theoretical Model 190

8.2 Recommendations for Future Work 192

REFERENCES 193

APPENDIX A CALIBRATION AND ERROR ANALYSIS FOR LABORATORY AIR INJECTION SYSTEM 208

APPENDIX B TESTING AND ERROR ANALYSIS FOR KC-135 AIR INJECTION SYSTEM 212

APPENDIX C SAMPLES OF SCIENTIST COMPUTER CODE 217

C.1 Uniform Speed Bubble Model Using Topham *et al.* Equations and Variable α 217

C.2 Uniform Speed Bubble Model, Revised Substantive Derivative, Variable α 219

C.3 Revised Uniform Speed Bubble Model with Lift Term and Variable α 220

C.4 Revised Uniform Speed Bubble Model with Lift Term and Constant α 222

C.5 Revised Uniform Speed Bubble Model with Lift Term, Constant α and C_L=1.0 224

LIST OF TABLES

Table		Page
4.1	Parameters for Water Depth and Air Volume Effect Experiments ($g = 1$, $\sigma = 70$ dynes/cm)	68
4.2	Parameters for Surface Tension Effects Experiments (Small Tank, $V = 8.0$ cm^3, $g = 1$, $H_w = 60$ cm)	73
4.3	Parameters for Gravity Effect Experiments (KC-135 Apparatus, $H_w = 60$ cm, $\sigma = 70$ dynes/cm)	77
4.4	Parameters for Dye Injection Experiments ($H_w = 60$ cm, $g = 1$, $\sigma = 70$ dynes/cm)	83
5.1	Variation of α_2 with Injected Air Volume	100
5.2	Bubble Group and Dye Vortex Expansion and Separation Data from Small and Large Tank Dye Injection Tests	121
7.1	Initial Conditions for 14 cm^3(ST) Bubble Group in Figure 7.1 with a Constant Fluid Vortex Velocity of 16.1 cm/s	151

LIST OF FIGURES

Figure		Page
2.1	Schematic of a Hill's Spherical Vortex (c) Developing from a Transient Pulse of Fluid (a) Injected into a Quiescent Ambient Fluid. Figure (b) Illustrates the Direction of Vortex Rollup in the Intermediate Stage of Growth	9
2.2	Development of the Radius *b* of Experimental Bubble "Thermals" with Height *z* vs. Equation (2.21) with $\alpha = 0.25$. Five Data Sets are Presented (L120-16.1 to L120-16.5) From the Large Tank Tests for a Water Depth of 120 cm and an Injected Air Volume of 16 cm^3(ST)	31
4.1	Schematic of Small Tank and Air Injection System	52
4.2	View of Large Tank and Air Injection System	56
4.3	View of Large Tank and Dye Injection System	57
4.4	Front View of Skid 1, KC-135 Apparatus (Water Tank and Air Injection System)	63
4.5	Side View of Skid 2, KC-135 Apparatus (Recording Equipment and Controls)	64
4.6	View of KC-135 Apparatus Installed in Aircraft	65
4.7	Schematic of Air Injection System, KC-135 Apparatus	66
4.8	Typical Acceleration Data for One Parabola (KC-135 Experiments)	79
4.9	Typical Microgravity Acceleration Data (KC-135 Experiments)	80
4.10	Typical Output from Pressure Transducer PT3 (KC-135 Experiments)	81
5.1	Increase of Bubble Group Radius at its Widest Point with Height Above Injector for Five Large Tank, 16 cm^3(ST), Data Sets at $H_w = 120$ cm. The Plot Shows Two Straight-Line Asymptotes for Reference: A Conventional Thermal Relationship with $\alpha = 0.25$ near the Source, and a Round Bubble Plume-Type Model with $\alpha = 0.03$ Closer to the Water Surface. It Should be Noted that These Asymptotes were not Determined Experimentally	89

LIST OF FIGURES (Cont'd)

Figure		Page
5.2	View of the Fluid Vortex Released from the Bubble Group in an Early Small Tank Run, Using Micro-Bubbles as Flow Tracers. The Arrow Indicates Vortex Location	91
5.3	Plot of Velocity Change with Height above the Injector for the Five Large Tank, 16 cm³(ST) Data Sets at H_w = 120 cm Shown in Figure 5.1. Velocities were Calculated by Dividing the Height Above the Injector of the Widest Point of the Bubble Group by the Time Interval Between Measurements	93
5.4	View of Bubble Group at the Free Surface of the Water	94
5.5	Measurements Included in the Database	97
5.6	Increase of Bubble Group Radius at its Widest Point with Height Above Injector for All 16 cm³(ST) Large Tank Data Sets at Five Water Depths. Over the Range of Data Examined, No Effect of Water Depth can be Observed	99
5.7	Increase of Bubble Group Radius at its Widest Point with Height Above Injector for All Injected Air Volumes of the Large Tank Data Set at H_w = 120 cm. The Figure Shows an Increase of Overall Bubble Group Radius with Height Following Separation of the Bubble Group and Fluid Vortex	101
5.8	Increase of Bubble Group Radius at its Widest Point with Height Above Injector for All 10 cm³(ST) KC-135 Data Sets at H_w = 60 cm and Three Levels of Gravitational Acceleration. The Figure Shows how Increasing the g-level Causes the Fluid Vortex to Release Further Away from the Injector, in Addition to Decreasing the Entrainment Coefficient α Following Release	105
5.9	Increase of Bubble Group Radius at its Widest Point with Height Above Injector for All 8 cm³(ST) KC-135 Data Sets at H_w = 60 cm and Three Levels of Gravitational Acceleration. The Figure Shows how Increasing the g-level Causes the Fluid Vortex to Release Further Away from the Injector, in Addition to Decreasing the Entrainment Coefficient α Following Release	106

LIST OF FIGURES (Cont'd)

Figure		Page
5.10	Plot of Bubble Group Velocity with Height Above Injector for All 10 cm^3(ST) KC-135 Data Sets at H_w = 60 cm and Three Levels of Gravitational Acceleration. The Figure Shows how Increasing the **g**-Level Causes an Increase in Average Velocity. The Scatter in the 1/6 and 1.8 **g** Data is Due to Variations in the Acceleration of the KC-135 Aircraft During the Tests.	107
5.11	Increase of Bubble Group Radius at its Widest Point with Height Above Injector for All 1.8 **g** KC-135 Data Sets at H_w = 60 cm and Three Levels of Injected Air Volume. The Figure Shows an Increase in Group Radius with Increasing Air Volume	109
5.12	Increase of Bubble Group Radius at its Wides Point with Height Above Injector for All 1.0 **g** Small Tank Data Sets at H_w = 60 cm and Three Levels of Injected Air Volume Corresponding to Figure 5.11. This Figure also Shows a Group Radius Increase with Increasing Injected Air Volume	110
5.13	Increase of Bubble Group Radius at its Widest Point with Height Above Injector for Several 16 cm^3(ST) Small Tank and Large Tank Data Sets at H_w = 60 cm. No Effect of Tank Size Can be Seen Before or After the Transition Region, but the Transition Region is Longer in the Small Tank, which Indicates a Slight Wall Effect	113
5.14	Increase of Bubble Group Radius at its Widest Point with Height Above Injector for Several 14 cm^3(ST) Small Tank and Large Tank Data Sets at H_w = 60 cm. No Effect of Tank Size Can be Seen Before or After the Transition Region, but the Transition Region is Longer in the Small Tank, which Indicates a Slight Wall Effect. This is Consistent With the Results Seen in Figure 5.13	115
5.15	Photograph of Small Tank Dye Injection Experiment	117
5.16	Increase of Bubble Group Radius *b* at its Widest Point and Dye Vortex Radius *a* at its Widest Point with Height above Injector *z* for a 16 cm^3(ST) Large Tank Dye Injection Test at H_w = 60 cm. The Figure Indicates that the Transition Region Lies Between Approximately 2 cm and 15 cm Above the Injector. Below 2 cm lies the Circulating "Thermal" Region, and Above 15 cm, the Bubble Group Expands at a Constant but Smaller Growth Rate	119

LIST OF FIGURES (Cont'd)

Figure		Page
5.17	Plot of the Height of Widest Point of Dye Vortex *a* Above Injector versus Time for the 16 cm³(ST) Bubble Group Shown in Figure 5.16 (H_w = 60 cm). The Figure Shows that the Dye Vortex Velocity is Essentially Constant	120
5.18	HYCAM Footage from Run #8, Showing the Development of the Vortex at 0.12, 0.15 and 0.22 s Following Release of the Bubble Group. The Arrows Indicate Vortex Location	124
5.19	HYCAM Footage from Run #8, Showing the Influence of the Fluid Vortex at 0.26 and 0.31 s Following Release of the Bubble Group. The Arrows Indicate Vortex Location	125
5.20	HYCAM Footage from Run #8, Showing the Beginning of the Bubble/ Vortex Separation at 0.43 and 0.49 s Following Release of the Bubble Group. The Arrows Indicate Vortex Location	126
6.1	Integration of the Background Fluid Equations (6.30) to (6.34) Gives the Motion of Fluid into an Expanding Spherical Vortex, which is Moving at a Constant Upward Velocity. The Figure is Plotted Using a Co-ordinate System in Which the Spherical Boundary is Fixed in Size. The Tangent of the Half-Angle of Spread is α = 0.25. The Right Side of the Diagram shows the Paths of Particles Which Started on a Plane at Right Angles to the Direction of Motion. This Figure is Similar to the Results of Turner (1964a) for an Expanding Spherical Vortex	144
7.1	Plot of the Increase in Bubble Group Radius *r* with Height *z* for 12 Bubbles Generated by the Simulation Model Using the Initial Conditions for a 14 cm³(ST) Air Volume Bubble Group (U = 16.1 cm/s and α_1 = 0.511) and r_b = 1 mm. The Starting Positions and Velocities for each Data Point are Provided in Table 7.1	150
7.2	A Comparison of Model Results using the Equations from Topham *et al.*, 1994 (Model 1), the Model 1 Equations with Corrected Substantive Derivative Terms (Model 2), and Model 2 Equations Including a Lift Force Term (Model 3). The Figure Shows the Increase in Radial Position *r* with Height *z* for Runs With Initial Parameters r_b = 1.3 mm, U = 12.3 cm/s, α_1 = 0.360 and α_2 = 0.073. The Starting Position for Each Run was *r* = 1.3 cm and *z* = 0 cm	154

LIST OF FIGURES (Cont'd)

Figure **Page**

7.3 Dimensionless Height *GAMMA* (z/(αUt)) versus Dimensionless Radius *BETA* (r/(αUT)) for the Figure 7.1 14 cm³(ST) Air Volume Bubble Group With U = 16.1 cm/s, r_b = 1 mm and Variable α (α_1 = 0.511 and α_2 = 0.034). The Starting Positions for the Bubbles are Provided in Table 7.1. The Arc Centred on the Origin is the Outline of the Fluid Vortex, Which has a Constant Radius of Unity 156

7.4 Dimensionless Height *GAMMA* (z/(αUt)) versus Dimensionless Radius *BETA* (r/(αUT)) for the Figure 7.1 14 cm³(ST) Air Volume Bubble Group With U = 16.1 cm/s, r_b = 1 mm and Constant α (α_1 = 0.511). The Starting Positions for the Bubbles are Provided in Table 7.1. The Arc Centred on the Origin is the Outline of the Fluid Vortex, Which has a Constant Radius of Unity 157

7.5 Plot of the Change of Radial Position r with Height z Showing the Effect of Varying Bubble Radius on the Model Results. Initial Conditions for the Simulation were r = 1.49 cm, z = 0.16 cm, u_{br} = 17.3 cm, u_{bz} = 1.82 cm, U = 17.4 cm/s, α_1 = 0.420 and α_2 = 0.082 159

7.6 Plot of the Change of Radial Position r with Height z Showing the Effect of Varying only the Entrainment Coefficients as Initial Parameter Values and Not Using the Matching Vortex Velocity. Initial Conditions for the Simulation were r = 1.49 cm, z = 0.16 cm, u_{br} = 17.3 cm, u_{bz} = 1.82 cm, U = 17.4 cm/s and r_b = 1 mm. Initial and Final Values of the Entrainment Coefficients were Taken from Table 5.2 for the Injected Air Volumes used in the Experiments 161

7.7 Plot of the Change of Radial Position r with Height z Showing the Effect of Varying only the Entrainment Coefficients as well as the Matching Vortex Velocity as Initial Parameter Values. Initial Conditions for the Simulation were r = 1.49 cm, z = 0.16 cm, u_{br} = 17.3 cm, u_{bz} = 1.82 cm, and r_b = 1 mm. Initial and Final Values of the Entrainment Coefficients were Taken from Table 5.2 for the Injected Air Volumes used in the Experiments 162

7.8 Plot of the Change of Radial Position r with Height z Showing the Effect of Varying the Gravitational Acceleration on the Model. Initial Conditions for the Simulation were r = 1.49 cm, z = 0.16 cm, u_{br} = 17.3 cm/s, u_{bz} = 1.82 cm/s, U = 17.4 cm/s, α_1 = 0.420, α_2 = 0.082, and r_b = 1 mm 163

LIST OF FIGURES (Cont'd)

Figure		Page
7.9	Plot of the Increase in Bubble Group Radius r with Height z for 12 Bubbles Generated by the Simulation Model Using the Initial Conditions for a 14 cm³(ST) Air Volume Bubble Group (U = 16.1 cm/s and α_I = 0.511) and r_b = 1 mm. The Starting Positions and Velocities for each Data Point are Provided in Table 7.1. The Simulation Results are Compared to Outlines of the Experimental Data Set from Large Tank Test L14-45.3 at the Same Time Intervals	166
7.10	Plot of the Increase in Bubble Group Radius r with Height z for the Outermost Bubble Path from Figure 7.9, which was Generated by the Simulation Model Using the Initial Conditions for a 14 cm³(ST) Air Volume Bubble Group (U = 16.1 cm/s and α_I = 0.511) and r_b = 1 mm. The Simulation Results are Compared to the Full Data Set from All Large Tank 14 cm³(ST) Tests with H_w = 120 cm	167
7.11	Plot of the Variation in Vertical Bubble Velocity u_z with Height z for the 12 Bubbles in Figure 7.9, which were Generated by the Simulation Model Using the Initial Conditions for a 14 cm³(ST) Air Volume Bubble Group (U = 16.1 cm/s and α_I = 0.511) and r_b = 1 mm. The Starting Positions and Velocities for each Data Point are Provided in Table 7.1	169
7.12	Plot of the Variation in Radial Bubble Velocity u_r with Height z for the 12 Bubbles in Figure 7.9, which were Generated by the Simulation Model Using the Initial Conditions for a 14 cm³(ST) Air Volume Bubble Group (U = 16.1 cm/s and α_I = 0.511) and r_b = 1 mm. The Starting Positions and Velocities for each Data Point are Provided in Table 7.1	170
7.13	Detail of the Plot of the Variation in Vertical Bubble Velocity u_z with Height z for the 12 Bubbles in Figure 7.9, which were Generated by the Simulation Model Using the Initial Conditions for a 14 cm³(ST) Air Volume Bubble Group (U = 16.1 cm/s and α_I = 0.511) and r_b = 1 mm. The Starting Positions and Velocities for each Data Point are Provided in Table 7.1	171
7.14	Plot of the Variation in Vertical Bubble Velocity u_z with Height z for the Outermost Bubble Path from Figure 7.9, which was Generated by the Simulation Model Using the Initial Conditions for a 14 cm³(ST) Air Volume Bubble Group (U = 16.1 cm/s and α_I = 0.511) and r_b = 1 mm. The Simulation Results are Compared to the Vertical Bubble Group Velocity u from each Data Set in the Large Tank 14 cm³(ST) Tests with H_w = 120 cm	172

LIST OF FIGURES (Cont'd)

Figure		Page
7.15	Plot of Height of the Widest Point of the Bubble Group z versus Time t for the Data Set for Large Tank Test L14-120.5 and for the Outermost Bubble Path from Figure 7.9, which was Generated by the Simulation Model Using the Initial Conditions for a 14 cm³(ST) Air Volume Bubble Group (U = 16.1 cm/s and $\alpha_1 = 0.511$) and $r_b = 1$ mm. The Plot Shows an Almost Exact Match Between Theory and Experiment	173
7.16	Plot of the Increase in Bubble Group Radius r with Height z for the Outermost Bubble Path from Figure 7.9 (Solid Line), which was Generated by the Simulation Model Using the Initial Conditions for a 14 cm³(ST) Air Volume Bubble Group (U = 16.1 cm/s and $\alpha_1 = 0.511$) and $r_b = 1$ mm. The Simulation Results are Compared to the Full Data Set from All Large Tank 14 cm³(ST) Tests with $H_w = 120$ cm. Also Plotted is the Effect on the Simulation of Using a Constant Initial Entrainment Coefficient, and of Doubling the Lift Coefficient	175
7.17	Plot of the Variation in Vertical Bubble Velocity $u_{\bar{}}$ with Height z for the Outermost Bubble Path from Figure 7.9 (Solid Line), which was Generated by the Simulation Model Using the Initial Conditions for a 14 cm³(ST) Air Volume Bubble Group (U = 16.1 cm/s and $\alpha_1 = 0.511$) and $r_b = 1$ mm. The Simulation Results are Compared to the Full Data Set from All Large Tank 14 cm³(ST) Tests with $H_w = 120$ cm. Also Plotted is the Effect on the Simulation of Using a Constant Initial Entrainment Coefficient, and of Doubling the Lift Coefficient	178
A.1	Schematic of Control Volume Calibration Apparatus	211
B.1	Typical Temperature Data (KC-135 Experiment)	216

NOMENCLATURE

a cross-sectional radius of vortex ring, cm

A area of manometer mercury column, m^2

A_c area of largest cross-sectional area of bubble thermal (Fannelop, 1982), m^2

A_f area of moving fluid at largest cross-sectional area of bubble thermal (Fannelop, 1982), m^2

b thermal radius, bubble group radius, cm

C_L lift coefficient

d orifice diameter, m

d_b bubble diameter, mm

D^* dimensionless thermal parameter

Eo Eötvos number

F_o total thermal buoyancy, N

g gravitational acceleration, m/s^2

Gr_b bubble Grashof number

h depth below free surface, m

Δh_A height of manometer mercury column above 0.0, "Hg

Δh_B height of manometer mercury column below 0.0, "Hg

H source depth, m

H_T total pressure, m

H_w water height in experiments, cm

NOMENCLATURE (Cont'd)

k	thermal inertial coefficient; or a constant
K	circulation, m^2/s
l	length
m	mass
m_g	mass flow rate of gas phase, m^3/s
p	pressure, Pa
p_a	sea level pressure, Pa
p_{at}	atmospheric pressure, mm Hg
p_c	calibration pressure, "Hg
p_{st}	pressure due to surface tension, Pa
P	impulse of vortex ring, kg^2/s^2
Q_g	volumetric flux of injected gas, m^3/s
r	radius of Hill's spherical vortex, cm
r	radial position of simulation bubble, cm
R	vortex radius, cm
r_b	bubble radius, cm
R_c	radius of curvature of spherical cap bubble top, m
R_g	gravity scale
R_l	length scale
r_p	particle radius, cm

NOMENCLATURE (Cont'd)

R_p	surface pressure scale
R_{v}	discharge scale
R_μ	viscosity scale
R_ρ	density scale
$R_{\Delta\rho}$	density difference scale
R_σ	interfacial tension scale
Ra	Rayleigh number
Re	Reynolds number
S	thermal strength parameter
t	time, s
T	energy of vortex ring, kg^3/s^4
T_{rm}	room temperature, °C
u	bubble group velocity, cm/s
u_{br}	initial radial starting velocity for simulation bubble, cm/s
u_{bz}	initial vertical starting velocity for simulation bubble, cm/s
u_r	simulation radial bubble velocity, cm/s
u_z	simulation vertical bubble velocity, cm/s
U	constant dye vortex velocity, cm/s
U_b	terminal velocity of a bubble, m/s
v	velocity of vortex ring, cm/s

NOMENCLATURE (Cont'd)

V_b volume of a single bubble, cm^3

V_c calibrated volume, m^3

V_g injected gas volume of a bubble group, m^3

V_t control volume, m^3

V_T injected gas volume at standard atmospheric conditions, m^3(ST)

w velocity of thermal front, m/s

w_c composite velocity of entrained liquid and gas phase (Fannelop, 1982), m/s

w_f fluid velocity (Fannelop, 1982), m/s

z thermal height above virtual origin, cm or m

z vertical position of simulation bubble, cm

α entrainment coefficient

α_i entrainment coefficient of experimental data in initial circulating stage

α_∞ asymptotic value of entrainment coefficient of experimental data after separation

γ momentum amplification factor

Δ thermal buoyancy parameter

λ dispersion ratio; ratio of corresponding geometric quantities

μ liquid dynamic viscosity, kg/m·s

μ_w viscosity of water in Equation (3.10), 0.0009 kg/m·s

ν kinematic viscosity, m^2/s

NOMENCLATURE (Cont'd)

ρ	density, kg/m^3
ρ_a	ambient density, kg/m^3
ρ_l	liquid density, kg/m^3 or g/cm^3
ρ_g	gas density, kg/m^3 or g/cm^3
ρ_{go}	gas density at sea bed, kg/m^3
ρ_o	initial thermal density, kg/m^3
ρ_T	gas density at standard atmospheric conditions, kg/m^3(ST)
σ	surface tension, dynes/cm or N/m
ψ	stream function, m^3/s

CHAPTER 1

INTRODUCTION

1.1 Problem

The rapid expansion in oil and gas exploration in offshore waters has brought with it a consequent risk to the environment in the event of an uncontrolled subsea blowout. Should a blowout occur, the buoyancy of the gas will cause hydrocarbons and entrained seawater to rise to the ocean surface in a structure which is commonly termed a bubble plume, because of its similarity to buoyant plumes in the atmosphere. At the ocean surface, the vertical motion induced by the rising bubbles will deflect radially outwards from the plume axis with little loss in momentum. This generates a shallow, fast-moving layer which is capable of transporting the oil in the plume a considerable distance from the blowout point. The large area and small thickness of the slick make containment and collection at the ocean surface difficult, and the probability that a fire will occur also increases.

Ideally, the hydrocarbons should be confined before the bubble plume has a chance to fully develop in order to minimize the risk of pollution. The optimum design of a capping or containment device requires a knowledge of the complex flow phenomena near the wellhead, since it is this behaviour which affects the overall development of the plume. A prediction of the liquid velocities at the blowout source is vital to the positioning of such equipment (Brown and Root, 1985). However, since there is normally a time lag between the occurrence of the blowout and the installation of a collecting device, an understanding of the developed-plume hydrodynamics is also necessary.

Another reason for the interest in predicting the structure of a blowout is to calculate the forces associated with momentum transfer and buoyancy loss generated by the plume on drillships or floating platforms at the surface above the wellhead. The vertical flow in the bubble plume can affect both the static and dynamic stability of a vessel. Some attempt (Milgram and Erb, 1984) has been made to estimate the effect of a blowout on semi-submersibles and other rigs, but only after a steady-flow regime has been established. The initial impact of a plume on such a structure has never been examined.

A number of predictive models have already been proposed for bubble plumes based on the assumption of steady flow in a fully-established plume. A comprehensive review of the literature has been given by Poon (1985). However, large-scale investigations into the behaviour of blowout plumes have shown that the starting-plume structure is like a single-phase thermal in appearance (Topham, 1983). The mechanism of gas release from the wellhead is also conducive to the production of thermal-like structures. As the gas emerges, a large bubble forms which rapidly shatters into smaller bubbles (Rowe and Topham, 1982). This phenomenon would tend to explain the frequently-observed unsteady nature of a bubble plume, which can lead to fluctuating dynamic forces on a rig. If the fluctuations occur at a frequency which excites a dynamic response in the vessel, oscillations may result which are likely to be considerably larger than the steady-flow predictions. A plume model based on the intermittent release of bubble groups is thus believed to be a more appropriate solution than the previous approaches which were based on a continuous steady-state flow of gas.

1.2 Background

In order to develop such a model, a fundamental knowledge of the dynamics of groups of bubbles is required. However, a search for previous work in this area revealed a surprising lack of information on these structures. It is the intent of this thesis to fill the gaps in the literature by providing experimental data, a qualitative description and a simple model of bubble group dynamics which may then be integrated into a blowout model by future investigators. It is also possible that this work will lead to a better understanding of the physical processes involved in such diverse applications as the deposition of minerals on the seabed by oceanic lava plumes and the mass transfer in the bubble columns and bioreactors.

When a group of bubbles is suddenly released into quiescent fluid, it will take on the configuration of a single-phase thermal with respect to both shape and growth pattern (Scorer, 1958). "Thermal" is a term commonly used in meteorological literature to denote the turbulent motion of a fluid parcel arising from a suddenly-released source of buoyancy into an infinite medium. The buoyancy of atmospheric thermals is due to a density difference between the thermal and the surrounding air, resulting from a difference in temperatures. However, buoyancy forces have also been induced in laboratory thermals by gradients of salt dissolved in water (Scorer and Ronne, 1956; Scorer, 1957; Woodward, 1959), chemical reactions (Turner, 1963a) and solid particles (Krishnappan, 1975; Yeomans, 1997)). These turbulent structures are normally described as being self-similar, because they exhibit a characteristic interior circulation pattern throughout their lifetimes.

As an atmospheric thermal penetrates its environment, it entrains the surrounding fluid by convective mixing through the density interface. However, the presence of a large

local density difference between the two immiscible phases in a rising bubble group implies that its behaviour could differ from that of a single-phase thermal, where the density variations are usually small.

Research into the behaviour or air-bubble plumes in water has demonstrated notable similarities and differences between two-phase and single-phase plumes, which are normally modelled using the same type of similarity argument used to describe thermal behaviour. The differences are largely due to the high density ratio between the dispersed and continuous phases and the uneven distribution of buoyancy within the plume structure. As air is so much lighter than water ($\rho_f/\rho_g \sim 800$), the gas bubbles tend to move faster than the surrounding liquid whether it is in motion or not. The differential, or slip, velocity between the rising air bubbles and water plume flow results in smaller overall plume velocities, thus reducing the vertical transport relative to that associated with a single-phase plume having the same buoyancy. On the other hand, the compressibility of air causes the buoyancy to increase with height as the gas bubbles expand due to decreasing hydrostatic pressure as they ascend. This is countered, however, by the tendency for larger bubbles to shatter due to the high level of turbulence found within bubble plumes.

Enough similarities exist, however, that it is possible to model two-phase plumes in the same manner as miscible plumes so long as the slip velocity between the two phases, the entrainment coefficient α, the dispersion ratio λ and the momentum amplification factor γ due to the presence of the gas phase are taken into account (Rowe *et al.*, 1989). These parameters must be included in a bubble plume model to reflect the fact that, instead of a density difference across the boundary between the plume and its surroundings, the fluid

inside the plume possesses more momentum than the fluid in the ambient environment, which is considered to be essentially quiescent. One of the objectives of this investigation is to determine if it is possible to model a bubble group as a single-phase thermal by the inclusion of comparable parameters in the equations.

1.3 Objectives

Specifically, the objectives of this thesis are:

(a) to review the available literature on thermals and vortex rings to provide a basis for the bubble-group model (Chapter 2);

(b) to determine the relevant geometric parameters to the problem, and to develop the appropriate scaling parameters required in order to apply the experimental results at a larger scale (Chapter 3);

(c) to discuss the bubble group experiments (Chapter 4) and examine the results in order to determine the physical basis on which to develop the mathematical formulation of the problem (Chapter 5);

(d) to develop a mathematical model describing the flow dynamics of bubble groups (Chapter 6);

(e) to evaluate any empirical relationships required for the model from the experimental data, and to verify the performance of the model (Chapter 7); and

(f) to make any recommendations for application of the results and for further study of the problem (Chapter 8).

CHAPTER 2

A REVIEW OF THERMALS AND VORTEX RINGS

2.1 Introduction

A literature review of single- and multi-phase thermals is presented in this chapter in order to provide a basis for the investigation of two-phase bubble groups. Because it is possible that the formation mechanisms may impart some initial momentum to a bubble group, a discussion of vortex rings begins the review.

If a bubble group is given an impulse when it is released, then it should behave more as a buoyant vortex ring than as a thermal in its early stages of development. However, all buoyant vortex rings ultimately evolve into thermals (Turner, 1960a), thus any distinction between the two phenomena is lost over time.

2.2 Vortex Rings

A vortex ring is an isolated closed or re-entrant vortex. Circular vortex rings do not normally occur in nature (Scorer, 1958), although there have been suggestions that vortex rings may be used to transport chimney wastes to high altitudes (Turner, 1960b) and that vortex rings may form from the trailing vortices behind aircraft and from flares in the solar atmosphere (Maxworthy, 1972). However, they may be artificially induced by dropping beads of one liquid into another, by puffing fluid out of a hole, or by exhaling smoke from a cigarette.

The theory and behaviour of vortex rings was first investigated in detail in the previous century. Based on the work of Helmholtz, Kelvin, Reynolds and Sir William Thomson, Thomson (1883) compiled a summary of the equations describing the motion in an inviscid fluid of isolated and multiple vortex rings. He applied these results to Kelvin's vortex atom theory of gases, and also proposed the rudiments of a vortex atom theory of chemical action.

A concise description of the known results for vortex rings in an perfect fluid of density ρ may be found in Lamb (1932). If it is assumed that the vorticity of a ring is concentrated near a circle of radius R, and is uniformly distributed over a circular cross-section of radius $a << R$, then the energy T, velocity v and impulse P of the ring may be given in terms of R, a and the circulation K by the following relations:

$$T = \frac{K^2 R \rho}{2}\left[\ln\frac{8R}{a} - \frac{7}{4}\right] \tag{2.1}$$

$$v = \frac{K}{4\pi R}\left[\ln\frac{8R}{a} - \frac{1}{4}\right] \tag{2.2}$$

$$P = \pi \rho K R^2 \tag{2.3}$$

A special case of a vortex ring in which the vorticity is spread over all of the moving region is that of Hill's spherical vortex. In terms of the mean radius R of the vortex, which is related to the radius r of the sphere by $R = (0.4)^{1/2}r$, the energy, velocity and impulse are:

$$T = \frac{1}{7} (0.4)^{1/2} \pi \rho K^2 R \tag{2.4}$$

$$v = \frac{1}{5} (0.4)^{1/2} \frac{K}{R} \tag{2.5}$$

$$P = \pi \rho K R^2 \tag{2.6}$$

Equations (2.4) to (2.6) represent a vortex moving with constant velocity and size through inviscid surroundings. The flow outside the sphere is the same as the potential flow of a stream passing around a solid sphere, and the velocity components are continuous at the boundary. Figure 2.1 shows the development of a Hill's spherical vortex from a transient pulse.

This model, with the addition of arbitrary parameters representing the aerodynamic interaction and the mass exchange of the vortex with the surrounding air, was used by Levine (1959) to describe the motion in the interior of cumulus clouds. His discussion, however, was restricted to the case of a vortex of constant size which is interchanging fluid with the surroundings in some unspecified way. Woodward (1959) also showed experimentally that the motion inside a thermal is instantaneously like that in a slightly-flattened spherical vortex. Other applications for Hill's spherical vortex include the motion of bubbles and droplets at high Reynolds number (Moore, 1962; Harper and Moore, 1968) and the formation of laminar wakes behind spherical cap bubbles (Wegener and Parlange, 1973).

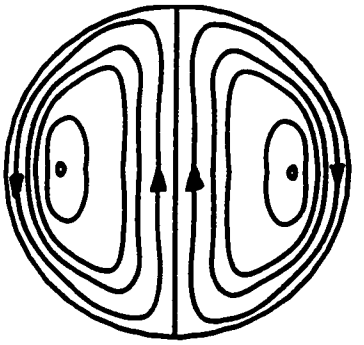

(c) Fully-Developed Hill's Spherical Vortex

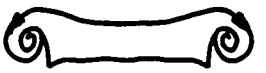

(b) Direction of Vortex Rollup in Intermediate Growth Stage

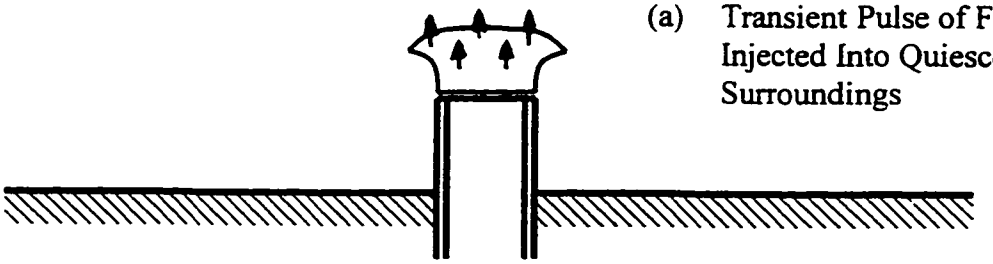

(a) Transient Pulse of Fluid Injected Into Quiescent Surroundings

FIGURE 2.1 - Schematic of a Hill's Spherical Vortex (c) Developing from a Transient Pulse of Fluid (a) Injected into a Quiescent Ambient Fluid. Figure (b) Illustrates the Direction of Vortex Rollup in the Intermediate Stage of Growth.

A mathematical analysis of Hill's spherical vortex was undertaken by Pozrikidis (1986) to study the effect of axisymmetric perturbations on the vortex shape and motion. He found that the perturbations varied as to whether the vortex became an oblate or prolate spheroid, and determined that the structure of the asymptotic rings arising from oblate vortices is similar to that of the family of vortices described by Norbury (1973).

In order to reconcile the observed slowing and expansion of a real vortex ring with time (Reynolds, 1876) with the inviscid models available in literature (Lamb, 1932), Saffman (1970) assumed that the initially small core of vorticity would grow by viscous diffusion. His resultant model correctly predicted the slowing of the ring, but because of his assumptions of constant circulation and impulse could not describe the increase of the mean radius with time.

Turner (1964a) modified the equations of a Hill's spherical vortex to allow for an expansion in radius proportional to the distance travelled in order to generate a kinematic model of the flow around and into a buoyant thermal. His model neglected viscosity in the external motion, and assumed that the only resistance to motion of the spherical vortex arose because of the addition or displacement of the external fluid, which must be accelerated from rest. The slowing of the vortex with time was not addressed in his investigation.

Maxworthy (1972) performed a series of experiments to determine the flow field, ring velocity and growth rate of laminar vortex rings. He determined, with the use of dye-injection and hydrogen-bubble techniques, that the vorticity of stable rings is distributed through a fluid volume larger than and moving with the visible core. Diffusion of the vorticity out of the moving ring into the outer, substantially irrotational, fluid caused some

of this fluid to be entrained into the interior of the ring, while the rest was left behind, accounting for the appearance of ring vorticity in a wake. He proposed a simple viscous entrainment model, in which the impulse of the moving fluid body remained constant, to describe the observed flow. It was found that this model was adequate unless the impulse shed to the wake accounted for a significant fraction of the initial impulse.

Maxworthy (1972) also suggested that vortex rings of high Reynolds number ($\geq 10^3$) are unstable, due to vorticity of the opposite sign generated in the boundary layer on the outside of the orifice and swept into the core during the roll-up process. An experimental investigation into these turbulent vortex rings (1974) showed that this core consists of fine-scale turbulence surrounded by a co-moving bubble of larger-scale turbulence. This bubble entrains outer fluid, mixes with it and deposits the majority into a wake together with a small fraction of the total vorticity of the ring. However, Maxworthy was unable to prove his theory that vorticity of the opposite sign was responsible for vortex-ring instability, and also shed doubts on Widnall and Sullivan's (1973) suggestion of a short wavelength instability of the core flow.

A further series of experiments on high Reynolds number vortex rings (1977) in both stratified and unstratified surroundings enabled Maxworthy to substantially confirm the turbulent ring model he developed in 1974. He also determined that the formation process of vortex rings was strongly Reynolds-number dependent, that vorticity of the opposite sign was incorporated into the core at the nozzle and that axial flow caused by normal instability waves in the form of a propagating wave had the effect of preventing further ring instability.

Observations of the interaction between two nearly-identical vortex rings travelling a common path led Maxworthy (1972) to dispute the common belief (Scorer, 1958) that rings would continually pass back and forth through one another. He found that the rearward ring would become entrained into the forward one to form a single large vortex. Only when the rearward ring had a much higher velocity than its partner could it emerge from the joining process and leave a slower-moving ring behind. However, Yamada and Matsui (1979) achieved recurring slip-though of identical pairs of vortices between Reynolds numbers of 800 and 2000. Above this value, the rings tended to coalesce once slip-though had been achieved.

Vortex-ring interaction was also used by Kiya *et al.* (1986) to understand how free-stream turbulence affects the vortex-pairing mechanism in shear layers. Because turbulent shear layers consist of structures which look like vortex pairs, rings and lines, the investigators were able to use these structures as models of external or free-stream vortices in their experiments and numerical model.

2.3 Buoyant Vortex Rings

Turner (1957) found that a vortex ring containing fluid with a density less than that of the surroundings will have a markedly different behaviour from that of a non-buoyant vortex ring. He postulated a theory for buoyant vortex rings based on the perfect-fluid equations described previously, but assumed that circulation would remain constant with time while the buoyancy would give a greater expansion rate and a lower velocity of rise.

He also found that in the case of a ring rising though a stably-stratified fluid with a constant density gradient, increasing the buoyancy would lead to a lower final height of the ring.

Turner (1960a) further suggested that a thermal released from rest can be regarded as a special case of a buoyant vortex ring with a small initial circulation. Because vorticity and vertical momentum produced from buoyancy increase proportionally to the time for which the buoyancy has operated, it will ultimately exceed any initial values imparted to the buoyant fluid from an impulse. Thus, any buoyant vortex ring will ultimately become a thermal, although increasing the initial circulation leads to a smaller value of the angle of spread and hence less mixing with the surroundings.

The laminar motion produced by an extremely small quantity of buoyancy was analyzed by Morton (1960). He obtained similarity solutions for the momentum and heat transfer equations through an expansion about the limit of zero Rayleigh number, and found the height risen by weak thermal vortex rings is directly proportional to Ra. Morton's analysis predicted a flow pattern similar to that of a turbulent thermal, with a growth process dominated by viscous and thermal diffusion, although there is no concentration of heat in the circular core of a weak vortex ring.

Fohl (1968) found that the expansion rate of buoyant vortex rings was a function of the size of the turbulent eddies which occurred during ring formation. The larger the size of the eddies in the initial phase, the larger was the expansion rate and the higher the uncertainty in predictions of the expansion rate.

2.4 Thermals

The term "thermal" has gained acceptance in meteorological literature to denote a parcel of fluid that rises under the influence of buoyancy forces, and evolves by mixing with its surroundings. Thermal motion studies have been used to predict the formation of cumulus clouds (Levine, 1959; Scorer, 1957) and the behaviour of fireballs from nuclear explosions (Taylor, 1950). The development of the ejected gas in a plasma-jet ignition system (Topham *et al.*, 1984) has also been described using a thermal model.

The buoyancy of atmospheric thermals is due to a density difference between the thermal and the surrounding air, resulting from a difference in temperatures. However, a density difference between two phases may also be a source of buoyancy. Single- and two-phase thermals will be discussed in the following sections.

2.4.1 Single-Phase Thermals

An ideal thermal can be either axially- or plane-symmetric, and is assumed to originate from a point or line source into a stagnant fluid. As its vertical motion progresses due to a density difference between the buoyant parcel and its surroundings, convective mixing develops across the interface. Two differing theoretical models have been postulated to describe this mixing process.

The first type of theory (Morton *et al.*, 1956; Scorer, 1957) assumes that as the turbulent thermal rises through quiescent surroundings, the action of the buoyancy forces produces internal circulation, which results in entrainment of the ambient fluid into the thermal through a vortex-ring-like motion (Woodward, 1959). The mixing between the

ambient fluid and the thermal itself leads to a reduction of the density difference and hence a weakening of the buoyancy force which drives the rising motion of the thermal.

Using dimensional arguments, a similarity solution can be formulated for a single-phase thermal based on powers of the height z above a point source and the total buoyancy $F_o = \Delta_o$ x (*total volume released*). This solution has the form

$$b = \alpha z \tag{2.7}$$

$$w \sim F_o^{1/2} z^{-1} \tag{2.8}$$

$$\Delta \sim F_o z^{-3} \tag{2.9}$$

where w is the velocity at the front of the thermal, and

$$\Delta = g \frac{\rho_o - \rho}{\rho_l} \tag{2.10}$$

i.e. it is the local density difference between the thermal and the environment at height z compared to the density at the source. This solution is only applicable to real sources by locating a virtual point source below the real source and measuring relative to the virtual source (Turner, 1969).

By assuming that the inflow velocity into a thermal is proportional to the mean upward velocity and surface area, Morton *et al.* (1956) were able to use the entrainment assumption to formulate the dynamics of thermals. This method is another type of similarity argument, which requires the same kind of turbulence structure and balance of forces at each

height (Turner, 1969). The equations of conservation of mass, momentum and buoyancy take the form

$$\frac{d}{dt}\left(b^3 \right) = 3\,\alpha\, b^2\, w \tag{2.11}$$

$$\frac{d}{dt}\left(b^3\, w \right) = b^3\, \Delta \tag{2.12}$$

$$\frac{d}{dt}\left(b^3\, \Delta \right) = b^3\, w\, g\, \frac{d\rho_o}{dz} \tag{2.13}$$

where α, the entrainment coefficient, is equal to the half angle of spread defined by Equation (2.7).

The second method of approach assumes that the thermal is a region of constant size which interchanges fluid with its surroundings at a rate governed by the turbulence level in the environment (Priestley, 1954). This type of thermal, or "open parcel", loses buoyancy and momentum to the surroundings at a size-dependent rate. Thus, two thermals of differing sizes would behave differently in the same environment. An example of this type of model is that proposed by Telford (1966) to describe isolated convective plumes and thermals.

Turner (1963b) attempted to reconcile the two theories of thermal mixing by proposing a model of a thermal in turbulent surroundings which accounted for the growth by entrainment and loss of buoyant fluid to the surroundings due to erosion by environmental turbulence. The outflow velocity was taken to be constant with height, and proportional to

a characteristic turbulent velocity in the environment which was found to be in the order of, but less than, the root-mean-square turbulent velocity. The model showed that the entire character of the motion of buoyant parcels could be dominated by small changes in environmental turbulence, especially in unstable surroundings.

It is possible to classify thermals as being either weak or strong by considering the density difference between the thermal and its surroundings. If the density of the thermal is close to that of the environment, the variation of density does not produce a sizeable variation in the inertia of fluid particles but does affect a buoyant force. This is the Boussinesq approximation, which is generally valid when the density difference $\Delta \rho$ divided by the surrounding density ρ_a is 0.1 or less. A thermal for which the Boussinesq approximation holds is a weak thermal, while strong thermals are those in which the effects of fluid inertia are significant.

Experimental investigations of weak buoyant thermals have been reported by Morton *et al.* (1956), Scorer and Ronne (1956), Scorer (1957) and Woodward (1959). In these experiments, initial positive or negative buoyancy was introduced by a sudden release of finely-dispersed precipitates of different density into the ambient fluid. It was found that in any given experiment α remained constant, with a mean value of 0.25 (Scorer, 1957), but there was considerable variation from one experiment to another. Strong buoyant thermals with a large density difference have been investigated experimentally by Wang (1971) and Lin *et al.* (1972). They found that the mass entrainment process penetrated deeply into the thermal structure, and that turbulent mixing proceeded at all depths. This differs from the findings of Batchelor (1954), who noted that in very light thermals the velocity fluctuations

produced by the internal motion cannot penetrate the external fluid because of the small inertia. The experiments of Lin *et al.* (1972) also indicated the existence of a thermal wake in strongly-heated thermals, which was also supported by the findings of Batt *et al.* (1984).

Baines and Hopfinger (1984) performed an analytical and experimental study of light and heavy thermals, and found that the effects of a large density difference are small and only exist over a short distance from the source. This was attributed to the large entrainment rate of all thermals, which ensures that the Boussinesq approximation is reached after a thermal rises or descends two diameters. In general, they found that the rate of growth for a heavy thermal is always larger than for the Boussinesq case, and smaller for a light thermal.

Laboratory observations of the behaviour of extremely viscous thermals with small Reynolds numbers and large Rayleigh numbers were made by Griffiths (1986). Although his thermals were similar in appearance to weak and turbulent thermals, their entrainment was found to be Rayleigh-number dependent. The results of the experimental work and a self-similar model based on a boundary-layer analysis were felt to be relevant to studies of thermal convection in magma and the earth's mantle.

Johari (1989) carried out a series of experiments on thermals with buoyancy reversal to simulate the evaporative cooling in cumulus clouds. He used a planar laser-induced fluorescence technique to show that mixing and entrainment in thermals is controlled by the large-scale motion in the vortex core rather than by the smaller-scale turbulent eddies located at the front and sides of the structure. His findings that the entrainment in thermals occurs chiefly through fluid entering from behind rather than by diffusion across the density interface supports Woodward's (1959) earlier conjectures.

Most of the laboratory investigations of thermals have been confined to experiments in an unstratified medium. Richards (1961) and Saunders (1962) observed the penetration of thermals through the interface between homogeneous fluids of varying densities. Richards found that the behaviour after the front of the negatively-buoyant thermal entered the lower layer was dependent on the value of a parameter S, which determined whether a thermal was strong or weak. Saunders showed that a weak stratification was capable of halting a thermal, but restoring buoyancy forces developed a reverse circulation when the lower layer was penetrated. For strong circulations, the dissipation of the thermal was associated with a gradual decay of the original circulation rather than a reverse circulation.

Except for several individual experiments reported by Scorer and Ronne (1956) and Morton *et al.* (1956), only Cerasoli (1978) and Sánchez *et al.* (1989) appear to have simulated a constant linear density gradient in the laboratory. Cerasoli observed that line thermals penetrated only a few initial diameters into the stratified medium due to efficient mixing between the thermals and their environment.

Sánchez *et al.* (1989) examined the transient behaviour of thermals previous to the development of self-similarity by releasing laboratory thermals from very close to a state of rest in both stratified and unstratified surroundings. They found that a thermal starting from rest exhibited a much smaller entrainment rate than a self-similar thermal for a distance of at least six initial diameters from its starting point. Numerical simulations carried out using an axisymmetric, two-fluid model predicted a linearly-increasing thermal volume, while the observed volume of their laboratory thermals exhibited an exponential increase.

If two thermals are released in succession from the same point, they will eventually amalgamate (Scorer, 1958). If the thermals are originally equal in size, the union will increase the overall rise rate by a factor of 2.5. Overcamp (1983) experimentally verified this behaviour, but found the factor was closer to 2.3.

2.4.2 Entrainment

Although the entrainment assumption of Morton *et al.* (1956) has already been discussed briefly, a more in-depth examination of this concept is appropriate since the majority of thermal models are based upon it.

Thermals belong to a class of turbulent motion which is generally described as self-similar. This implies that once the motion is established, all velocities remain in fixed proportion and the motion remains geometrically similar, differing only in scale (*i.e.* there is no fixed physical length scale). Thermals have a well-defined edge which divides the turbulent interior from its quiescent surrounding. The entrainment hypothesis states that the rate at which ambient fluid is incorporated into the turbulent interior across this interface is proportional to the surface area of the interface and a characteristic velocity difference between the turbulent and the ambient fluids. The similarity of the velocity fields during the course of the motion allows for any easily observable velocity to be used as a basis for the entrainment coefficient. Also, because the rate of entrainment is proportional to velocity, the angle of spread is independent of the total buoyancy released as long as no additional momentum is injected at the source.

It should be noted here that the entrainment hypothesis, as applied to thermals, always assumes that the rate of spread is linear with height, regardless of any other properties of the thermal. Turner (1986) has questioned the propriety of describing thermal growth as an 'entrainment' process *per se*, as his previous work has shown that the expansion of buoyant plumes is nonlinear and depends on other properties of the system in addition to the entrainment coefficient α (Turner, 1973).

The evolution of the entrainment hypothesis can be closely identified with the history of cumulus cloud research. Entrainment was first postulated qualitatively by Namias (1939), but the first definitive proof of cloud entrainment was provided by Stommel (1947) , who measured the temperature profiles inside clouds. Almost concurrently, measurements taken in the Thunderstorm Project by Byers and Hull (1949) provided evidence of lateral cumulus entrainment.

Cumulus research also led to the first laboratory experiments on thermals. The entrainment characteristics of cumuli and laboratory thermals were found to be quite similar by Scorer and Ludlam (1953). Their investigation was followed by a host of similar experiments, including those of Morton *et al.* (1956), whose theoretical analysis of their results has remained the basis of most of the plume and thermal models to this day.

Reviews of the history of cumulus cloud entrainment can be found in Simpson (1983) and Reuter (1986). The major controversy in this area over the years has been whether cumuli entrain through their sides or through their tops. Laboratory studies of thermals have played an integral role in determining the answer to this problem, by demonstrating that

single-phase thermals entrain the surrounding fluid primarily through fluid entering from the bottom.

2.4.3 Virtual or Added Mass

If a solid body is accelerated through a fluid otherwise at rest, some of the surrounding fluid is set into motion. The apparent inertia of this moving fluid can be represented by an "added" or "virtual" mass term superimposed on the mass of the body. The concept of virtual mass provides a simplistic means of accounting for the disturbance of a moving body inside the fluid, and is much less complex than calculating the pressure distribution over the body surface.

Darwin (1953) showed that, when a solid body moves through an incompressible ideal fluid, it induces a drift in the fluid so that the hydrodynamic mass of fluid should be added to that of the body in order to calculate its kinetic energy. He defined a drift volume as that enclosed between the initial and the final position of the wall of fluid particles at right angles to the motion of a sphere. Multiplying the drift volume by the density of the fluid gave what he termed the "drift mass", which is identical to the concept of added or virtual mass. Darwin found a value of 0.5 for the drift mass of a sphere without considering the effects of any viscous forces or neighboring spheres. This value has been corroborated by the work of Benjamin (1986) and Kowe *et al.* (1988).

The concept of virtual mass can also be extended to a moving fluid mass accelerating through a fluid at rest, although in this case it is generally described as added mass or virtual

inertia. The effect of added mass was included by Escudier and Maxworthy (1973) in their analysis of the motion of a turbulent thermal. By revising the momentum equation (2.12) to

$$\frac{d}{dt} [b^3 (\rho + k \rho_o) w] = b^3 g (\rho_o - \rho) \qquad \textbf{(2.14)}$$

where k is the inertial coefficient for a thermal, they found that neglecting the virtual inertia term would introduce large errors into the calculations whether the density difference between the thermal and its surroundings was large or small. They suggested a value for k of 0.5, assuming a spherical shape for the thermal, although they thought that this value might depend to some extent on the entrainment rate, as the external flow around an impermeable sphere could differ from that around an entraining sphere.

Although Turner (1957) had previously assumed that the main features of thermal behaviour would not be very sensitive to the effect of virtual mass, he later (1963b, 1964b) included a virtual mass coefficient in the momentum equation buoyancy terms to take some account of the motion in the environment near the thermal. He also determined that using the virtual mass coefficient for a sphere instead of the more accurate value for an oblate spheroid of revolution would only introduce errors of approximately five percent into his calculations.

2.4.4 Solid-Particle Two-Phase Thermals

Solid particle thermals have been investigated by Edge and Dysart (1972) and Koh and Chang (1973), who studied the dispersion and settling of dredged wastes in the ocean by assuming that the solid particles could be treated as a denser liquid. Koh and

Chang identified three stages of motion for dumped material: convective descent; collapse; and long-term dispersion by ambient turbulence. In at least the first of these stages, the flow in the "cloud" of dumped material follows the self-similar type of motion found in atmospheric thermals.

A similar approach was taken by Nakatsuji, Tamai and Murota (1990) in their experiments with glass bead and sand clouds in water, although they only identified two typical flow patterns: "thermal-like" motion, and "settling" motion. The major drawbacks to their assumption of self-similarity is that it ignores the fact that the density of the particles remains constant and that they eventually reach a terminal velocity which may not equal the speed of the liquid which they set into motion. Thus, the fluid inside a solid particle thermal should be differentiated from the surrounding fluid by a momentum difference rather than by a density difference at the boundary.

Krishnappan (1975) carried out a series of laboratory experiments on the behaviour of solid particle clouds in order to develop a simple method of modelling their behaviour. In contrast to the previous work in this area by Koh and Chang (1973) and Edge and Dysart (1972), he realized that the behaviour of solid particles moving in a liquid medium is different from that of an equivalent denser liquid moving in the same medium. Krishnappan identified two stages of flow development for solid particle clouds as a result of his observations: an initial "entrainment" stage where the cloud size grows due to the incorporation of external fluid; and a "settling" phase where the cloud velocity equals the terminal velocity of the individual solid particles and the radius of the cloud remains constant. Krishnappan used dimensional analysis to determine an entrainment coefficient

and a velocity coefficient for the entrainment stage, which were both assumed to be functions of a Grashof number representative of both the solid and fluid phases. Terminal velocities in the settling phase were determined by the relationship between the Reynolds number and the Grashof number. After separation of the particles and the fluid, he extended the single-phase model using the theory of turbulent diffusion by assuming a Gaussian concentration of solid particles and a diffusion coefficient that followed the 4/3 power law.

Lee (1992) carried out a series of experiments in which polystyrene beads and fluorescein (green) dye were released into a large water tank. The beads used in these tests had densities slightly heavier than that of water, and the release mechanism was designed to minimize any initial momentum from the equipment. Lee found that the evolving motion of particle thermals before the settling phase can be subdivided into three stages: single-phase, two-phase and separation. Lee developed one-dimensional theoretical models for each of these stages, and the results from these models showed a reasonable agreement with his experimental data.

Noh and Fernando (1993) studied the sedimentation of two-dimensional solid particle thermals by examining the release of glass beads and dye into a water tank. They determined a critical depth at which particle clouds pass from a "thermal" regime, where the clouds move with the convectional fluid motions characteristic of thermals, to a "particle-settling" regime, where the particles descend with little disturbance to the ambient fluid. Noh and Fernando found that this critical depth corresponded to a point where the thermal fluid velocity was greater than the terminal velocity of the glass particles, not where they were equal, and that

the turbulence generated in the thermal regime continued for a period of time after the transition between the two regimes was reached.

Further work was carried out by Luketina and Wilkinson (1994) to determine the maximum depth at which particles would reach when dumped into deep water. They found that debris dumped in water behaved as a two-phase thermal with negative buoyancy, and that the thermal reached its maximum depth when its downward motion was slowed by a loss of buoyancy due to both entrainment of the surrounding fluid and separation of the particles from the thermal.

The most recent experimental analysis of two-phase solid particle thermal behaviour is that of Yeomans (1997), who performed a series of experiments using four different glass particle grain sizes and dye released without impulse into undisturbed water. Yeomans also proposed a two-phase model using both Stokes and non-Stokes drag relationships, which allowed for uniform and non-uniform thermal speeds. The model was based on the work of Topham *et al.* (1994), who assumed that the particle motion was taking place against a background fluid flow field consisting of a Hill's spherical vortex within the thermal and potential flow outside.

2.4.5 Gas-Liquid Two-Phase Thermals

In contrast to the well-developed literature on single-phase and solid particle thermals, there are few available references on gas-liquid or bubble "thermals". Scorer (1958) investigated the behaviour of clouds of bubbles produced by injecting air through a perforated orifice into water. He found that these rising bubble groups resembled single-

phase thermals in shape and linear growth pattern, and had an updraft in their wakes which rose at two to three times the speed of the thermal cap. This phenomenon was attributed to the virtual mass effect in the updraught formed by the overlapping wakes of the circulating individual bubbles. Other than these few qualitative observations, however, his work was not well-documented.

Turner (1963a) simulated the behaviour of single-phase thermals with increasing buoyancy by chemically releasing small gas bubbles in liquid. He investigated thermals with both constant acceleration and constant velocity, and in both cases reported a linear relationship between radius and height, with the mean angles of spread slightly smaller than they would be for constant-buoyancy thermals in neutral, unstratified surroundings.

Johari and Briedenthal (1987) conducted experiments on thermals with buoyancy reversal by releasing a heavy liquid into a uniform aqueous tank. A chemical reaction between the two fluids produced tiny gas bubbles which were sufficiently small that they merely altered the effective mean density of the thermal and did not rise away from the surrounding liquid. The dynamics of these thermals were found to be dependent on a dimensionless density parameter D^*. It was demonstrated that above a certain threshold value of D^*, the mixing was dramatically inhibited compared to mixing in non-reacting thermals and a bifurcation, or splitting, of the thermals was always observed. At very large values of D^*, the thermal would leave mixed fluid behind in its wake so that the core of the structure remained unmixed.

Fraser (1981) produced bubble thermals which exhibited an initial linear entrainment stage characterized by accelerating cap velocity, followed by an abrupt transition to a phase

of constant velocity and no expansion. He also found that flow tracers were left behind when the thermal reached a certain height, which was a function of the initial volume of air released.

Fannelop (1982) attempted to produce bubble thermals without any initial impulse, but was only able to generate spherical cap bubbles. He did, however, propose a pseudo-single-phase model which accounted for the isothermal expansion of gas with reduced hydrostatic pressure during the ascent of the bubble group to the water surface. Following the entrainment assumption of Morton *et al.* (1956), he gave the continuity equation as:

$$\frac{d}{dt}(b^3) = 3\alpha w_c b^2 \qquad \textbf{(2.15)}$$

where b is the thermal radius, α is an entrainment coefficient assumed to be between 0.2 and 0.3 as for atmospheric thermals, and w_c is a composite velocity of the entrained liquid plus the gas phase defined by:

$$w_c A_c = w_f A_f + \frac{\dot{m}_g}{\rho_g} \qquad \textbf{(2.16)}$$

where A_c is the area of the largest cross section of the thermal, and A_f is the cross-sectional area of the moving fluid at that height. This composite velocity was therefore not assumed to be equal to the slip velocity of the individual bubbles.

The momentum equation was given as:

$$\frac{d}{dt}\left(b^3 w \right) = F_o \frac{H}{H - z} \qquad \textbf{(2.17)}$$

The buoyancy parameter F_o relates to the initial gas volume at the source V_{go} by:

$$F_o = \frac{V_{g_o}}{2\ \pi}\ g = constant \tag{2.18}$$

and the $H/(H-z)$ term accounts for the expansion as the gas rises. Fannelop assumed that:

$$H - h = 10\ m = h + \frac{p_a}{g\ \rho_{g_o}} \tag{2.19}$$

where h is the water depth, ρ_{go} is the gas density at the sea bed and p_a is the sea level pressure.

Solutions for the thermal radius and upward rise velocity of the form:

$$b = \alpha\ z \tag{2.20}$$

$$w = \left[\frac{2\ F_o\ H}{\alpha^3} \right]^{1/2} z^{-3} \left[H^3 \ln\left(\frac{H}{H - z} \right) \frac{z^3}{3} + \frac{H\ z^2}{2} + H^2\ z \right]^{1/2} \tag{2.21}$$

were expressed by Fannelop to satisfy the momentum and continuity requirements.

Fannelop's model assumed that the gas phase is well mixed with the liquid phase, and that the "thermal" is a perfect sphere. In addition, the buoyancy is the sole parameter which was said to govern the motion, and this was related back to the initial conditions. Although this theory takes into account the gas-phase expansion as the thermal rises, as well as a virtual mass term of 0.5 which is appropriate for a sphere, it did not address the manner in

which the bubbles are actually distributed in the fluid. In addition, the only resistance to motion which was accounted for in Fannelop's model was that due to the entrainment of external fluid into the expanding sphere, and by the virtual mass effect due to the displacement of the surrounding fluid. The contributions of the individual bubbles were ignored.

The initial experimental work in this research quickly demonstrated that Fannelop's model was inadequate to describe the motion of two-phase gas-liquid "thermals". Figure 2.2 shows that bubble groups tend to develop similarly to a solid particle cloud dumped into water, rather than expanding at a constant rate of entrainment. In addition, the velocity distribution of Equation (2.21) was not evidenced by any of the experimental bubble "thermals". As a result, a systematic research program was developed, in order to generate a database on which to base a model more appropriate to the behaviour of bubble groups in water. This program is described in the following chapters.

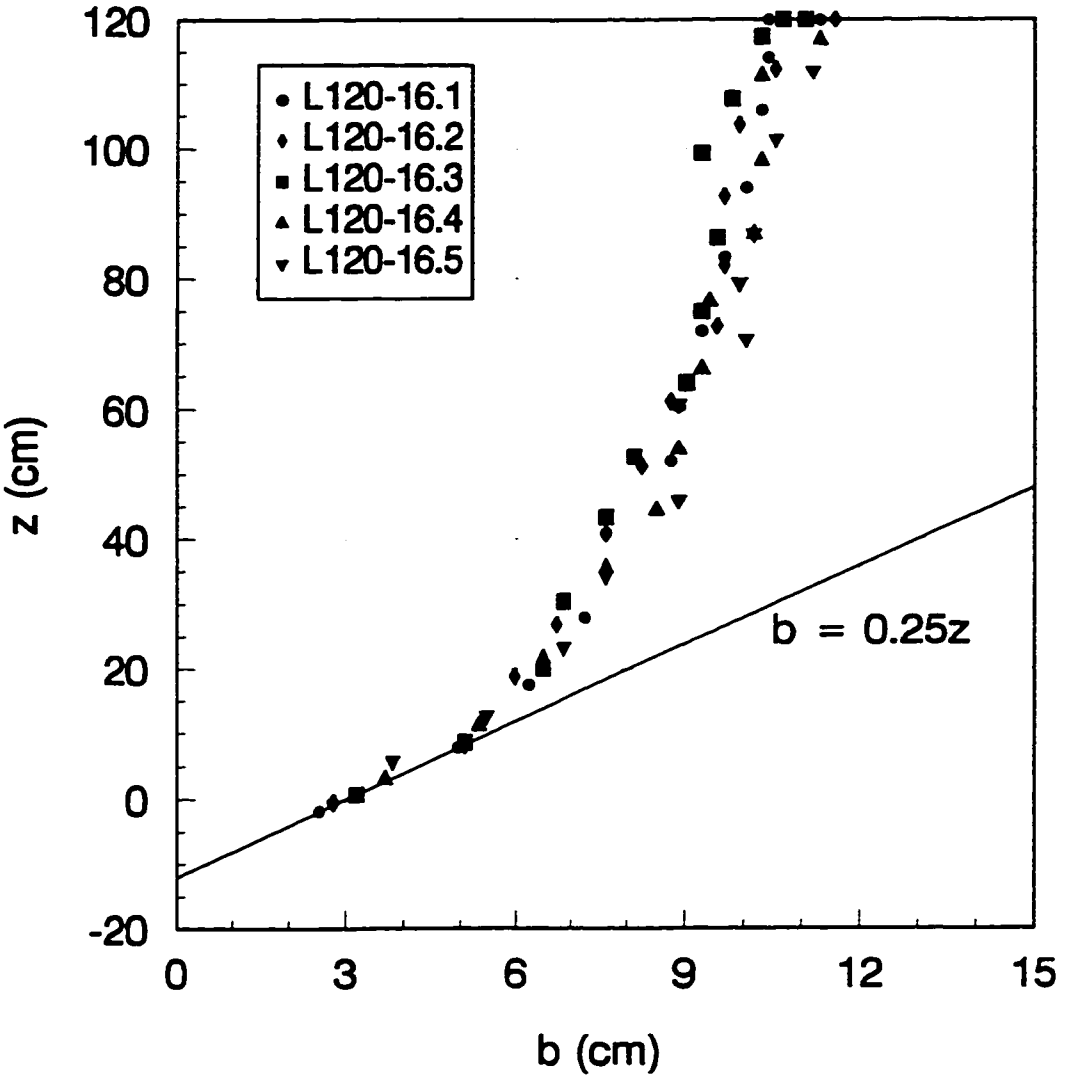

FIGURE 2.2 - Development of the Radius b of Experimental Bubble "Thermals" with Height z vs. Equation (2.21) with $\alpha = 0.25$. Five Data Sets are Presented (L120-16.1 to L120-16.5) from the Large Tank Tests for a Water Depth of 120 cm and an Injected Air Volume of 16 cm^3(ST)

CHAPTER 3

DIMENSIONAL ANALYSIS AND SCALING PARAMETERS

3.1 Model Theory

A model is a device or means which is so designed that it can be used to predict accurately the performance of a full-scale physical system or prototype. The model will be scientifically valid if a number of its measurable characteristics are related to their counterparts in the prototype by certain constant proportions which satisfy definite mathematical conditions. These constants of proportion are called scaling parameters, and the mathematical conditions which must be satisfied are called the criteria of similitude.

The use of invariant groups in the design of hydraulic models has been popular since the late 19th century. Because these groups of quantities retain a constant numerical value regardless of the system of fundamental units (mass, m; length, l; and time, t) used to formulate them, they are useful when expressing mathematically the relationships existing between the corresponding characteristic quantities of processes taking place at different scales. The application of these relationships to the formulation of a research program is commonly known as "model theory" (Ivicsics, 1975).

The existence of a unique mathematical relationship between fluid phenomena at the scale of the laboratory and full-size systems makes it possible to generalize the results obtained by a relatively small number of measurements. However, care must be taken in choosing the characteristic variables used to form the invariant or dimensionless groups. If a quantity which has a dominant influence on the course of a physical phenomenon is

omitted, this will lead to erroneous results when measurements and observations made at the experimental scale are transferred to a prototype.

In order for a process to be termed similar, the ratio of the corresponding characteristic quantities (length, mass and time) involved must be constant. The process will be dynamically similar if the criteria of geometrical, kinematic and dynamic similarity are all satisfied simultaneously. The chief drawback with the use of invariant groups in the modelling of fluid systems lies in the difficulty of obtaining a consistent solution to the criteria of similitude between the scales of the model and prototype. A well-known example of this problem is found in ship design, where the Froude and the Reynolds numbers are the relevant dimensionless groups in determining the resistance of a hull moving through water. If the ratio of corresponding geometrical quantities is denoted by λ, it can easily be shown that the scale factor of the velocities would be $\lambda^{1/2}$ on the basis of the Froude number, and λ^{-1} on that of the Reynolds number. The force, acceleration and time quantities are also affected. Since similitude implies the identity of all the dimensionless laws governing the model and the prototype phenomena, it is obvious that in this case the realization of a mechanically similar model is impossible.

In practice, it is possible to overcome this particular difficulty by resolving the full resistance into two components. The magnitudes of the individual components may be converted to the prototype scale with the use of appropriate conversion factors and then combined, thus yielding the correct value without violating the criteria of similitude. However, in many cases, the only solution is to construct a partially-similar or distorted

model, where only some of the properties are reproduced accurately. Such models are only reliable in the limited range for which they are designed.

Despite the practical difficulties involved in the use of model theory in the design of a laboratory research program, this approach has remained popular because of its simplicity, its economic advantages and because it facilitates the evaluation of the measured data. Model theory also has the advantage of providing qualitative as well as quantitative information about the fluid phenomena under examination. Because it was felt that the positive aspects of model theory outweigh the drawbacks, it was decided to apply this approach to the investigation of bubble group behaviour.

The development of a reliable model requires the determination of the similarity criteria and the pertinent scaling parameters. In what follows, the selection of the important bubble group parameters is discussed, as are the physical constraints encountered in the establishment of the scaling laws.

3.2 Dimensional Considerations

A number of methods are available in the literature for the determination of invariant groups, *i.e.* Ivicsics (1975) lists eight. The choice of which approach to use is usually made on the basis of convenience, as most of these methods are interrelated. Dimensional analysis was selected for the derivation of the appropriate dimensionless groups to describe bubble group behaviour, because it has the advantage of suggesting the pattern which the experimental work should follow as well as simplifying the presentation of the experimental results.

Prior to the development of the important bubble group parameters, a short literature review discussing bubble generation and the estimation of the terminal velocities has been included. The size and slip velocity of the individual bubbles in the group will affect their collective behaviour, and thus the physical variables which control the former may also be important for the latter.

3.2.1 Bubble Size

It is important to understand the ways in which bubbles can be formed, as bubble size has an influence on the dynamics of a bubbly mixture, and it must often be specified in terms of the mechanism of bubble generation. This influence appears in the form of fluid dynamic and interfacial forces due to injection momentum, inertia of the displaced liquid, buoyancy, interfacial tension and drag during rise. Bubble size is also a function of the distance travelled from the point of injection, not only due to hydrostatic expansion, but to the tendency of bubbles to coalesce as they touch each other if they are smaller than the maximum stable size for the prevailing shear field. Conversely, if they are larger than a critical size, they will break up and grow again (Thomas, 1981).

If the bubbles are formed by injection through an orifice, their size is in general a function of the orifice diameter d, the density ρ_g and volumetric flux Q_g of the injected gas and the properties of the surrounding liquid: density ρ_f, viscosity μ, surface tension coefficient σ, and the acceleration of gravity g. Tekeli and Maxwell (1978) have shown this dependence in dimensionless form:

$$\frac{d_b}{d} = f\left[\frac{\sigma}{g\,(\rho_f - \rho_g)\,d^2},\ \frac{Q_g^2}{g\,\frac{(\rho_g - \rho_g)}{\rho_f}\,d^5},\ \frac{\rho_f\,Q_g}{\mu\,d} \right] \tag{3.1}$$

Experimental and analytical studies (Wallis, 1969) indicate that for small orifices with low gas flow rates, the above relationship becomes:

$$d_b = k\left[\frac{\sigma\,d}{g\,(\rho_f - \rho_g)} \right]^{1/3} \quad for \quad d < \left[\frac{\sigma}{g\,(\rho_f - \rho_g)} \right]^{1/2} \tag{3.2}$$

that is, the buoyancy forces balance the surface tension forces.

With increased flowrate, surface tension and orifice size effects become negligible and, in liquids of low kinematic viscosity like water, the bubble size depends only on buoyancy and liquid inertia forces:

$$d_b = k\left[\frac{Q_g^2}{g} \right]^{1/5} \tag{3.3}$$

Values of k = 1.38 and 1.49 have been found by Davidson and Schuler (1960) and Krevelen and Hoftijzer (1950), respectively.

Common practice (*e.g.* Krevelen and Hoftijzer, 1950; Hayes *et al.*, 1959) is to divide bubble formation into two regimes according to gas flowrate: the static regime for low values of Q_g, and the dynamic regime which occurs when the flowrate is increased past a critical value (Walters and Davidson, 1962):

$$Q_c \leq 4.95 \left(g\, d^5 \right)^{1/2} \tag{3.4}$$

Equation (3.2) will thus apply in the static regime, and (3.3) in the dynamic regime.

A third turbulent regime has also been identified at still higher flowrates in which the bubbles are no longer formed individually but the gas leaves the orifice in the form of a jet which eventually breaks up into smaller bubbles with random non-uniform sizes (Wallis, 1969; Silberman, 1957). The condition for the formation of a jet is, from Wallis:

$$Q_g > 3.18 \left[\frac{\sigma^3}{g \left(\rho_f - \rho_g \right) \rho_g^2 \, d^{12}} \right]^{1/4} \tag{3.5}$$

Silberman (1957) predicted the maximum bubble size in this regime by a relationship in the form of Equation (3.3) with $k = 1.41$.

In general, bubble size is noted to reduce in the presence of both induced or forced liquid motion around the orifice. In the turbulent regime, the reduction is proportional to the 1/2 power of the relative liquid velocity (Silberman, 1957).

3.2.2 Terminal Bubble Velocity

The terminal rise velocity U_b of an individual bubble is dependent on fluid properties and is often defined in terms of an equivalent bubble radius r_b which is equal to half the bubble diameter d_b of the previous section:

$$\frac{4}{3} \pi r_b^3 = V_b \tag{3.6}$$

where V_b is the volume of the bubble.

For very small bubbles, which are approximately perfect spheres because of the dominant effect of surface tension on their shape, the terminal velocity is given by:

$$U_b = \frac{k\, d_b^2\, g\, (\rho_f - \rho_g)}{\mu} \tag{3.7}$$

where k varies between 0.083 and 0.055 depending on the level of surface-active contamination in the fluid (Wallis, 1974).

When bubbles are very large, the effects of surface tension and viscosity are negligible and the rise velocity has been given by Davies and Taylor (1950) as:

$$U_b = \frac{2}{3}\left[\frac{g\,(\rho_f - \rho_g)\,R_c}{\rho_f}\right]^{1/2} \tag{3.8}$$

where R_c is the radius of curvature in the region of the bubble's nose. This size of bubble takes the form of a spherical cap with an included angle of about 100°.

Between these two extremes, the effects of liquid inertia, surface tension, viscosity and purity are important, as well as whether the bubbles rise in straight lines, oscillate or describe a spiral path. Wallis (1969) suggests a division into four regions, where the range of applicability of each equation for bubble terminal velocity is determined by the bubble Reynolds number.

For the range of bubbles examined in this thesis, Clift *et al.* (1978) give the following correlation:

$$U_b = \frac{\mu}{\rho_f d_b} M^{-0.149}(J - 0.857) \tag{3.9}$$

where:

$$J = 0.94H^{0.757} \quad (2 < H \leq 59.3)$$

$$J = 3.42H^{0.441} \quad (H > 59.3)$$

$$H = \frac{4}{3} Eo\, M^{-0.149} \left(\frac{\mu}{\mu_w}\right)^{-0.14} \tag{3.10}$$

and:

$$M = \frac{g\mu^4 \Delta\rho}{\rho_f^2 \sigma^3}, \quad Eo = \frac{g\Delta\rho d_b^2}{\sigma}$$

where μ_w is the viscosity of water, taken as 0.0009 kg/m·s.

Any contamination of the interface between a bubble and its surroundings has a significant effect on the drag coefficient and the terminal velocity, especially between the two extremes of small bubbles with dominant surface tension effects and spherical cap bubbles where the effect of this variable is negligible. This reflects the role surface tension plays in inhibiting the internal circulation in a bubble, which delays the onset of flow separation and wake formation (Clift *et al.*, 1978).

3.3 Dimensional Analysis for a Bubble Group

The preceding sections have shown that the individual bubble properties of size and velocity are functions of the following physical variables: gas density ρ_g; liquid density ρ_f, viscosity μ, and surface tension σ; gravitational acceleration g; orifice diameter d; and gas volumetric flux Q_g. However, when evaluating the dynamics of a bubble group, it cannot be assumed that these are the only parameters which must be considered.

As has previously been stated, one of the purposes of this experimental work is to investigate whether a thermal analogy can be applied to a two-phase problem. If a thermal is to be approximated, the gas phase must be injected into the liquid instantaneously rather than over a period of time. The volumetric flux term Q_g should therefore be considered as an injected gas volume V_g.

Gas bubbles rising in a liquid medium will expand with height above the source due to a reduction in the ambient pressure. The pressure on a bubble at a depth h below a free surface is the sum of the hydrostatic pressure at that depth plus the pressure produced by the surface tension of the bubble:

$$p = p_{at} + \rho_f g h + p_s \qquad \textbf{(3.11)}$$

However, unless the gas bubble is small enough that it falls within the static regime defined by Equation (3.2) where the motion is subject to Stokes Law, the pressure produced by the surface tension will be insignificant compared with the hydrostatic pressure (Tsang, 1984). Thus there are only two pressure terms which must be accounted for in the bubble group analysis: the atmospheric pressure and the hydrostatic pressure. The maximum possible hydrostatic pressure is represented by the source depth H. Since these two pressure terms always act in conjunction with one another, the simplest approach is to express atmospheric pressure by its equivalent head of liquid and to sum the two terms as total pressure H_T. This method was used by Poon (1985) in his study of bubble plumes. However, a study by Rowe *et al.* (1989) has shown that a better description of plume behaviour is given with the use of source depth alone, so the total pressure H_T approach will not be used in this analysis.

Any variation in the submergence depth of the source will also vary the injected gas volume V_g due to the compressibility of the bubbles. There are two ways to approach this problem: to use the discharge at the source, thus making a comparison with other experimental results difficult unless the source depths are identical; or to express the injected gas volume at standard atmospheric conditions, which actually represents the total volume that the gas bubbles will expand to upon reaching the surface. The latter approach has been used successfully by investigators (Kobus, 1968; Tekeli and Maxwell, 1978) into the behaviour of bubble plumes, and it is intended to follow it in this study as well. Henceforth, the injected gas volume at standard atmospheric conditions will be referred to as V_T.

It should be noted that the injected gas volume term could also be stated as a combination of the number of bubbles and the volume of each individual bubble. However, total injected volume will be used herein, as it is easier to determine experimentally.

The expansion of the injected gas volume is a function of temperature as well as pressure. However, when a group of bubbles rises, it sets up a mixing motion due to the entrainment of ambient fluid into the bubble wakes. As a result of this mixing, the ambient fluid within the group will attain a uniform temperature and the expansion of the bubbles may be considered approximately isothermal (Tsang, 1984).

The liquid density ρ_l used to calculate the hydrostatic pressure in Equation (3.9) should correctly be a function of pressure and temperature also. However, as most common liquids have densities which are not highly sensitive to pressure and temperature changes, ρ_l will be considered constant over the range of this experimental program.

In the preceding sections dealing with bubble velocity and radius, the gas density ρ_g always appears in conjunction with the liquid density ρ_f. The variable $(\rho_f - \rho_g)$ will also be used in the analysis of bubble group behaviour, since this combination is standard in buoyancy-related problems. As with the injected air volume V_T, the gas density will be expressed at standard atmospheric conditions as ρ_T.

Bubble plume experiments by Bulson (1968), Kobus (1968) and Tekeli and Maxwell (1978) showed that the source orifice size has little effect on the structure of the plume. For a group of bubbles formed by the shattering of a large bubble, such as would occur in the event of a subsea oilwell blowout, orifice size should also not be a factor in determining the overall behaviour of the structure. The orifice size d has therefore been eliminated from the list of variables affecting bubble group dynamics. Proper design of the experimental apparatus will ensure that the exclusion of this factor will not affect the results obtained.

Any dimensionless group which may be used to describe the behaviour of bubble groups should therefore be a function of the following physical variables:

$$\textit{Dimensionless Group} = f\left[\ \rho_f - \rho_T\ ,\ \rho_f\ ,\ \mu\ ,\ \sigma\ ,\ g\ ,\ V_T\ ,\ H\ ,\ p_{at}\ \right] \qquad \textbf{(3.12)}$$

The application of dimensional analysis to these variables results in the following relationships:

$$\left[\ \frac{V_T^{1/3}}{H}\ ,\ \frac{\rho_f\, V_T^{2/3}\, g}{\sigma}\ ,\ \frac{\rho_f\,(\,V_T\, g\,)^{1/2}}{\mu}\ ,\ \frac{\rho_f - \rho_T}{\rho_f}\ ,\ \frac{p_{at}}{\rho_f\, g\, H}\ \right] \qquad \textbf{(3.13)}$$

The first can be recognized as a length ratio, the second as an Eötvos number, the third as a dynamic similarity number which combines the liquid Reynolds number and the Froude

number, and the fourth as a density ratio. The last term is an expansion parameter which accounts for the expansion of the bubble volumes as they rise due to the reduction in ambient pressure.

The Eötvos number, which is actually the Weber number divided by the Froude number, is commonly known in two-phase flow studies to determine the bubble regime. Smaller ellipsoidal bubbles fall within the Weber number or surface-tension dominated region, while spherical cap bubbles are Froude number- or gravity-dominated. This dimensionless group is not useful in the Stokes flow regime where the bubbles are spherical and very small. In this region, the bubbles follow the liquid flow since the buoyancy forces equal the total drag force. A bubble group composed of bubbles of this type would behave as a single-phase thermal, and the Eötvos number would then be irrelevant.

The third dimensionless number is actually the liquid Reynolds number divided by the square root of the Froude number. Squaring this group and combining it with the density ratio gives a form of Grashof number, which is the buoyancy force over the viscous force:

$$Gr_b = \frac{(\rho_f - \rho_T) g V_T}{\rho_f \nu^2} \qquad (3.14)$$

Krishnappan (1975) found that the Grashof number was the dominant dimensionless group in determining solid-particle thermal behaviour, and it is quite possible that this may prove to be the controlling parameter in bubble group behaviour. However, since the density of most gases is much less than the density of liquids, the density ratio for a bubble group will

be approximately unity and the Grashof number will reduce to the form of Reynolds number originally derived.

Previous investigations into the behaviour of bubble plumes (Wilkinson, 1979; Tsang, 1984; Poon, 1985) found that the Weber number was the dominant dimensionless group controlling air-bubble plume behaviour. Rowe *et al.* (1989) showed that, for the same data sets used by the other researchers, better results could be obtained by using a bubble Reynolds number rather than a Weber number. Since the Eötvos number appears at first glance to be useful only in determining the regime of the bubbles in a bubble group, the Reynolds or Grashof number will probably prove to be the important dimensionless group in this investigation. The determination of the controlling parameter is one of the aims of the experimental portion of this thesis.

3.4 Scaling Parameters and Physical Constraints

Mechanical similarity between a model and prototype requires that geometric, kinematic and dynamic similarity be achieved simultaneously. In order to generalize the results of the current research to full-scale situations, the scaling parameters which govern the proper simulation of bubble groups must be established. Observation of the conditions ordained by the scaling parameters will ensure that similarity may be achieved.

In order to correctly scale the entrainment effects in a bubble group, undistorted geometric similarity must be provided (Tekeli and Maxwell, 1978). An examination of the length ratio developed in Equation (3.13) shows that for geometric similarity, the following equation must hold true:

$$\left(\frac{V_T^{1/3}}{H} \right)_m = \left(\frac{V_T^{1/3}}{H} \right)_p \tag{3.15}$$

where the subscripts m and p denote model and prototype, respectively. This can be rewritten as:

$$R_L = \frac{H_m}{H_p} = \left(\frac{V_{Tm}}{V_{Tp}} \right)^{1/3} = R_V^{1/3} \tag{3.16}$$

where the length scale R_L is the ratio of the source depths of the model and prototype, and the discharge scale R_V is the ratio of the injected air volumes. Equation (3.16) states that, for geometric similarity alone, the length scale must equal the cube root of the discharge scale. Although it appears a simple matter to meet this requirement, difficulties do arise when attempting to achieve simultaneously dynamic and kinematic similarity.

Evaluating the other dimensionless groups in (3.13) in the same manner as (3.15) gives the following equations:

$$\left(\frac{\rho_f V_T^{2/3} g}{\sigma} \right)_m = \left(\frac{\rho_f V_T^{2/3} g}{\sigma} \right)_p \tag{3.17}$$

$$\left(\frac{\rho_f (V_T g)^{1/2}}{\mu} \right)_m = \left(\frac{\rho_f (V_T g)^{1/2}}{\mu} \right)_p \tag{3.18}$$

$$\left(\frac{\rho_f - \rho_T}{\rho_f} \right)_m = \left(\frac{\rho_f - \rho_T}{\rho_f} \right)_p \tag{3.19}$$

$$\left(\frac{p_{at}}{\rho_f g H} \right)_m = \left(\frac{p_{at}}{\rho_f g H} \right)_p \tag{3.20}$$

Equations (3.17), (3.18), (3.19) and (3.20), respectively, may be rewritten as:

$$R_\sigma = \frac{\sigma_m}{\sigma_p} = \frac{\rho_{fm}}{\rho_{fp}} \frac{g_m}{g_p} \left(\frac{V_{Tm}}{V_{Tp}} \right)^{2/3} = R_\rho \cdot R_g \cdot R_L^2 \qquad \textbf{(3.21)}$$

$$R_\mu = \frac{\mu_m}{\mu_p} = \frac{\rho_{fm}}{\rho_{fp}} \left(\frac{g_m}{g_p} \frac{V_{Tm}}{V_{Tp}} \right)^{1/2} = R_\rho \cdot (R_g \cdot R_L^3)^{1/2} \qquad \textbf{(3.22)}$$

$$R_\rho = \frac{\rho_{fm}}{\rho_{fp}} = \frac{\Delta \rho_{fm}}{\Delta \rho_{fp}} = R_{\Delta\rho} \qquad \textbf{(3.23)}$$

$$R_p = \frac{p_{atm}}{p_{atp}} = \frac{\rho_{fm}}{\rho_{fp}} \frac{g_m}{g_p} \frac{H_m}{H_p} = R_\rho \cdot R_g \cdot R_L \qquad \textbf{(3.24)}$$

where R_σ, R_ρ, R_g, R_μ, $R_{\Delta\rho}$, and R_p are the interfacial tension scale, the density scale, the gravity scale, the viscosity scale, the density difference scale and the surface pressure scale, respectively. All of these scaling relationships must be observed if the similarity requirements are to be satisfied between the model and the prototype.

Performing a similar analysis on Equation (3.14) gives the following relationship:

$$\left(\frac{(\rho_f - \rho_T)}{\rho_f} \frac{\rho_f^2 \, g \, V_T}{\mu^2} \right)_m = \left(\frac{(\rho_f - \rho_T)}{\rho_f} \frac{\rho_f^2 \, g \, V_T}{\mu^2} \right)_p \qquad \textbf{(3.25)}$$

which can be rearranged as:

$$R_\mu^2 = R_{\Delta\rho} \cdot R_\rho \cdot R_g \cdot R_V \qquad \textbf{(3.26)}$$

which may then, using (3.16) and (3.23), be further simplified to give:

$$R_\mu = R_\rho \cdot (R_g \cdot R_L^3)^{1/2} \qquad (3.27)$$

Equation (3.27) is the same expression as (3.22), which indicates that the scaling relationship derived from the Grashof number will give exactly the same result as that derived from the bubble Reynolds number. This agrees with the conclusion drawn earlier; *i.e.* that the two relationships are substantially the same.

It has been shown that for complete similitude between model and prototype, a total of eight scaling parameters must be observed concurrently. However, for most practical purposes, R_g is always equal to unity (unless experiments are conducted away from the Earth's gravitational field) and this number may be reduced to seven.

As has previously been demonstrated, the relationship between the length and discharge scale stated in Equation (3.16) is easily observed, since it is independent of the fluids used for the continuous and dispersed phases in the model and prototype. Satisfaction of the relationships shown in (3.21), (3.22) and (3.24), however, is subject to physical constraints dictated by the choice of fluids.

Equation (3.24) states that, for geometric similarity between the model and the prototype, the surface pressure scale should be the product of the density scale, the gravity scale (which is normally unity) and the length scale. Thus, if the prototype is exposed to atmosphere (a valid assumption for a blowout situation), the model and the prototype continuous phases are the same, and the model is smaller than the prototype (which is usual for economic reasons), then the surface pressure of the model must be less than atmospheric pressure. In other words, the model study must be conducted under vacuum. The only

means of avoiding this requirement is by choosing a model fluid which is much denser than the continuous phase in the prototype, thereby allowing atmospheric conditions to prevail in both cases.

Conducting a study under partial vacuum has two major drawbacks. The first of these is the likelihood of the continuous phase coming to a boil during the experiments, with the resultant problems of changing surface pressure and disturbance of the ambient flow field. The second problem is expense; an apparatus which is designed to operate under pressures of less than atmospheric will of necessity be much more elaborate and costly than one which is open to the air.

Because of the disadvantages of working under vacuum, it appears that it would be preferable to choose a heavier fluid for the model. However, this option introduces other constraints with respect to the viscosity and interfacial tension scales. Most common fluids have an interfacial tension with air in the range between 0.01 and 0.1 N/m, and thus the smallest value of R_σ which may be obtained is approximately 1/10. It therefore follows from Equation (3.21) that, unless the continuous phase in the model is much denser than that of the prototype, the smallest length scale available for the model is about 1/3.5 (Tsang, 1984). Although a much wider variation in viscosity ratio is possible, finding a combination of density, viscosity and interfacial tension scales which meets the combined requirements of (3.21), (3.22) and (3.24) is extremely difficult.

A realistic approach to these problems would be to use the same ambient fluid for both the model and the prototype, and then to evaluate the distortion caused by the infringement of similitude. This method was used by Tekeli and Maxwell (1978) in their

study of bubble plumes. They found that the distortion was maximum at the source, and gradually disappeared as the surface was approached. By comparing their results with other published data, these researchers determined that the infringement was not as serious as had been initially indicated, although they did retain a distortion factor which depended on the expansion parameter (3.20) of the prototype.

In the interests of creating a practical model for bubble group experiments, it was decided to follow this type of approach. Water was selected as the continuous phase and air as the dispersed phase for the primary reason that all of the published data for bubble plumes is for air-water systems under atmospheric conditions. Thus, a basis for comparison between bubble groups and bubble plumes is automatically provided for. Also, the scaling parameters R_p, R_μ, $R_{\Delta\rho}$ and R_ρ become unity for the purposes of this work and the number of variables to be investigated is thus reduced to four: injected air volume, water depth above the source, surface tension and gravitational acceleration.

Although interfacial tension and the force of gravity could normally also be considered constant, an investigation of the sensitivity of bubble group behaviour to these variables was deemed necessary in order to fully determine the influence of the Reynolds and Eötvos numbers. The existence and magnitude of a distortion factor similar to that of Tekeli and Maxwell will also be explored through systematic experimentation.

CHAPTER 4

EXPERIMENTAL EQUIPMENT AND PROCEDURES

4.1 Description of the Research Program

The original intent of the research program was to carry out all of the experiments in one small tank. Photography was to be used to make measurements of bubble group growth and velocity, and the velocity of the group's wake was to be validated using a DISA single-component laser-Doppler anemometer (LDA). The size of the tank was thus dictated by the optical requirements of the anemometer.

After the tank was constructed, the LDA system was set up and a machine-language interface program was written to transmit the data to a Commodore PET computer. The system was calibrated, and a user's manual was written for the laser-Doppler anemometer (Laureshen and Rowe, 1986) to supplement the incomplete instructions supplied by the manufacturer. Although velocities were recording during the commissioning of the apparatus, it was found that the system would require considerable upgrading before the objectives of the research program could be satisfied.

To this end, a Commodore 64 computer was purchased, as well as new Bragg cells for the LDA system. The upgraded equipment also required a complete rewrite of the assembler code. When the code was complete, it was decided that time could be more constructively spent on other aspects of this research project, as the LDA component did not fit in with the overall direction that the project was taking. Therefore the anemometry component of the research has not been included in this thesis.

As was described in the previous chapter, the dimensional analysis for the bubble groups showed that the four variables identified for investigation in this study were injected air volume, water depth above the source, surface tension, and graviational acceleration. It was envisioned that a database of bubble group behaviour could be generated by varying the first three parameters in the laboratory, while holding the force of gravity constant; however, the opportunity arose to carry out experiments under a variety of gravitational conditions on board NASA's Boeing KC-135 aircraft, which is primarily used for microgravity experiments, based at the Johnson Space Centre in Houston, Texas. Thus, the scope of this research program covers all of the important variables affecting bubble group behaviour. The equipment and procedures used to generate the database are discussed in this chapter, as well as some associated qualitative experiments which were carried out to clarify certain aspects of bubble group behaviour.

4.2 Experimental Apparatus

Three separate sets of experimental equipment were designed and constructed in order to complete this research. A description of each test apparatus is given in the following sections.

4.2.1 Small Tank

A schematic of the small tank is shown in Figure 4.1. It was constructed of 12 mm aluminum plate, and was 0.27 x 0.27 x 0.79 m in size. As was discussed in Section 4.1, the size of the small tank was originally dictated by the requirements of the LDA system. It had

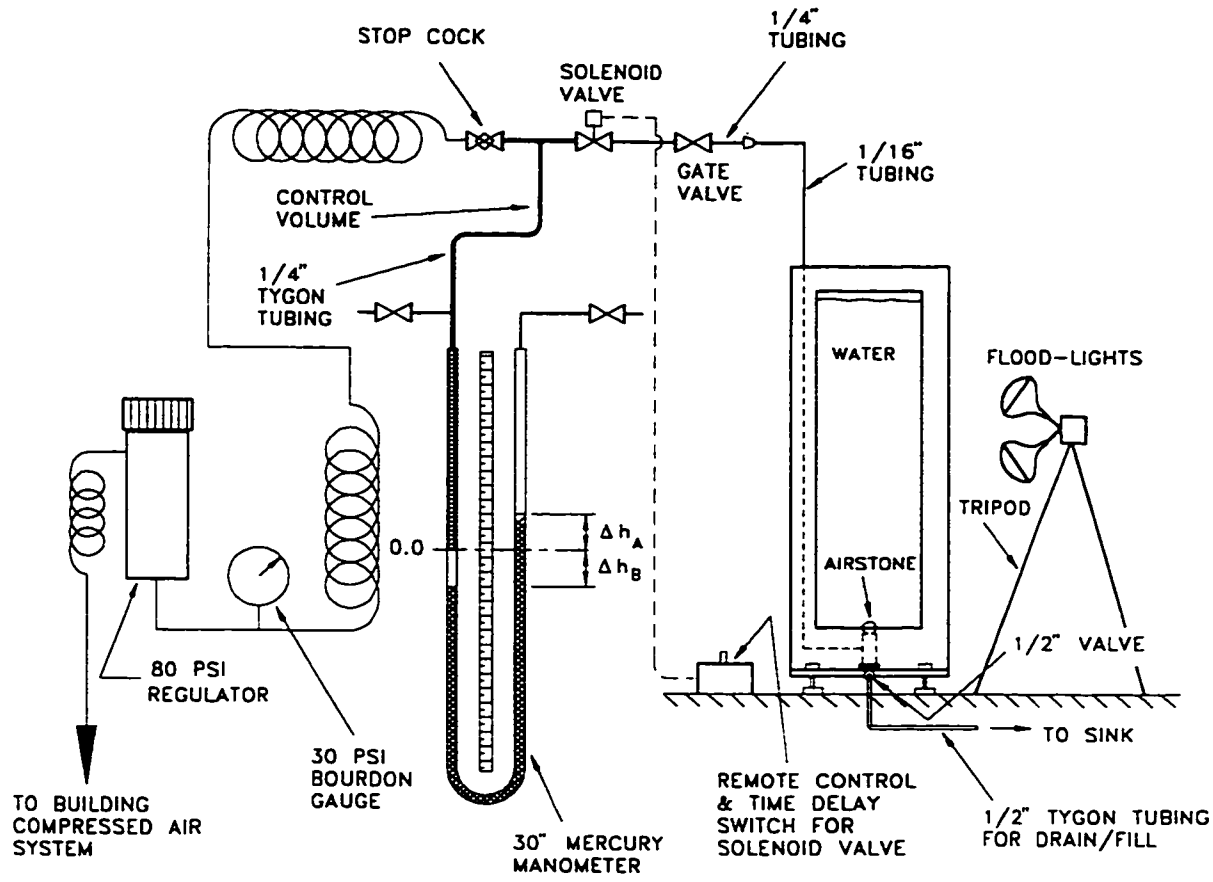

FIGURE 4.1 - Schematic of Small Tank and Air Injection System

glass viewing windows inserted on three sides; these were tested for impurities which might interfere with the laser beams using a Schlieren system. The tank back was reversible, and was covered with matte black plastic on one side and white plastic on the other in order to provide a backdrop for black-and-white and color photographs. The back and sides of the tank were sealed using continuous gaskets made of Viton O-ring material, and the windows were sealed with silicone.

One advantage of using a small tank is that it allows for the economic use of distilled water. Because contamination of the interface between a bubble and its surroundings affects its drag coefficient and terminal velocity, it was thought that using distilled water would be necessary for accuracy in the experimental results. However, a comparison of the data from a trial set of runs using distilled water against a series using water from the building supply showed no distinguishable differences. A subsequent chemical analysis of the building water showed that the tap water had a relatively low level of total solids (less than 230 mg/l), and it was determined that more contamination of the bubble interfaces would be introduced through the building air supply (the dirt and oil in the air could not be totally be removed, even with a filtering system) than in the water. Because the cost of using bottled compressed air as opposed to the building supply was prohibitive, this meant that some level of contamination was inevitable. Thus, it was decided to use tap water in the experimental program instead of the distilled water which was originally deemed necessary.

The tank was drained and filled by means of a long piece of 12 mm tygon tubing which could be connected either to the tap or drain of a sink which was located nearby in the laboratory. The tubing was attached to a 12 mm drain valve set in the base of the tank.

Air was supplied to the tank from the building supply through an oil/water separator and an 80 psi (550 kPa) regulator to a calibrated control volume with an electric solenoid valve at one end and a 30" (760 mm) mercury manometer at the other. A time delay switch opened the solenoid and released air over a period of approximately 0.5 seconds to the bubble injection device mounted at the tank base. The length of tubing between the solenoid valve and the bubble injection device acted as a reservoir to dampen the possible pressure fluctuations which could be caused by the opening of the solenoid valve. This reservoir (the tubing) could also be filled with dye for the dye injection experiments. The volume of injected air was calculated using the pressure change in the control volume. A description of the calibration procedure and an error analysis of the injected air volume calculation is given in Appendix A.

A number of bubble injection devices were tested at the beginning of the project to ensure that consistent bubble sizes and shapes were maintained. In addition to the standard fish tank bubblers made of plastic in round and cylindrical shapes, orifice plates made of perforated steel, sintered glass and brass frit were also examined. The most consistent results were obtained using a 12 mm radius spherical Fisher Scientific sintered aluminum oxide airstone (60 μm pore size). As the airstone had a 25 μm particle retention capability, it also cut down on the particulate contamination from the building air supply, although a bi-weekly soaking in methyl alcohol was required to keep the pores from plugging.

The release of air using an airstone produced uniformly-sized bubbles ranging in effective diameter from two to eight millimetres. Because all of the bubbles were within the same size range, and thus in the same regime for terminal velocity and rise behaviour, it was

therefore possible to drop the orifice diameter d from the dimensional analysis for the bubble group.

Because the experimental data were to be recorded photographically, some means was required to ensure that accurate measurements could be taken from the film. This was accomplished by constructing a grid which could be lowered into the water at the exact centreline of the airstone. The grid was made of a mylar sheet divided into one inch (25 mm) squares glued onto a plexiglass panel. The lines on the mylar were drawn with waterproof black ink. Prior to each test run, a picture was taken of the grid with the camera in the same position as it would be for the rest of the run, and a transparency made from this picture could then be used to take the measurements from the run photos. In this manner, the diffraction of light through the glass front of the tank and the water and the parallax of the camera lens were accounted for, since any distortion in the pictures would be reflected in the shape of the grid in the photo.

4.2.2 Large Tank

The large tank, which is shown in Figures 4.2 and 4.3, was designed and built to address concerns that proximity of the bubble groups to the wall was affecting the small tank results. The tank, which was 1.13 x 1.13 x 1.22 m in size, had 18 mm thick plexiglass walls on four sides and a 12 mm thick aluminum base. The walls were sealed at the corners and the base with continuous gaskets made of Viton O-ring material. Steel bracing was used at the depth of maximum deflection of the walls to ensure that the plexiglass would not distort when the tank was full of water, since any curvature could possibly affect the photographic

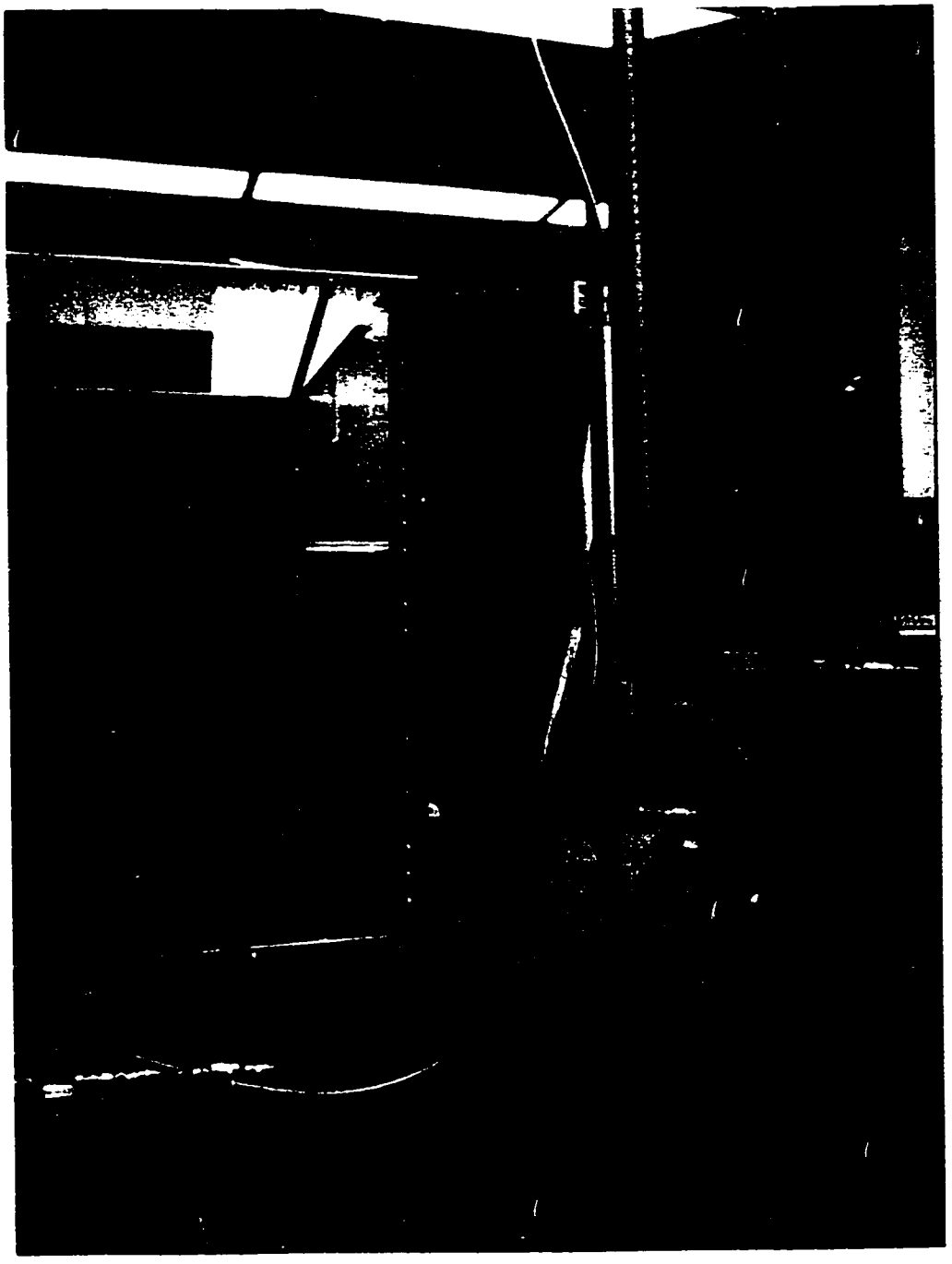

FIGURE 4.2 - View of Large Tank and Air Injection System

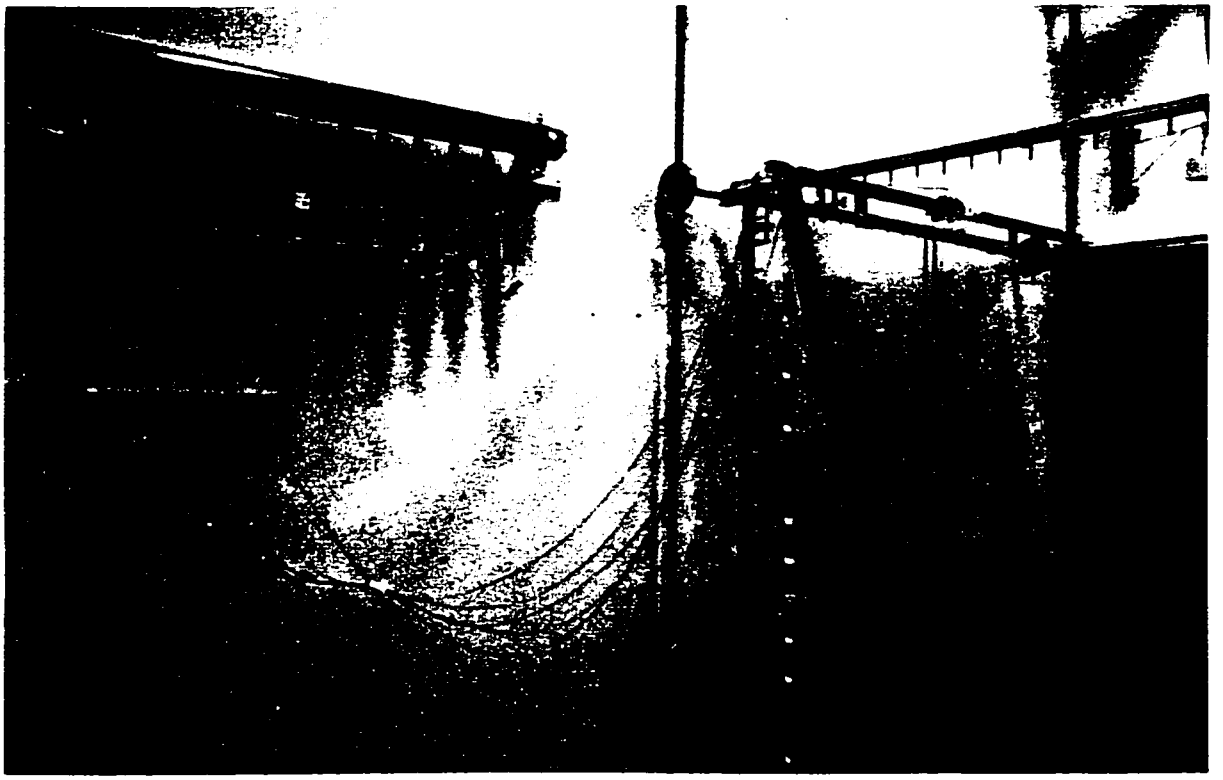

FIGURE 4.3 - View of Large Tank and Dye Injection System

results. The tank was supplied with a 12 mm diameter fill pipe connected to the building water supply, an 18 mm diameter drain pipe, and a mount for the airstone in the centre of the baseplate.

The air injection system used in this tank was basically the same as that used in the small tank, with several minor differences. An extra T-connection was added to the piping upstream of the control volume in order to supply compressed air to a dye layering system, which was designed to inject thin sheets of dye horizontally at five height intervals in the tank. A small reservoir was also added between the airstone and the supply line to dampen possible pressure fluctuations which could be caused by the opening of the solenoid valve. This reservoir was also filled with dye for the dye injection experiments. To ensure continuity between the experiments, the same airstone was used in both tanks. It was removed from the small tank and installed in the large tank when required by the test schedule. Figure 4.2 gives a view of the large tank air system.

A pulley-driven carriage spanned the top of the tank to carry the dye layering rack from right to left relative to the front viewing panel. The pulley was manually operated, and was placed so that a single operator could operate the dye layering system and drive the pulley simultaneously.

The dye layering system was pneumatically driven by compressed air from the building supply. Air was supplied to a wall-mounted pressure vessel which evenly pressurized eleven dye-filled cylindrical reservoirs to move the liquid dye through 1/32" (0.8 mm) I.D. tygon tubing to the injection rack. Only five of these reservoirs were actually used in the system. The reservoir was supplied with a three-way valve connecting to the pressure

vessel and to atmosphere so that the flow of air could be instantaneously shut off, and the flow of dye in the tubing was regulated using laboratory pinch locks, which varied the tubing area between the fully-open and fully-shut positions.

The rack was made up of five 1/16" (1.6 mm) I.D. stainless steel tubes strung horizontally between two vertical plexiglass airfoils, which were stiffened by a 1/4" (6 mm) diameter copper rod at the bottom and a steel channel at the top. The centre three feet (0.91 m) of the tubes had tiny holes drilled in a line at 1/4" (6 mm) intervals, and these were covered in shrink-wrapped plastic. Needle pricks were then made in the plastic at the hole locations so that the dye would come out through a very small orifice. When dye was pushed into the rack, a small jet would issue from each hole, and by moving the rack across the tank a thin layer of dye could be laid down horizontally while minimally disturbing the water in the tank. Because of the design of the dye layering system, it was possible to use different colours of dye for each layer. Figure 4.3 shows the dye layering system for the large tank.

The tank was equipped with two curtains, one white and one black, which were hung behind the rear wall as photographic backdrops. The black curtain was used for the black-and-white film sessions because it provided the best contrast, while the other was used with color film. The bottom of the tank was usually covered with black vinyl both to moderate the reflection of the light off the bubbles, and to prevent corrosion of the aluminum.

To ensure accurate experimental results, a vertical grid was constructed which could be lowered into the water at exactly the centreline of the airstone. A pulley mounted at the ceiling was used to raise and lower the grid, which was similar to, although larger than, the

one used in the small tank. It was made of a mylar sheet glued onto a plexiglass panel, with the face divided into one inch (25 mm) squares marked with waterproof black ink.

4.2.3 KC-135 Zero-Gravity Apparatus

Although it is a simple matter to alter physical variables such as water depth, injected gas volume and surface tension in a normal laboratory situation, it is extremely difficult to modify the force of gravity. However, research facilities for this purpose are available; the best of these are owned and operated by the United States National Aeronautics and Space Administration (NASA). The NASA facilities include two drop towers and a Learjet Model 25 at the NASA Lewis Research Centre, and a KC-135 aircraft at the Lyndon B. Johnson Space Centre. Each provides free fall or semi-free fall where the force of gravity is offset by linear acceleration, thereby simulating a reduced gravity condition.

The NASA KC-135 is a modified Boeing 707 transport turbojet which provides a "weightless" environment similar to that of space. The KC-135 is flown in a series of parabolic arcs to provide 20 to 25 second periods of near-zero gravity (better than 10^{-2} **g**). Each parabolic maneuver is accompanied by a pull-up and pull-out of between 1.8 and 2.0 **g**. The Space Division of the National Research Council of Canada (NRC) charters the KC-135 in March and October of every year to conduct Canadian experiments under microgravity conditions. The University of Calgary Bubble Group Experiment was one of thirteen Canadian projects accepted by the NRC in November, 1988 to take part in their March, 1989 series of flights at the Johnson Space Centre in Houston, Texas.

The KC-135 experiment was designed to gather bubble group velocity and radius measurements for a single water height and various injected air volumes. Under the low gravity available in the aircraft, it was also intended to observe the initial momentum of the bubble group after injection uncoupled from the buoyancy force which is always present under normal gravitational acceleration.

In order to perform tests on the KC-135, it was necessary to design and build two equipment skids which could be bolted to the floor of the aircraft. The first skid held the small water tank used in the 1.0 **g** laboratory experiments, which had been modified to meet NASA structural testing requirements. The glass windows were replaced by 6 mm thick plexiglass panels sealed with rubber gaskets on both sides; these were reinforced with steel bars to prevent the windows from bowing out and releasing water into the aircraft cabin as the pressure increased within the tank. A sealed plenum was added to the top of the tank to keep the air pressure at the top of the tank at a relatively constant value. The air from the bubble groups passed from the water to the plenum through a brass frit which had been treated with silicon spray to prevent the water from rising into the plenum during periods of microgravity. Located next to the tank was the pressurized air system used to release the bubble groups into the water, and the control volume pressure signal conditioner and digital display.

The second skid carried the VCR and video camera which recorded the bubble group data, and the remote controls for the air injection system. The instrumentation was protected by a tubular steel frame, which also served as a handhold for the operator during microgravity since all of the experiments were controlled from this location. Both the frame

on Skid 2 and all of the sharp corners on Skid 1 were covered with thick foam to protect against personnel injury in case of a sudden change in acceleration.

Drawings of each skid are given in Figures 4.4 and 4.5. The skids were located near the walls of the aircraft 36" (0.90 m) apart. Skid 1 was installed facing the tail of the aircraft and Skid 1 facing the nose. Figure 4.6 is a view of both skids installed in the KC-135.

Figure 4.7 is a schematic of the air injection system, which was controlled by pressing two buttons on the remote control panel located on Skid 2. One button operated a solenoid valve which filled the control volume full of air and remained open so long as the button was held down. A pressure transducer, which was selected for its insensitivity to acceleration forces, relayed the control volume pressure to a digital display. The other button activated the solenoid valve which released air from the control volume to the airstone. This valve was operated through a time delay switch similar to that on the 1.0 g air injection system, so that pressing down on the button held the solenoid open for approximately 0.5 seconds. A description of the pressure and leak tests, the calibration procedure for the control volume and an error analysis of the injected air volume is given in Appendix B.

Power was supplied to the skids from the aircraft's 120 V AC power supply. The major power requirement was from the 300 W light which was used to illuminate the tank when the interior lights of the aircraft were shut off during the 1.8 g pull-outs.

Full drawings of this apparatus, along with the equipment specifications, structural testing procedures and the electrical loads may be found in the Test Equipment Data Package (TEDP) which was prepared for NRC Space Division (Laureshen, 1989). This document

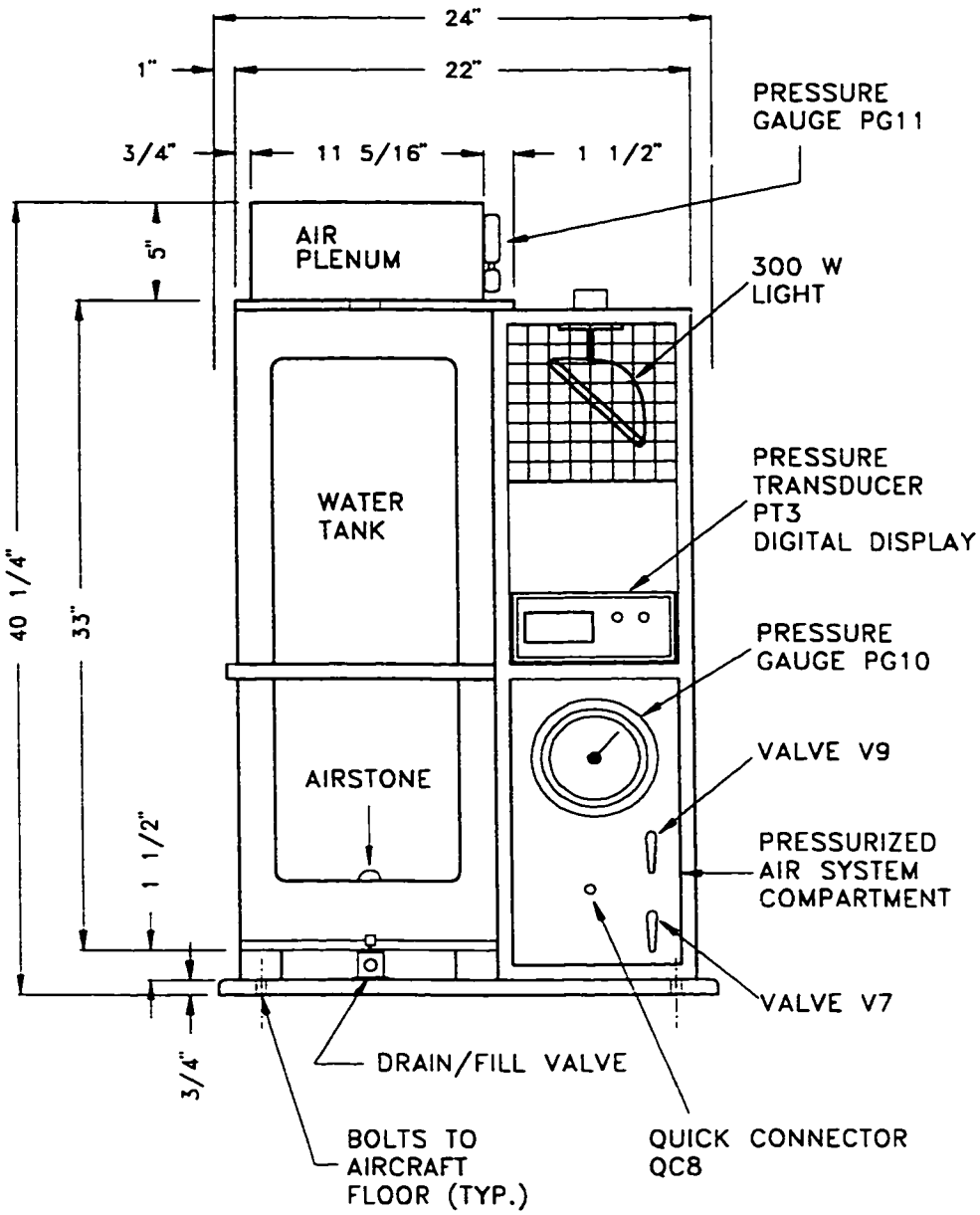

FIGURE 4.4 - Front View of Skid 1, KC-135 Apparatus (Water Tank and Air Injection System)

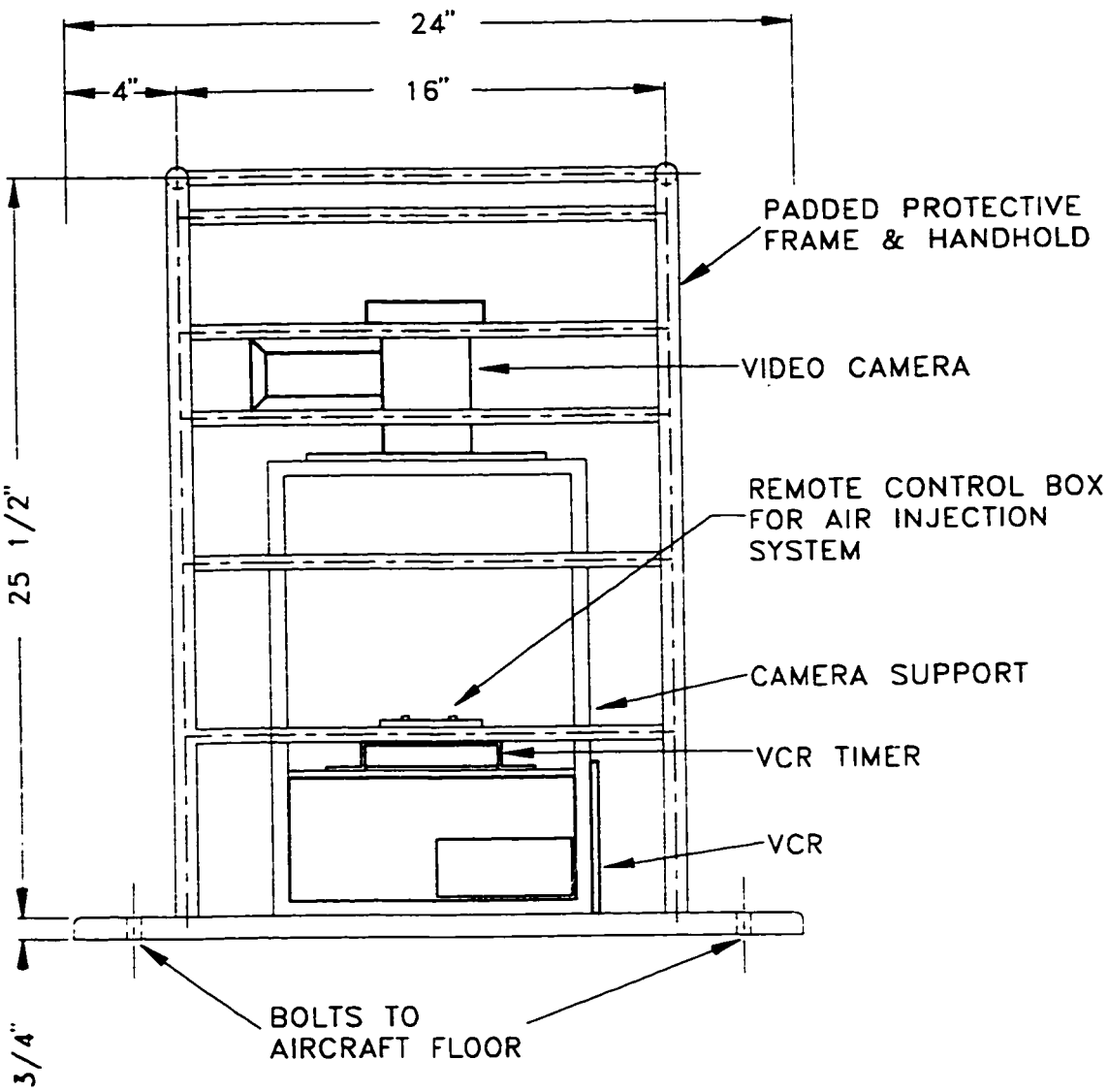

FIGURE 4.5 - Side View of Skid 2, KC-135 Apparatus (Recording Equipment and Controls)

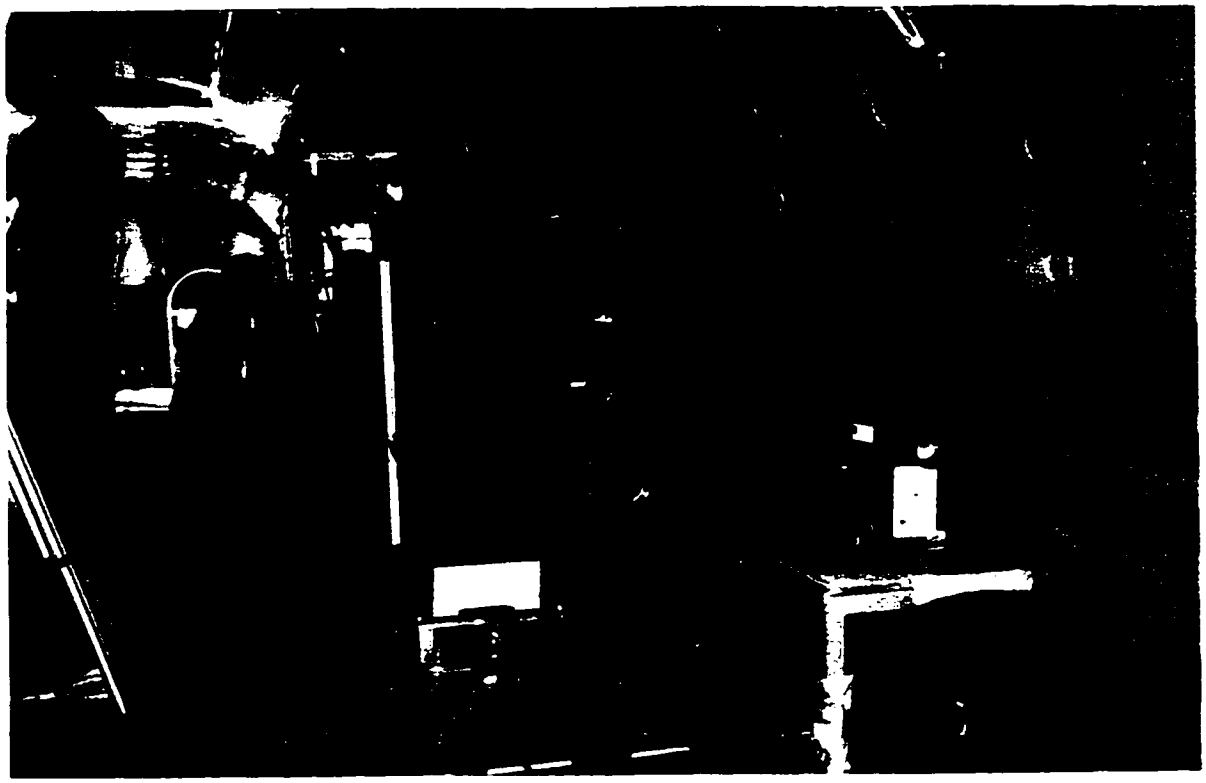

FIGURE 4.6 - View of KC-135 Apparatus Installed in Aircraft

LEGEND	
V1	1/8" TOGGLE VALVE
V2 & V4	1/4" SOLENOID VALVE
PT3	ENDEVCO 8531-100 PRESSURE TRANSDUCER
PV5 & PV6	PARKER 500cc SAMPLE CYLINDER
V7, V9 & V13	1/4" BALL VALVE
QC8	FEED QUICK CONNECTOR
PG10	3D INSTRUMENTS 25544-22B25 PRESSURE GAUGE
PG11	MARSH WO274 DIAPHRAGM GAUGE
PRV12	3 PSI RELIEF VALVE
RV14	1/8" REGULATING VALVE

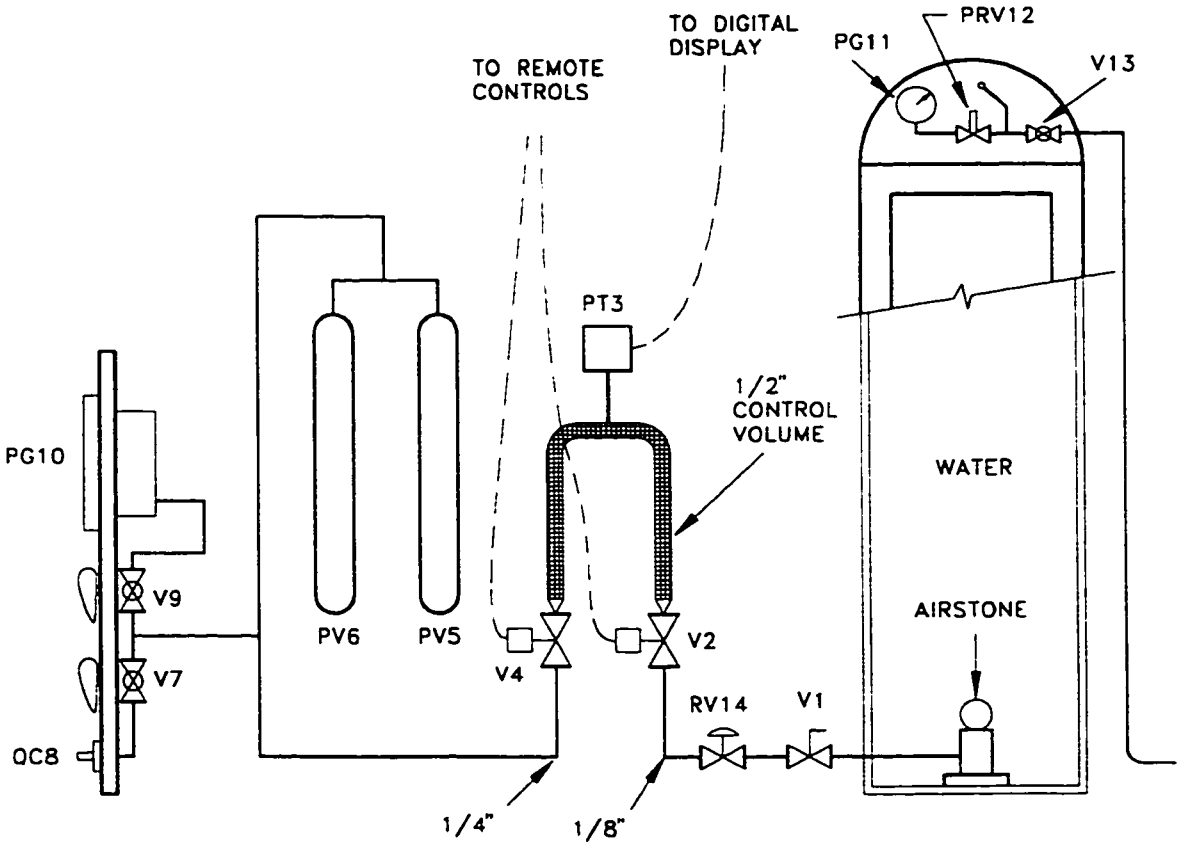

FIGURE 4.7 - Schematic of Air Injection System, KC-135 Apparatus

was reviewed and approved by a panel of NASA engineers prior to installing the equipment onboard the KC-135.

4.3 Experimental Procedures

This section describes the procedures followed while investigating the effects of water depth, injected air volume, interfacial tension and gravitational acceleration on the behaviour of bubble groups. Other tests which were performed to determine the flow patterns near the airstone and the interactions between the bubbles and the water are also discussed.

4.3.1 Experiments to Test Water Depth and Air Volume Effects

The effects of water depth and injected air volume were investigated in a series of experiments, and the parameters for each experiment are given in Table 4.1. Five different air volumes (8.0, 10.0, 12.0, 14.0 and 16.0 cm^3) were examined for each water depth. In the large tank, water heights of 30, 45, 60, 90 and 120 cm were used. It was possible to examine only the first three of these depths in the small tank. Each experiment was repeated at least five times to ensure statistical validity in the results. Black-and-white still pictures were made of each test run, and all measurements were taken from the photographs.

The range of injected air volumes used in the experiments was chosen because, within the limits of 8.0 and 16.0 cm^3, the bubble sizes formed by the airstones were consistent, as were the rise characteristics of the groups. When a larger air volume was used, the majority of the air was released as several spherical cap bubbles which rose at a faster

Apparatus	Small Tank Test No.			Large Tank Test No.				
Water Depth (cm) Volume (cm^3)	30	45	60	30	45	60	90	120
8	S30-8.1 S30-8.2 S30-8.3 S30-8.4 S30-8.5 S30-8.6	S45-8.1 S45-8.2 S45-8.3 S45-8.4 S45-8.5 S45-8.6	S60-8.1 S60-8.2 S60-8.3 S60-8.4 S60-8.5	L30-8.1 L30-8.2 L30-8.3 L30-8.4 L30-8.5	L45-8.1 L45-8.2 L45-8.3 L45-8.4 L45-8.5	L60-8.1 L60-8.2 L60-8.3 L60-8.4 L60-8.5	L90-8.1 L90-8.2 L90-8.3 L90-8.4 L90-8.5 L90-8.6	L120-8.1 L120-8.2 L120-8.3 L120-8.4 L120-8.5
10	S30-10.1 S30-10.2 S30-10.3 S30-10.4 S30-10.5	S45-10.1 S45-10.2 S45-10.3 S45-10.4 S45-10.5	S60-10.1 S60-10.2 S60-10.3 S60-10.4 S60-10.5 S60-10.6	L30-10.1 L30-10.2 L30-10.3 L30-10.4 L30-10.5	L45-10.1 L45-10.2 L45-10.3 L45-10.4 L45-10.5	L60-10.1 L60-10.2 L60-10.3 L60-10.4 L60-10.5	L90-10.1 L90-10.2 L90-10.3 L90-10.4 L90-10.5	L120-10.1 L120-10.2 L120-10.3 L120-10.4 L120-10.5 L120-10.6
12	S30-12.1 S30-12.2 S30-12.3 S30-12.4 S30-12.5 S30-12.6	S45-12.1 S45-12.2 S45-12.3 S45-12.4 S45-12.5 S45-12.6	S60-12.1 S60-12.2 S60-12.3 S60-12.4 S60-12.5 S60-12.6	L30-12.1 L30-12.2 L30-12.3 L30-12.4 L30-12.5	L45-12.1 L45-12.2 L45-12.3 L45-12.4 L45-12.5	L60-12.1 L60-12.2 L60-12.3 L60-12.4 L60-12.5	L90-12.1 L90-12.2 L90-12.3 L90-12.4 L90-12.5	L120-12.1 L120-12.2 L120-12.3 L120-12.4 L120-12.5 L120-12.6

TABLE 4.1 - Parameters for Water Depth and Air Volume Effect Experiments
($g = 1$, $\sigma = 70$ dynes/cm)

Apparatus	Small Tank Test No.			Large Tank Test No.				
Water Depth (cm) Volume (cm^3)	30	45	60	30	45	60	90	120
14	S30-14.1 S30-14.2 S30-14.3 S30-14.4 S30-14.5 S30-14.6	S45-14.1 S45-14.2 S45-14.3 S45-14.4 S45-14.5 S45-14.6 S45-14.7	S60-14.1 S60-14.2 S60-14.3 S60-14.4 S60-14.5	L30-14.1 L30-14.2 L30-14.3 L30-14.4 L30-14.5	L45-14.1 L45-14.2 L45-14.3 L45-14.4 L45-14.5	L60-14.1 L60-14.2 L60-14.3 L60-14.4 L60-14.5	L90-14.1 L90-14.2 L90-14.3 L90-14.4 L90-14.5	L120-14.1 L120-14.2 L120-14.3 L120-14.4 L120-14.5 L120-14.6
16	S30-16.1 S30-16.2 S30-16.3 S30-16.4 S30-16.5	S45-16.1 S45-16.2 S45-16.3 S45-16.4 S45-16.5 S45-16.6	S60-16.1 S60-16.2 S60-16.3 S60-16.4 S60-16.5 S60-16.6	L30-16.1 L30-16.2 L30-16.3 L30-16.4 L30-16.5 L30-16.6 L30-16.7	L45-16.1 L45-16.2 L45-16.3 L45-16.4 L45-16.5	L60-16.1 L60-16.2 L60-16.3 L60-16.4 L60-16.5	L90-16.1 L90-16.2 L90-16.3 L90-16.4 L90-16.5	L120-16.1 L120-16.2 L120-16.3 L120-16.4 L120-16.5

TABLE 4.1 (Cont'd) - Parameters for Water Depth and Air Volume Effect Experiments
($g = 1$, $\sigma = 70$ dynes/cm)

rate than the remainder of the bubble group. At lower air volumes, although the bubble sizes were consistent with those in the test range, the bubble groups were very small and did not exhibit the rise characteristics as obviously as did the larger groups.

After each burst of bubbles was released, the water in the tank was allowed to stabilize so that the following bubble group would be released into quiescent water. As motion in the water was visible with floodlights directed at the tank, the existence of any currents could easily be verified during the course of the experiments.

Room temperature during the tests was 20°C according to the mercury thermometer which was mounted on the wall across from the laboratory, and the building compressed air supply was assumed to be at the same temperature, as it did not draw air from outside the building. Additionally, it was assumed that there was sufficient piping between the compressor and the outlet to allow enough heat transfer for the air to cool to room temperature following compression. After the tanks were initially filled, the water was allowed to warm up only to a temperature of 17°C prior to starting the experiments and the tanks were maintained at this level throughout the experiments. It was found that, in the large tank, allowing the water to fully reach room temperature initiated very slow convection currents which could not be eliminated. Thus, a small amount of heat transfer between the air and the water undoubtedly occurred, but, due to the short residence time of the bubbles in the liquid and the turbulence of the flow in the immediate vicinity of the bubbles, the isothermal flow assumption which was discussed in Chapter 3 was considered as a reasonable approximation for these experiments.

A Nikon N2000 camera with a power winder set for 2.5 frames per second, and a Nikkor 50 mm *f*1.4 lens, was used to take the photographs. The batteries in the power winder were changed at each water depth to ensure a relatively constant interval between each frame. Kodak T-Max 400 ASA 36 exposure film was used throughout.

Because the power winder could not provide a verifiably-constant time between successive exposures, a clock with a 0.01 second resolution was incorporated into all of the photographs. The films yielded measurements of bubble group size and vertical position as a function of time. The height of the group above the airstone was measured by overlaying each photograph with a transparency of the grid. A picture of the grid was taken at the beginning of each series of shots (*i.e.* at every water depth), and the camera location, exposure and focus was kept fixed for the remainder of the tests. The transparency which was traced from the grid shot thus accounted for the camera parallax and the refraction characteristics of the water and plexiglass for each series of photos.

The grid shots were lit from the front of the tank using a large 1 kW floodlamp. The bubble group photographs were illuminated using the same floodlamp mounted overhead, and four smaller 275 W floods directed from the side of the tank. A 100 W light focussed on the clock ensured that the times could be read from the pictures.

Video films of some of these experiments were also taken using a RCA CKC020 video camera connected to a RCAVLP950HP VHS video cassette recorder. The videos were taken from the front, side and top of each tank to verify that the bubble groups were centred over the airstone throughout their rise. This ensured that the measurements taken using the grid were actually the centreline values. The playback speed of the videos could also be

slowed to give a good indication of the flow patterns close to the airstone, and the trajectories of the individual bubbles as they rose to the surface of the water.

It must be remembered that, at the time these experiments were performed, computers were not nearly as sophisticated as they are at the time of publication, and technology such as scanners was not readily available to the author.

4.3.2 Experiments to Test Surface Tension Effects

In this set of tests, the surface tension of the water in the small tank was lowered using 2-propanol as a surfactant from a value of 65.6 dynes/cm to 35.5 dynes/cm. The volume of 2-propanol in the water was successively reduced by draining the small tank to the halfway mark, and then refilling it with tap water. The value of the surface tension was calculated using an average of five tests on a tensiometer, and the temperature of the mixture was recorded. Only the 60 cm water height was used in these experiments.

Initial calibration tests to determine the correct initial pressure needed to establish the required air volumes showed that consistent bubble group volumes could not be obtained. The tank was left to stabilize for a 12-hour period, and then the tests were attempted again. After five successive runs using the same initial manometer pressure yielded air volumes ranging between 3.0 and 6.6 cm^3, it was decided that only one air volume would be attempted in the surface tension experiments. As the larger injection volumes were more difficult to attain, the 8.0 cm^3 volume was chosen as the representative amount.

Black-and-white still photographs and video recordings were made of the experiments, and the run parameters are given in Table 4.2. The camera and lens used for

TABLE 4.2 - Parameters for Surface Tension Effects Experiments
(Small Tank, V = 8.0 cm³, g = 1, H_w = 60 cm)

	Camera	
σ (dynes/cm)	Video Test No.	Still Test No.
35.5	ST35.5-1 ST35.5-2 ST35.5-3 ST35.5-4 ST35.5-5 ST35.5-6 ST35.5-7	ST35.5-8 ST35.5-9
45.3	ST45.3-1 ST45.3-2 ST45.3-3 ST45.3-4 ST45.3-5 ST45.3-6 ST45.3-7 ST45.3-8	ST45.3-9 ST45.3-10
54.1	ST54.1-3 ST54.1-4 ST54.1-5 ST54.1-6 ST54.1-7 ST54.1-8	ST54.1-1 ST54.1-2
61.0	ST61.0-1 ST61.0-2 ST61.0-3 ST61.0-4 ST61.0-5 ST61.0-6	ST61.0-7 ST61.0-8
65.5	ST65.5-3 ST65.5-4 ST65.5-5 ST65.5-6 ST65.5-7 ST65.5-8	ST65.5-1 ST65.5-2

the water depth and injected air volume tests was also utilized for these runs. The lighting was also very similar to that used in the previous tests, and the same grid was used to take the measurements. The water/propanol mixture was also allowed to stabilize between successive runs, and the temperature of the mixture was a constant 17°C.

4.3.3 Experiments to Test the Effect of Gravity

Personnel wishing to conduct experiments onboard the KC-135 are required to pass a Ministry of Transport Civil Aviation Medical Examination and to undergo Pressurized Transport Aircraft Aeromedical Training (AMT) with the Canadian Forces Air Command. The AMT involves eight hours of classroom instruction and two simulated flights in a high-altitude chamber. The Type I flight is a depressurization to the equivalent of 25,000 feet above sea level plus hypoxia tests, and the Type IV flight is a rapid decompression from 4,000 to 18,000 feet. The author received her certification in January, 1989 at the Canadian Forces Base Griesbach in Edmonton, Alberta.

After the equipment was completed and calibrated in late February of 1989, it was packed into crates and shipped to the Ellington Air Field in Houston, Texas where the KC-135 hangar is located. Arrangements were also made to have a cylinder of compressed air shipped from a local Houston supplier to the hangar. Both the crates and the air cylinder arrived prior to March 9, 1989, which was the date the investigator flew in from Calgary.

The first day in Houston was spent unpacking and assembling the equipment, and undergoing a Test Readiness Review by ten NASA engineers. After the apparatus and the Test Equipment Data Package had been approved, the tank was filled and both skids were

installed on the aircraft. The three backup operators (Christin Choma, Ken Money and Glen Campbell) provided by NRC Space Division were then trained on the equipment. The actual tests were scheduled to take place on March 14, 15 and 16, but due to problems with the aircraft's hydraulic system, the third flight was postponed by one day. As this coincided with the investigator's return flight to Calgary, Glen Campbell of NRC Space Division ran the experiments on the third flight day. The equipment was removed from the plane and the crates were repacked and shipped back to the University of Calgary by NRC Space Division personnel.

A total of 106 parabolas were allotted to this experiment: 40 on the first flight; 46 on the second; and 20 on the third day of flights. The extra six parabolas flown on the second day included three at Moon gravity (1/6 **g**) and three at Mars gravity (1/3 **g**). Bubble groups were released under microgravity conditions and also during the 1.8 **g** pull-out. Data were recorded for 76 of the parabolic maneuvers; the remaining 30 were lost due to problems with the VCR and with the operator on the last flight day.

Before takeoff, the air storage cylinders were pressurized with the compressed air cylinder, which was then taken back to the hangar. A fully-charged Nicad battery was installed in the VCR before it was put into its holder. The same video recording system was used for the microgravity experiments as was used for the remainder of the laboratory runs. The plenum was removed and video shots were taken of the small-tank grid so that measurements could be made from the films. The plenum was replaced, and the air in the plenum was brought to ambient pressure. The ambient temperature and pressure were recorded, as well as the injection system pressure. During each flight, the control volume

was filled by remotely activating solenoid valve V4, and the pressure was recorded with transducer PT3 (see Figure 4.7 for the instrument locations). Bubble groups were released by opening solenoid valve V2. The volume of air in each bubble group was calculated using the pressure difference in the control volume before and after injection using Equation (B.1) from Appendix B. The control volume was then filled for the next run. After the flight, the pressure in the air system and the plenum was read, the system was drained of air and the VCR was removed from the holder so that the batteries could be recharged.

Due to the limited storage volume in the pressurized air system, the pressure in the control volume decreased slightly with each run and the pressure in the plenum increased. Because of this, each bubble group's volume was lower than that of its predecessor. The difference was small enough, however, that the volume could be considered constant for comparison purposes within a short range. Enough valid data were gathered to provide information for three air volumes at 1.8 **g**, and for one air volume each at the other two **g**-levels (all tests were taken at the one water height). The parameters for these runs are given in Table 4.3. It was not possible to determine group radius and velocity values from the zero-**g** runs, but bubble group behaviour under microgravity conditions will be discussed in Chapter 5.

Measurements from the KC-135 experiments were taken by making a transparency of the grid shots taken at the beginning of the video sequence, and fixing it to a video monitor with a flat screen. Values of bubble group diameter and height above the airstone were recorded as the tape was advanced frame by frame. The time between each video frame was measured using the VHS system's built-in clock, which had a 0.01 second resolution.

TABLE 4.3 - Parameters for Gravity Effect Experiments
(KC-135 Apparatus, H_w = 60 cm, σ = 70 dynes/cm)

	g		
Volume (cm^3)	1.8	1/6	1/3
8	G1.8-8.1 (24) G1.8-8.2 (26) G1.8-8.3 (27) G1.8-8.4 (28) G1.8-8.5 (29)		G1/3-8.1 (84b) G1/3-8.2 (85c) G1/3-8.3 (86a) G1/3-8.4 (86b) G1/3-8.5 (86c)
10	G1.8-10.1 (71) G1.8-10.2 (72) G1.8-10.3 (73) G1.8-10.4 (74) G1.8-10.5 (75)	G1/6-10.1 (81a) G1/6-10.2 (81b) G1/6-10.3 (82c) G1/6-10.4 (83a)	
12	G1.8-12.1 (52) G1.8-12.2 (53) G1.8-12.3 (54) G1.8-12.4 (55) G1.8-12.5 (58)		

Note: ( ) = Parabola Number

In order to determine the exact value of the gravitational acceleration at the time each group was released, the output from the control volume pressure transducer PT3 was recorded on computer by Dr. Bjarni Tryggvason, the Canadian astronaut responsible for monitoring the linear and angular accelerations of the KC-135 during the flights. Figure 4.8 is a sample trace of the z-acceleration for an entire parabola, and Figure 4.9 is an expanded view of the same trace for the microgravity period only. Figure 4.10 is a sample trace of the output from the pressure transducer. The level of gravitational acceleration at the time a bubble group was injected could be determined by comparing the time of the pressure drop in the control volume as shown in Figure 4.10 with the value of the z-acceleration at the same time on the equivalent plot to either Figure 4.8 or 4.9.

4.3.4 Dye Injection Experiments

Two series of dye injection experiments were carried out. The first set involved the release of different colours of dye at five levels in the large tank to form coloured planes in the water. The dye layering apparatus described in Section 4.1.2 was used to inject the dye. Three different water-soluble dyes were utilized, either separately or in combination: fluorescein (green), gentian violet (purple) and eosin (red).

When the bubble groups were released, the movement of the dye tracked the liquid motion generated by the bubbles. The results were recorded using a Nikon F camera and motor drive on colour print and slide film. This set of experiments was only carried out at one water depth (120 cm) for all five air volumes. The tank was drained and refilled between each run to remove all traces of dye from the previous test. The purpose of these

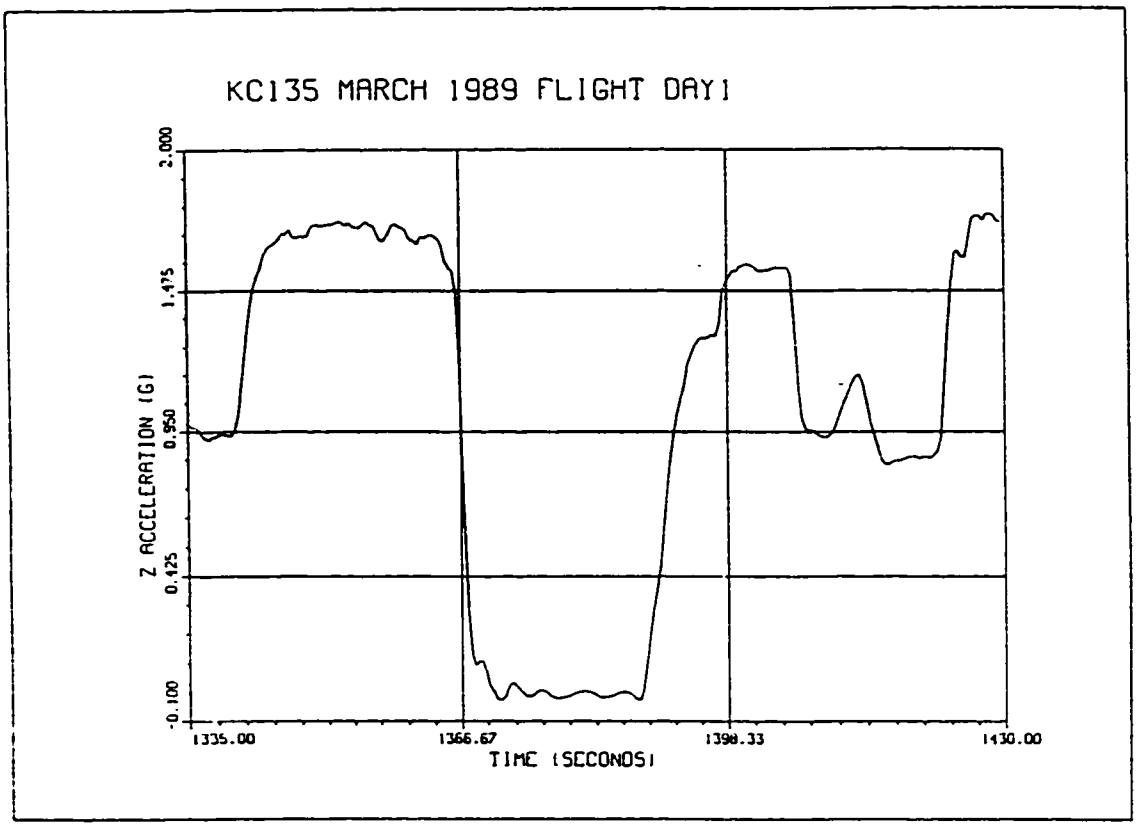

FIGURE 4.8 - Typical Acceleration Data for One Parabola (KC-135 Experiments)

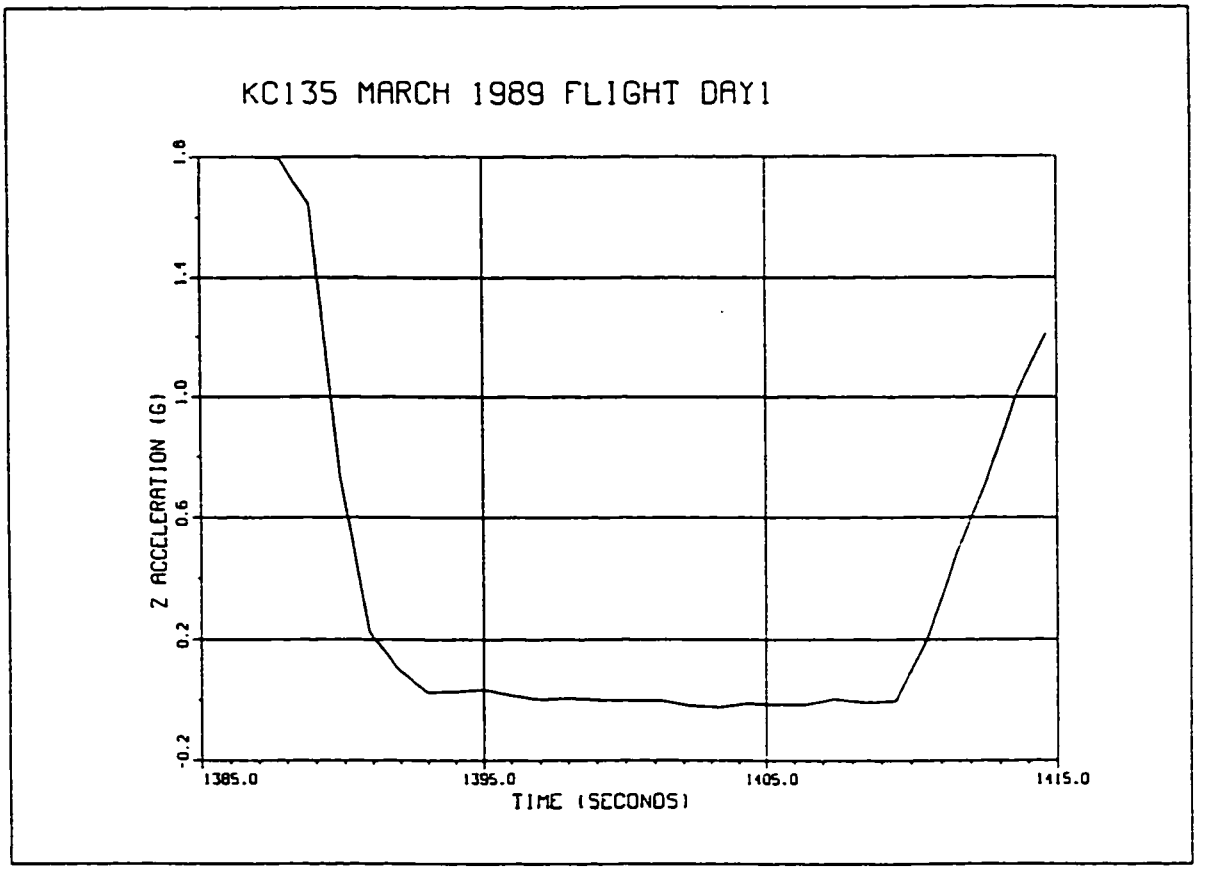

FIGURE 4.9 - Typical Microgravity Acceleration Data (KC-135 Experiments)

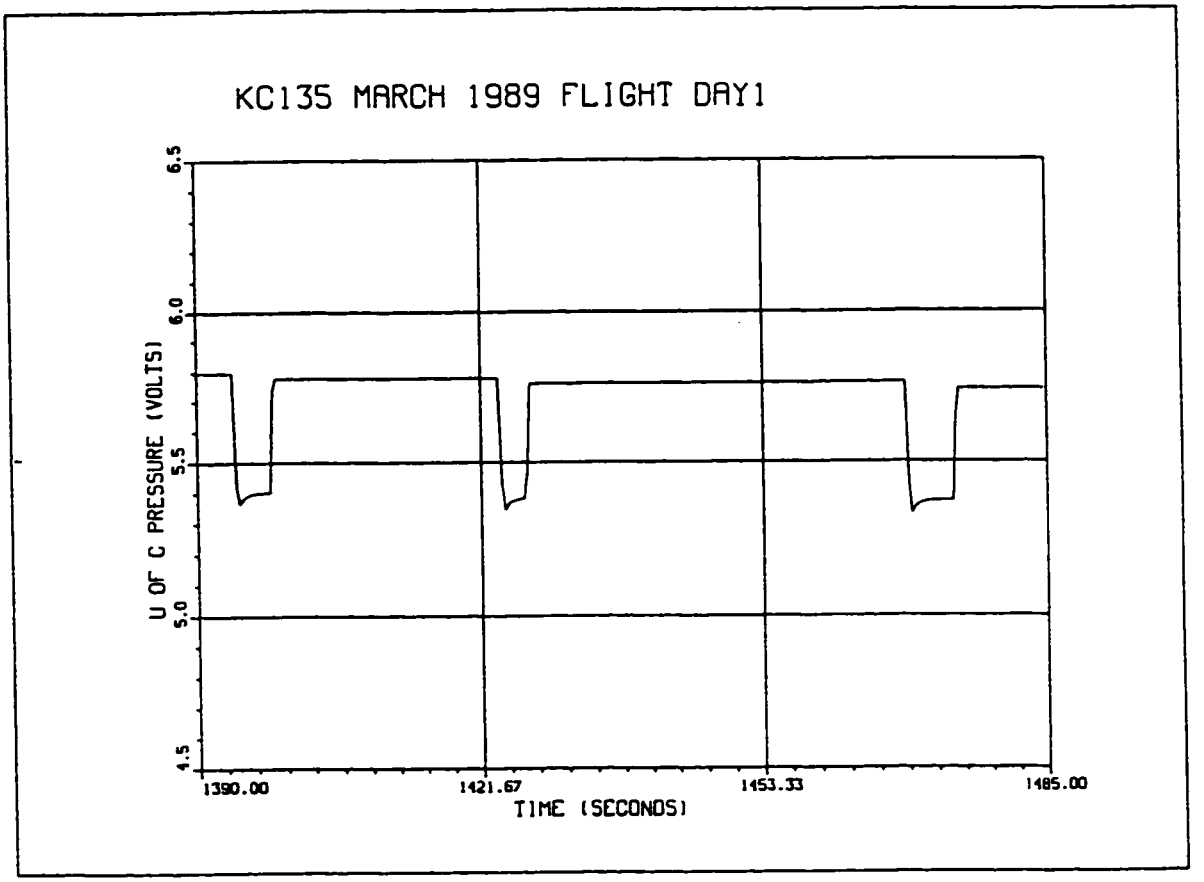

FIGURE 4.10 - Typical Output from Pressure Transducer PT3 (KC-135 Experiments)

experiments was qualitative rather than quantitative, and no measurements were made from the runs.

The second set of experiments was carried out by surrounding the airstone with a strong solution of fluorescein dye so that the liquid movement near the airstone could be tracked. For the small tank, the dye was injected through a separate tube strapped to the side of the tank so that it surrounded the airstone. Any turbulence caused by the injection process was allowed to subside prior to injection of the bubble group. In the case of the large tank, the reservoir immediately ahead of the airstone was filled with dye, which caused a small amount of dye to accompany each bubble group out of the injector. VHS videos were taken of the bubble and liquid behaviour for the large and small tanks, and color photographs were also taken of the small tank behaviour.

These tests were carried out in both the large and small tanks at a 60 cm water depth, and were repeated at least five times for each of the five air volumes. As in the first set of dye experiments, the tank had to be drained and refilled between each run to remove the dye from the previous test.

Measurements for the second set of dye injection experiments were taken by photographing the grid for each respective tank prior to each series of runs (*i.e.* for each air volume). A transparency of the grid was constructed and attached to a flat video monitor screen, and the measurements were made directly from the screen as the tape was advanced frame by frame. The time between each video frame was measured using the VHS system's built-in clock, which has a 0.01 second resolution. Parameters for each of these runs are shown in Table 4.4.

TABLE 4.4 - Parameters for Dye Injection Experiments
(H_w = 60 cm, g = 1, σ = 70 dynes/cm)

	Apparatus	
Volume (cm^3)	Small Tank	Large Tank
8	DS-8.1 DS-8.2 DS-8.3 DS-8.4 DS-8.5 DS-8.6 DS-8.7 DS-8.8 DS-8.9 DS-8.10	DL-8.1 DL-8.2 DL-8.3 DL-8.4 DL-8.5 DL-8.6 DL-8.7
10	DS-10.1 DS-10.2 DS-10.3 DS-10.4 DS-10.5 DS-10.6 DS-10.7 DS-10.8	DL-10.1 DL-10.2 DL-10.3 DL-10.4 DL-10.5 DL-10.6 DL-10.7 DL-10.8
12	DS-12.1 DS-12.2 DS-12.3 DS-12.4 DS-12.5 DS-12.6 DS-12.7 DS-12.8 DS-12.9 DS-12.10 DS-12.11 DS-12.12 DS-12.13	DL-12.1 DL-12.2 DL-12.3 DL-12.4 DL-12.5 DL-12.6 DL-12.7 DL-12.8 DL-12.9 DL-12.10 DL-12.11

TABLE 4.4 (Cont'd) - Parameters for Dye Injection Experiments
(H_w = 60 cm, g = 1, σ = 70 dynes/cm)

	Apparatus	
Volume (cm^3)	Small Tank	Large Tank
14	DS-14.1 DS-14.2 DS-14.3 DS-14.4 DS-14.5 DS-14.6 DS-14.7 DS-14.8	DL-14.1 DL-14.2 DL-14.3 DL-14.4 DL-14.5 DL-14.6 DL-14.7 DL-14.8
16	DS-16.1 DS-16.2 DS-16.3 DS-16.4 DS-16.5	DL-16.1 DL-16.2 DL-16.3 DL-16.4 DL-16.5 DL-16.6 DL-16.7 DL-16.8 DL-16.9 DL-16.10

4.3.5 Experiments Using High-Speed Photography

In order to examine the flows close to the airstone, a camera capable of recording high-speed phenomena was required. A HYCAM Model 41-004 16 mm motion picture camera was borrowed to perform these tests.

Nine rolls of film were taken using the HYCAM, at rates of between 1000 and 3000 frames per second. The highest speeds were necessary to freeze the bubble motion in the photographs of the flow near the airstone, where the bubble velocities were large. These films were used to determine if the air bubbles and water were circulating together in a thermal-like fashion. When the field of view was expanded to examine behaviour further from the airstone, lower film speeds were adequate as the bubble velocities in this region were considerably slower. In addition, the expanded field of view also necessitated a diffusion of the light sources with a resultant lowering of the intensity of the illumination, and thus it was impossible to film at higher speeds.

In general, the lighting needed to be much more intense than that used in the photography of the other bubble group experiments. An Ealing Stabilarc 250 lamphouse with a 200 W mercury vapour lamp and an optical feedback amplifier was the primary light source used in the shots close to the airstone, because its beam could be focussed on a very small area. For the photographs where a larger field of view was required, this lamp was supplemented by an Ealing Stabilarc 100 lamphouse with a 100 W tungsten halogen lamp, two 100 W mercury vapour light sources normally used in the Mechanical Engineering Department Schlieren apparatus, and the large 100 W floodlamp utilized in the other bubble group experiments.

The film used with the HYCAM was Eastman 4X 400 ASA black-and-white negative film in 100 foot rolls. The film was obtained from Kodak in Toronto, and it was necessary to send it to Alpha Cine Service in Vancouver for processing, as no local developer was available. Because it was difficult to determine with a light meter whether or not the illumination was sufficient for the film speeds used, several of the runs were not of very good quality. Therefore, only four positive prints were made of the best negative rolls for screening on a projector.

The HYCAM camera is subject to considerable vibration during operation. In order to film the flows in the large tank, where the airstone was located near the floor of the laboratory, it was necessary to design and construct a stand for the camera which could withstand these vibrations and also be tilted so that the lens could be focussed on the airstone. The stand was weighted with sandbags during the filming sessions to further reduce the possibility of camera motion. A heavy tripod was utilized to mount the camera for filming small-tank flows.

All of the bubble groups examined using the HYCAM camera had an injected air volume of 8.0 cm^3. No significant differences in overall bubble group behaviour with increasing air volume had been observed prior to the high-speed camera experiments. Thus, it was determined that a representative value would give valid qualitative results for all of the bubble groups that fell in the range examined in this experimental program.

CHAPTER 5

EXPERIMENTAL RESULTS

5.1 Introduction

The results of the laboratory portion of this project, in which groups of bubbles were released without any initial impulse into undisturbed fluid, are discussed in this chapter. One of the main difficulties in designing the air injection system was to determine whether or not the release of the bubbles was providing any initial impulse to the flow field, and it was not until the KC-135 experiments were performed that this lack of impulse was confirmed.

As was mentioned in the previous chapter, a total of five different air volumes (8.0, 10.0, 12.0, 14.0 and 16.0 cm^3(ST)) were examined at five different water depths in the large tank (30, 45, 60, 90 and 120 cm) and at three depths in the small tank (30, 45 and 60 cm) in the laboratory at 1 **g**. Due to the operating constraints on board the KC-135, it was only possible to utilize one water depth, but three different air volumes and three values of gravitational acceleration were examined. However, in all tests, the same airstone was used to ensure that bubble sizes were consistent.

Because no measurements were taken from the high-speed motion pictures, the qualitative results derived from the HYCAM tests will not be discussed separately. Instead, the insight gained from these films will be incorporated into the following sections.

5.2 Growth Patterns of Bubble Groups

Scorer (1958) noted that when groups of bubbles are suddenly released into quiescent fluid, they take on a configuration similar to that observed in single-phase thermals. This was also seen by Fraser (1981), and similar shapes were also observed in the current set of laboratory experiments. However, the results of this work also demonstrate that two-phase bubble groups do not exhibit the group circulation and constant overall entrainment characteristic of conventional thermals.

Atmospheric thermals have been previously described as rising vertically with a constant rate of spread; in thermal models, the radius is linearly related to the height above a point source by a proportionality constant which is usually termed the entrainment coefficient α (see Equation 2.7). This type of similarity solution is possible for a thermal because it exhibits a similar interior circulation pattern throughout its existence. Scorer (1957) and subsequent researchers found that, on the average, the entrainment coefficient had a value of approximately 0.25. Figure 5.1 is a plot of the raw data for a bubble group released in the large tank with an injected air volume of 16 cm^3(ST). The figure shows that, for about 10 cm above the airstone, the data can approximately be fit by a conventional thermal model using a value of 0.25 for α.

It should be noted that the plot of radius versus height implies the existence of radial symmetry for the bubble group. For thermal models, it has always been assumed that these structures are perfectly spherical, and that the radius measured at the widest point describes all dimensions of the thermal. However, even though bubble groups were found to be

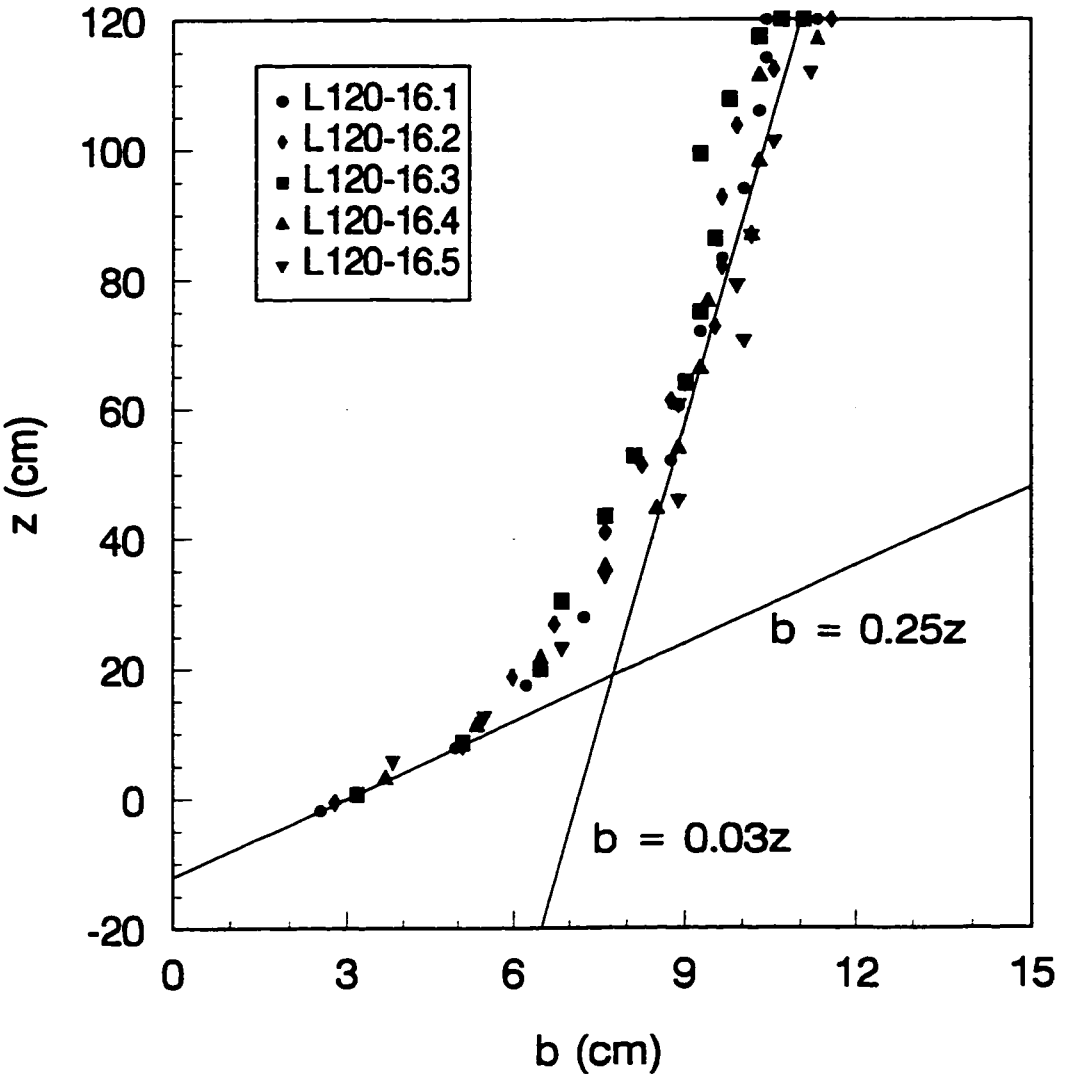

FIGURE 5.1 - Increase of Bubble Group Radius at its Widest Point with Height Above Injector for Five Large Tank, 16 cm^3(ST), Data Sets at H_w = 120 cm. The Plot Shows Two Straight-Line Asymptotes for Reference: a Conventional Thermal Relationship with α = 0.25 Near the Source, and a Round Bubble Plume-Type Model with α = 0.03 Closer to the Water Surface. It Should be Noted that These Asymptotes were not Determined Experimentally.

radially symmetric, they were actually elliptical in shape with a flattened bottom, similar in configuration to a cumulus cloud.

The data in Figure 5.1 can then be seen to deviate from the similarity solution until they approach asymptotically another straight-line approximation with a proportionality constant which is an order of magnitude smaller than that of a single-phase thermal. It should be noted that this second line is not a best-fit line to the data, but has only been drawn for reference. Experimentally-derived values for α will be discussed later in this chapter. It should also be noted that the entrainment coefficient used to draw this line is of the order of those for round bubble plumes (Poon, 1985).

An examination of Figure 5.1 implies that bubble groups have two main stages of growth, and this was verified by the experimental results. Close to the airstone, the bubbles circulate with the liquid as a two-phase thermal; this initial convective stage was verified by the dye-injection studies and HYCAM footage. In the second phase, the bubbles rise vertically, away from the still-circulating liquid. The transition between the two growth periods is characterized by the release of a vortex ring from the main body of the bubble group. The vortex ascends in the wake of the bubbles, and, as it rises, it expands in diameter and eventually decelerates. On the average, the vertical velocity of a bubble group was found to be almost double that of the vortex. The vortex continues to rise even after the bubbles break through the free surface.

Figure 5.2 is a photograph of the original tank that was built for the LDA experiments. In these early experiments, before the air injection system had been finalized, a number of very small bubbles (with diameters in the Stokes-flow range) were always

observed to trail behind the main bubble group following injection. These micro-bubbles served as flow tracers for the fluid, and they clearly show the trailing fluid vortex behind the bubble group in this figure. It should be noted that, because the overall injected air volume was the same for each run of a series, there were no appreciable differences in bubble group behaviour between early tests such as the one shown in Figure 5.2, and the later runs where most of the micro-bubbles had been eliminated.

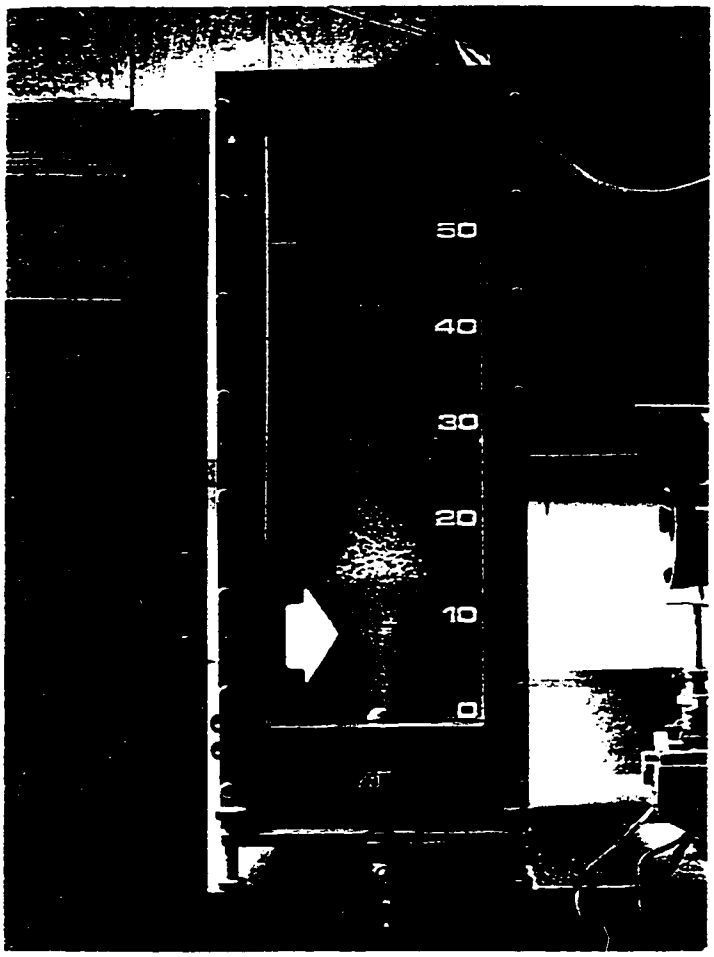

FIGURE 5.2 - View of the Fluid Vortex Released from the Bubble Group in an Early Small Tank Run, Using Micro-Bubbles as Flow Tracers. The Arrow Indicates Vortex Location.

The experimental results described to this point have shown that it is not possible to describe bubble groups using the "thermal" model proposed by Scorer (1958), Fraser (1981) and Fannelop (1982). For bubble groups to act as true thermals, they would have to maintain two-phase circulation throughout their entire period of growth; however, thermal-like behaviour is only evidenced close to the injector. The transition between this state and the second growth phase, where the circulating fluid is left behind, appears to start when the individual bubbles in the group reach terminal velocity. Figure 5.3, which is the velocity plot corresponding to the series of tests shown in Figure 5.1, shows that the velocity for the bubble group becomes approximately constant when the widest point of the group is about 10 cm above the top of the injector. This height corresponds to the end of the region in Figure 5.1 where the bubble group leaves the conventional thermal fit line.

Examination of Figure 5.3 shows that the actual velocity of each bubble group tended to oscillate around an average value. This is a reflection of the behaviour of the individual bubbles in each group; because the bubbles were not perfectly spherical in shape, but rather were slightly-flattened oblate spheroids, they rose in helical paths and not in straight lines. The level of the oscillation was seen to increase with air volume; for the 8.0 cm^3(ST) bubble groups, there was almost no deviation from the average velocity.

An average velocity for all of the runs shown in Figure 5.3 in the region above 10 cm is about 25 cm/s. The terminal velocity for a single bubble determined using the correlation given by Clift, *et al.* (1978) in Equation (3.9) is 23 cm/s. for a bubble radius of 4 mm. It is assumed that the reason why the group velocity is somewhat higher is because of the

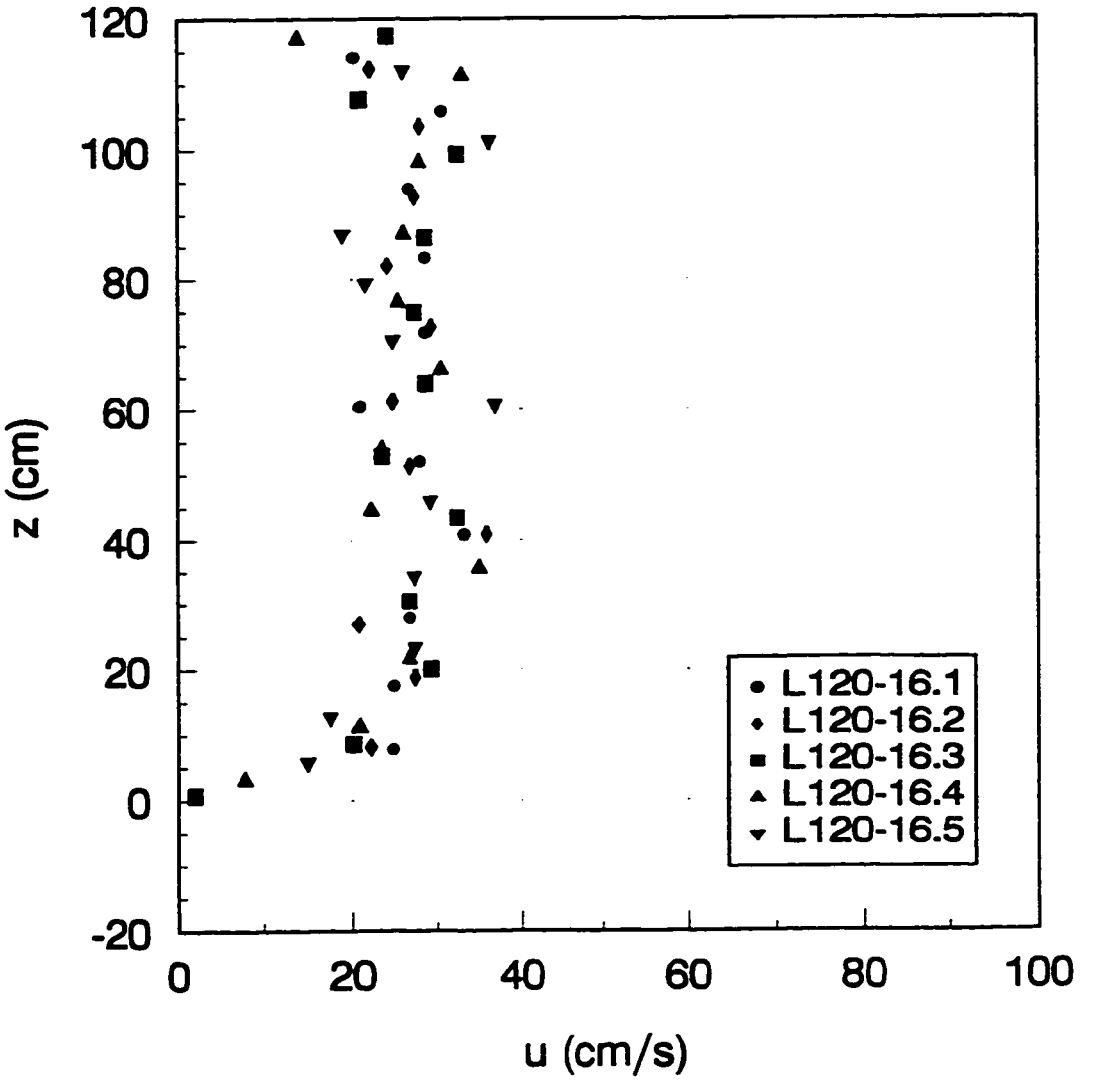

FIGURE 5.3 - Plot of Velocity Change with Height above the Injector for the Five Large Tank, 16 cm^3(ST), Data Sets at H_w = 120 cm Shown in Figure 5.1. Velocities were Calculated by Dividing the Height Above the Injector of the Widest Point of the Bubble Group by the Time Interval Between Measurements.

"slipstream" effect of the bubble wakes; as this velocity measurement was taken at the widest point of the bubble group, the bubbles at the top of the group would affect those following.

Another characteristic of the transition between thermal-like, or pseudo-single-phase, behaviour and complete separation of the bubbles and the fluid vortex was the tendency for the bubbles to accumulate around the outside of the circulating fluid. This is similar to the behaviour observed by Yeomans (1997) for solid-particle thermals. Once separation of the two phases was complete, the bubbles maintained this pattern until the free surface was reached. Figure 5.4 shows the rear of a bubble group breaking the surface in the large tank; note that the bubbles are clustered around the outside of the group, instead of being uniformly scattered throughout.

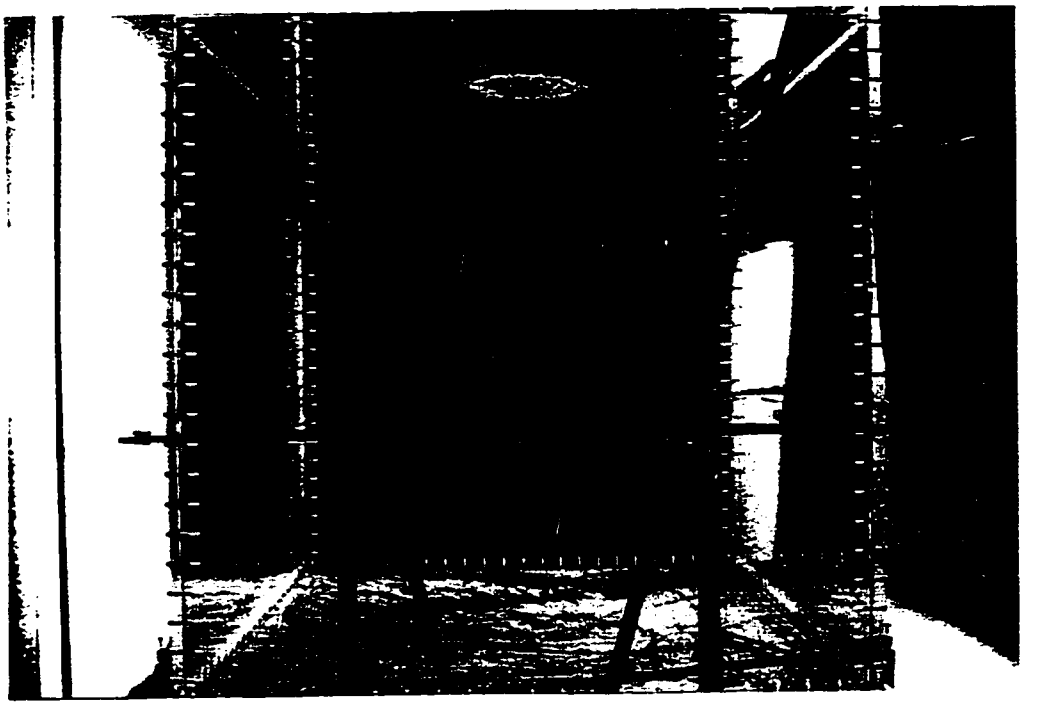

FIGURE 5.4 - View of Bubble Group at the Free Surface of the Water

It was observed in the experiments that, when bubble groups were released sequentially with a time delay between each injection, the rearward groups were seen to rise at a faster velocity than the preceding ones. Eventually, all of the bubble groups would amalgamate to form a plume-like structure; this observation supports the validity of a bubble plume model based on the intermittent release of bubble groups. It is postulated that the updraft in the centre of the trailing fluid vortices behind the bubble groups was the primary contributor to this behaviour, as was the slipstream effect of the higher bubble groups.

5.3 Bubble Group Database

One of the primary aims of this research program was the generation of a database of bubble group measurements. This was achieved with the publication of the raw data from the experimental work as a departmental report (Laureshen, 1992). The report includes all of the measurements from the small tank and large tank experiments (Appendix A and Appendix B), the KC-135 microgravity experiments (Appendix C), and the dye injection experiments (Appendix D). As it was only possible to generate qualitative and not quantitative results from the surface tension experiments and the films taken with the HYCAM camera, this information was not included in the report. However, these results are discussed herein.

It was originally intended to include the database as appendices to this dissertation. However, it was deemed preferable to publish the additional 257 pages separately, rather than add an extra volume to this work.

Figure 5.5 explains the type of measurements that were included in the database. In addition to the dimensions of the bubble groups and fluid vortices, the distances travelled from the point of release and times between the successive measurements were also recorded. Velocity data was not included in the report, as this is easily calculated by dividing the distance travelled by the time. As was explained in the previous chapter, the small tank, large tank and dye injection data were evaluated by placing a clear mylar grid over each photograph in the series; this mylar grid was calibrated from the photograph of the actual tank grid which was always the first photograph in the set. Times were recorded from the large stopwatch (12" × 12") that was always present in each picture. For the KC-135 data, measurements were taken by freezing successive frames of the video recordings and taking measurements from the monitor screen; the time was visible on each video frame.

There are some differences in terminology between Figure 5.5 and the tables given in the database. For the small and large tank data given in Appendices A and B of the report, as well as the KC-135 data in Appendix C, z is the height of the bubble group at its widest point (*i.e.* $z_{bubbles}$) and z_r corresponds to the height of the trailing vortex (z_{dye}), determined using micro-bubbles as flow tracers. For the dye-injection data in Appendix D, the terminology matches, except that the dye vortex width a is given as b_{dye}.

It should be noted that, at the time the data were evaluated, modern technologies such as scanners and digitizers were not widely available at the University of Calgary for the purposes of measurement. However, it is not believed that the accuracy of the database has been compromised because the data were recorded manually, since extreme care was taken with each of the measurements.

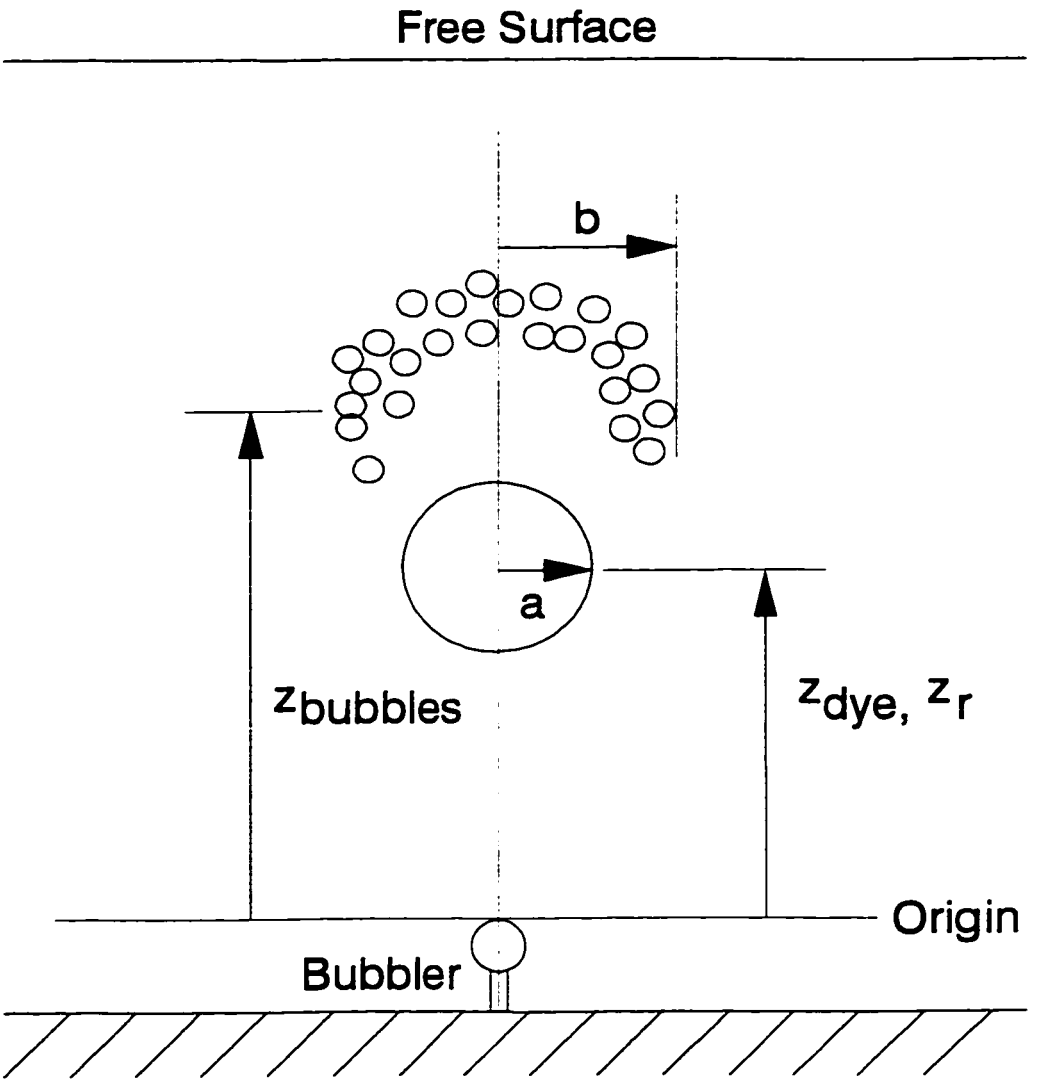

a = maximum radius of dye vortex
b = maximum radius of bubble group
z = vertical distance to the maximum radius of the bubble group or dye vortex
z_r= vertical distance to the maximum radius of the microbubble vortex trace

FIGURE 5.5 - Measurements Included in the Database

5.4 Effects of Varying Experimental Parameters

The bubble group experiments investigated the effects on bubble group behaviour of varying the following parameters: water depth, injected air volume, interfacial or surface tension and gravitational acceleration. This section discusses the effect that each of these parameters had on the bubble group behaviour

5.4.1 Effect of Water Depth

Table 4.1 in Chapter 4 lists the parameters for the experiments which investigated the effects of water depth and injected air volume. Five different air volumes (8.0, 10.0, 12.0, 14.0 and 16.0 cm^3(ST)) were examined for each water depth; in the large tank, water heights of 30, 45, 60, 90 and 120 cm were used, and only the first three of these depths were looked at in the small tank. Plots of the change in radius with water depth for each of these runs are included as Figures A.1 to A.15 of Appendix A (Small Tank Data) and Figures B.1 to B.25 of Appendix B (Large Tank Data) in the database report (Laureshen, 1992).

Figure 5.6 was created by superimposing database Figures B.21 to B.25 (16 cm^3(ST) injected air volume) to determine if water height had any effect on the change in group radius with water depth. The figure shows that there is no observeable depth effect which can be seen over the range of data examined. The same procedure was followed for all of the other air volumes in both the large and small tanks, and similar results were obtained for each data set. In the interests of brevity, these other figures have not been included as they were all similar to Figure 5.6.

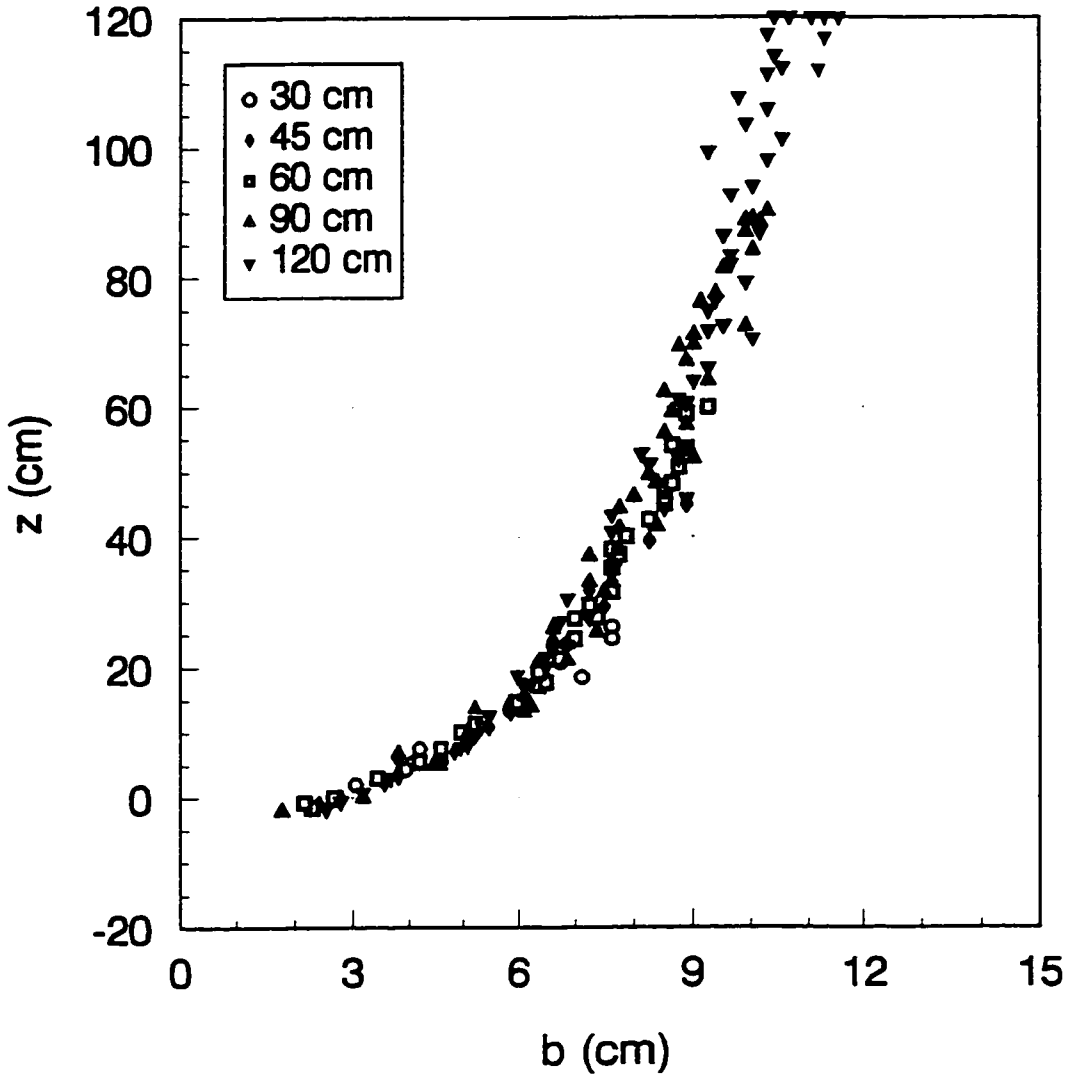

FIGURE 5.6 - Increase of Bubble Group Radius at its Widest Point with Height Above Injector for All 16 cm³(ST) Large Tank Data Sets at Five Water Depths. Over the Range of Data Examined, No Effect of Water Depth can be Observed.

5.4.2 Effect of Injected Air Volume

Figure 5.7, which is a plot of the change of bubble group radius with water height above the source for all injected air volumes in the large tank, shows that all of the bubble groups behaved similarly in their thermal-like stage, regardless of air volume. However, following transition, injected air volume had a noticeable effect on the proportionality constant relating radius to height above the airstone. If it is assumed that separation of the bubble group and the vortex ring is complete at 40 cm above the airstone, linear regression of the data above this point give the following values of α_2 for each air volume:

TABLE 5.1 - Variation of α_2 with Injected Air Volume

Injected Air Volume (cm^3(ST))	α_2
8.0	0.024
10.0	0.028
12.0	0.029
14.0	0.034
16.0	0.035

Varying the height at which separation was assumed had a minimal effect on the results given in Table 5.1, so long as the start of the regression was above the transition region (about 20 cm above the airstone). The results were found to be independent of water depth and tank size; *i.e.* similar results were obtained by regressing all data points for each air volume at all of the water depths examined in both the large and small tanks, except for the

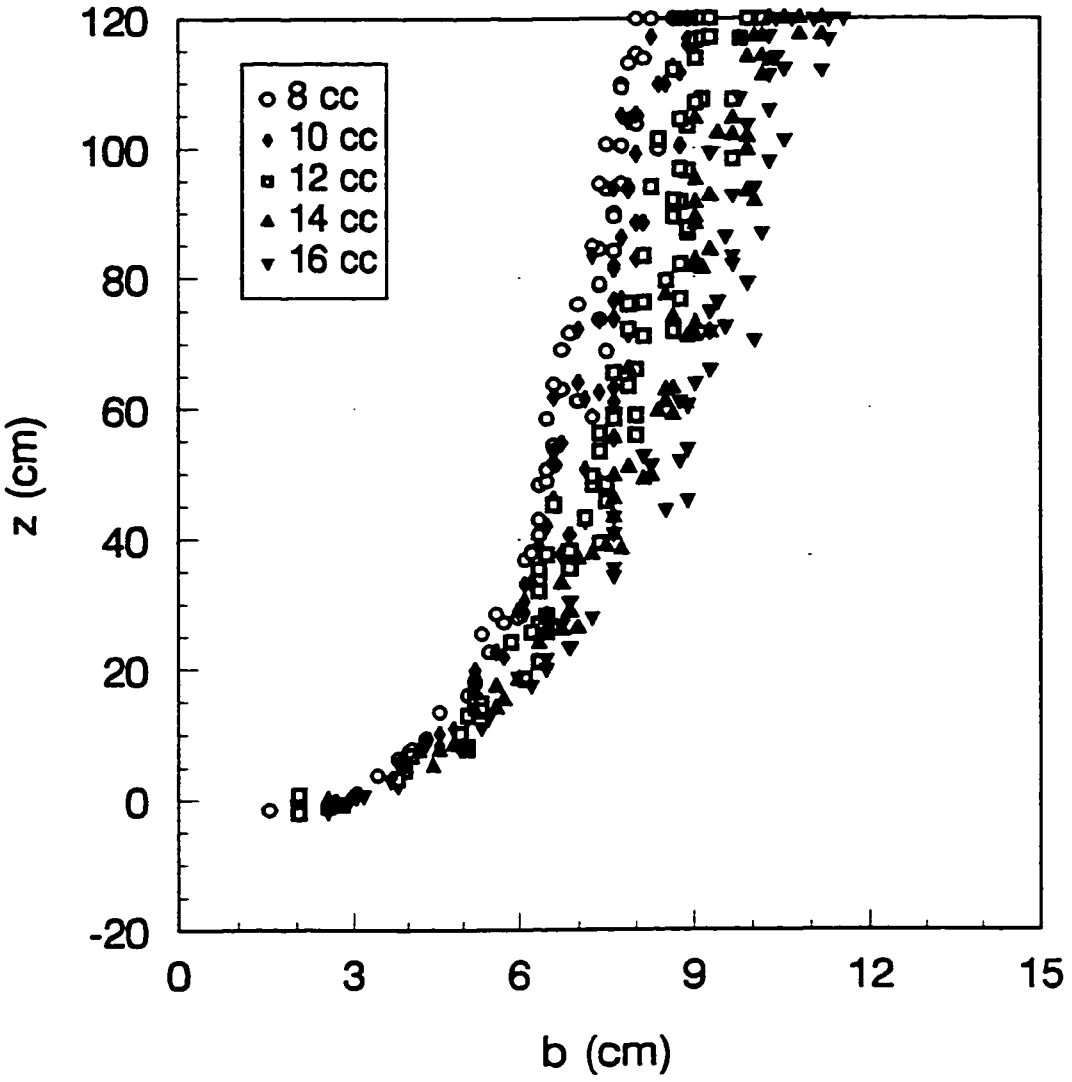

FIGURE 5.7 - Increase of Bubble Group Radius at its Widest Point with Height Above Injector for All Injected Air Volumes of the Large Tank Data Set at H_w = 120 cm. The Figure Shows an Increase of Overall Bubble Group Radius with Height Following Separation of the Bubble Group and Fluid Vortex.

30 cm water height. As the bubble sizes were relatively constant for each air volume examined due to the use of the airstone, it is probable that this effect is due to the increasing number of bubbles for the larger air volumes.

5.4.3 Effect of Surface Tension

The surface tension experiments were performed to determine if reducing surface tension would slowly decrease the size of the bubbles injected. However, adding a very small amount of surfactant (0.05% by weight) had a drastic effect on reducing the size of only some of the bubbles; most of the bubbles were of the sizes seen in the non-surface tension experiments. Futher increases in the surfactant concentration increased the number of the very small bubbles until, eventually, the bubble groups were entirely composed of micro-bubbles. After this point, no further reduction in bubble diameter could be obtained.

It was noted that the groups composed entirely of micro-bubbles followed thermal-like behaviour for much longer periods of time, *i.e.* the bubbles travelled with the fluid vortex. However, these experiments were carried out in the small tank only, so as not to cloud the plexiglass walls of the large tank with the 2-propanol surfactant and ruin it for further use. As a result, wall effects soon became dominant, because the micro-bubble groups expanded with the initial entrainment coefficient throughout, rather than exhibiting a lower value of α_2 following separation, as was seen in the remainder of this study.

It was decided not to pursue the surface tension experiments further for two main reasons. The first was that there was no money available to line the large tank with glass to prevent the plexiglass walls from becoming so clouded that they could not be used in further

photographic experiments. The second. and most important, reason was that the micro-bubbles seen in the surface tension experiments moved in the Stokes-flow regime, where drag forces are dominant. This meant that no valid comparisons could be made between the new data and those from the range of bubble sizes studied in the rest of this project.

5.4.4 Effect of Gravitational Acceleration

It was shown previously in Table 4.3 that enough valid data were gathered in the KC-135 experiments to provide bubble group radius and velocity measurements for three air volumes at 1.8 **g**, and for one air volume each at the other two **g**-levels; all tests were carried out at one water depth (60 cm). Plots of the change in radius with water height for each of these runs are included as Figures C.1 to C.5 of Appendix C in Laureshen (1992).

It should be noted that several occurrences during the flights may have affected the quality of the results. At the beginning of each 0 **g** portion of a parabola, there was usually a short period of negative **g**, which caused the air in the plenum on top of the tank to form a large bubble in the water. Sometimes, if the **g**-force was strong enough, this large bubble would travel all the way to the bottom of the tank and break up the smaller bubble group. Lateral accelerations in the aircraft also caused some migration of the bubble groups away from the injector axis, which is where the radii and velocities were measured. During each period of Moon and Mars gravity, more than one bubble group was sequentially released in order to gather as much data as possible for these **g**-levels. The water in the tank was therefore not completely quiescent between runs, which may have affected these measurements to a small degree.

Figure 5.8, which is a plot of bubble group radius versus height above the top of the airstone for a 10 cm^3(ST) volume at three **g**-values (1/6, 1.0 and 1.8 **g**), illustrates the two stages of bubble group growth discussed in Section 5.2. The significant feature illustrated in this plot is that, the higher the **g**-level, the higher in the tank the transition from the "thermal" stage to the vertical rise stage occurs. The flight videos also confirm that the vortex ring release takes place further away from the airstone with increasing **g**. This can be explained by the increased buoyancy of a bubble group for an equivalent air volume as the **g**-level becomes stronger. The resultant increase in momentum is transferred to the water, thus enabling the liquid to stay with the bubbles for a further distance. Also, the size of the bubbles released at the injector was smaller with increasing **g** due to the shorter time period it took for the bubbles to form. The surface tension experiments discussed previously showed that smaller bubbles tend to follow the liquid flow for a much longer period of time than do large bubbles. With a decrease in surface tension, however, the entrainment coefficient remained at its initial value throughout. Figure 5.8 illustrates a decrease in α with increase in gravitational acceleration after the transition point. Similar behaviour can also be seen in Figure 5.9, which shows the increase in bubble group radius versus height above the top of the airstone for an 8 cm^3(ST) volume at three values of gravitational acceleration (1/3, 1.0 and 1.8 **g**). It should be noted, however, that the time frame for the occurrence of the vortex release was the same for all levels of gravitational acceleration (approximately one second), even though the distance from the airstone was further.

The velocity of the bubble groups was also affected by gravity, increasing as the **g**-level increased. This trend is illustrated in Figure 5.10 by the same data set as was used in

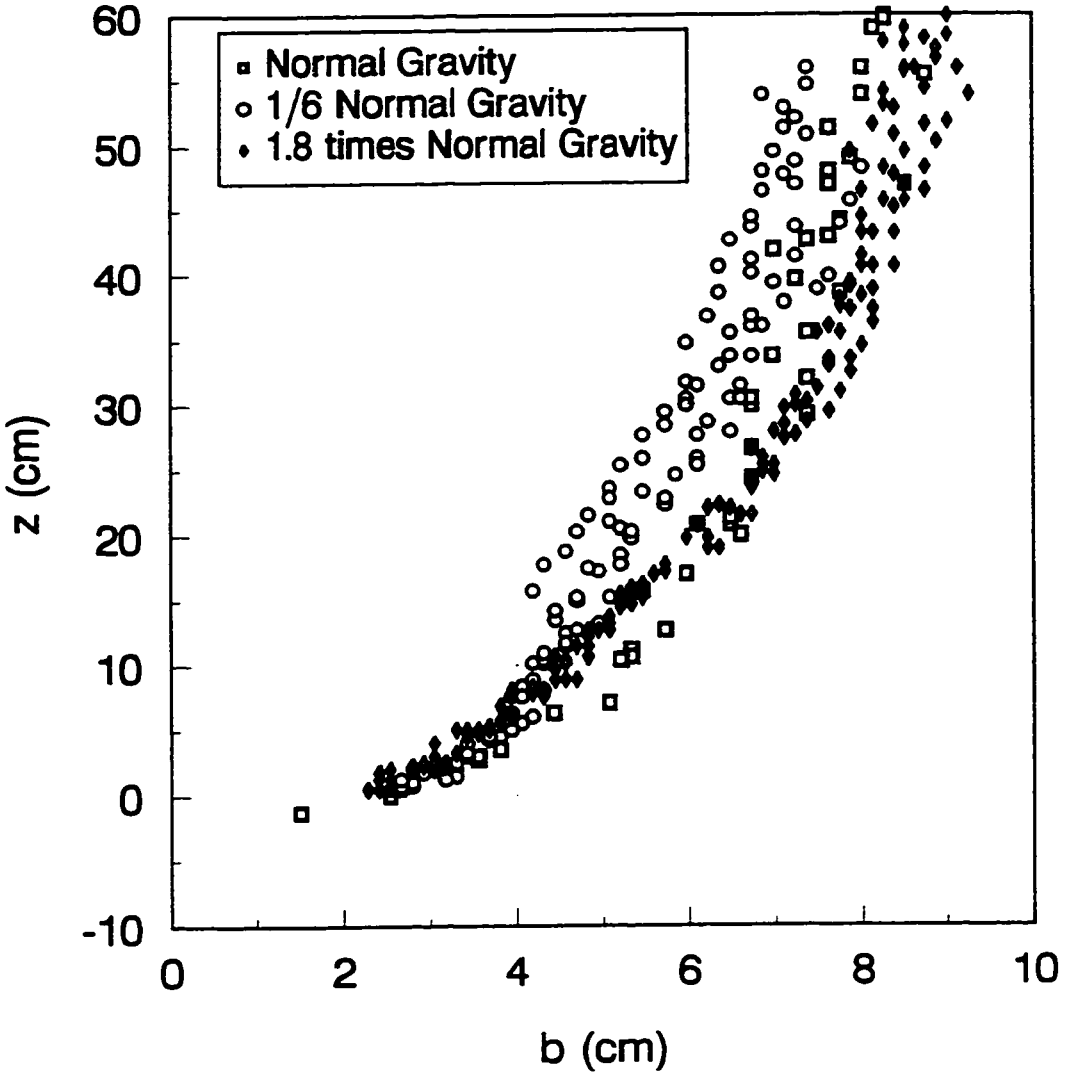

FIGURE 5.8 - Increase of Bubble Group Radius at its Widest Point with Height Above Injector for All 10 cm³(ST) KC-135 Data Sets at H_w = 60 cm and Three Levels of Gravitational Acceleration. The Figure Shows how Increasing the g-Level Causes the Fluid Vortex to Release Further Away from the Injector, in Addition To Decreasing the Entrainment Coefficient α Following Release.

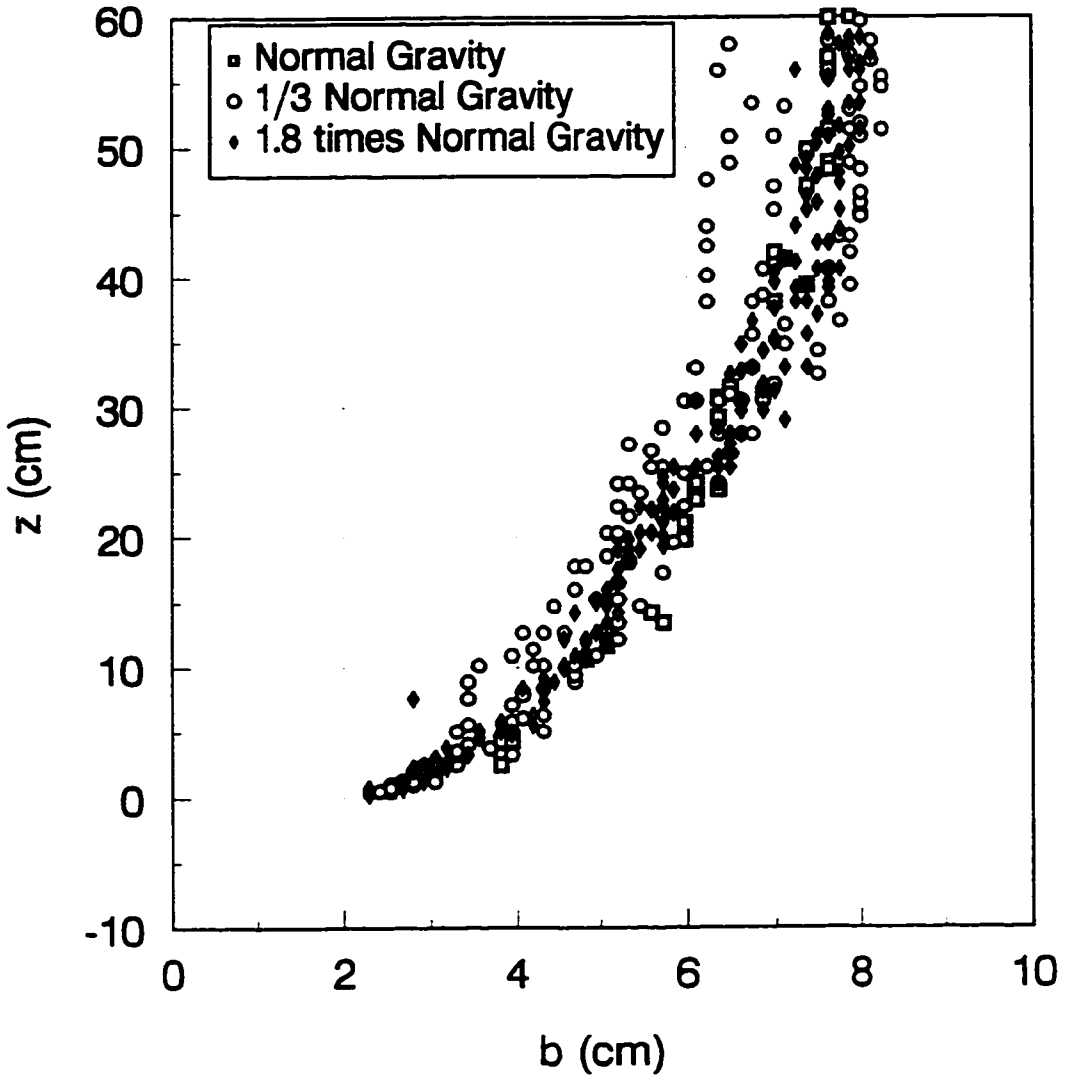

FIGURE 5.9 - Increase of Bubble Group Radius at its Widest Point with Height Above Injector for All 8 cm³(ST) KC-135 Data Sets at H_w = 60 cm and Three Levels of Gravitational Acceleration. The Figure Shows how Increasing the g-Level Causes the Fluid Vortex to Release Further Away from the Injector, in Addition To Decreasing the Entrainment Coefficient α Following Release.

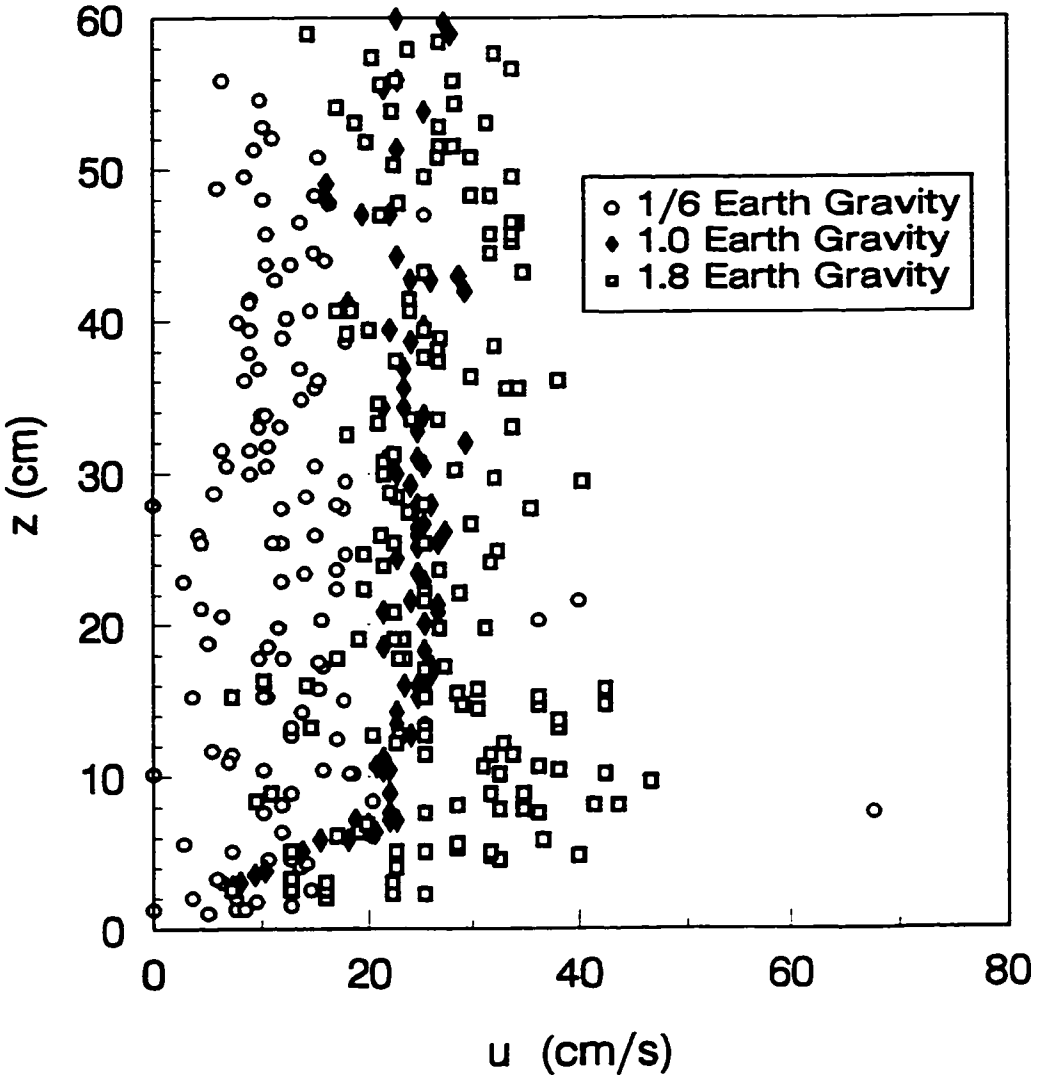

FIGURE 5.10 - Plot of Bubble Group Velocity with Height Above Injector for All 10 cm³(ST) KC-135 Data Sets at H_w = 60 cm and Three Levels of Gravitational Acceleration. The Figure Shows how Increasing the g-Level Causes an Increase in Average Velocity. The Scatter in the 1/6 and 1.8 g Data is Due to Variations in the Acceleration of the KC-135 Aircraft During the Tests.

Figure 5.8. The significant scatter in the 1/6 and 1.8 **g** data is attributed to the variations in the acceleration of the KC-135 during these runs. Examination of Figure 4.8 will show that, although great care was taken by the pilots to maintain the microgravity portion of each parabola, this was not the case for the remainder of the cycle. Since all of the other experiments on the aircraft were designed to be carried out at 0 **g**, the pilots concentrated on the peaks of the parabolas, where microgravity occurs, rather than the troughs.

An average of each of the data sets illustrated in Figure 5.10 gives mean values of 12.9 cm/s for the 1/6 **g** bubble groups, 22.6 cm/s for 1.0 **g** and 26.5 cm/s for 1.8 **g**. Due to the limited data from the microgravity experiments, it was not possible to develop an exact mathematical relationship, but it appears that bubble group velocity increases almost logarithmically with gravitational acceleration. This overall trend cannot be attributed to the small decrease in bubble size with increasing **g**, as all of the bubble diameters observed in the experiments should have had terminal velocities in a similar range (Haberman and Morton, 1954).

Figure 5.11 illustrates bubble group radius plotted against height above the airstone at 1.8 **g** for three different air volumes (8, 10 and 12 cm^3(ST)). The figure shows that the group radius increased with injection volume in the second stage of growth, which was similar to the results found in the laboratory at normal gravity (see Figure 5.12).

The results of this set of experiments were consistent with the 1.0 **g** laboratory experiments in that the entrainment coefficient was shown to be constant in the initial stage of bubble group development, and was proportional to the injected air volume in the second phase of growth. This conclusion is valid at any of the levels of gravitational acceleration

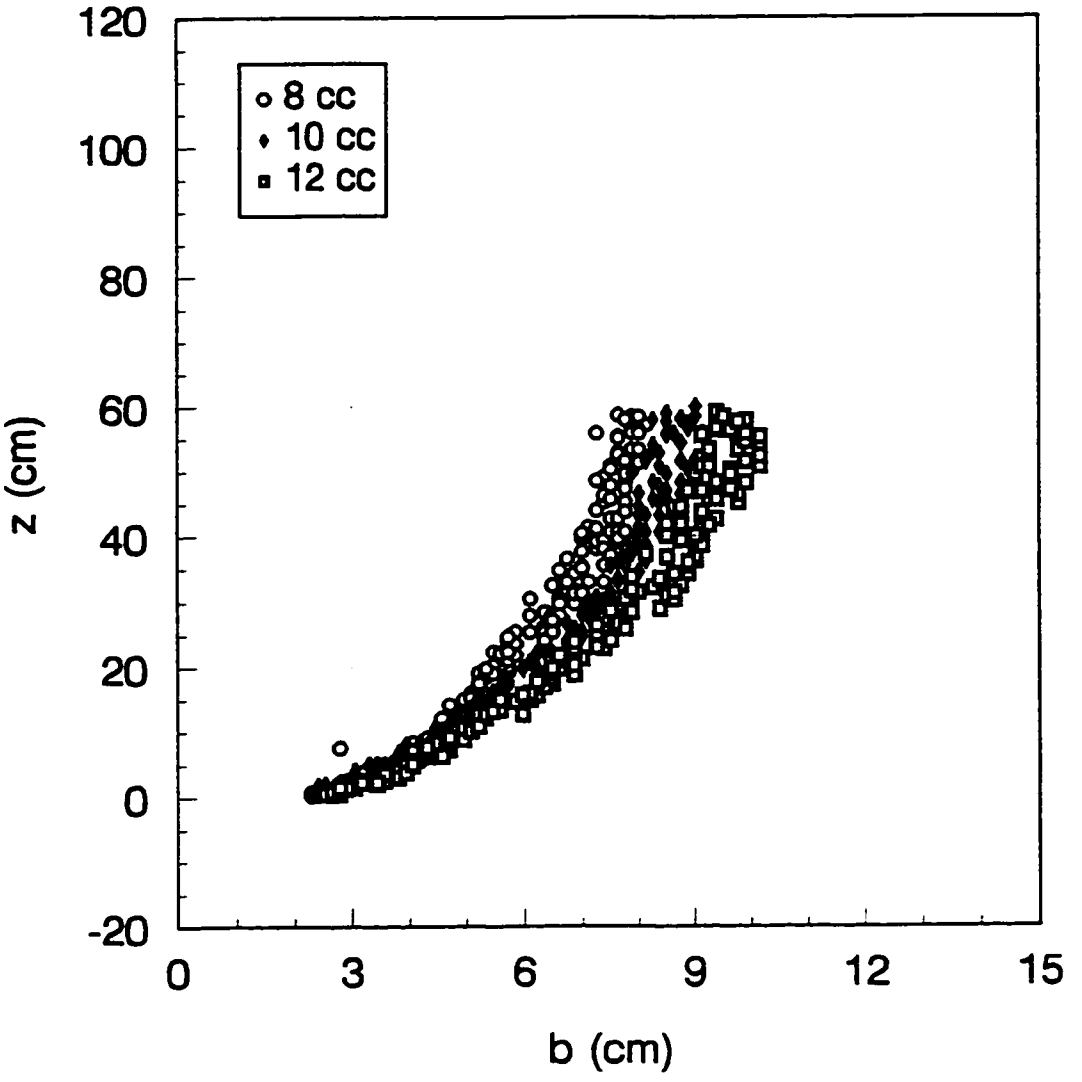

FIGURE 5.11 - Increase of Bubble Group Radius at its Widest Point with Height Above Injector for All 1.8 g KC-135 Data Sets at $H_w = 60$ cm and Three Levels of Injected Air Volume. The Figure Shows an Increase in Group Radius with Increasing Air Volume

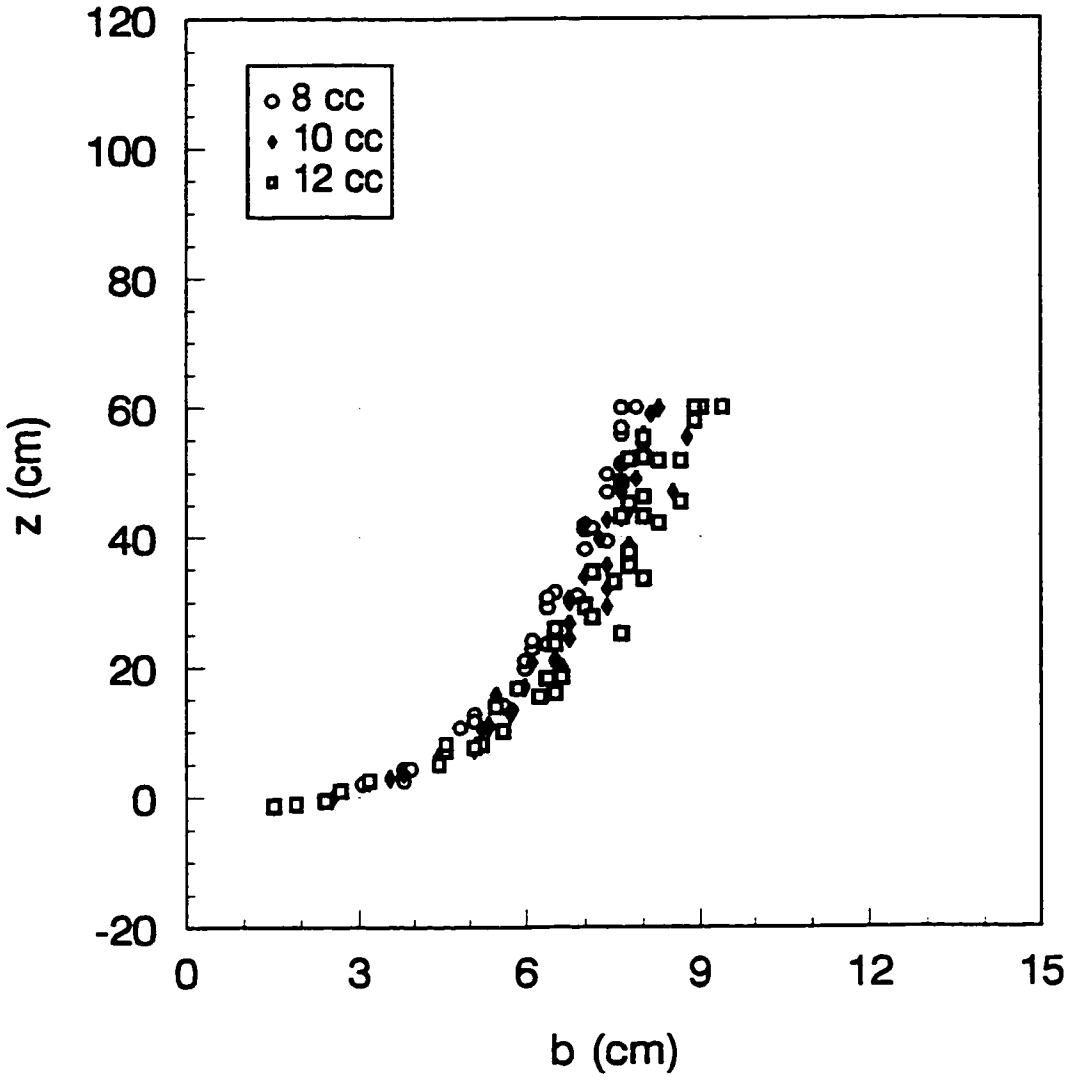

FIGURE 5.12 - Increase of Bubble Group Radius at its Widest Point with Height Above Injector for All 1.0 g Small Tank Data Sets at H_w = 60 cm and Three Levels of Injected Air Volume Corresponding to Figure 5.11. This Figure also Shows a Group Radius Increase with Increasing Injected Air Volume.

investigated except for 0 **g**. Since α is a local and not a global variable in bubble plumes (*i.e.* it varies with the distance from the origin), it is not surprising to note that the entrainment coefficient of approximately 0.2 seen for bubble groups in their formative stage is of the same order of magnitude as the value at the source of a bubble plume (Rowe *et al.*, 1989).

Higher gravitational acceleration also lengthened the distance before transition occurred from the circulating region to the vertical rise stage. It also delayed the detachment of the vortex ring from the main body of the bubbles, although the time at separation was the same for all **g**-levels. This agrees with the overall increase in bubble group velocity with gravity which was observed in the KC-135 experiments.

Increasing the **g**-level had the further effect of decreasing the size of the bubbles released at the airstone. Smaller bubbles are better able to follow the circulating liquid flow due to a lower slip velocity, although the bubble sizes observed in the experiments should not have had an appreciable difference in terminal velocity. Thus, it is assumed that the longer distance to transition is due to the increased momentum imparted to the bubble group from an increase in buoyancy, rather than to a smaller bubble diameter.

In comparison with the surface tension experiments described previously, increasing gravitational acceleration gradually reduced the initial size of each bubble in the group, rather than reducing radically the size of some of the bubbles. Also, a gravity increase tended to reduce the entrainment coefficient in the second stage, while lowering surface tension resulted in an increase in α.

As was mentioned previously in Section 4.3.3, it was not possible to draw any quantitative conclusions from the bubble groups released under microgravity conditions. The

primary reason for this was that, at 0 **g**, the bubbles would form on the airstone, but would not detach until they were forced to release because of a small variation in the acceleration level of the plane. The bubbles formed in microgravity were significantly larger than those formed under any level of gravity. When the bubble group did detach from the airstone, no transfer of momentum to the water was ever evidenced by the release of a vortex ring. However, if a bubble group was released just prior to a period of 0 **g**, a vortex ring would form in the water and continue to rise through the bubble group, which would remain stationary due to its lack of buoyancy in microgravity.

The one significant conclusion which could be drawn from the microgravity experiments was that the equipment itself was not contributing any initial impulse to the bubble groups. Had this been the case, the bubbles should have detached from the airstone at 0 **g** rather than remaining attached until acceleration changes caused their release. This result made it possible to determine that the trailing vortex behind the bubble group was formed solely by the bubble group wakes, and was not due to momentum imparted by the equipment.

5.4.5 Effect of Tank Size

One of the primary reasons for building the large tank was the concern that proximity to the tank wall was affecting the small tank data. Figure 5.13, which compares several 16 cm^3(ST) data sets from both tanks at a water depth of 60 cm, shows that there was a slight effect of tank size on the data.

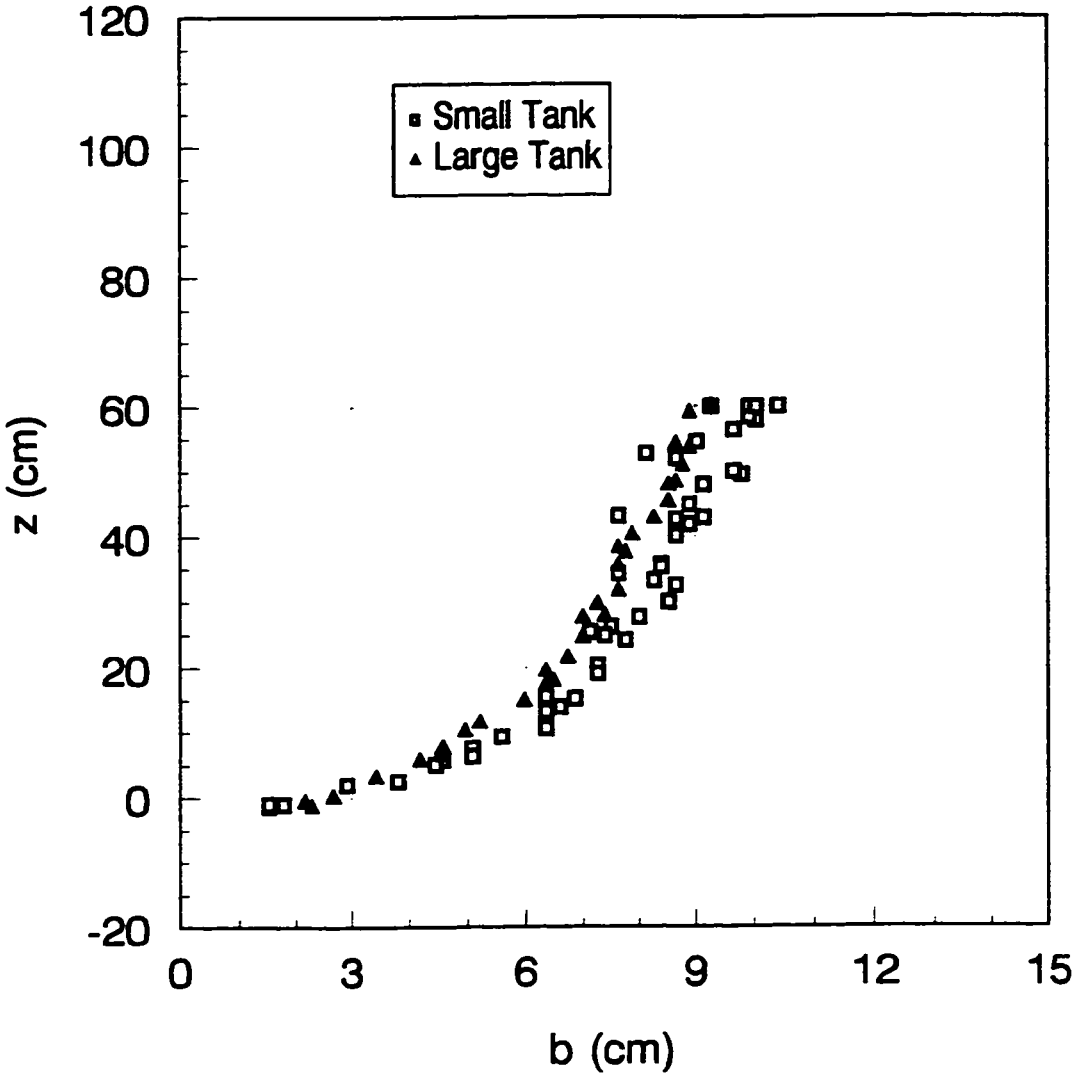

FIGURE 5.13 - Increase of Bubble Group Radius at its Widest Point with Height Above Injector for Several 16 cm³(ST) Small Tank and Large Tank Data Sets at H_w = 60 cm. No Effect of Tank Size Can be Seen Before or After the Transition Region, but the Transition Region is Longer in the Small Tank, which Indicates a Slight Wall Effect.

Figure 5.13 shows that all of the bubble groups behaved similarly in their thermal-like stage, regardless of tank size. Additionally, following transition, tank size had no effect on the proportionality constant relating radius to height above the airstone (see Table 5.1). The primary difference in the data lies in the transition region, which was longer in the small tank because of the attraction of the bubbles to the tank walls. This resulted in slightly larger bubble group radii in the small tank than were observed in the large tank, although the values of α were the same, and somewhat higher velocities for the bubble group. Bubble velocity increases due to wall proximity are well-documented in the literature (Yip, 1966).

Figure 5.14, which is a plot of several 14 cm^3(ST) data sets from both tanks at a water depth of 60 cm, shows that the effect of tank size was consistent, even with smaller air volumes. As a result of this finding, it is suggested that any further work carried out on the database concentrate on the large tank results, rather than the small tank data. However, the general conclusions drawn from the microgravity experiments are still valid, regardless of tank size, although the recorded velocities and radii might be slightly overestimated.

5.5 Results of Dye Injection and HYCAM Experiments

Two different types of dye injection experiments were carried out. In the first set, different colors of dye were injected at five heights in the large tank to form colored planes in the water. The purpose of these tests was to see if the upward motion in the water was caused by the bubble wakes, or whether the primary effect was due to the rising fluid vortex.

The dye layers were not completely flat, as the dye formed jets when forced through the pinholes in the injection lines. As the injection apparatus was moved across the tank,

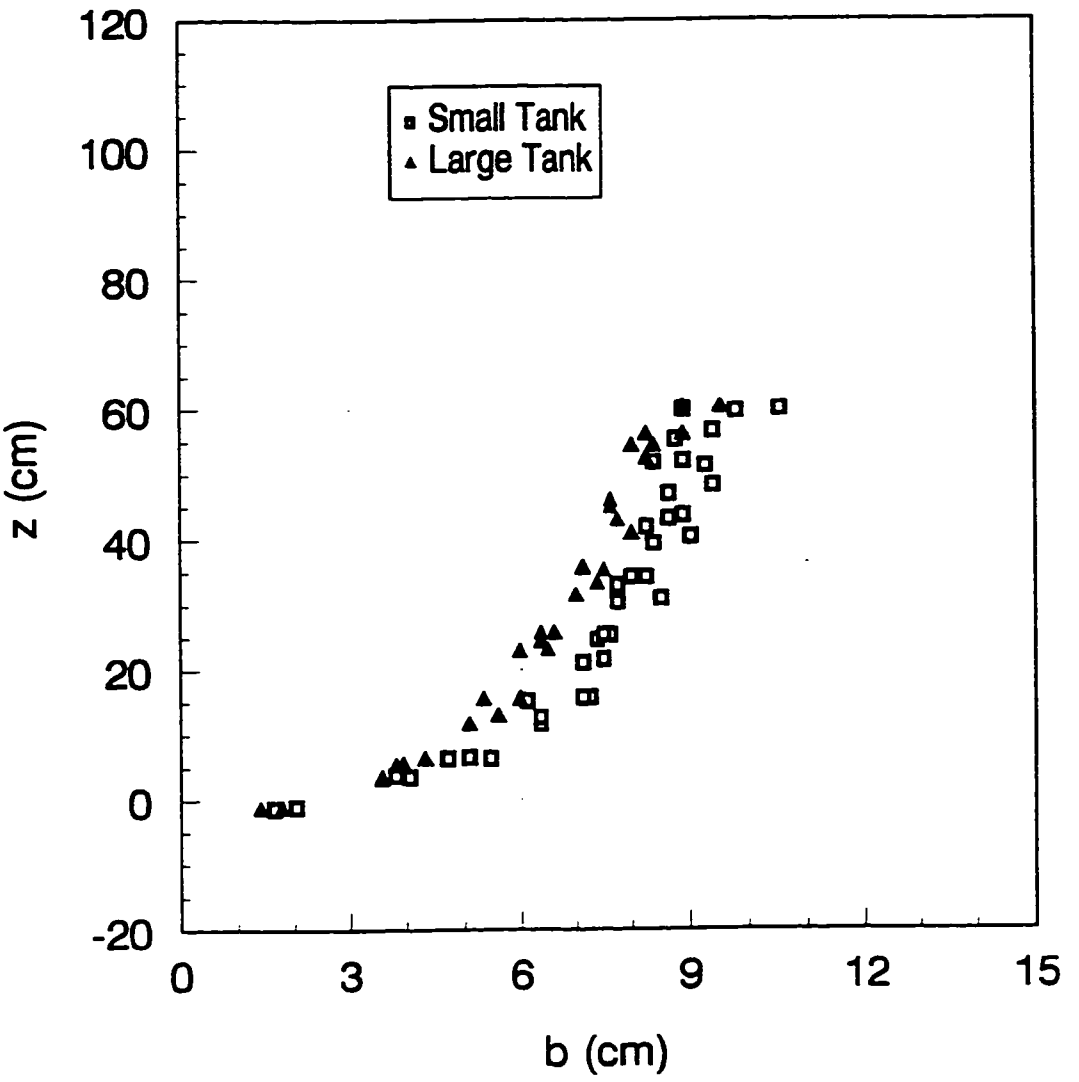

FIGURE 5.14 - Increase of Bubble Group Radius at its Widest Point with Height Above Injector for Several 14 cm^3(ST) Small Tank and Large Tank Data Sets at H_w = 60 cm. No Effect of Tank Size Can be Seen Before or After the Transition Region, but the Transition Region is Longer in the Small Tank, which Indicates a Slight Wall Effect. This is Consistent With the Results Seen in Figure 5.13.

these jets spread out and formed a dye plane approximately 5 to 8 cm thick. This method of injection caused a certain amount of turbulence to be present in the water even before a bubble group and vortex rose through the dye layers. However, the jets were directed orthogonally to the motion of the bubbles and the vortex, and care was taken to allow any large-scale eddies to dissipate prior to the injection of the bubble group.

The general conclusion which was drawn from these experiments is that the rising bubbles had little or no effect on the dye layers, but the vortex set off a large-scale upward motion in the water. The circulating vortex entrained the dye in each of the layers, and carried it upwards towards the surface. Circulation in the vortex could clearly be seen because of the entrained dye; it was upwards in the vortex centre, with the downward motion spread evenly around the outside. The vortex diameter appeared to grow larger with height, although not as much as for the bubble group. The vortex also slowed as it approached the water surface, unlike the bubble group, which appeared to rise at a constant velocity.

Because of the turbulence which was present from the injection process, the previous comment about the effect of the bubble wakes on the water cannot be taken as conclusive. If the scale of turbulence in the wakes of the rising bubbles was of the same order of magnitude as that in the dye jets, any effect from the bubbles would not be obvious.

No measurements were taken from this set of experiments, because of the inexact method of dye injection used. More accurate results could have been obtained by using a laser light sheet to illuminate a thin cross-section of the tank, but no suitable laser was available for use in the faculty at the time this option was investigated.

The second set of dye injection experiments was carried out by surrounding the airstone with a strong solution of fluorescein dye so that the liquid movement near the injector could be tracked. As was described in Chapter 4, this process was carried out differently in the small tank and the large tank, and it was hoped to determine if the method of dye placement made a difference in the results.

Figure 5.15 is a photograph of a dye injection run in the small tank. In this figure, the movement of the fluid vortex following the bubble group is clearly visible at the top of the dye cloud surrounding the airstone. Note that the fluid vortex is approximately circular in shape, similar to a single-phase thermal.

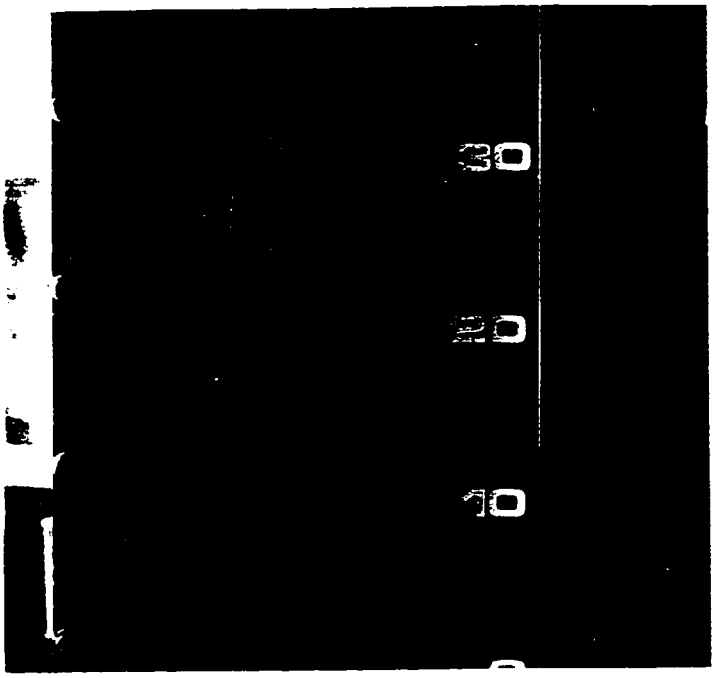

FIGURE 5.15 - Photograph of Small Tank Dye Injection Experiment

Figure 5.16 is a sample of the data recorded from the second set of dye injection experiments. It shows a plot of bubble group and dye vortex radius growth with height for one 16 cm^3(ST) bubble group. Although all of this type of dye injection experiment were carried out at a water depth of 60 cm, measurements were only recorded for the first 20 cm of height from the top of the airstone, as the purpose of these runs was to garner initial conditions for the bubble group simulations. It has previously been noted that bubble groups reach a constant velocity by a height of about 10 cm above the injector, and it was decided that a height of 20 cm would cover the initial two-phase growth period, the transition stage and part of the region where the fluid vortex and dye rise separately.

The figure shows that the dye and bubbles circulate together only for a height of 2 cm above the top of the injector. The transition region appears to lie between this height, and a height of about 15 cm above the airstone, and then the bubble group expands at a constant but smaller growth rate from that point to the water surface.

Throughout the entire transition region, the dye vortex velocity remains constant. This is shown in Figure 5.17, which plots height versus time for the same 16 cm^3(ST) run as was used in Figure 5.16. However, the previous set of dye injection experiments indicated that the vortex did eventually slow over time, as more of the quiescent surrounding fluid was entrained into the vortex.

Table 5.2 lists the measurements which were taken from the second set of dye injection experiments for use in the simulations. Given in the table are the entrainment coefficients in the two-phase region, the transition region and the asymptote value for the final growth stage from Table 5.1. Also presented are the radius and height of the two-phase

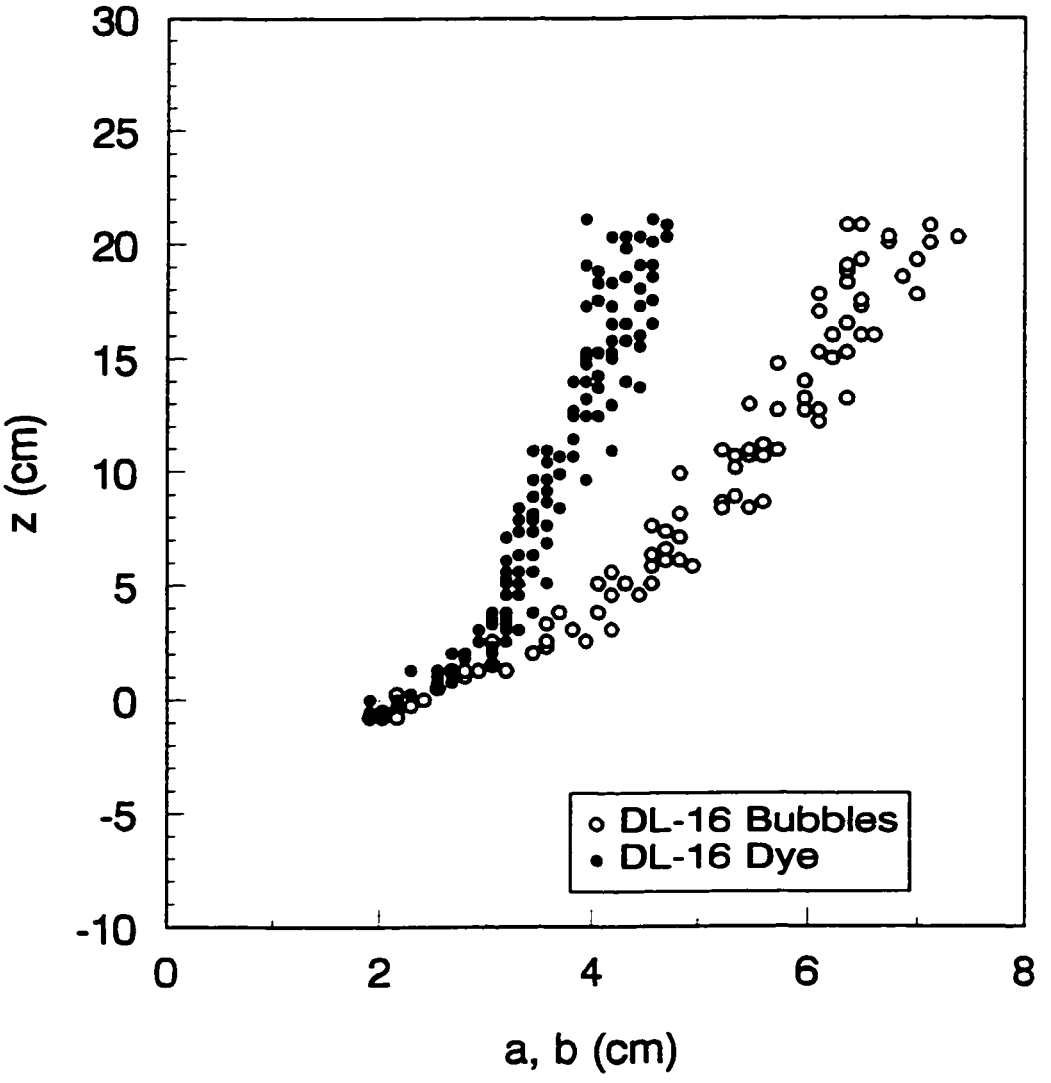

FIGURE 5.16 - Increase of Bubble Group Radius *b* at its Widest Point and Dye Vortex Radius *a* at its Widest Point with Height Above Injector *z* for a 16 cm³(ST) Large Tank Dye Injection Test at H_w = 60 cm. The Figure Indicates that the Transition Region Lies Between Approximately 2 cm and 15 cm Above the Injector. Below 2 cm lies the Circulating "Thermal" Region, and Above 15 cm, the Bubble Group Expands at a Constant but Smaller Growth Rate.

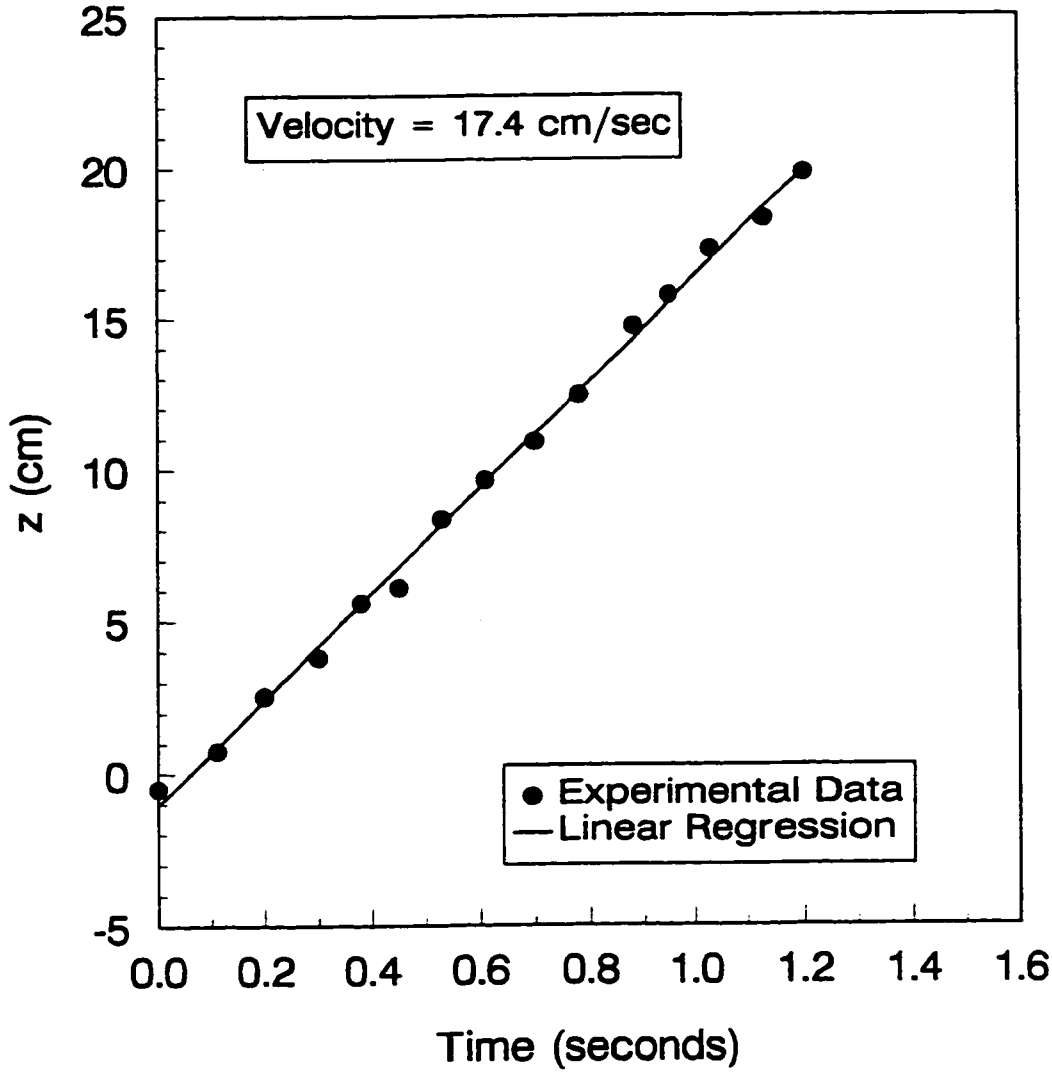

FIGURE 5.17 - Plot of the Height of Widest Point of Dye Vortex *a* Above Injector versus Time for the 16 cm^3(ST) Bubble Group Shown in Figure 5.16 (H_w = 60 cm). The Figure Shows that the Dye Vortex Velocity is Essentially Constant.

TABLE 5.2 - Bubble Group and Dye Vortex Expansion and Separation Data from Small and Large Tank Dye Injection Tests

Volume (cm^3(ST))	8	10	12	14	16
Small Tank Tests					
α_1 (Bubbles and Dye before Separation)	0.375	0.472	0.438	0.510	0.430
Height at Separation (cm)	4	3.5	3	2.5	1.5
Radius at Separation (cm)	3.5	≈3.7	≈3.3	≈2.6	≈2.6
α_d (Dye Vortex after Separation)	0.059	0.071	0.110	0.126	0.108
α_b (Bubble Group Immediately after Separation)	0.090	0.131	0.135	0.158	0.172
α_2 (Asymptote Value from Table 5.1)	0.024	0.028	0.029	0.034	0.035
Average Dye Vortex Velocity (cm/s)	12.65	13.57	13.15	16.03	19.25
Average Bubble Group Velocity (cm/s)	24.53	23.11	23.42	23.40	25.04
Average Bubble Group Velocity from Small Tank Experiments without Dye (cm/s)	23.14	22.81	22.90	22.72	22.42
Large Tank Tests					
α_1 (Bubbles and Dye before Separation)	0.360	0.363	0.437	0.511	0.420
Height at Separation (cm)	4	3.5	3	2.5	1.5
Radius at Separation (cm)	3.1	≈3.2	≈3.1	≈3.2	≈3.1
α_d (Dye Vortex after Separation)	0.073	0.078	0.107	0.090	0.082
α_b (Bubble Group Immediately after Separation)	0.091	0.125	0.139	0.152	0.174
α_2 (Asymptote Value from Table 5.1)	0.024	0.028	0.029	0.034	0.035
Average Dye Vortex Velocity (cm/s)	12.3	14.4	14.1	16.1	17.4
Average Bubble Group Velocity (cm/s)	22.34	22.44	22.12	22.91	22.61
Average Bubble Group Velocity from Large Tank Experiments without Dye (cm/s)	24.33	23.84	24.53	23.76	24.50

mixture at separation, the average dye vortex and bubble group velocities, and the average bubble group velocities from the small and large tank experiments. Note that, in general, the bubble group velocities are higher for the dye runs than the non-dye runs for the small tank data, and slower for the large tank data. This indicates that the method of dye injection most probably did have an effect on the final results. The differences between the small tank velocities ranged between 0.3 and 2.62 cm/s, or from 1.3 to 11.7 percent, and in the large tank, the differences lay in the other direction between 0.85 and 2.41 cm/s, or from 3.7 to 10.9 percent. Also, the dye vortex velocities were higher for the large tank, except at the highest air volume, which reflects the lower bubble group velocities. Effectively, with the dye and the bubbles being injected together rather than separately, the bubbles were losing some momentum by pushing the dye out of the airstone ahead of themselves. However, this was very similar to what was happening in the non-dye injection runs, as the reservoir tended to fill with water between tests. An arbitrary decision was therefore made to use the large tank values in the simulations, as the differences in the data were within a reasonable range.

Variation between the tanks is less apparent in the region up until separation. The height at separation was the same for both tanks, although the radius at separation was larger for the first three small tank air volumes, and smaller for the 14 and 16 cm^3(ST) data. In general, the entrainment coefficients were very close in both tanks during the two-phase growth period, although α_1 for the 10 cm^3(ST) data in the small tank was significantly larger than the large tank value (about 30 percent). It is not known why this is the case, although it is probable that not enough time was allowed for the injected dye to settle in the small tank prior to injecting the air bubbles. This was the first set of runs that was carried out in the

small tank, and the injection procedure was probably not as consistent as it was for the later tests.

Following separation of the dye vortex and the bubbles, the proportionality constants relating bubble group radius to height were extremely close. This was also true for the asymptote values from Table 5.1, which were the same for both tanks.

The HYCAM experiments were carried out in order to get a closer view of the behaviour of the bubble group close to the airstone and in the transition region. Figure 5.18, which covers the time period between 0.12 and 0.22 s following the opening of the solenoid valve, clearly shows the formation of the vortex ring just below the top of the airstone. It can be seen in the figure that not all of the bubbles in the bubble group are circulating with the fluid, but only those closest to the airstone. The other thing that is clear from this series of photographs is that the bubbles are not all released at the same time, but continue to be formed as the front end of the bubble group rises.

Figure 5.19 shows the same bubble group at 0.26 and 0.31 s after the opening of the injection valve. Here, the influence of the fluid vortex is clearly obvious, as the bubbles which are being formed after the initial group releases are being drawn towards the centre axis by the upward motion of the vortex. Also, the sides of the main bubble group have moved downwards with respect to its centre, thus indicating that there is some two-phase circulation occurring.

Figure 5.20, which occurs at 0.43 and 0.49 s following injection, shows that by this time, the only bubbles being formed are much smaller than those in the main body of the bubble group. The beginning of the separation phase, where the bubbles are rising away

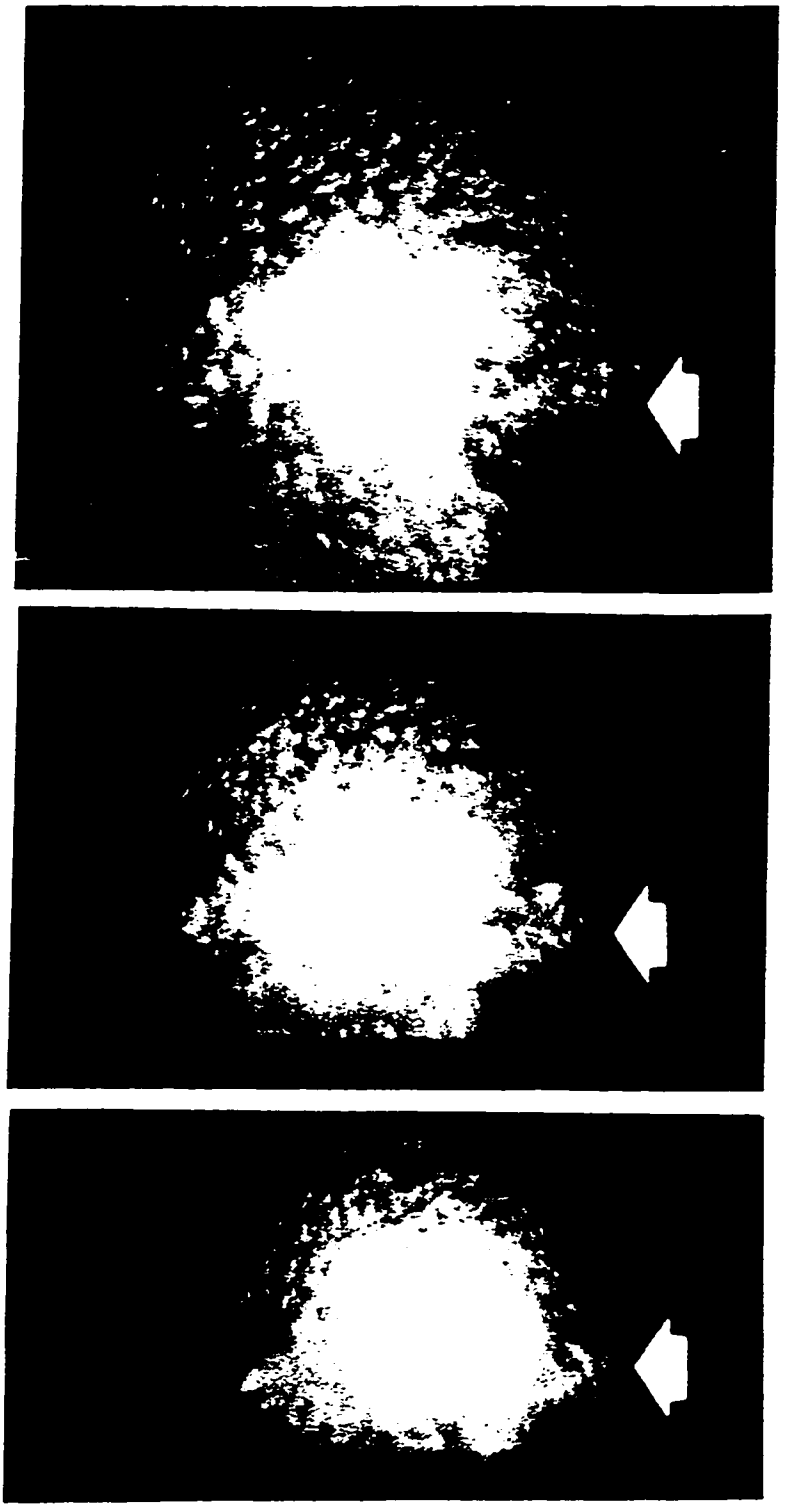

FIGURE 5.18 - HYCAM Footage from Run #8, Showing the Development of the Vortex at 0.12, 0.15 and 0.22 s Following Release of the Bubble Group. The Arrows Indicate Vortex Location.

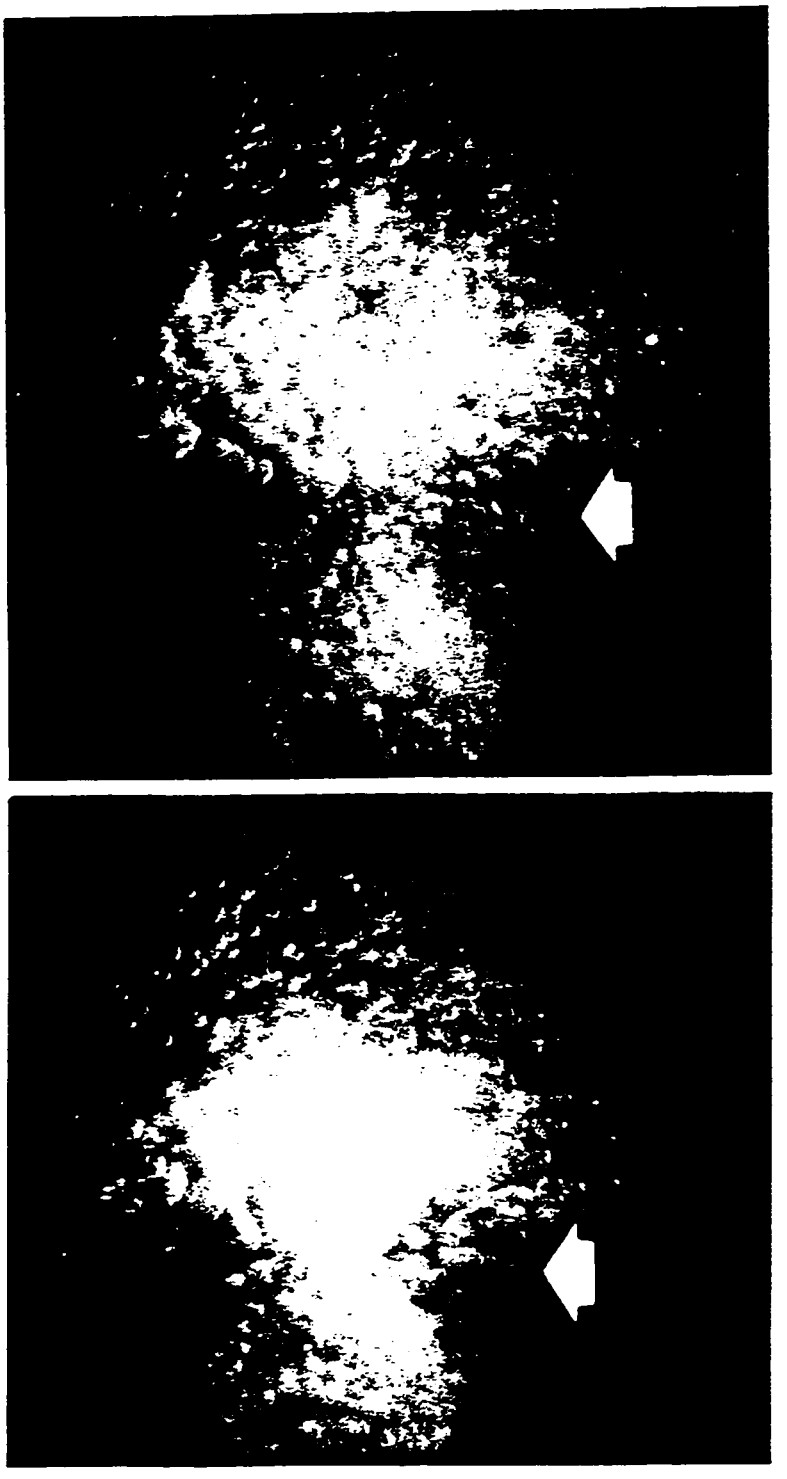

0.31 s

0.26 s

FIGURE 5.19 - HYCAM Footage from Run #8, Showing the Influence of the Fluid Vortex at 0.26 and 0.31 s Following Release of the Bubble Group. The Arrows Indicate Vortex Location.

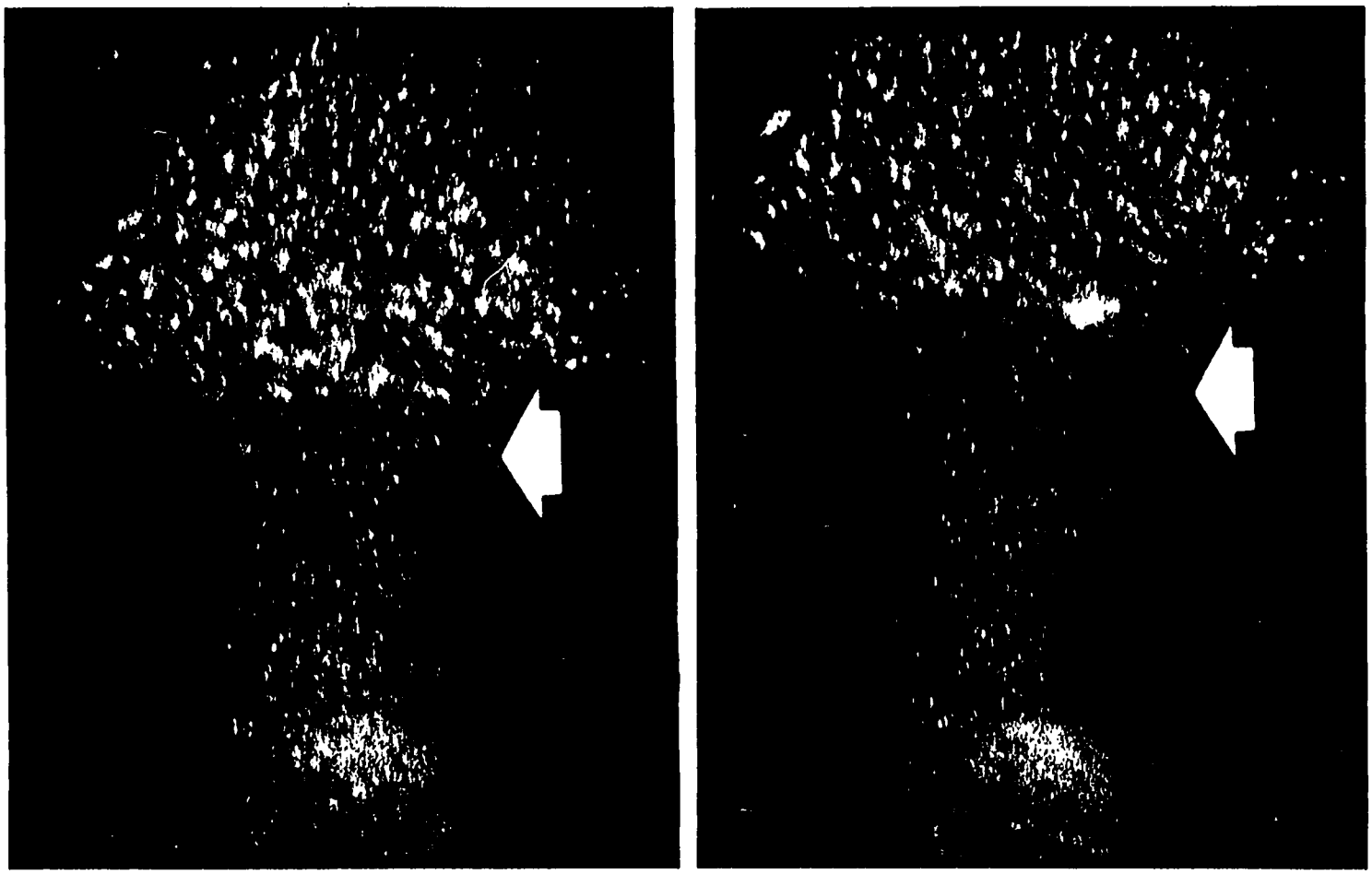

0.43 s

0.49 s

FIGURE 5.20 - HYCAM Footage from Run #8, Showing the Beginning of the Bubble/Vortex Separation at 0.43 and 0.49 s Following Release of the Bubble Group. The Arrows Indicate Vortex Location.

from the fluid vortex, is visible in the first photograph, and by 0.49 s, some circulation in the smaller bubbles behind the main bubble group is visible. Note that, in the second photograph, the bottom of the main bubble group is moving upwards with respect to its centre, as it is being pushed up by the now-trailing vortex. It is believed that this behaviour is what causes the bubbles all to migrate to the outside of the bubble group to form a hollow half-sphere, as was seen in Figure 5.4.

It can be seen in the HYCAM footage that not all of the bubbles are being released from the airstone at the same time. In a blowout situation, the shattering of a large bubble into small bubbles would be close to instantaneous, which was clearly not the case in this set of experiments. However, in general, the experimental program showed that consistent long-term results could be obtained, thus indicating that, in the long run, the delayed release of some of the bubbles was not that serious a problem.

CHAPTER 6

PREDICTIVE MODEL FOR BUBBLE PATHS

6.1 Modelling of Bubble Transport in Vortex Flows

A number of papers have recently been published describing the modelling of the transport of solid particles in various types of shear flows, and an excellent review of the available literature is given by Yeomans (1997). However, the motion of bubbles has been studied to a much lesser degree, chiefly because the equations of motion for a bubble are much more complex than those for a solid particle.

To date, there have been two main approaches to the calculation of bubble trajectories, based on whether or not viscous forces are assumed to be dominant. Probably the most well known of the viscous models is that of Maxey and Riley (1983), who derived an equation for the motion of small rigid spheres in an unsteady nonuniform flow field by assuming unsteady Stokes flow. At very low particle Reynolds numbers, and small particle concentrations, Maxey and Riley's equation can be used to calculate the trajectories of bubbles. Auton *et al.* (1988) took a somewhat different approach, in that they assumed inviscid flow over the bubble to develop an equation of bubble motion, which expressed the resultant force acting on a bubble as the sum of separate and uncoupled contributions from inertial effects, buoyancy, drag and lift. Although the basic premise of both types of model is different, both have demonstrated a tendency for bubbles to be trapped by coherent structures such as vortices because of the existence of regions of low pressure.

This type of flow has been simulated by a number of researchers. Maxey (1987) performed a numerical study of bubbles in a Langmuir cellular flow field, and found that entrapment would occur if the bubble rise speed was sufficiently small. Tio *et al.* (1993) found that buoyant particles may be trapped in stable equilibrium points located within a periodic Stuart vortex flow, and Reutsch and Meiburg (1993), in their examination of small spherical bubbles in two-dimensional vortical flows, also found that equilibrium points existed, with a rate of entrapment that was dependent on an inverse Stokes number. Sene *et al.* (1994) examined entrapment in isolated and shear layer vortices, and determined two dimensionless groups which determined whether or not these structures could trap bubbles. Although this is not a complete list of all of the available literature in this area, these papers are representative of the general trend of the current research, which entails numerical simulation of bubble trajectories in the presence of vortices but, it should be noted, little or no experimental verification of the results.

6.2 Basis of Current Model

As was discussed in the previous chapter, the bubble group experiments showed that the injection of a group of bubbles into a quiescent fluid results in the formation of a vortex in the fluid. In the early stages of development, the vortex is close to spherical in shape, and the bubbles appear to circulate within the vortex. However, the bubbles quickly rise through the front of the vortex and continue to ascend to the surface as a coherent group, but at a faster rate than the circulating fluid, which also continues to progress upwards. Close to the injector, both the bubble group and the fluid vortex grow together at a constant rate of

spread. As the bubble group rises out of the vortex, there is a distinct change in the spread rate for the vortex, which marks the transition from the bubbles moving with the fluid to permanent separation of the two phases. In this respect, bubble "thermal" behaviour differs from solid particle "thermals", which demonstrate no change in radial growth for the vortex following separation (Yeomans, 1997). It should be noted that the two phases move together only for a very short time (< 1s), and that separation occurs within several centimetres above the injector.

Throughout this two-phase region, the bubble group accelerates from rest, then decelerates until it reaches the terminal velocity of the individual bubbles. Until that time, the vortex velocity is more or less constant, except for an extremely short period of acceleration (~ 0.2 seconds) when the bubbles are moving with the fluid. Once the bubbles have reached their terminal velocity, the influence of the bubbles on the fluid vortex lessens, and the vortex slowly begins to decelerate.

An earlier publication of this author's work (Topham *et al.*, 1994) showed reasonably good agreement between experimental data from this thesis and an equation of motion for bubbles based on a simplified viscous model similar to that of Maxey and Riley (1983) for the region in which the motion of the bubbles strongly influences the fluid flow. The background fluid motion for this model was described using potential flow around an expanding Hill's spherical vortex, which was the approach used by Turner (1964a) to describe a buoyant single-phase thermal. It was also assumed that the vortex was translating upwards with a constant velocity and was expanding linearly with height due to entrainment.

Since the time of publication, this model has been modified to make it more representative of the conditions pertaining to the bubble motion, rather than the motion of solid particles. The final form of the model now more closely resembles the approach of Auton *et al.* (1988), as it considers both the forces on an undisturbed flow field, and those generated by considering the motion of a flow field disturbed by a small rigid sphere. The forces in the bubble equation of motion will be discussed in the next section, followed by a derivation of the equations describing the background fluid flow.

6.3 Bubble Equation of Motion

A general force balance on a bubble in a liquid flow can be written as:

$$\rho_b V_b \frac{d\mathbf{u}_b}{dt} = m_b \frac{d\mathbf{u}_b}{dt} = \mathbf{F}_{buoyancy} + \mathbf{F}_{drag} + \mathbf{F}_{lift} + \mathbf{F}_{added\ mass} + \mathbf{F}_{pressure} + \mathbf{F}_{Basset} \qquad (6.1)$$

where ρ_b denotes the gas density, V_b is the bubble volume, m_b is the bubble mass, and $\mathbf{u}_b$ is the velocity of the bubble (Auton *et al.*, 1988). The terms on the right-hand side of the equation denote the buoyancy force, the drag force, the lift force, the added mass force, the pressure gradient force, and the Basset history term, respectively. Each of these forces are discussed in detail in the following sections.

6.3.1 Buoyancy Force

The buoyancy force for a bubble can be written as:

$$\mathbf{F}_{buoyancy} = (m_b - m_f)\mathbf{g} \qquad (6.2)$$

where m_f is the fluid mass, m_b is the bubble mass and g is gravity (assumed positive in the downwards direction). Buoyancy is the body force arising from gravitational acceleration.

6.3.2 Drag Force

In the form of the bubble equation published in Topham *et al.* (1994), a linear Stokes drag term ($f_d = 1$) was utilized based on the argument given by Sene *et al.* (1994). Yeomans (1997) used a similar approach in his study of solid particle thermals, in which departures from Stokes drag were accounted for by dividing through by the terminal velocity of a particle in still water. An alternate approach is given by Reutsch and Meiberg (1993), who empirically modified their inertia parameter A (the inverse of the Stokes number) to extend the range of validity of their drag term to $Re_b < 20$, where Re_b is the bubble Reynolds number based on the slip velocity (fluid velocity u - bubble velocity u_b):

$$Re_b = \frac{2r_b|u - u_b|}{\nu} \tag{6.3}$$

where r_b is the bubble radius and ν is the kinematic viscosity. For the range of experiments in this work, Re_b was between approximately 160 and 170, which should mean that Reutsch and Meiberg's form of the drag force term is not strictly applicable. However, the work of Tio *et al.* (1993) demonstrated that this drag correlation:

$$f_d = 1 + 0.1315 Re_b^{0.82 - 0.05\log_{10} Re_b} \tag{6.4}$$

which was originally given by Clift *et al.* (1978) for rigid particles, could be used over the range of $0 < Re_b < 200$ with an error of less than 2%. In Equation (6.4), the first term on the

right-hand side corresponds to the Stokes drag, while the second term accounts for the correction of non-zero Re_b.

Oliver and Chung (1987) also proposed a drag correlation for bubbles in terms of Re_b that was valid for the Stokes regime and beyond, but their methodology was awkward to implement and there was no estimate given as to the accuracy of the results from using this correlation. As a result, the approach of Reutsch and Meiberg is the form which has been chosen for the drag force term in the bubble equation:

$$\mathbf{F}_{drag} = 6 \pi r_b \mu f_d (\mathbf{u} - \mathbf{u}_b) \tag{6.5}$$

where μ is the dynamic viscosity, and f_d is the drag correlation from Clift et al. (1978) given in Equation (6.4).

It should be noted that this form of the equation for the drag force is based on the work of Maxey and Riley (1983), but differs from the original in that the Faxen corrections for a nonuniform flow field have been neglected. The Faxen relations correct for the modification of the drag force on a sphere at low Reynolds number by velocity curvature, and also affect the added mass and the Basset history terms. However, these corrections are only valid at extremely low Reynolds numbers ($Re_b \ll 1$), and thus have been dropped from the current analysis.

6.3.3 Lift Force

There are two types of lift forces that can affect a bubble rising in a fluid. The first, which is often termed the "Saffman lift", is due to the shear in the fluid and is considered in

the potential flow region. Tio *et al.* (1993) give an equation for the Saffman lift, but note that is only applies in the Stokes regime (Re_b « 1). As this is well below the Reynolds number region studied in the experimental work herein, the Saffman lift term has been dropped from the bubble equation.

The second lift term is due to rotation or vorticity in the liquid. Auton *et al.* (1988) write this lift force term as:

$$\mathbf{F}_{\text{lift}} = m_f C_L (\mathbf{u} - \mathbf{u}_b) \times \omega \tag{6.6}$$

where C_L is the lift coefficient of a bubble in uniform shear, equal to 0.5 for a sphere, and ω is the vorticity of the fluid ($\omega = \nabla \times \mathbf{u}$). It should be noted that Equation (6.6) is applicable to inviscid flows, where $Re_b \to \infty$. Mei (1992) developed an approximate correlation for the lift force in the region where Re_b « 100, but as this correlation was derived using Saffman's results in the Stokes regime, it was felt that Auton *et al.*'s lift force term was preferable for inclusion in the bubble equation.

6.3.4 Added Mass Force

Reutsch and Meiberg (1993) give the added mass term as:

$$\mathbf{F}_{\text{added mass}} = \frac{1}{2} m_f \frac{d}{dt} (\mathbf{u} - \mathbf{u}_b) \tag{6.7}$$

where:

$$\frac{d}{dt} = \frac{\partial}{\partial t} + \mathbf{u}_b \cdot \nabla \tag{6.8}$$

which denotes the derivative along the bubble path. Equation (6.7) is identical to the form used by Maxey and Riley (1983), except that the Faxen relations correcting for the curvature in the velocity profile because of the effect of velocity gradients have been dropped. However, Auton *et al.* (1988) showed that, for potential flow about a spherical bubble when the ambient flow is unsteady, rotational and nonuniform, the form of this equation should be:

$$\mathbf{F}_{\text{added mass}} = \frac{1}{2} m_f \left(\frac{D\mathbf{u}}{Dt} - \frac{d\mathbf{u}_b}{dt} \right) \tag{6.9}$$

where:

$$\frac{D}{Dt} = \frac{\partial}{\partial t} + \mathbf{u} \cdot \nabla \tag{6.10}$$

is the derivative following the fluid element. Maxey and Riley pointed out that, at low Reynolds numbers, there is no distinction between the two forms since the slip velocity is negligible. However, for the purposes of this analysis, the form of the added mass term given by Auton *et al.* in Equation (6.9) is utilized, as the bubble experiments were well beyond the Stokes regime.

It should be noted that the constant of 1/2, which is the first term of Equation (6.7) and (6.9), is the virtual mass coefficient k for a sphere. As was discussed in Section 2.4.3, Turner (1963a, 1964b) found that using the virtual mass coefficient for a sphere instead of a more accurate value for an oblate spheroid of revolution would only introduce errors of approximately five percent into his calculations.

6.3.5 Pressure Gradient Force

The pressure gradient term in the force equation describes the force that a fluid sphere of the same size would experience in the absence of a bubble. Although this term is generally written in the literature as (see, for example, Clift *et al.*, 1978):

$$\mathbf{F}_{pressure} = m_f \frac{D\mathbf{u}}{Dt} - \nu \nabla^2 \mathbf{u} \tag{6.11}$$

Maxey and Riley (1983) found, by using a change of reference frame, that the following form is physically more realistic:

$$\mathbf{F}_{pressure} = m_f \frac{D\mathbf{u}}{Dt} \tag{6.12}$$

This is the form of the pressure gradient term for the bubble equation which was published previously in Topham *et al.* (1994), and it has been retained for this analysis.

6.3.6 Basset History Term

The Basset history term indicates the effect of the history of relative accelerations, and accounts for the diffusion of the vorticity generated at the bubble surface into the surrounding fluid. It is often said to represent the "memory" retained by the fluid from the motion of the bubble. A form of the history term, including the Faxen corrections, is given by Maxey and Riley (1983):

$$\mathbf{F}_{Basset} = -6\pi r_p^2 \mu \int_0^t \frac{d}{d\tau} \left(\mathbf{u}_b - \mathbf{u} - \frac{1}{6} r_p^2 \nabla^2 \mathbf{u} \right) \frac{d\tau}{[\pi \nu (t - \tau)]^{1/2}} \tag{6.13}$$

where r_p is the radius of a particle. The validity of Equation (6.13) was brought into question by Reeks and McKee (1984), who concluded that the Basset history term had a negligible effect when there was a relatively-large initial velocity difference between the fluid and a particle. Additionally, Mei *et al.* (1991) documented the fact that departing from Stokes flow lessens the history effect. They pointed out that this equation is valid only in the Stokes regime, and even there, it is not uniformly valid over the entire time domain; the kernel behaves as $t^{-1/2}$ only for a short time and decays much faster for long time for finite Reynolds numbers. As a result, the Basset history term has not been retained in the bubble equation.

6.3.7 Equation of Motion for a Bubble

From the general force balance given in Equation (6.1) and the discussion of each term in the previous sections, the equation of motion for a bubble can be written as:

$$m_b \frac{d\mathbf{u}_b}{dt} = (m_b - m_f)\mathbf{g} + 6\pi r_b \mu f_d(\mathbf{u} - \mathbf{u}_b) + m_f C_L(\mathbf{u} - \mathbf{u}_b)\times\omega + \frac{1}{2} m_f \left[\frac{D\mathbf{u}}{Dt} - \frac{d\mathbf{u}_b}{dt} \right] + m_f \frac{D\mathbf{u}}{Dt} \tag{6.14}$$

where f_d takes the form given in Equation (6.4). The vorticity ω in Equation (6.14) is equal to

$$\omega = \nabla\times\mathbf{u} = \left(\frac{\partial u_r}{\partial z} - \frac{\partial u_z}{\partial r} \right)\theta \tag{6.15}$$

in the θ-direction, assuming a cylindrical coordinate system (in Equation (6.15), θ represents the unit vector in that direction).

The fluid equations described in the following section utilize cylindrical coordinates and an axisymmetric flow field; thus, the same convention will be used for the bubble equation of motion. In the radial direction, Equation (6.14) becomes:

$$(m_b + 0.5m_f)\frac{du_{b_r}}{dt} = 6\pi\mu r_b f_d(u_r - u_{b_r}) + 1.5m_f\left(\frac{\partial u_r}{\partial t} + u_r\frac{\partial u_r}{\partial r} + u_z\frac{\partial u_r}{\partial z}\right) - 0.5m_f(u_z - u_{b_z})\left(\frac{\partial u_r}{\partial z} - \frac{\partial u_z}{\partial r}\right) \tag{6.16}$$

and, in the vertical direction:

$$(m_b + 0.5m_f)\frac{du_{b_z}}{dt} = (m_b - m_f)g + 6\pi\mu r_b f_d(u_z - u_{b_z}) + 1.5m_f\left(\frac{\partial u_z}{\partial t} + u_r\frac{\partial u_z}{\partial r} + u_z\frac{\partial u_z}{\partial z}\right) - 0.5m_f(u_r - u_{b_r})\left(\frac{\partial u_r}{\partial z} - \frac{\partial u_z}{\partial r}\right) \tag{6.17}$$

Although the previous chapter indicated that the bubbles generated in the experimental portion of this thesis ranged from spherical in shape to oblate spheroids, for the purposes of simplifying the derivation of Equations (6.16) and (6.17), it was assumed that all of the bubbles are spherical in shape. This is a reasonable assumption, as the majority of the bubbles released in each group had a spherical geometry and were approximately the same size; those few that were larger than the norm tended to travel in advance of the remainder of the bubble group and thus were discounted when making the measurements. It should also be noted that a condition of incompressibility was used in the development of the model. This condition is met if the bubbles do not expand with decreasing hydrostatic pressure, and the previous chapter demonstrated that the effect of water depth was negligible

over the range of the experiments. However, when the model is used for water depths greater than those seen in the experimental program, the incompressibility condition introduces a source of error in the model, as the effect of water depth can no longer be ignored. One further assumption is that there is no mass transfer between the bubbles and the surrounding fluid, *i.e.* continuity is satisfied.

It must be noted that the bubble equation of motion was derived following the path of one bubble, and does not take into account the effect of other bubbles in the flow field. Thus, in order to model the trajectories of multiple bubbles, such as is the case in a bubble group, it must be assumed that the bubble concentration is dilute, and that the different bubble trajectories do not affect one another. However, the continuing expansion of the bubble groups following separation from the vortex indicates that this is probably not the case, which introduces another possible source of error in the model.

6.4 Equations of Motion for the Background Fluid Flow

The consistent thermal-like behaviour of the fluid which was seen in the bubble group experiments suggests that the expanding vortex model of Turner (1964a) can be used as a background fluid flow for the examination of individual bubble trajectories. The following sections examine the derivation of the equations of motion for the flow inside and outside the fluid vortex.

6.4.1 Flow Outside the Vortex

A sphere moving upward at constant speed through quiescent fluid can also be described mathematically as a fixed sphere in a uniform stream. The stream function for a uniform stream of speed U is given in spherical polar coordinates by:

$$\psi = -\frac{1}{2}Ur^2\sin^2\theta \tag{6.18}$$

The sphere is superimposed upon the uniform stream with the addition of the stream function for an opposing dipole:

$$\psi = -\frac{1}{2}Ur^2\sin^2\theta - \frac{A}{r}\sin^2\theta \tag{6.19}$$

where A is a constant. For ψ to equal 0 on the sphere's surface where $r = a$ (the vortex radius):

$$\theta = 0, \pi \quad or \quad r = \left(\frac{2A}{U}\right)^{1/3} \tag{6.20}$$

therefore:

$$A = \frac{a^3 U}{2} \tag{6.21}$$

and:

$$\begin{aligned} \psi_o &= -\frac{1}{2}Ur^2\sin^2\theta - \frac{1}{2}U\frac{a^3}{r}\sin^2\theta \\ &= -\frac{1}{2}Ur^2\sin^2\theta\left(1 - \frac{a^3}{r^3}\right) \end{aligned} \tag{6.22}$$

The subscript o denotes that the flow is outside of the vortex. In cylindrical coordinates, this is written as:

$$\psi_o = -\frac{1}{2} U r^2 \left(1 - \frac{a^3}{(z^2 + r^2)^{3/2}} \right) \tag{6.23}$$

6.4.2 Flow Inside the Vortex

In order to contain the vorticity completely within the sphere, the particles of fluid must be assumed to move in closed paths. This condition, and that of $r = a$ being a stream surface, is uniquely satisfied by Hill's spherical vortex, for which the stream function is:

$$\psi_i = \frac{3}{4} U r^2 \sin^2\theta \left(1 - \frac{r^2}{a^2} \right) \tag{6.24}$$

where the subscript i denotes the flow is inside the vortex. Translated into cylindrical coordinates, the stream function inside the vortex is:

$$\psi_i = \frac{3}{4} \frac{U r^2}{a^2} (a^2 - r^2 - z^2) \tag{6.25}$$

6.4.3 Vortex Expansion

Following Turner (1963a), it will be assumed that the vortex is expanding at a constant rate as it rises. According to the experimental data, this will be true at least until separation. Experimental data also supports the conclusion that the vortex is rising at a constant rate; the upwards vortex velocity is a constant for each bubble group.

In a coordinate system which is at rest relative to the centre of the sphere, the expansion of the sphere as proportional to the distance travelled is:

$$a = \alpha Ut \tag{6.26}$$

where α is the half angle of spread, which is assumed to be a constant. Thus:

$$\psi_o = -\frac{1}{2}Ur^2\left[1 - \frac{(\alpha Ut)^3}{(z^2 + r^2)^{3/2}}\right] \tag{6.27}$$

$$\psi_i = \frac{3}{4}\frac{Ur^2}{(\alpha Ut)^2}\left[(\alpha Ut)^2 - r^2 - z^2\right] \tag{6.28}$$

It should be noted that at separation, the expansion α of the sphere changes to a lesser value, which is also a constant.

6.4.4 Velocity Equations for the Background Fluid Flow

From Paterson (1983), the velocity vectors are given by:

$$v_r = \frac{1}{r^2\sin\theta}\frac{\partial\psi}{\partial\theta}, \quad v_\theta = -\frac{1}{r\sin\theta}\frac{\partial\psi}{\partial r} \tag{6.29}$$

Thus, the velocity vectors outside the vortex, given in expanding vortex form, are:

$$u_{r_o} = \frac{3Urz(\alpha Ut)^3}{2(z^2 + r^2)^{5/2}} \tag{6.30}$$

$$u_{z_o} = -U\left[1 - \frac{(\alpha Ut)^3}{2(z^2 + r^2)^{5/2}}(r^2 - 2z^2)\right] \tag{6.31}$$

The velocity vectors inside the vortex, again given in expanding vortex form, are:

$$u_{r_i} = \frac{3Urz}{2(\alpha Ut)^2} \tag{6.32}$$

$$u_{z_i} = -\frac{3U}{2(\alpha Ut)^2}\left[2r^2 + z^2 - (\alpha Ut)^2\right] \tag{6.33}$$

Also:

$$u_r = \frac{dr}{dt}, \quad u_z = \frac{dz}{dt} \tag{6.34}$$

Integrating this set of equations numerically using a fourth-order Newton-Raphson iteration technique with values of U = 1 and α = 0.25 gives the streamlines shown in Figure 6.1, which agree with those given by Turner (1964a) for a rising single-phase buoyant thermal. The location of each fluid element has been non-dimensionalized by dividing its position at every time interval by the expanding radius of the thermal to give a dimensionless radius of unity. The figure shows that, as the vortex moves upwards, it is possible for external fluid to be entrained within the vortex, depending on its initial position with respect to the moving sphere. Note that only the right-hand side of the vortex is shown; the flow field is assumed to be axisymmetric. It should also be noted that the frame of reference for these equations is fixed to the centre of the moving vortex.

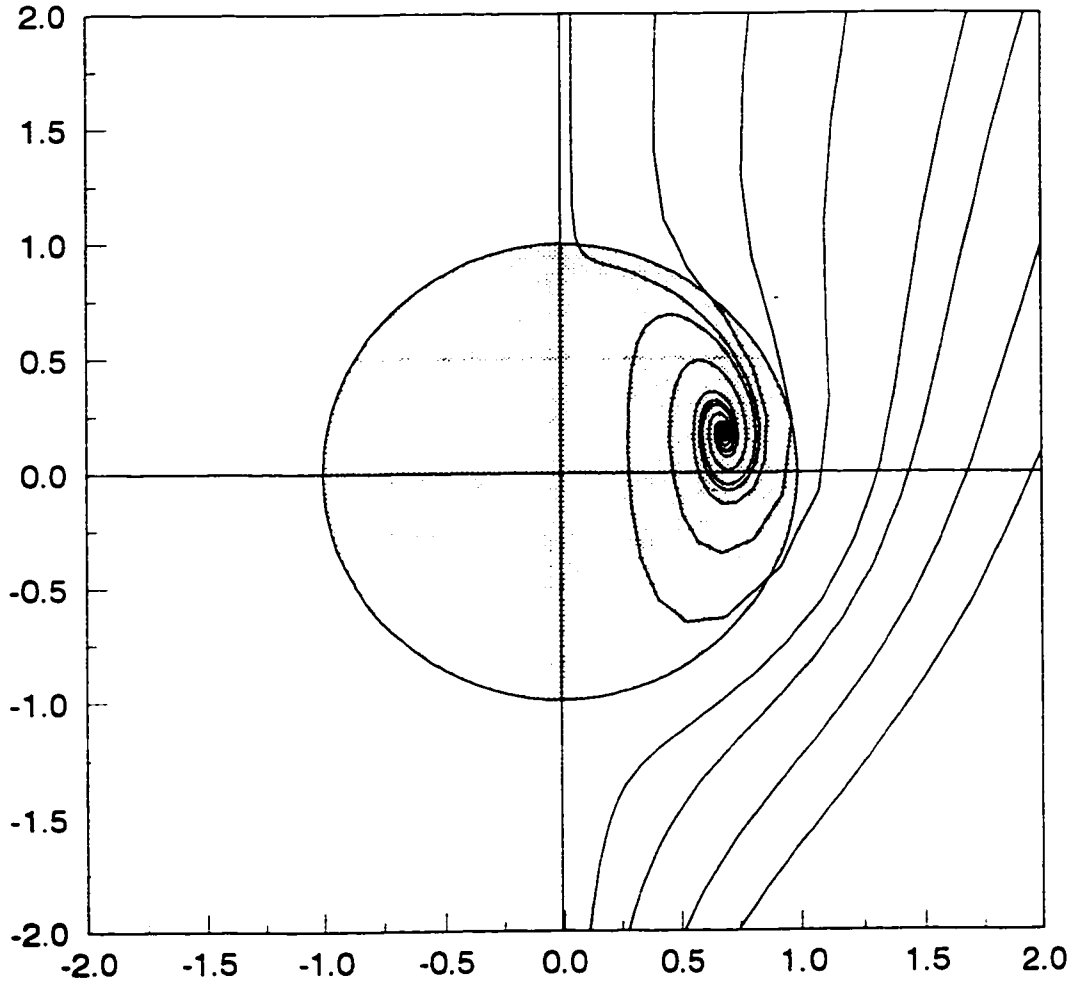

FIGURE 6.1 - Integration of the Background Fluid Equations (6.30) to (6.34) Gives the Motion of Fluid into an Expanding Spherical Vortex, which is Moving at a Constant Upward Velocity. The Figure is Plotted Using a Co-ordinate System in Which the Spherical Boundary is Fixed in Size. The Tangent of the Half-Angle of Spread is $\alpha = 0.25$. The Right Side of the Diagram shows the Paths of Particles Which Started on a Plane at Right Angles to the Direction of Motion. This Figure is Similar to the Results of Turner (1964a) for an Expanding Spherical Vortex.

6.4.5 Assumptions Underlying the Fluid Flow Equations

The fluid motion described by Equations (6.30) to (6.33) consists of an expanding Hill's spherical vortex, in which the fluid is rotational, surrounded by an inviscid irrotational potential flow field. A distinct boundary exists between the two regions, and it is assumed that any entrained fluid quickly shares the vorticity of the fluid inside the vortex *i.e.* there are only small instantaneous differences in vorticity due to expansion and mixing.

Another assumption that was made in the derivation of the background fluid motion was that the fluid vortex was spherical in shape. In actual fact, the shape of the fluid vortex was closer to that of an oblate spheriod; however, the errors introduced by the assumption of sphericity are very small (see Section 6.3.4).

The fluid velocity equations are also based on the assumption that the expanding Hill's spherical vortex rises upwards at a constant velocity, which was the approach used by Turner (1964a). As was discussed in Section 2.2, an actual vortex ring generally expands and decelerates over time. Turner's treatment of the velocity flow field correctly described the expansion of the vortex, but did not address the slowing of the vortex. An alternate approach was given by Saffman (1970), who correctly predicted the slowing of a Hill's spherical vortex due to viscous diffusion, but could not describe the increase of the radius with time. It was not possible to reconcile the two techniques, because of radical differences in the modelling of the vortex; as a result, Turner's method was deemed to be more representative of the behaviour seen in the bubble group experiments.

The assumption of constant vortex velocity for the model confirmed experimentally in the previous chapter. Figure 5.17 showed that, except for an extremely short period of

acceleration (~ 0.2 s) where the bubbles moved with the fluid, the vortex velocity followed a linear relationship. Thus, the assumption of constant velocity in the model should be valid at least until bubble terminal velocity is reached.

This behaviour differs from that seen for single-phase thermals (Scorer, 1958) and solid particle "thermals" (Yeomans, 1997), which often exhibit a non-uniform translational velocity which is inversely proportional to the square root of the time. It is believed that, because of the very short period of time that the bubbles are resident within the fluid vortex, bubble groups do not act as a true "thermal"; small solid particles, on the other hand, can move with the fluid for a much longer period of time due to their lower density difference. Thus, in the case of bubble groups, the fluid motion is primarily due to momentum transfer from the vortices shed periodically from the bubble wakes, rather than the effects of buoyancy, and the fluid behaviour is more like that of a vortex ring than a thermal.

CHAPTER 7

A COMPARISON OF THE RESULTS OF THEORY AND EXPERIMENTS

7.1 Introduction

Equations for the trajectory of a single bubble as a function of time were given in the previous chapter. Using numerical simulation, it is possible to solve for the location of a group of bubbles released simultaneously, as long as it can be assumed that each of the bubbles has a negligible effect on the motion of the other bubbles. For this project, the simulation was carried out using a software program called *Scientist for Experimental Data Fitting*, Microsoft Windows Version 2, which was developed by MicroMath Scientific Software, Salt Lake, Utah. The software was loaded on an IBM ThinkPad Pentium laptop computer with 31.0 MB of RAM.

Scientist provides four standard numerical integration routines (Euler's method, Runge-Kutta fourth order method, error-controlled Runge-Kutta method, and the Bulirsch-Stoer method) as well as a stiff equation package called EPISODE, which was the method used to solve the bubble equations. EPISODE is an initial value ODE solver for stiff and non-stiff systems. It uses variable coefficient Adams-Moulton and Backward Differentiation Formula (BDF) methods in Nordsieck form. The BDF method generates the Jacobian matrix from the analytic forms of the partial derivatives with respect to each dependent variable. This is generally faster than calculating the matrix by using a differencing scheme, and it is invariably more accurate, which makes a difference in the number of steps required to solve some very stiff equations. However, the Adams-Moulton method, or the non-stiff option,

was utilized, as Yeomans (1997) found that this gave the most consistent results for his simulations, and trial runs of the current model utilizing both methods also showed this to be the case. The relative error size for the integration was set for 1×10^{-5}.

Numerical simulations to be carried out using *Scientist* must be entered in computer code which is specific to the program. The mathematical model used in the simulations for this project contained the code for the differential equations for the bubble motion in radial and vertical coordinates as given in Equations (6.16) and (6.17), the differential equations for the fluid model as given in Equations (6.30) to (6.34), the list of dependent variables which were to be solved in terms of the independent variable t, values for the constants, parameters, initial conditions, and the time duration of the simulation. Samples of the computer code are given as Appendix C of this dissertation.

The code was written so as to match the experimental parameters as closely as possible. In Chapter 5, it was noted that the bubble group had two main stages of growth: a circulating region where the bubbles moved with the fluid, and the zone where the bubbles had separated from the moving fluid. Different values of entrainment coefficient were calculated for each region from the experimental data, and the values are given in Table 5.2. These two stages of growth and their matching entrainment coefficients were accounted for in the bubble model.

The parameters which could be varied during the simulations were the velocity of the fluid vortex U, the initial entrainment coefficient of the fluid plus the bubbles α_1, the entrainment coefficient of the vortex following separation of the bubbles from the circulating fluid α_2, the gravitational acceleration g, the density ρ_f and viscosity μ_f of the fluid, the

density of the air ρ_g, and the bubble radius r_b. Parametric values used for the fluid vortex speed U and the entrainment coefficients α_1 and α_2 were taken from Table 5.2. Densities and viscosities of the air and water phases were calculated at the temperatures and pressures utilized for the experiments, and the bubble radii were varied over the range seen in the laboratory.

The number of bubbles within any bubble group is a function of the size of the total injection air volume which is to be modelled, and the individual bubble radius. In order to give totally accurate results from the model, ideally the actual number of bubbles should be simulated. However, depending on the bubble radius chosen, this could run into hundreds or even thousands of bubbles in each group. Yeomans (1997) found that reasonable results could be obtained by using 14 initial data points for his solid particle "thermals"; these gave a fairly accurate picture of the progression of the particle "thermal" front. It was therefore decided that a smaller number of bubbles could probably be used in the bubble group model as well.

Figure 7.1 is a plot of the increase of bubble group radius with height as generated by the computer model, using the initial parameters for a 14 cm^3(ST) bubble group given in Table 5.2 and a bubble radius of 1 mm. The bubble group was generated using 12 points which were distributed evenly at a radius of 1.5 cm from the origin starting from the vertical axis and proceeding at 6 or 12° intervals in the clockwise direction. The assumption of symmetry around the vertical axis meant that only one side of the bubble group had to be calculated, and the configuration of the bubbler used in the experiments determined the angle below the horizontal at which bubbles could be generated. The radial and vertical starting

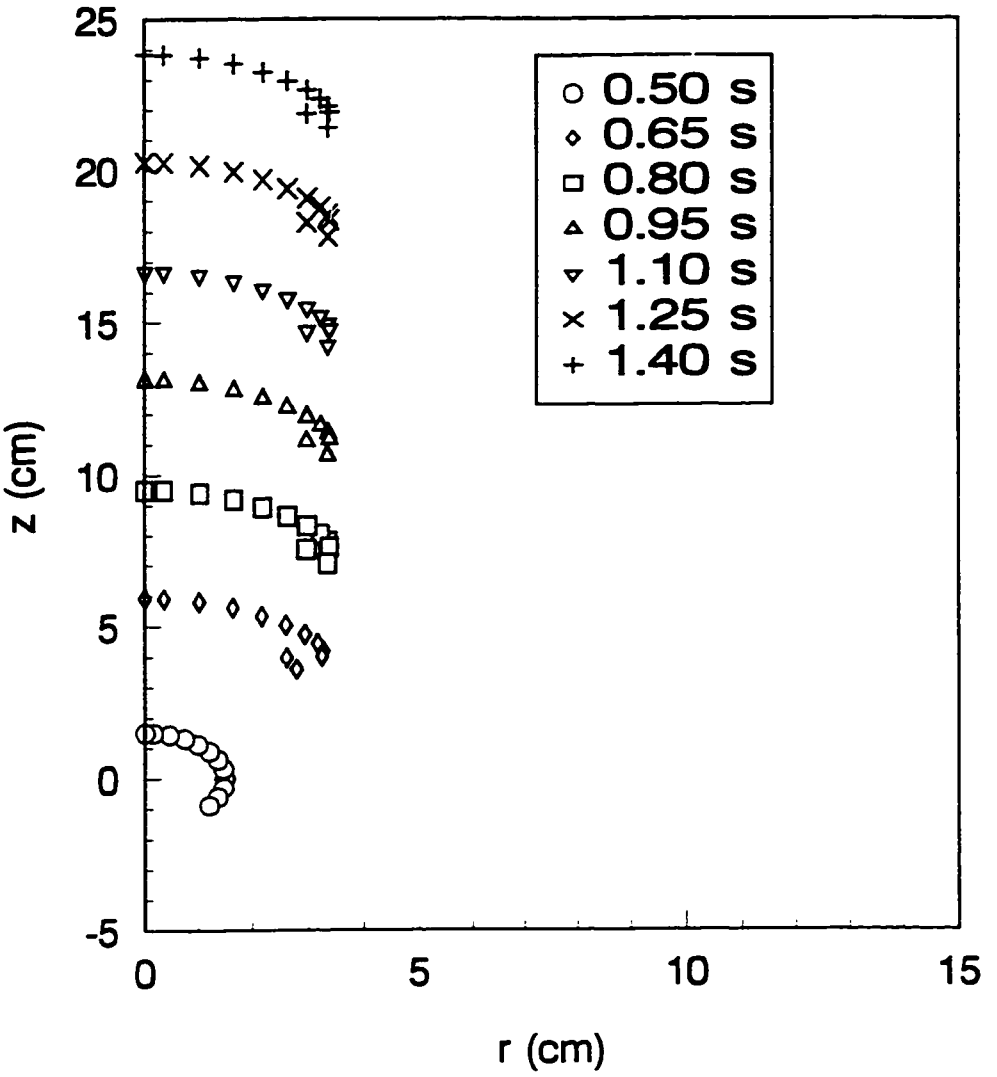

FIGURE 7.1 - Plot of the Increase in Bubble Group Radius r with Height z for 12 Bubbles Generated by the Simulation Model Using the Initial Conditions for a 14 cm³(ST) Air Volume Bubble Group (U = 16.1 cm/s and α_l = 0.511) and r_b = 1 mm. The Starting Positions and Velocities for each Data Point are Provided in Table 7.1.

velocities for each bubble, u_{br} and u_{bz}, were assigned by determining the radial and vertical velocity components of the fluid flow field. The initial conditions for the plot in Figure 7.1 are given in Table 7.1.

TABLE 7.1 - Initial Conditions for 14 cm³(ST) Bubble Group in Figure 7.1 with a Constant Fluid Vortex Velocity of 16.1 cm/s

Bubble No.	r (cm)	z (cm)	u_{br} (cm/s)	u_{bz} (cm/s)
1	0.00	1.50	0.00	16.10
2	0.16	1.49	1.68	16.01
3	0.46	1.43	4.98	15.31
4	0.75	1.30	8.05	13.94
5	1.00	1.11	10.77	11.96
6	1.21	0.88	13.02	9.46
7	1.37	0.61	14.71	6.55
8	1.47	0.31	15.75	3.35
9	1.50	0.00	16.10	0.00
10	1.47	-0.31	15.75	-3.35
11	1.37	-0.61	14.71	-6.55
12	1.21	-0.88	13.02	-9.46

The simulation in Figure 7.1 was carried out between a time of 0.21 s and 1.5 s, which generated data to a height of approximately 24 cm. The starting time was determined by dividing the radius of the starting bubble group by the initial entrainment coefficient α_1 and the constant vortex velocity. It was possible to vary the time frame of the simulations

in order to generate results over the full range of the water depth of the experiments, thus allowing comparisons to be made between theory and the laboratory work. However, prior to comparing the results of the model to those of the experiments, it would be useful to examine the model more closely.

7.2 Comparison of Bubble Path Predictive Model with Early Published Version

The bubble path predictive model is based on the equations derived in Chapter 6 for a single bubble moving upwards in a background fluid flow field described by potential flow around a rising Hill's spherical vortex. It was also mentioned in Chapter 6 that these equations are similar to those published previously by the author in Topham *et al.* (1994). However, in rederiving the equations for the bubble model, an omission was discovered in the form of the pressure force and added mass term given by Topham *et al.* in that only part of the expansion of the substantive derivative was included. In other words, the expression for the axial velocity term of the substantive derivative in Topham *et al.*:

$$\frac{\partial u_z}{\partial t} + u_z \frac{\partial u_z}{\partial z} \tag{7.1}$$

should correctly be given as:

$$\frac{\partial u_z}{\partial t} + u_z \frac{\partial u_z}{\partial z} + u_r \frac{\partial u_z}{\partial r} \tag{7.2}$$

The expression for the radial velocity term should also be expanded similarly. It should be noted that this omission was carried over into the thesis of Yeomans (1997), who modelled the behaviour of solid particle "thermals" using the Topham *et al.* equations.

The equations given in Chapter 6 also differ from those given in Topham *et al.* by the inclusion of a lift force term. This term was neglected in the earlier version of the model in order to simplify the equations of motion for a bubble. However, Yeomans found that the lift term is not necessary when modelling solid particle motion.

It was decided to compare the original version of the equations as described in Topham *et al.* (Model 1) with the corrected version accounting for the complete substantive derivative (Model 2), and also to the Equations as given in Chapter 6, which include the lift force term (Model 3), to see if the extra terms made any difference to the simulation. This comparison is shown in Figure 7.2. The initial conditions are the same for all three cases (a radius of 1.3 cm and a height of 0 cm), and the parameters used were a bubble radius of 1.3 mm, a vortex velocity of 12.3 cm/s, an initial entrainment coefficient of 0.360 and a final entrainment coefficient of 0.073. The comparison was carried out between times of 0.5 and 1 s, as it was assumed that most, if any, of the differences between the models would be obvious near the beginning of the simulation.

Figure 7.2 shows that, although all three models have the same general behaviour, the effect of the extra substantive derivative term in Model 2 is to move the radial position of the bubble outwards by about 0.2 cm, or 30 percent. For Model 3, adding the lift term as well as the corrected derivative moves the radial position outwards by about 0.7 cm, or approximately 100 percent. Thus, it is possible that there could be discrepancies of the order

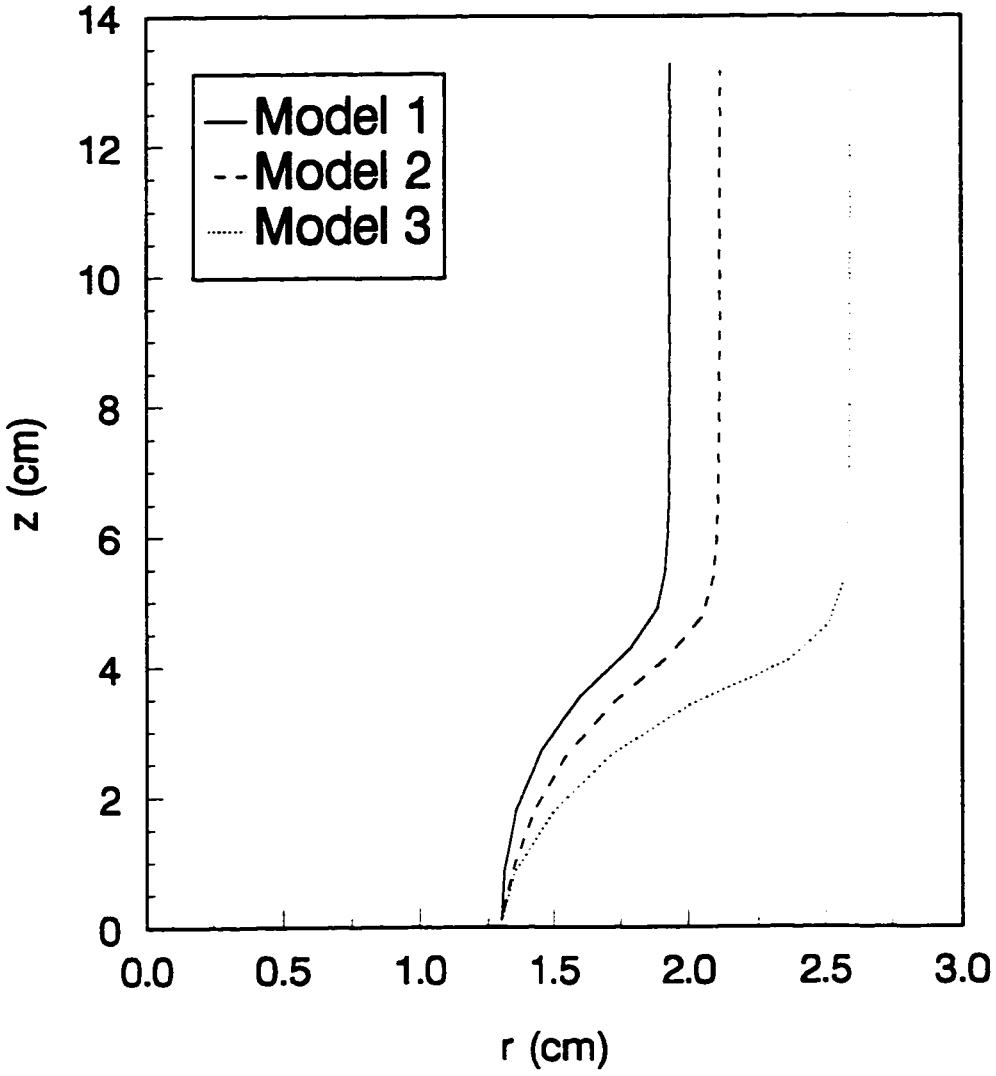

FIGURE 7.2 - A Comparison of Model Results using the Equations from Topham *et al.*, 1994 (Model 1), the Model 1 Equations with Corrected Substantive Derivative Terms (Model 2), and Model 2 Equations Including a Lift Force Term (Model 3). The Figure Shows the Increase in Radial Position r with Height z for Runs With Initial Parameters r_b = 1.3 mm, U = 12.3 cm/s, α_1 = 0.360 and α_2 = 0.073. The Starting Position for Each Run was r = 1.3 cm and z = 0 cm.

of 30 percent in Yeomans' simulation results, due to the form of the substantive derivative that was used in his equations.

Both the bubble model results in Topham *et al.* and the current model account for the change in entrainment coefficient which was seen in the experiments when the bubbles separated from the fluid vortex. This was not found necessary for solid particle "thermals", as these expand at a constant rate until the "particle-settling" regime is attained (Yeomans, 1997). The use of the smaller entrainment coefficient following separation accounts for the minimal change in radius with height seen in the region above 5 cm in Figure 7.2.

The effect of the change in entrainment coefficient is more obvious in Figures 7.3 and 7.4. Both figures plot dimensionless height *GAMMA*, or $z/(\alpha Ut)$, versus dimensionless radius *BETA*, which is $r/(\alpha Ut)$, for the bubble group shown in Figure 7.1. In a dimensionless plot, the fluid vortex at all times has a radius of unity, so the interaction between the bubbles and the fluid flow field can be visualized more clearly. In both plots, it can be seen that the residence time of the bubbles within the fluid vortex is very short (approximately 0.6 seconds). The difference between the two figures lies in the value of the term (αUt) in the potential flow region of the fluid flow. In Figure 7.3, the value of entrainment coefficient used is α_2, which is the experimentally-determined value from Table 5.2 for the entrainment coefficient of the fluid vortex after separation from the bubbles. Figure 7.4 uses α_1 for both the vortex and the potential flow region. This is the experimental value of entrainment coefficent for the circulating two-phase region. A comparison of the two figures shows that using the smaller value α_2 in the potential flow region has the effect of reducing the

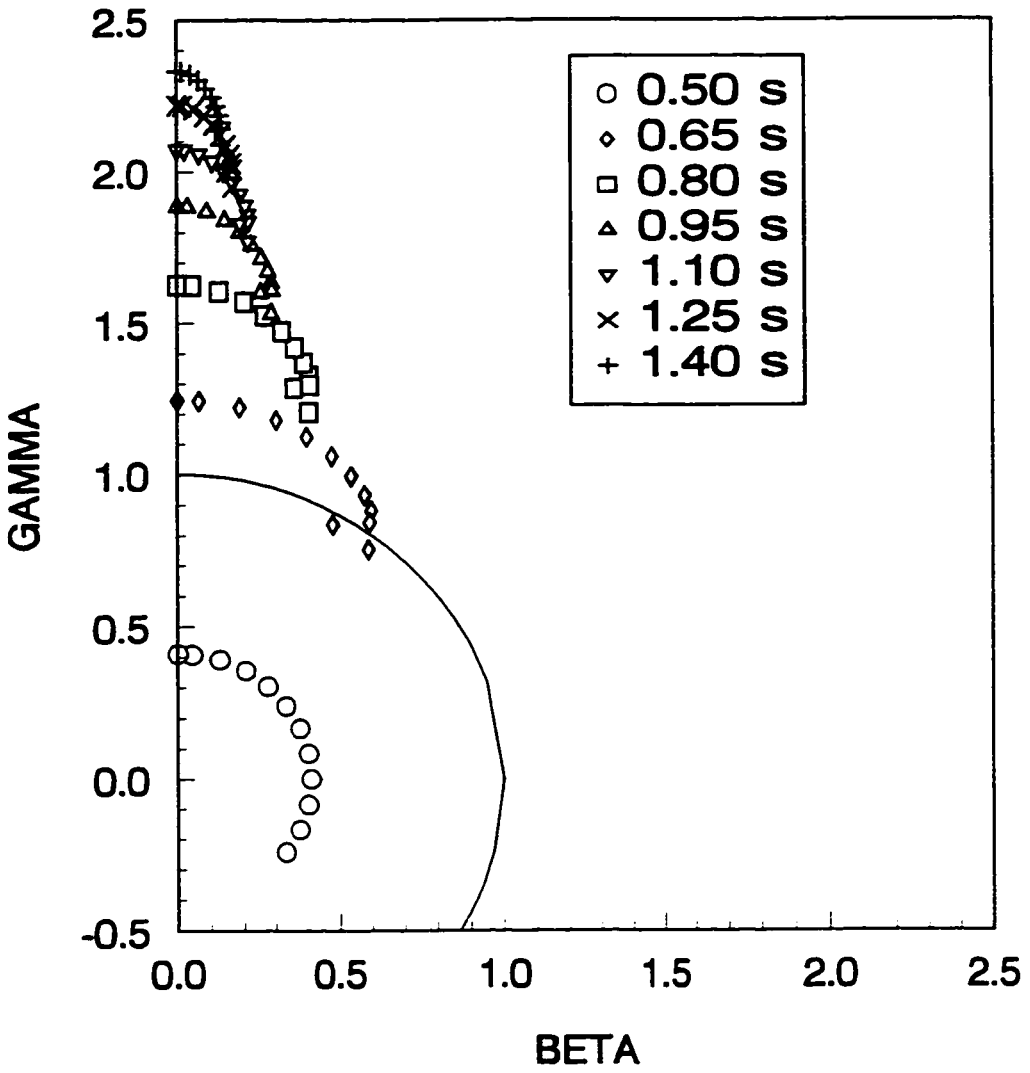

FIGURE 7.3 - Dimensionless Height *GAMMA* (z/(αUt)) versus Dimensionless Radius *BETA* (r/(αUt)) for the Figure 7.1 14 cm³(ST) Air Volume Bubble Group With U = 16.1 cm/s, r_b = 1 mm and Variable α (α_1 = 0.511 and α_2 = 0.034). The Starting Positions for the Bubbles are Provided in Table 7.1. The Arc Centred on the Origin is the Outline of the Fluid Vortex, Which has a Constant Radius of Unity.

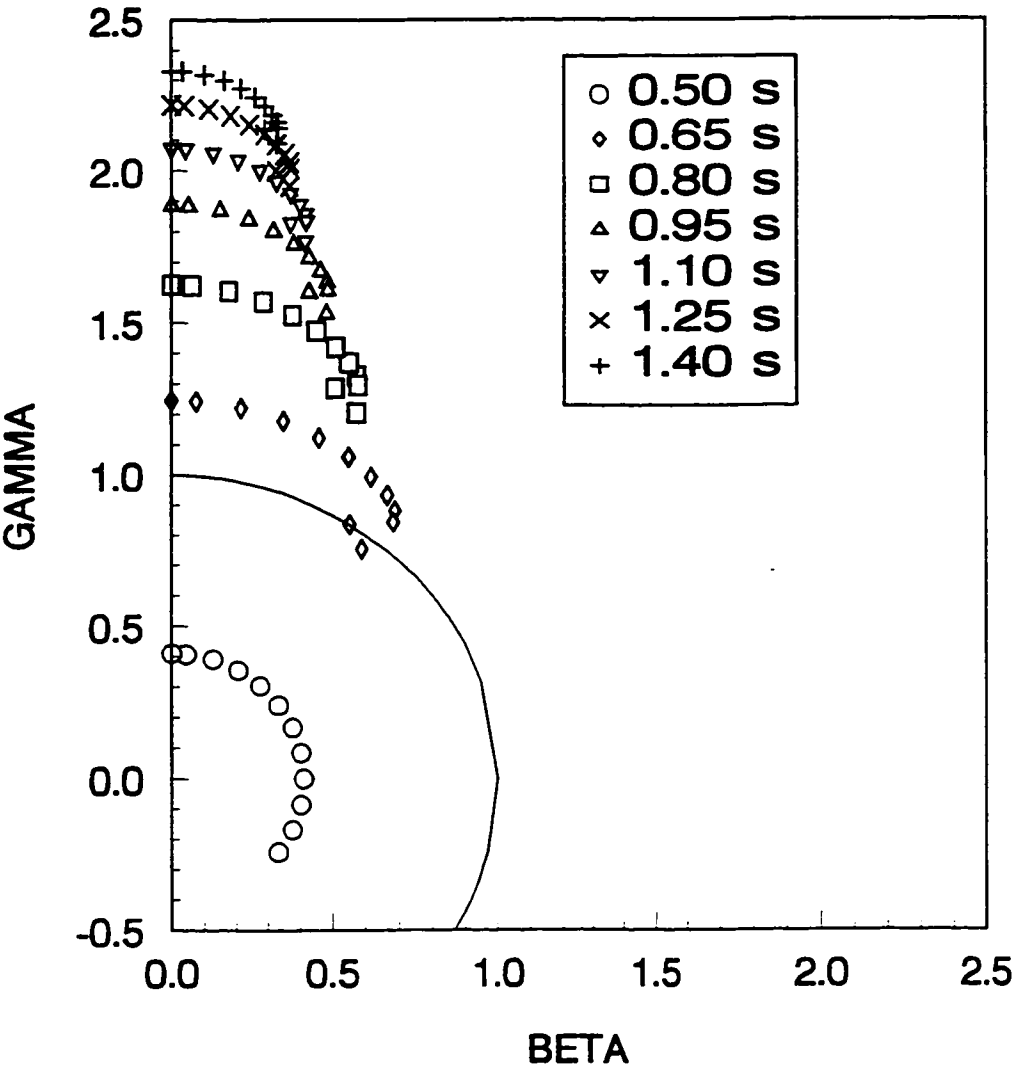

FIGURE 7.4 - Dimensionless Height *GAMMA* (z/(αUt)) versus Dimensionless Radius *BETA* (r/(αUt)) for the Figure 7.1 14 cm³(ST) Air Volume Bubble Group With U = 16.1 cm/s, r_b = 1 mm and Constant α (α_I = 0.511). The Starting Positions for the Bubbles are Provided in Table 7.1. The Arc Centred on the Origin is the Outline of the Fluid Vortex, Which has a Constant Radius of Unity.

dimensionless radius with height more significantly than is the case when the entrainment coefficient is assumed to remain constant throughout.

7.3 Effect of Altering Bubble Model Parameters

The effects of varying the model parameters of bubble radius, entrainment coefficient, fluid vortex velocity and gravitational acceleration were also studied, in order to determine if the model reacted similarly to the experiments when parameters were changed. For all of these simulations, the time period ranged from 0.5 to 1.5 seconds to highlight the results in the transition region between the bubbles circulating with the fluid, and the separation of the two phases. Early on in the modelling process, it was found that the behaviour of the bubble groups did not change significantly with height once the phases had separated; this was similar to the results for the water depth parameter experiments.

Figure 7.5 illustrates the effect that varying the radius of the bubble had on the simulation. A range of bubble sizes similar to those identified in the experiments were studied, and the initial conditions used were a starting radius of 1.49 cm, a starting height of 0.16 cm, initial bubble radial and axial velocities of 17.3 and 1.82 cm/s, respectively, an initial entrainment coefficient of 0.420 and a final entrainment coefficient of 0.082. The figure shows that an increase in bubble radius increased both the radial and the vertical components of the bubble velocity. This could be inferred from the fact that the both the radial and vertical distance travelled by the bubble increased with bubble size, even though the time it took to move this distance was the same. The results of these simulations confirmed the experimental observation that the bubble sizes remained approximately

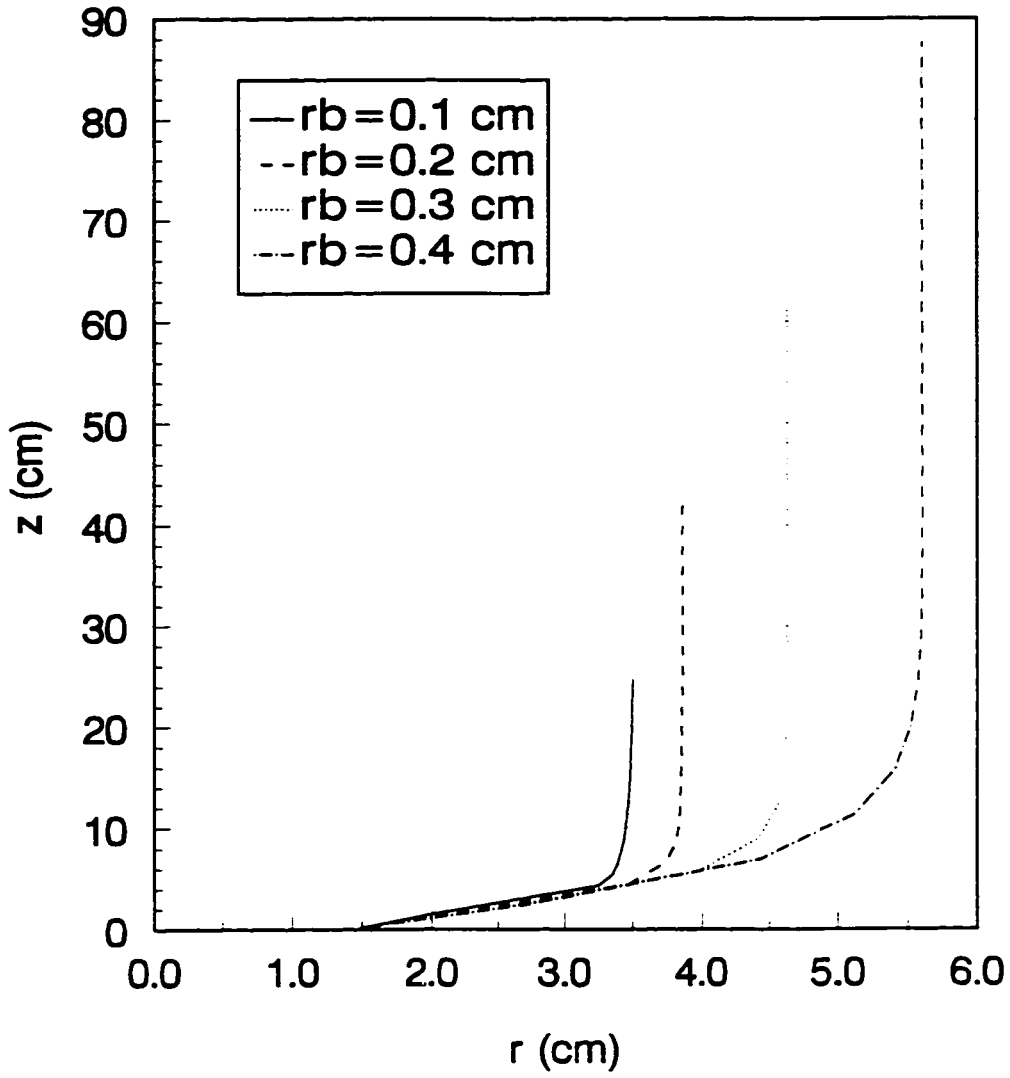

FIGURE 7.5 - Plot of the Change of Radial Position r with Height z Showing the Effect of Varying Bubble Radius on the Model Results. Initial Conditions for the Simulation were r = 1.49 cm, z = 0.16 cm, u_{br} = 17.3 cm/s, u_{bz} = 1.82 cm/s, U = 17.4 cm/s, α_1 = 0.420 and α_2 = 0.082.

constant throughout the experiments. Referring back to Table 5.2, it can be seen that the bubble group velocities only varied about three percent over the range of injected air volumes. If the bubble size was increasing with air volume (that is, the number of bubbles being injected was constant), then the bubble group velocity should have increased as well. However, if the simulation is correct, then the higher injected air volumes were breaking up into an increasing number of bubbles of the same diameter.

Figure 7.6 examines the effect of varying the entrainment coefficients both in the vortex and the potential flow region of the simulation. The initial conditions were the same as those for Figure 7.5, but a bubble radius of 1 mm was used throughout and a constant vortex velocity of 17.4 cm/s was assumed. The initial and final values of the entrainment coefficient were taken from Table 5.2 for the injected air volumes used in the experiments. The figure shows a general trend of increasing radial distance travelled by a bubble as the injected air volume increases; the one exception is the curve for the 14 cm^3(ST) bubble group values, which overlies the 10 cm^3(ST) line. However, Figure 7.7 illustrates how this problem can be corrected. Figure 7.7 is basically the same plot as Figure 7.6, but the vortex velocity for each curve in the simulation has been matched to the correct experimental value in Table 5.2, thus these curves are more reflective of the behaviour seen in the laboratory. Figures 7.6 and 7.7 reflect the importance of matching all of the significant parameters when mathematically modelling real phenomena, as they show how neglecting a term can skew the results of the model.

The effect of varying the gravitational acceleration is illustrated in Figure 7.8 for a bubble radius of 1 mm and the same initial conditions as were utilized in Figure 7.5. The g-

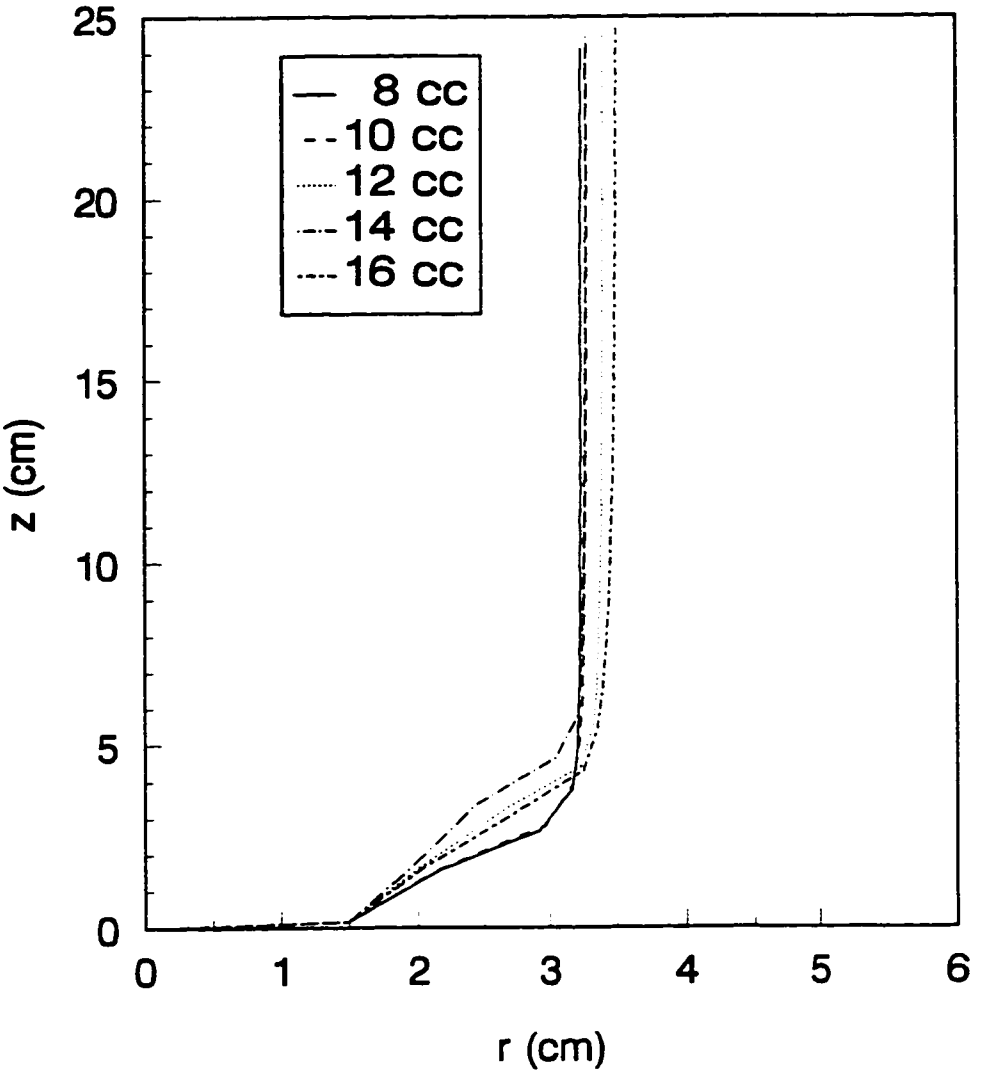

FIGURE 7.6 - Plot of the Change of Radial Position r with Height z Showing the Effect of Varying Only the Entrainment Coefficients as Initial Parameter Values and Not Using the Matching Vortex Velocity. Initial Conditions for the Simulation were r = 1.49 cm, z = 0.16 cm, u_{br} = 17.3 cm/s, u_{bz} = 1.82 cm/s, U = 17.4 cm/s, and r_b = 1 mm. Initial and Final Values of the Entrainment Coefficients were Taken from Table 5.2 for the Injected Air Volumes used in the Experiments.

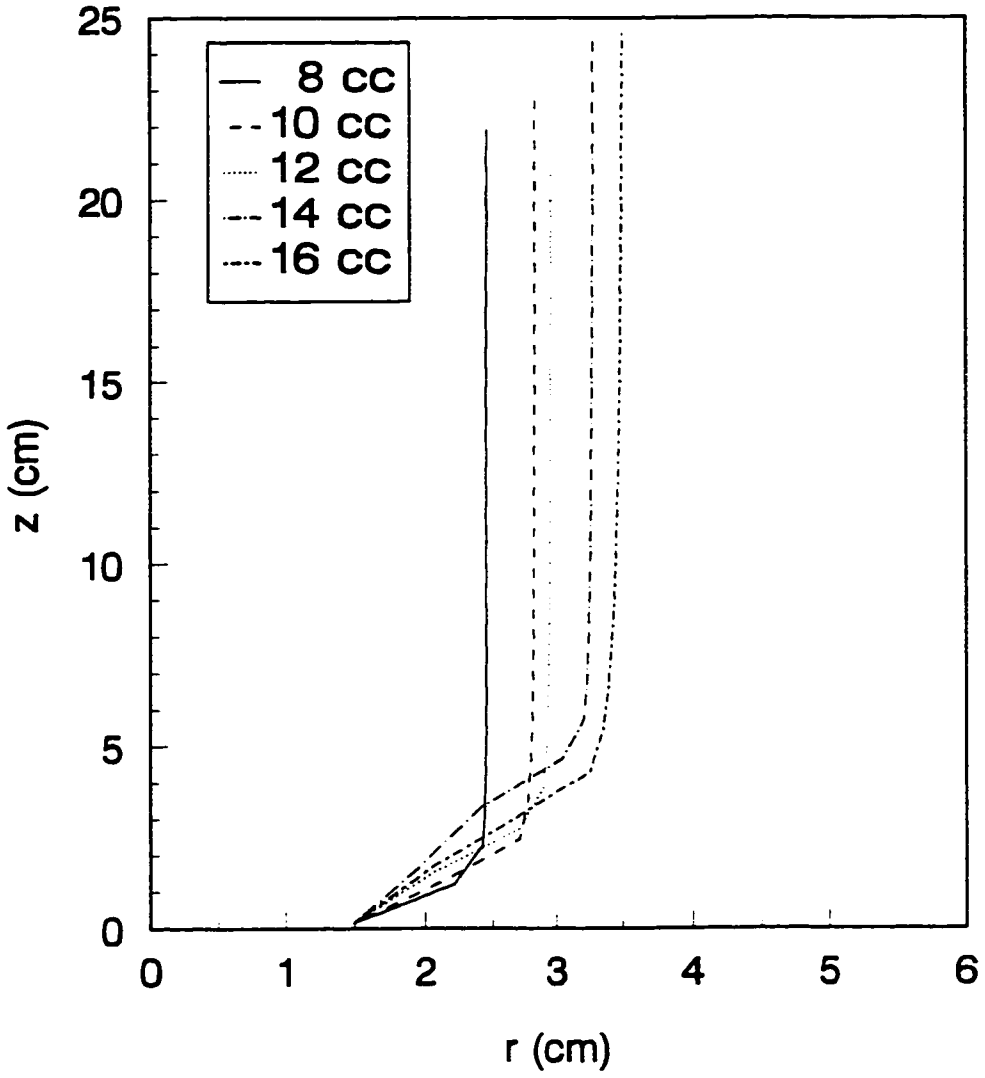

FIGURE 7.7 - Plot of the Change of Radial Position r with Height z Showing the Effect of Varying the Entrainment Coefficients as well as the Matching Vortex Velocity as Initial Parameter Values. Initial Conditions for the Simulation were r = 1.49 cm, z = 0.16 cm, u_{br} = 17.3 cm/s, u_{bz} = 1.82 cm/s, and r_b = 1 mm. Initial and Final Values of the Entrainment Coefficients, as well as the Matching Vortex Velocity, were Taken from Table 5.2 for the Injected Air Volumes used in the Experiments.

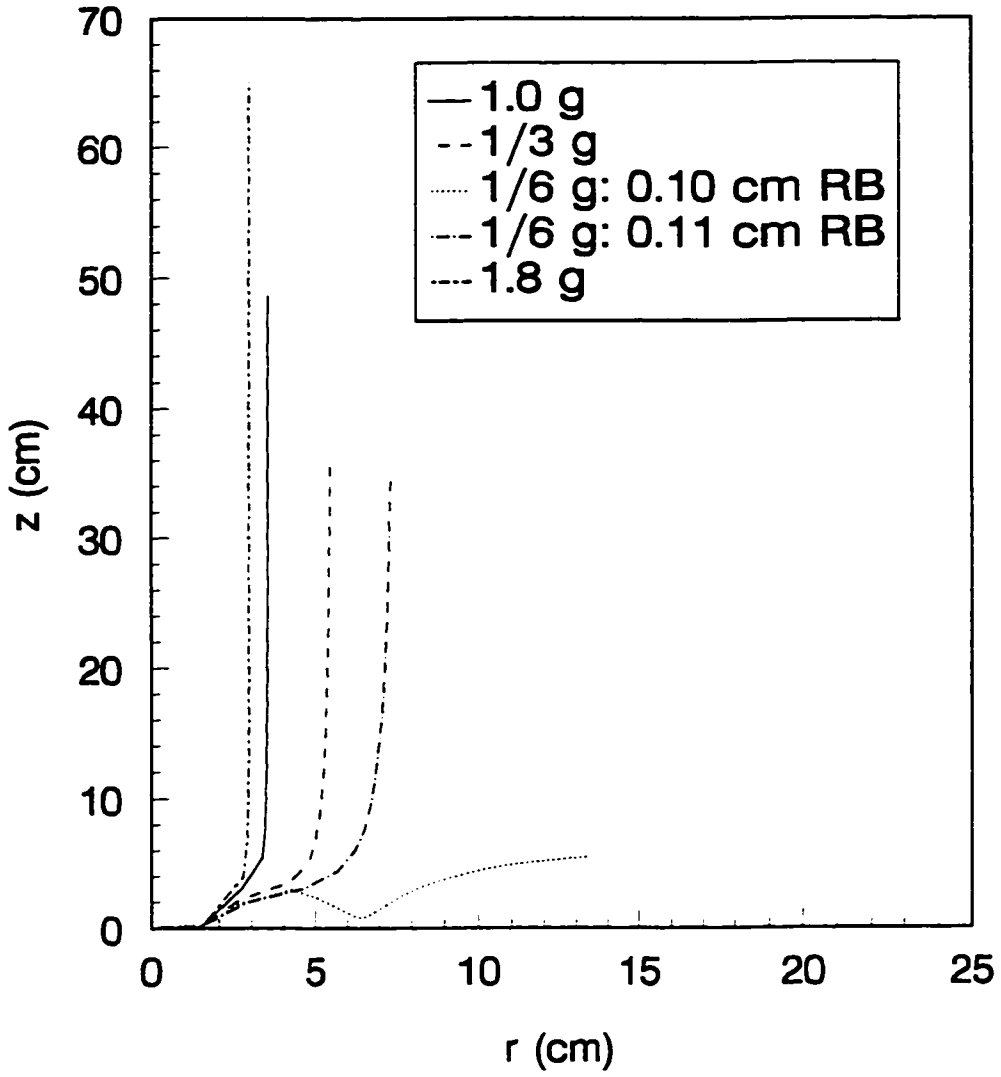

FIGURE 7.8 - Plot of the Change of Radial Position r with Height z Showing the Effect of Varying the Gravitational Acceleration on the Model. Initial Conditions for the Simulation were r = 1.49 cm, z = 0.16 cm, u_{br} = 17.3 cm/s, u_{bz} = 1.82 cm/s, U = 17.4 cm/s, α_1 = 0.420, α_2 = 0.082, and r_b = 1 mm.

levels examined in the simulation were the same as those used for the microgravity experiments. In general, the model results show a decrease in radial velocity and an increase in vertical velocity with increasing g-level; this can be inferred by the decreasing radial distance and increasing axial distance over the same time period. Similar behaviour was seen in Figures 5.8 and 5.9, which showed a decrease in α with increase in gravitational acceleration after the transition point for the experimental results.

The most interesting feature of Figure 7.8 was the behaviour of the 1/6 **g** curve for the 1 mm bubble radius, which was totally different from anything seen in the experiments. The bubble rose to a height of about 3 cm, dropped back to its original starting position, then bounced back to a height of approximately 5 cm, all the while travelling a radial distance of 13.5 cm. However, increasing the bubble radius by 0.1 mm brought the curve back into line with the rest of the simulations. It was noted in Chapter 5 that bubble sizes tended to be larger at the lower g-levels due to the longer time it took for the bubbles to form, and they were smaller at 1.8 **g** because they detached more quickly from the bubbler. If the same bubble sizes could have been maintained in the KC-135 experiments as were seen in the laboratory, then it may have been possible for this type of behaviour to occur.

7.4 Comparison of Simulations with Experimental Results

The primary difficulty in matching the simulations to the experimental data lies in the starting positions of both sets of results. The simulations were carried out assuming a point source centred in the bubbler, which had a diameter of 2.5 cm, while the origin for the experimental data values was positioned at the top of the injector, or 1.25 cm above. In

addition, if the data points in the initial stages of bubble group growth are extrapolated back to an imaginary point source, this would lie approximately 7 cm below the top of the bubbler.

This qualification should be taken into account when examining Figure 7.9, which repeats the model bubble group results shown in Figure 7.1. The solid lines in Figure 7.9 is the outline of the experimental bubble group from the large tank Test L14-45.3. It can be seen in this figure that the general outlines of the experimental and model curves are similar, and, for the first three time steps, the model z values lie about 7 cm below the curve outlining the experimental data, which was the expected result. However, once the bubbles separate from the vortex, the distance between model and experiment starts to increase with each time step.

The significant feature about Figure 7.9 is the difference between the radial sizes of the laboratory and the model bubble group. Over the full range of the times examined, the actual data has approximately twice the radius of the model. This discrepancy is much more obvious in Figure 7.10, which plots the outermost model bubble trace from Figure 7.9 against the full data set for the 14 cm^3(ST) bubble groups at a water depth of 120 cm. The data set and simulation would have reasonable agreement near the origin if the curves were adjusted to start from the same point source, but near the full height of the tank, the bubble group radius is about three times larger than that of the model. This appears to be a serious flaw in the simulation model, and it was consistent with the results seen for all of the other air injection volume data when plotted against the matching theoretical curve.

The problem with the model appears to lie primarily in the radial velocity term of the bubble equations, since an increase in radial velocity would have a similar effect on the radial

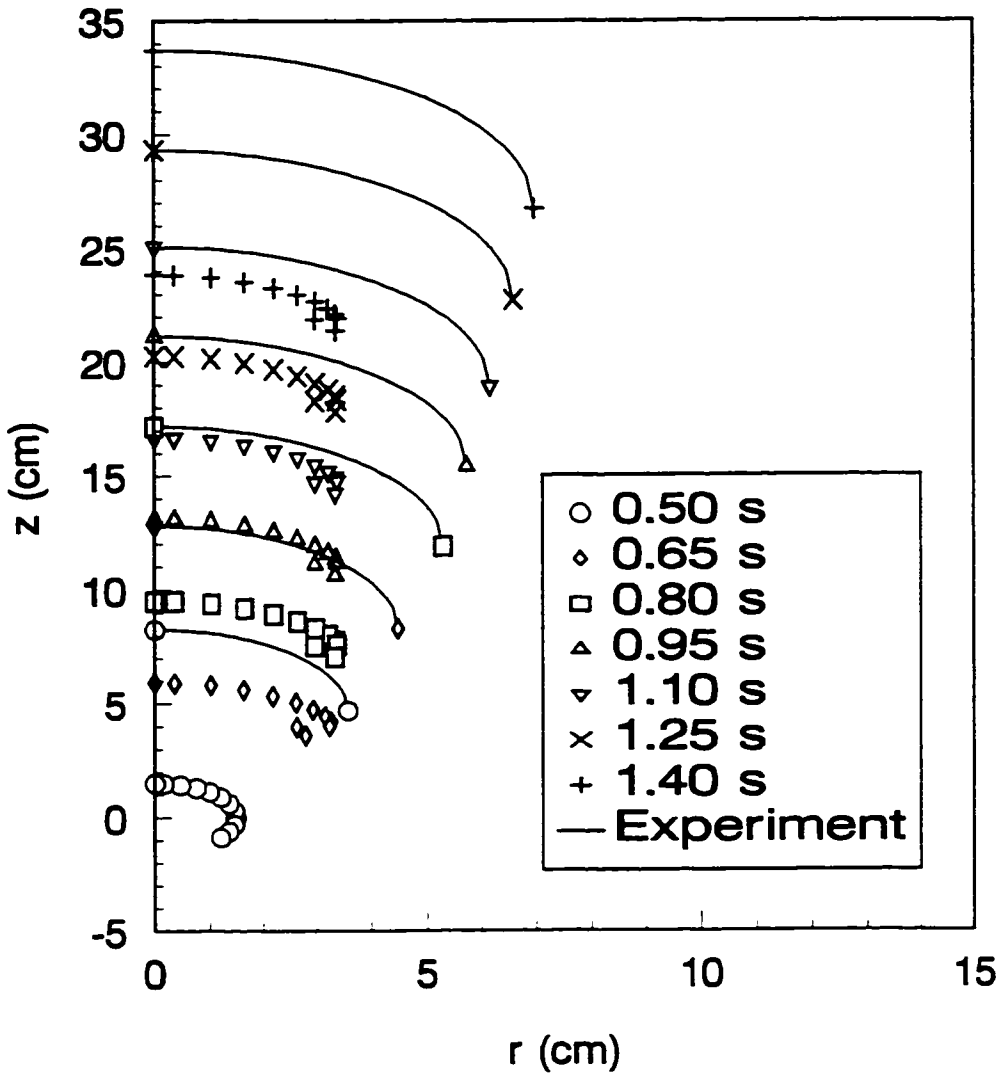

FIGURE 7.9 - Plot of the Increase in Bubble Group Radius r with Height z for 12 Bubbles Generated by the Simulation Model Using the Initial Conditions for a 14 cm³(ST) Air Volume Bubble Group (U = 16.1 cm/s and $\alpha_1 = 0.511$) and $r_b = 1$ mm. The Starting Positions and Velocities for each Data Point are Provided in Table 7.1. The Simulation Results are Compared to Outlines of the Experimental Data Set from Large Tank Test L14-45.3 at the Same Time Intervals.

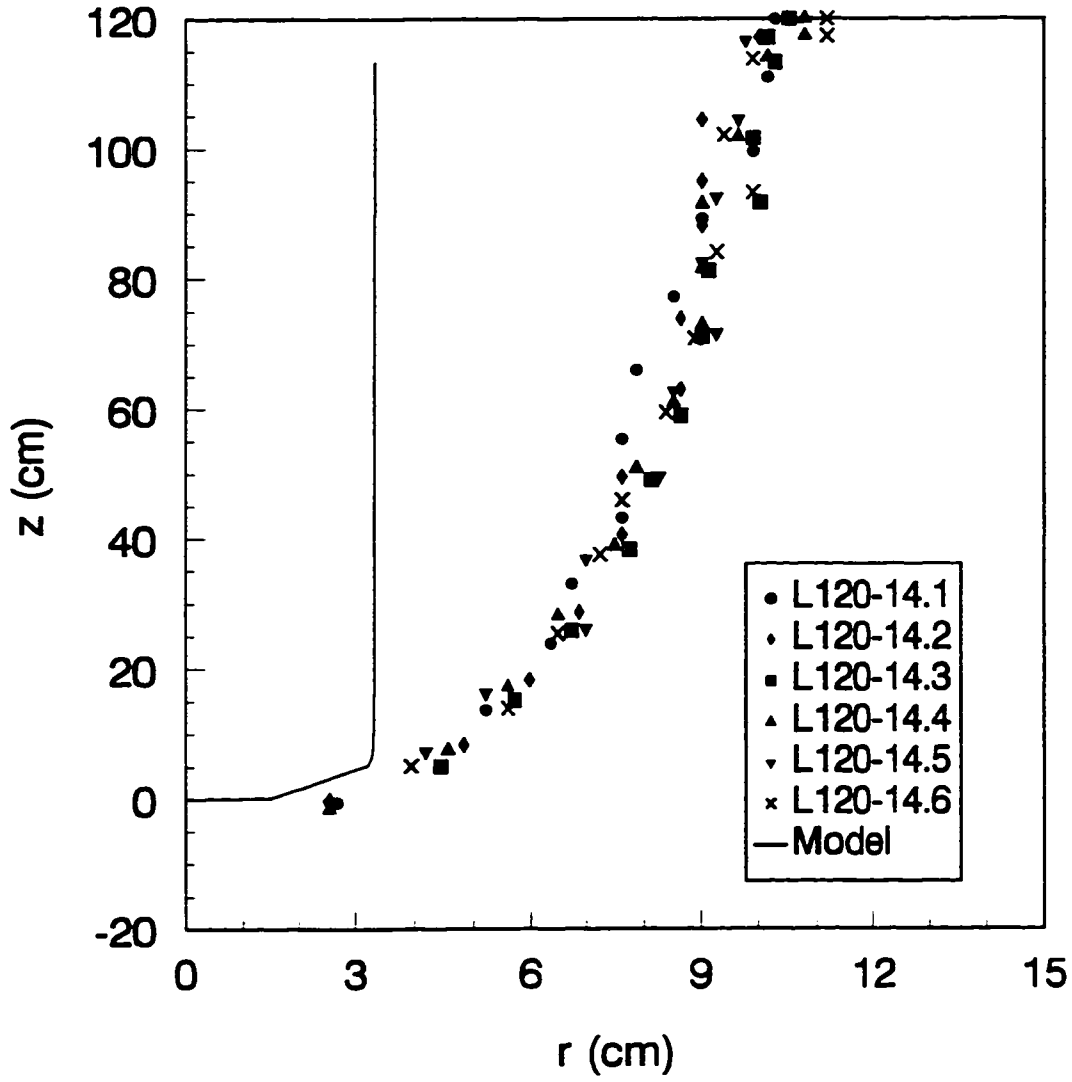

FIGURE 7.10 - Plot of the Increase in Bubble Group Radius r with Height z for the Outermost Bubble Path from Figure 7.9, which was Generated by the Simulation Model Using the Initial Conditions for a 14 cm³(ST) Air Volume Bubble Group (U = 16.1 cm/s and $\alpha_1 = 0.511$) and r_b = 1 mm. The Simulation Results are Compared to the Full Data Set from All Large Tank 14 cm³(ST) Tests with H_w = 120 cm.

distance in the integration. Figures 7.11 and 7.12 are, respectively, the matching axial and radial velocity plots to the simulation given in Figure 7.9. In Figure 7.11, the axial velocity term for each bubble quickly accelerates within the fluid vortex until a constant terminal velocity is reached at a height of about 4 cm. Figure 7.12 shows a large radial acceleration followed by a similar deceleration over the same range as the axial acceleration, and then the radial velocity term drops almost to zero. Figure 7.13 shows the same radial velocity plot in much more detail, and it can be seen that, by the time the height of the simulation has reached 15 cm, the effect of the radial velocity is negligible.

Figure 7.14 is the axial velocity plot which matches the simulation from Figure 7.10, and it shows that there is very good agreement between the model vertical velocity term and the experimental results. Figure 7.15 plots height z versus time t for the large tank test L14-120.5 and the simulation used in Figure 7.10, and it shows an almost exact match between model and experiment. Because of the excellent agreement between theory and the laboratory work in the axial direction, it is obvious that, to correct the simulation model, it must be adjusted carefully so as not to affect the vertical velocity terms.

7.5 Correction of the Bubble Group Simulation Model

An examination of the bubble equations (6.16) and (6.17) shows that radial velocity appears only in the pressure force and added mass term, and in the lift term. However, adjustment of the added mass coefficient would also affect the vertical, as well as the radial, velocity. It has already been seen in Figure 7.2 that the addition of the lift term shifted the model curve outwards in the radial direction without affecting the vertical rise of the bubble.

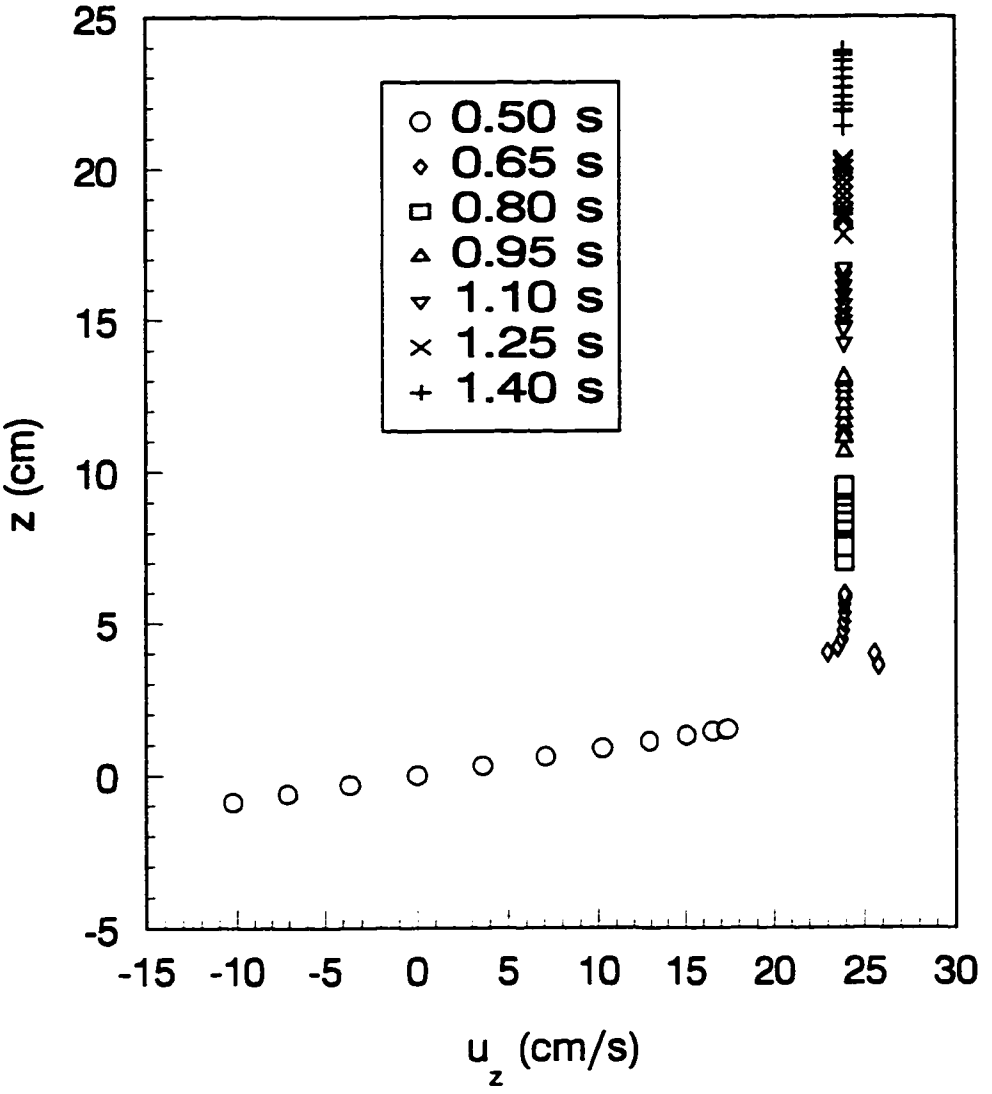

FIGURE 7.11 - Plot of the Variation in Vertical Bubble Velocity u_z with Height z for the 12 Bubbles in Figure 7.9, which were Generated by the Simulation Model Using the Initial Conditions for a 14 cm³(ST) Air Volume Bubble Group (U = 16.1 cm/s and $\alpha_f = 0.511$) and $r_b = 1$ mm. The Starting Positions and Velocities for each Data Point are Provided in Table 7.1.

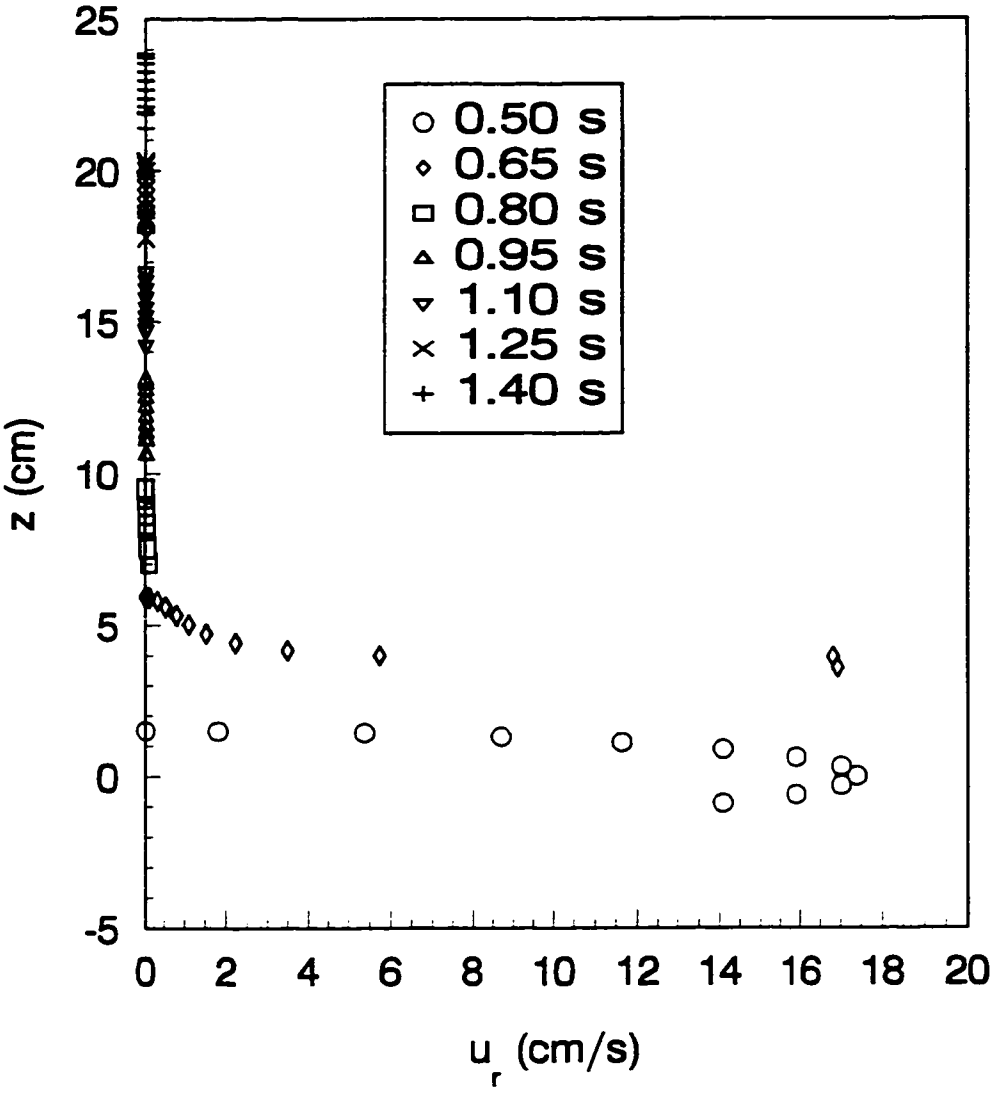

FIGURE 7.12 - Plot of the Variation in Radial Bubble Velocity u_r with Height z for the 12 Bubbles in Figure 7.9, which were Generated by the Simulation Model Using the Initial Conditions for a 14 cm³(ST) Air Volume Bubble Group (U = 16.1 cm/s and $\alpha_j = 0.511$) and $r_b = 1$ mm. The Starting Positions and Velocities for each Data Point are Provided in Table 7.1.

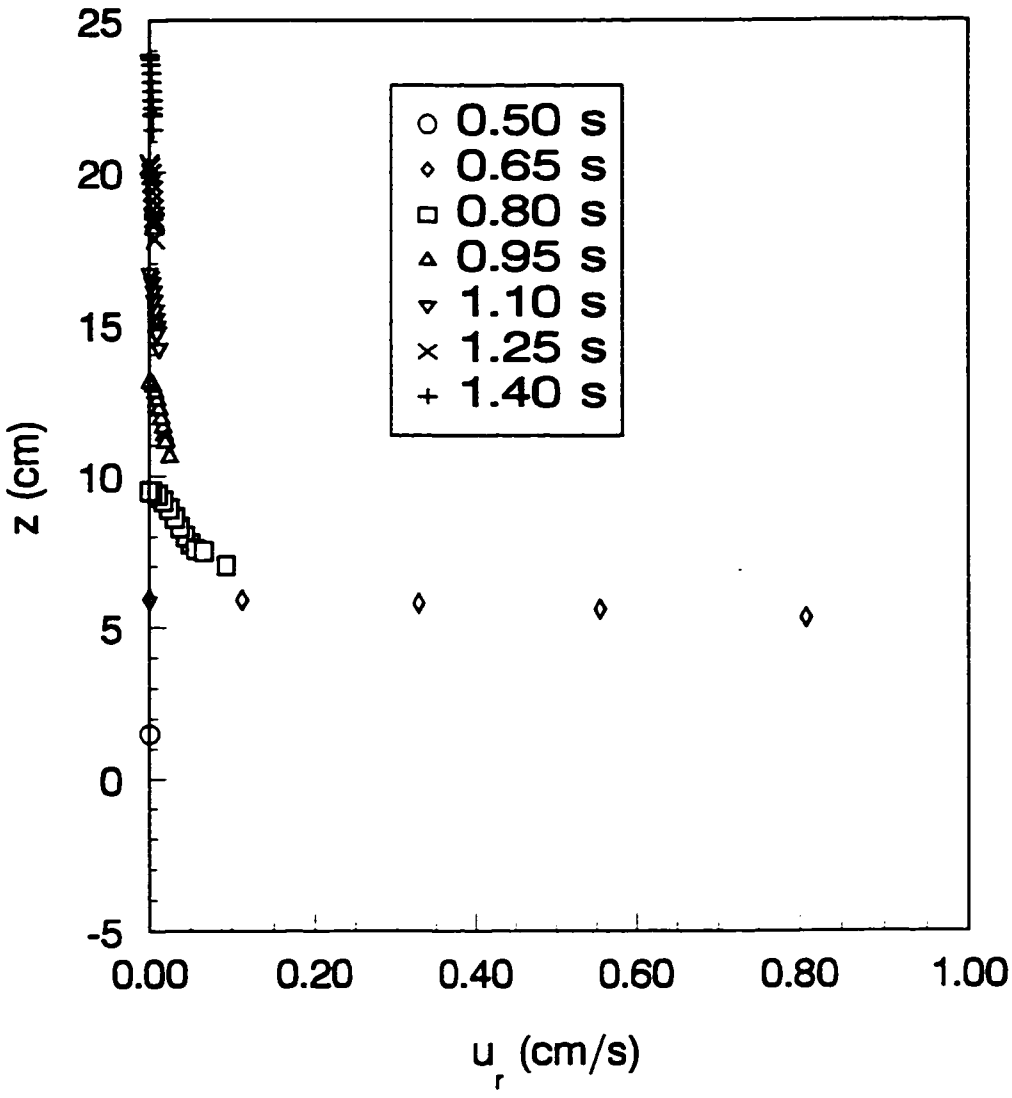

FIGURE 7.13 - Detail of the Plot of Variation in Radial Bubble Velocity u_r with Height z Shown in Figure 7.12 for the 12 Bubbles in Figure 7.9, which were Generated by the Simulation Model Using the Initial Conditions for a 14 cm³(ST) Air Volume Bubble Group (U = 16.1 cm/s and α_f = 0.511) and r_b = 1 mm. The Starting Positions and Velocities for each Data Point are Provided in Table 7.1.

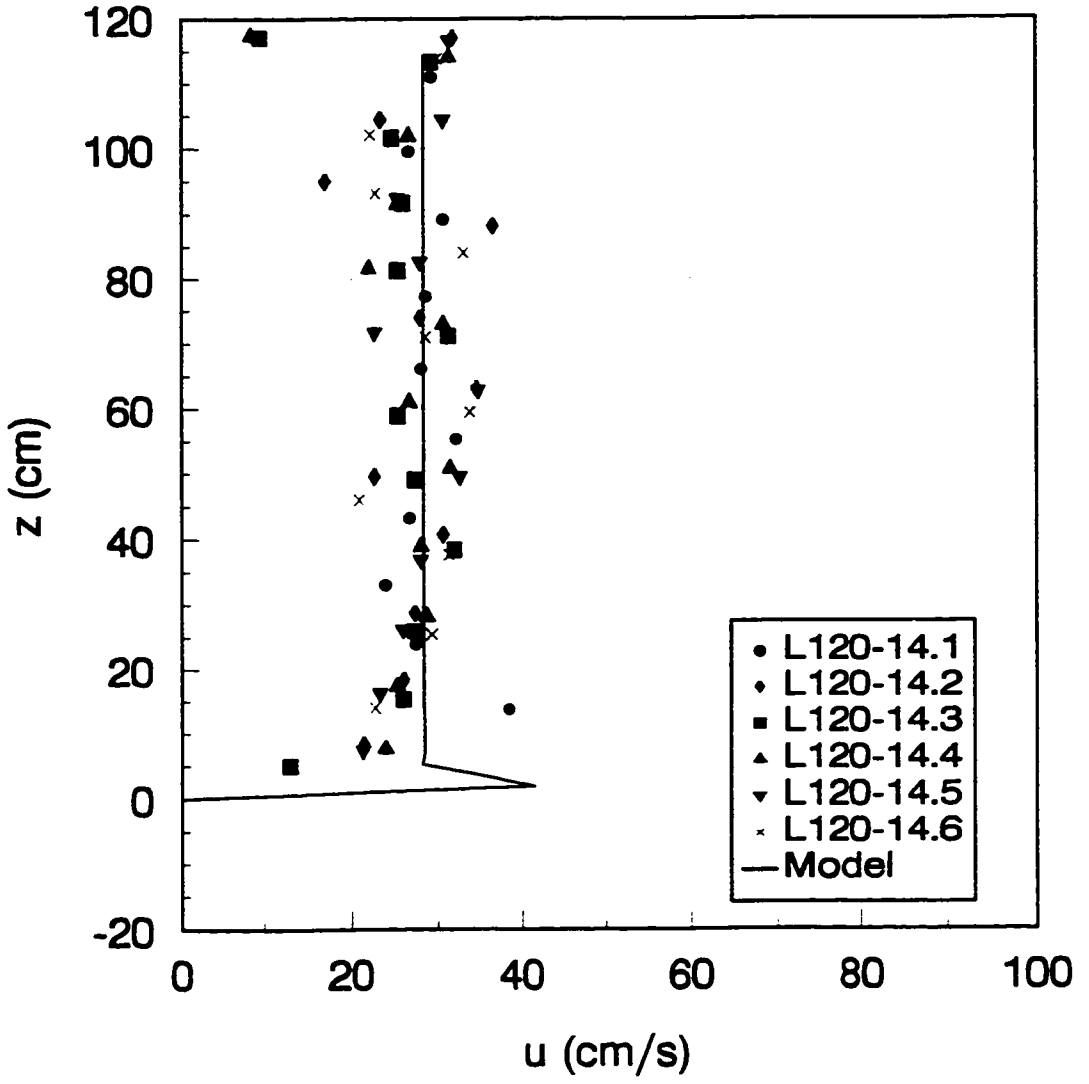

FIGURE 7.14 - Plot of the Variation in Vertical Bubble Velocity u_z with Height z for the Outermost Bubble Path from Figure 7.9, which was Generated by the Simulation Model Using the Initial Conditions for a 14 cm³(ST) Air Volume Bubble Group (U = 16.1 cm/s and α_I = 0.511) and r_b = 1 mm. The Simulation Results are Compared to the Vertical Bubble Group Velocity u from each Data Set in the Large Tank 14 cm³(ST) Tests with H_w = 120 cm.

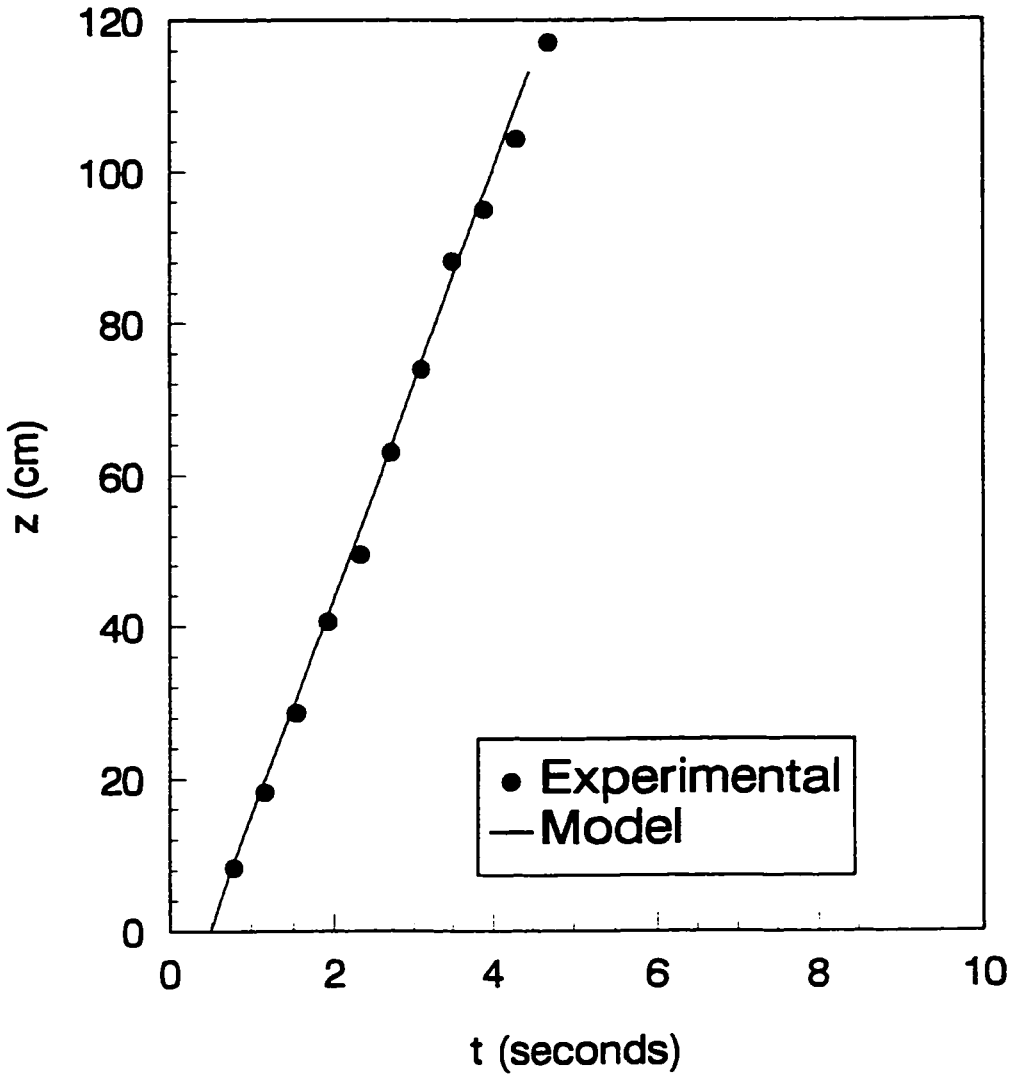

FIGURE 7.15 - Plot of Height of the Widest Point of the Bubble Group z versus Time t for the Data Set for Large Tank Test L14-120.5 and for the Outermost Bubble Path from Figure 7.9, which was Generated by the Simulation Model Using the Initial Conditions for a 14 cm³(ST) Air Volume Bubble Group (U = 16.1 cm/s and $\alpha_1 = 0.511$) and $r_b = 1$ mm. The Plot Shows an Almost Exact Match Between Theory and Experiment.

The lift term could easily be weighted by adjusting the lift coefficient, which was assumed to take the value of 0.5, which is representative of a spherical bubble. It was found that doubling the lift coefficient from 0.5 to 1.0 increased the radial distance on any simulation approximately 10 to 15 percent. Increasing this term could possibly be justified, as the experiments showed that the the bubbles rose in helical paths, and an increase in the rate of spin of a sphere has the effect of increasing the lift coefficient (Tritton, 1977). However, this correction is not thought to be viable, as there was no actual evidence that the spin rate of the bubbles was increasing in the experiments.

Another means of increasing the radial velocity, and thus the radial distance travelled, for a bubble is to examine the entrainment coefficient term. It was assumed when formulating the model that, because the experimental bubble groups expanded at a different rate inside and outside the fluid vortex, that this should be accounted for in the model. In other words, it was assumed that once the bubbles had left the fluid vortex, that the vortex no longer had any effect on the bubble motion. However, if this is not the case, then the entrainment coefficient should be constant throughout the lifetime of the bubble group, and only the initial value from the two-phase region should be used.

To test both of these corrections, the model was revised to examine the effect of using a constant α, and that of increasing the lift coefficient. Figure 7.16 presents the results of these simulations compared to the experimental results for all large tank 14 cm^3(ST) runs at a 120 cm water depth. The solid curve in the figure is the same as the one shown in Figure 7.10, and it illustrates the path of a bubble when the entrainment coefficient is forced to change after the bubble leaves the vortex. The dashed curve represents the path of a bubble

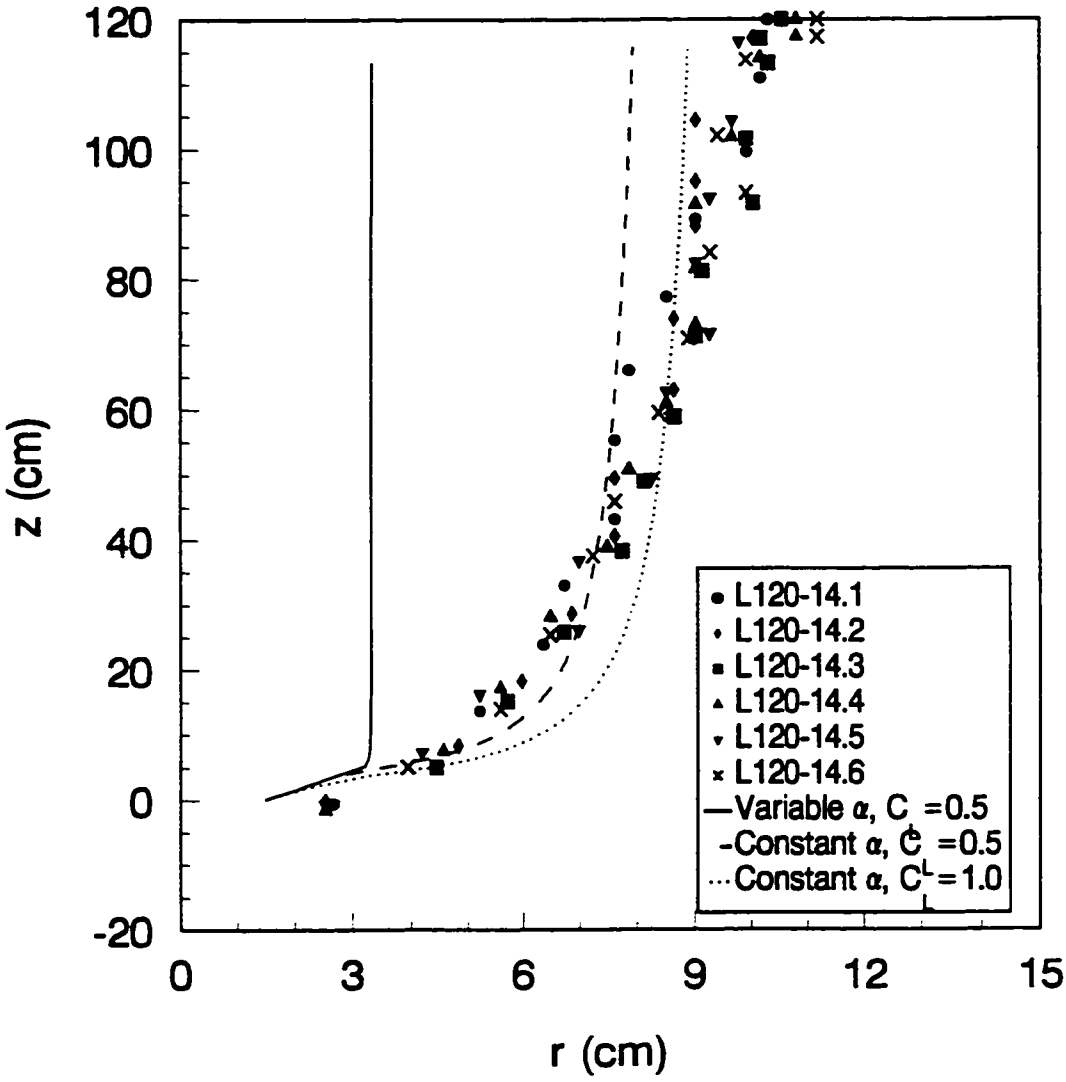

FIGURE 7.16 - Plot of the Increase in Bubble Group Radius r with Height z for the Outermost Bubble Path from Figure 7.9 (Solid Line), which was Generated by the Simulation Model Using the Initial Conditions for a 14 cm³(ST) Air Volume Bubble Group (U = 16.1 cm/s, $\alpha_1 = 0.511$, $\alpha_2 = 0.034$) and r_b = 1 mm. The Simulation Results are Compared to the Full Data Set from All Large Tank 14 cm³(ST) Tests with H_w = 120 cm. Also Plotted is the Effect on the Simulation of Using a Constant Initial Entrainment Coefficient, and of Doubling the Lift Coefficient.

when the entrainment coefficient remains constant at its initial value throughout the simulation. When the different starting heights of the model and the simulation are accounted for, this curve shows excellent agreement with the data near the source (for about the first 25 percent of the simulation), then deviates from the experimental values at a constant rate with height. This rate of deviation is approximately equal to 0.034, which is the asymptotic value of entrainment coefficient which was calculated for the experimental bubble groups in their second stage of growth and was given in Table 5.1. Thus, the simulation could be moved even closer to the experimental data points by adding this final entrainment coefficient to the intial value. However, there is no physical justification for this step, other than using the second-stage entrainment coefficient as a scaling parameter.

The dotted curve in Figure 7.16 shows the result of doubling the lift coefficient. Although increasing this term brings the simulation closer to the topmost experimental values, it shifts the entire curve outwards, and thus destroys the good agreement between theory and experiment which was previously seen at the low end of the curve.

A possible correction factor which could be used is a variable lift coefficient, which changes with water height above the injector. There is some justification for this move, as the spin on the bubbles was observed to increase somewhat with height. However, a more probable explanation lies in the fact that, because of the assumption of axial symmetry, only the z-direction lift remains in the equations when the vorticity term is expanded. The helical rise of the bubbles indicates that there should also be some vorticity in the r- and θ-directions. Thus, it is suggested that the model be expanded to include these lift terms as

well. The pressure and added mass term would also be affected by the addition of another partial derivative term; however, the influence of these terms on the model is very slight.

Figure 7.17, which is the corresponding vertical velocity plot for Figure 7.16, shows that either changing the lift coefficient or using a constant entrainment coefficient throughout the simulation has a negligible effect on the rise velocity of the bubble. One other method of increasing the radius of the bubble group with height is to choose a larger initial bubble size for the model. Figure 7.5 illustrated the effect of increasing the bubble radius, and it was seen that larger bubble volumes moved the curve outwards in the radial direction. However, this occurs through an increase in the buoyancy force, which affects the vertical rise velocity in addition to the radial velocity. Thus, care must be taken when utilizing this term as a means of correcting the model, in order to avoid unwanted effects.

It is possible that there is some expansion of the bubbles with decreasing water depth from the free surface, even though this effect was not apparent in the experimental results. If this is the case, then the bubble volume is actually increasing with height above the orifice, which would have a gradually increasing effect on the overall bubble group radius through the increasing buoyancy force term.

7.6 Relevance of Dimensionless Groups and Scaling Parameters to the Model

In Chapter 3, a number of scaling parameters governing bubble group rise were established in order to simplify the design of the experiments, and to determine the conditions affecting geometric, kinematic and dynamic similarity. It was found that satisfying all of the similarity requirements simultaneously was next to impossible, and a

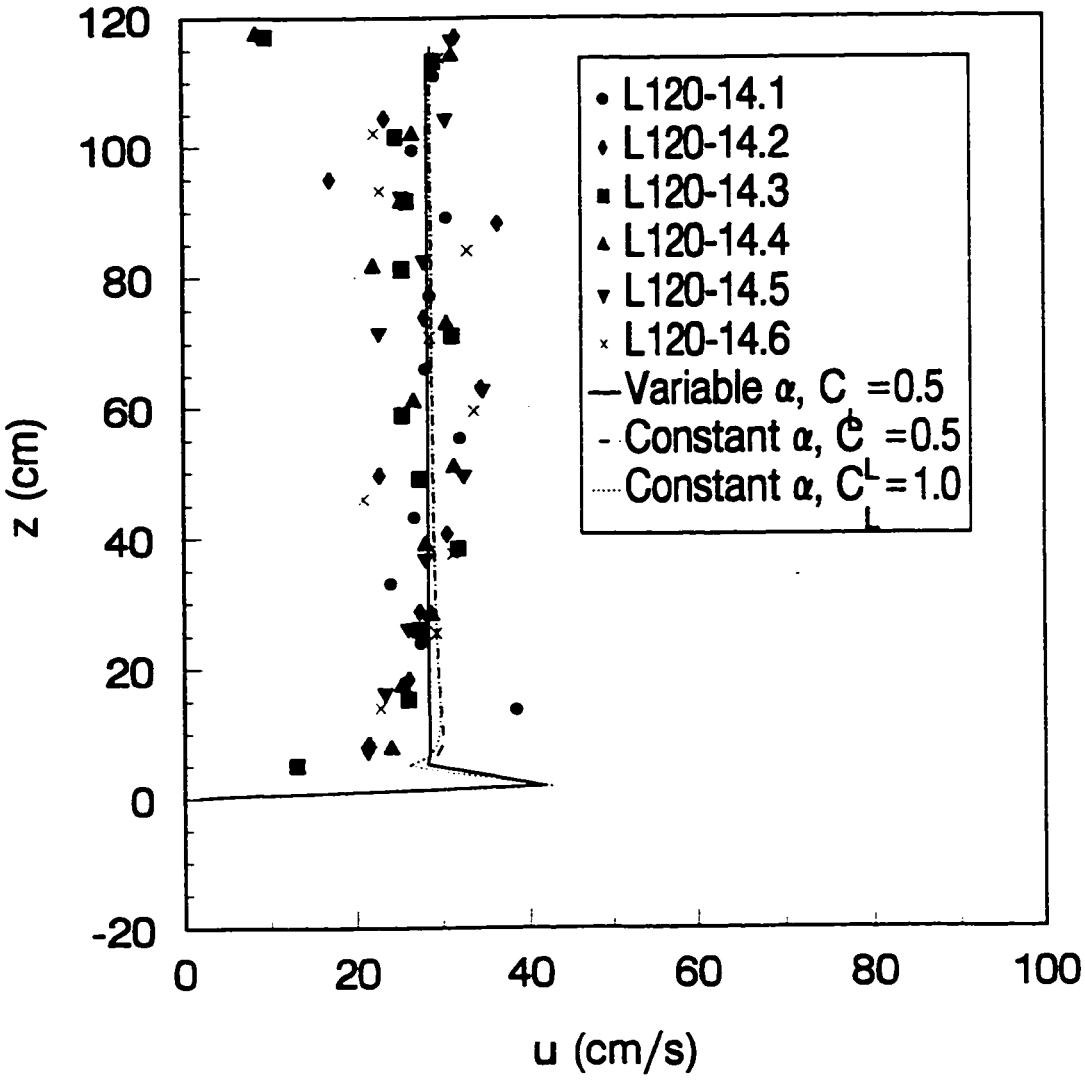

FIGURE 7.17 - Plot of the Variation in Vertical Bubble Velocity u_z with Height z for the Outermost Bubble Path from Figure 7.9 (Solid Line), which was Generated by the Simulation Model Using the Initial Conditions for a 14 cm³(ST) Air Volume Bubble Group (U = 16.1 cm/s, $\alpha_1 = 0.511$, $\alpha_2 = 0.034$) and $r_b = 1$ mm. The Simulation Results are Compared to the Full Data Set from All Large Tank 14 cm³(ST) Tests with $H_w = 120$ cm. Also Plotted is the Effect on the Simulation of Using a Constant Initial Entrainment Coefficient, and of Doubling the Lift Coefficient.

decision was made to use the same fluid for both the model and the prototype, and then to evaluate the distortion caused by this infringement of similitude.

The use of scaling parameters enabled the number of variables investigated in the experimental work to be reduced to four: injected air volume, water height above the source, surface tension and gravitational acceleration. The experimental work showed that increasing the air volume injected increased the overall radius of the bubble group with height, which resulted in a rise of the asymptotic value of the entrainment coefficent by 45 percent over the range of air volumes investigated. Increasing the water height above the source had no apparent effect over the range of water heights studied. The effect of reducing the surface tension was immediate and was difficult to quantify; lowering the surface tension drastically changed the size of the bubbles, so that they fell into a regime which could not be compared with the rest of the experimental results. Altering the gravitational acceleration had a definite effect on the buoyancy force of the bubbles and, in general, bubble group radius decreased slightly with increasing g-force.

For practical application in a blowout plume model, the gravity effects can be discounted. The effect of water depth, however, would become more important. Although no influence of water depth was seen in the current set of experiments, this is because atmospheric pressure is dominant to a water depth of approximately 1 m, according to the surface pressure scale derived in Equation (3.20). Tekeli and Maxwell (1978) found that geometric similarity was necessary in order to correctly scale the entrainment effects in a bubble plume, and they used a distortion factor based on (3.20) to correct for deviation from similitude, which they found to be greatest at the source. It is interesting to note that Tekeli

and Maxwell's experiments took place in shallower water than was the case for this project. Thus, it is speculated that they were correcting their observed deviations with a factor which does not really apply to the range of their experiments, although it would certainly be important at larger depths.

For the current experimental program, the injected volume and surface tension effects provided the most significant findings. Injected air volume had a definite effect on the entrainment coefficient in the second growth stage. This term appears in the bubble Reynolds number of Equation (3.13), and surface tension in the form of Eötvos number derived in the same dimensional analysis. Although the Eötvos number is useful for determining the flow regime of the individual bubbles, as it indicates whether the flow is dominated by surface tension or gravity effects (*i.e.* small or large bubbles), it does not provide as good a basis for a scaling parameter or distortion factor for a bubble group as does the bubble Reynolds number. This is the same conclusion which was drawn by Rowe *et al.* (1989) for bubble plumes.

The equations for the theoretical model assume that the bubble regime is known, *i.e.* that the bubble radius is a known quantity or can be estimated. This eliminates the need for the Eötvos number, and leaves no option other than using the bubble Reynolds number as the basis for a distortion factor or scaling parameter.

Referring back to Figure 7.16, it can be seen that the best match to the experimental data in general shape is the curve which uses the constant initial value of entrainment coefficient throughout. However, following separation of the bubble from the fluid vortex, this curve deviates from the experimental data by what is basically a linear relationship with

height. This relationship is slightly larger than the asymptotic values of entrainment coefficient given in Table 5.1, which were shown to increase with increasing bubble group volume. When the simulation was recalculated using a value of $\alpha_1 + \alpha_2$ as the entrainment coefficient following separation, the model curve moved even closer to the data, but still lay inside the data points.

What this suggests, in terms of a simple correction factor for the theoretical model, is that a relationship between the bubble Reynolds number and α_2 be pursued, in order to provide a weighting parameter for the curve following separation of the bubbles and the vortex. However, the effect of three-dimensional vorticity should be investigated first, as this is a more physically-probable solution to the fit of the curve.

The linear deviation of the model and the experimental data also suggests that hydrostatic pressure might be playing a role in bubble group behaviour, despite previous assumptions to the contrary. Although the observed radial growth of the bubble groups was similar at all water depths, it was consistently linear with height, which implies that α_2 could be a function of the hydrostatic pressure.

There is one further option that should be pursued, in that the model itself may not appropriate for bubbles as large as those studied in this experimental program. The majority of the bubbles were between two and eight millimetres in diameter, which places them well above the Stokes-flow regime. As a result, all of the bubble groups had very short residence times in their fluid vortex, so the influence of the moving fluid on the overall group behaviour was probably very small.

CHAPTER 8

CONCLUSIONS AND RECOMMENDATIONS

8.1 Conclusions

A number of conclusions can be drawn from the work presented in this dissertation. As the conclusions generally derive either from the experimental program, or from the theoretical model, these results will be discussed separately.

8.1.1 Conclusions from the Experimental Portion of the Study

1. A literature review of single- and multi-phase thermals and vortex rings was carried out to provide a basis for the investigation of two-phase bubble groups. It was found that, although similar studies have been carried out in the area of solid-particle "thermals" (several of them studied under the same supervisor as the author, and utilized equipment designed by the author and built for the bubble-group study), very little attention has been paid to the problem of bubble-group dynamics. Only one model for bubble group behaviour was found in the literature, and the first experiments showed that this model would not work.

2. A dimensional analysis was used to derive the appropriate dimensionless groups describing bubble group behaviour. Five relationships were identified: a length ratio, an Eötvos number, a dynamic similarity number obtained from a combination of the liquid Reynolds number and the Froude number, a density ratio, and an

expansion parameter which accounts for the expansion of the bubble volumes as they rise due to the reduction in ambient pressure. Combining the Reynolds/Froude number with the density ratio gave a form of Grashof number, but this basically reduced back to the Reynolds number group because of the large density difference between the phases. It was speculated that the bubble Reynolds number would be the most important dimensionless group in this investigation, and this was borne out by the results of the experiments.

3. A set of eight scaling parameters were derived to describe the necessary criteria for similitude between a model (experiment) and a prototype (blowout bubble plume). These scaling relationships were used in the design of the experimental program. It was found that it was impossible to satisfy the requirements of geometric, dynamic and kinematic similarity at the same time, so a decision was made to use the same ambient fluid (water) for both model and prototype, and to investigate the distortion caused by the infringement of similitude. This effectively reduced the number of variables to be investigated to four: injected air volume, water depth above the source, surface tension, and gravitational acceleration.

4. As was mentioned previously, the use of scaling parameters enabled the number of variables investigated in the experimental work to be reduced to four: injected air volume, water height above the source, surface tension and gravitational acceleration. The experimental work showed that increasing the air volume injected increased the

overall radius of the bubble group with height, which resulted in a rise of the asymptotic value of the entrainment coefficent by 45 percent over the range of air volumes investigated. Increasing the water height above the source had no apparent effect over the range of water heights studied. The effect of reducing the surface tension was immediate and was difficult to quantify; lowering the surface tension drastically changed the size of the bubbles, so that they fell into a regime which could not be compared with the rest of the experimental results. Altering the gravitational acceleration had a definite effect on the buoyancy force of the bubbles and, in general, bubble group radius decreased slightly with increasing **g**-force.

5. The KC-135 microgravity experiments also validated the design of the air injection system by proving that bubbles were being released from the airstone with no initial momentum imparted from the injection process. This meant that the existence of the fluid vortex was due only to the bubbles in the bubble group, and not to the equipment.

6. It was shown that the transition region was longer, which had the effect of slightly increasing the overall bubble group radius, in the small tank because of the proximity of the walls. Thus, it is suggested that the large tank data be used preferentially when working from the database. However, because of the low water heights in the dye injection experiments, it is felt that the small tank data is more accurate, because there was less of an effect on the results of the dye injection process.

7. Because of the marked effect which injected air volume and gravitational acceleration had on the behaviour of the bubble groups, it was inferred that the bubble Reynolds number from Equation (3.13) was the most important dimensionless group in this investigation. The Eötvos number from the same equation was found to be useful only in determining whether the bubbles were dominated by surface tension forces, or by gravity forces.

8. In general, bubble groups were found to have two stages of growth: an initial convective stage where the bubbles circulated with the liquid, and a phase where the bubble group rises to the surface at a speed faster than the still-circulating fluid vortex in its wake. Because of the separation of the two phases, it was found that bubble groups did not fit a single-phase thermal model, as this requires group circulation and constant entrainment throughout the lifetime of the structure. However, it was determined that the entrainment coefficients in the initial stage were of the same order of magnitude, although larger, than the value of 0.25 which is standard for single-phase thermals. Following the vortex separation, the entrainment coefficients for the bubble groups were in the range associated with round bubble plumes. This lends credence to the concept of modelling a blowout plume as a sequential release of bubble groups.

8.1.2 Conclusions from the Theoretical Model

1. A set of equations for the motion of a single bubble travelling against a background flow field of a Hill's spherical vortex and potential flow was derived, working from a general force balance on the bubble. These equations was very similar to the set published previously by the author in Topham *et al.* (1994). However, when rederiving the equations to include the addition of a lift term, an omission of part of the substantive derivative was discovered in the published version. This omission was found to have the effect of changing the radial distance calculated by the model by about 30 percent for the example simulation. It was also found that the addition of the lift force increased the model radial distance even further, with a change of about 100 percent.

2. The model assumes that the Hill's spherical vortex rises upwards at a constant velocity. This assumption was corroborated by the results of the dye injection experiments. This behaviour differs from that seen for single-phase thermals and solid-particle "thermals", which often exhibit a non-uniform translational velocity which is inversely proportional to the square root of the time.

3. The model also assumes the the flow field is axisymmetric, *i.e.* the azimuthal terms in the equations can be neglected. However, this is not necessarily the case. It was concluded that the addition of the other two lift terms to the model might give better results.

4. Because the computer code was written to match the experimental parameters as closely as possible, different values of entrainment coefficient were used within and outside of the fluid vortex, to represent the different values of entrainment coefficient seen before and after the bubbles separated from the moving fluid. However, this methodology provided a very poor match of the simulations with experimental data in the region following separation, and it was found that much better results could be obtained by assuming a constant initial entrainment coefficient throughout the simulation. This indicates that the fluid vortex continues to interact with the bubbles, even after the phases have separated.

5. When model parameters were varied during the simulations, similar results were obtained as was seen in the experiments. An increase in bubble radius led to an increase in bubble group radius, which was similar to the behaviour observed with an increase in bubble group injected air volume. Increasing the level of gravitational acceleration led to a smaller bubble group diameter, which paralleled the lower entrainment coefficients observed at higher g-levels during the KC-135 experiments.

6. As was stated previously, the theoretical model only tracks the path of one individual bubble. In order to get a representative view of a bubble group, the motion a number of bubbles must be calculated using different starting positions but otherwise similar initial conditions, then the group behaviour can be observed by taking a time slice across all of the data sets. For the group simulations discussed herein, a total of 12

points were used, with starting positions spread evenly around the origin. It was found that bubble groups simulated in this manner had similar shapes to the experimental structures, but smaller radii. This was a result of using variable entrainment coefficients during the simulation, as was mentioned previously. As well, the model assumes that the concentration of bubbles in the group is dilute enough that there is no interaction between the bubbles. It is more likely that the trailing wakes behind the bubbles in the experiments interacted, and pushed the bubbles apart, thus leading to a higher radius than would be seen assuming no interaction.

7. There was a height discrepancy between the simulated bubble groups and the actual data, due to the different origins of the simulation and the experiments. This can be resolved easily by taking the experimental data as starting from a theoretical origin, which can be obtained by extending the starting slope of the height-radius plot back to the axis, then matching this theoretical origin to the origin of the simulations.

8. Excellent vertical velocity correlation was found between the model and the experimental data. However, the fit was not as good when plotting the increase in radius with height for the model against the experimental data. As was mentioned previously, it was determined that the fit could be improved by assuming a constant initial entrainment coefficient throughout the simulation. Increasing the lift coefficient also moved the simulation curve outwards, but by a constant amount with

height. However, this solution was deemed to have little physical basis for viability. It was noted that the fit could be improved by either increasing the entrainment coefficient following separation by slightly more than the asymptotic value calculated from the experimental data which was recorded in Table 5.1. Another solution would be the use of a lift coefficient that varied with height. Both of these corrections had the effect of moving the simulation curve outwards without affecting the excellent fit of the vertical velocity term, and both can be explained physically. The increased entrainment coefficient could be due to the effect of bubble interaction over and above the initial effect of the vortex formation. A gradually-increasing lift coefficient could be attributed to an increase in bubble spin as it rises. Increasing the bubble radius was not found to be a viable option, as it increases the vertical as well as the radial velocity.

9. It was suggested that the bubble Reynolds number could be correlated with an increased entrainment coefficient in order to improve the fit of the model to the data. This would be a meaningful solution, as both the bubble Reynolds number derived in the dimensional analysis and the entrainment coefficient after separation increase with increasing air volume injected.

8.2 Recommendations for Future Work

1. To improve the fit of the model, the first step would be to add the other vorticity terms to the lift coefficient to analyze their effect. Following that, the correlation between the bubble Reynolds number and the entrainment coefficient could be pursued, as well as a correlation which would increase the lift coefficient with height above the origin.

2. The initial bubble velocity in the model is also an area worth investigating. It was assumed that the intial velocity was equal to that of the background flow field, but it is possible that another velocity might be appropriate.

3. The dye layering experiments were not accurate enough to get a good indication as to whether or not there was any interaction of the bubble wakes. This line of research could be pursued using a laser light sheet to visualize the flow conditions. The flow around the injector could also be visualized more clearly using this type of apparatus, in conjunction with a high-speed camera such as the HYCAM.

4. The effects of surface tension could be investigated more stringently. Surface tension effects are certain to be present in an actual blowout situation, and thus this topic should be pursued further.

5. An investigation could also be made of the effect on parameters such as the entrainment coefficient when bubble groups are released intermittently. It was observed in the laboratory that this appears to increase the vertical velocity, but has no overall effect on the radial extent of a bubble group. However, if this idea is to be expanded to a plume model, some actual data will be required.

REFERENCES

Auton, T.R., Hunt, J.C.R. and Prod'homme, M., "The Force Exerted on a Body in Inviscid Unsteady Non-uniform Rotational Flow", J. Fluid Mech., 197, 241-257, 1988.

Baines, W.D. and Hopfinger, E.J., "Thermals With Large Density Difference", Atmos. Env., 18, No. 6, 1051-1057, 1984.

Batchelor, G.K., "Heat Convection and Buoyancy Effects in Fluids", Quart. J. Roy. Met. Soc., 80, 339-358, 1954.

Batt, R.G., Bigoni, R.A. and Rowland, D.J., "Temperature-Field Structure Within Atmospheric Buoyant Thermals", J. Fluid Mech., 141, 1-25, 1984.

Benjamin, T.B., "Note on Added Mass and Drift", J. Fluid Mech., 169, 251-156, 1986.

Brown and Root Dev. Inc., *Development of an Engineering and Cost Analysis of a Ship-Mounted Subsurface Collector System*, U.S. Dept. of the Interior, Minerals Management Service, Contract No. 14-12-0001-30135, Vol. 2, 1985.

Bulson, P.S., "The Theory and Design of Bubble Breakwaters", Proc. of the 11th Coastal Eng. Conf., London, England, 2, Part 3, 995-1015, 1968.

Byers, H.R. and Hull, E.C., "Inflow Patterns of Thunderstorms as Shown by Winds Aloft", Bull. Amer. Met. Soc., 30, 90-96, 1949.

Cerasoli, C.P., "Experiments on Buoyant Parcel Motion and the Generation of Internal Gravity Waves", J. Fluid Mech., 86, 247-271, 1978.

Clift, R., Grace. J.R. and Weber, M.E., *Bubbles, Drops and Particles*, Academic Press, New York, 1978.

Darwin, C., "Note on Hydrodynamics", Proc. Camb. Phil. Soc., 49, 342-354, 1953.

Davidson, J.F. and Schuler, B.O.G., "Bubble Formation at an Orifice in an Inviscid Liquid", Trans. Inst. Chem. Eng., 38, 335-342, 1960.

Davies, R.M. and Taylor, G.I., "The Mechanics of Large Bubbles Rising Through Extended Liquids and Through Liquids in Tubes", Proc. Roy. Soc. A, 200, 375-390, 1950.

Edge, B.L. and Dysart, B.C., *Transport Mechanisms Governing Sludges and Other Materials Barged To Sea*, Report of the Departments of Civil and Environmental Systems Engineering, Clemson University, 1972.

Escudier, M.P. and Maxworthy, T., "On the Motion of Turbulent Thermals", J. Fluid Mech., 61, 541-552, 1973.

Fannelop, T.K., "Laboratory Experiments With Bubble Plumes", Proc. 2nd Sub-sea Containment Workshop, Oslo, Norway, 77-108, 1982.

Fohl, T., "Turbulent Effects in the Formation of Buoyant Vortex Rings", J. Appl. Phys., 38, 4097-4098, 1968.

Fraser, J., "Observations of Small-scale Bubble Interactions", Report of Physics Co-op Summer Work Project, Institute of Ocean Sciences, Sidney, B.C., 1981.

Griffiths, R.W., "Thermals in Extremely Viscous Fluids, Including the Effects of Temperature-dependent Viscosity", J. Fluid Mech., 166, 115-138, 1986.

Harper, J.F. and Moore, D.W., "The Motion of a Spherical Liquid Drop at High Reynolds Numbers", J. Fluid Mech., 32, 367-391, 1968.

Hayes, W.B., Hardy, B.W. and Holland, C.D., "Formation of Gas Bubbles at Submerged Orifices", AICHE J., 5, No. 3, 319-324, 1959.

Ivicsics, L., *Hydraulic Models*, Water Resources Publications, Ft. Collins, Colorado, 1974.

Johari, H., *An Experimental Investigation in Mixing in Buoyant Flows*, Ph.D. Thesis, University of Washington, Washington, 1989.

Johari, H. and Briedenthal, R., "Chemically Reacting Thermals with Buoyancy Reversal", 3rd Int. Symp. on Strat. Flow, Caltech, Calif., Feb. 3-5, 1987.

Kiya, M., Ohyama, M. and Hunt, J.C.R., "Vortex Pairs and Rings Interacting with Shear-layer Vortices", J. Fluid Mech., 172, 1-15, 1986.

Kobus, H.E., "Analysis of the Flow Induced by Air-bubble Systems", Proc. of the 11th Coastal Eng. Conf., London, England, 2, Part 3, 1016-1031, 1968.

Koh, R.C.Y. and Chang, Y.C., *Mathematical Model for Barged Ocean Disposal of Wastes*, United States Environmental Protection Agency Report No. EPA-660/2-73-029, 1973.

Kowe, R., Hunt, J.C.R., Hunt, A., Couet, B. and Bradbury, L.J.S., "The Effects of Bubbles on the Volume Fluxes and the Pressure Gradients in Unsteady and Non-uniform Flow of Liquids", Int. J. Multiphase Flow, 14, 587-606, 1988.

Krevelen, D.W. and Hoftijzer, P.J., "Studies of Gas-bubble Formation: Calculation of Interfacial Area in Bubble Contractors", Chem. Eng. Progress, 46, No. 1, 29-35, 1950.

Krishnappan, B.G., *Dispersion of Granular Material Dumped in Deep Water*, Scientific Series No. 55, Information Canada, Ottawa, 1975.

Lamb, H., *Hydrodynamics*, 6th Ed., Dover Publications, New York, 1932.

Laureshen, C.J., "Bubble Group Experiments: Further Study in NASA KC-135", Test Equipment Data Package for NRC Space Division and NASA, 52 p., 1989.

Laureshen, C.J., "The Behaviour of Bubble Groups: An Experimental Study", Proc. 23rd Cong. Intl. Ass. Hydraulic Res. (IAHR), Ottawa, Ontario, Aug. 21-25, S, 67-74, 1989.

Laureshen, C.J., *Dynamics of Bubble Groups: Raw Data*, Department of Mechanical Engineering Report No. 468, University of Calgary, 1992.

Laureshen, C.J. and Rowe, R.D., "A User's Manual for the One-component Laser-doppler Anemometer", Department of Mechanical Engineering, University of Calgary, Report No. 375, 76 p., 1986.

Laureshen, C.J. and Rowe, R.D., "Bubble Group Behaviour Under Microgravity Conditions Applied to Subsea Blowout Plume Modelling", Proc. 12th Arctic and Marine Oilspill Technical Seminar (AMOP), Calgary, Alberta, June 7-9, 23-31, 1989.

Lee, Y.G., *An Investigation of the Dynamics of Solid Particle Thermals*, M.Sc. Thesis, Department of Mechanical Engineering, University of Calgary, Calgary, Alberta, 1992.

Levine, J., "Spherical Vortex Theory of Bubble-like Motion in Cumulus Clouds", J. Meteorol., 16, 653-662, 1959.

Lin, S.C., Tsang, L. and Wang, C.P., "Temperature Field Structure in Strongly Heated Buoyant Thermals", Phys. Fluids, 15, No. 12, 2118-2128, 1972.

Luketina, D. and Wilkinson, D., "Particle Clouds in Density Stratified Environments", Proc. of the 4th Int. Symp. on Stratified Flows, Vol. 2, 1994.

Maxey, M.R., "The Motion of Small Spherical Particles in a Cellular Flow Field", Phys. Fluids, 30, 1915-1928, 1987.

Maxey, M.R. and Riley, J.J., "Equation of Motion for a Small Rigid Sphere in a Nonuniform Flow", Phys. Fluids, 26(4), 883-889, 1983.

Maxworthy, T., "The Structure and Stability of Vortex Rings", J. Fluid Mech., 51, 15-32, 1972.

Maxworthy, T., "Turbulent Vortex Rings", J. Fluid Mech., 64, 227-239, 1974.

Maxworthy, T., "Some Experimental Studies of Vortex Rings", J. Fluid Mech., 81, 465-495. 1977.

Mei, R., "An Approximate Expression for the Shear Lift Force on a Spherical Particle at Finite Reynolds Number", Intl. J. Multiphase Flow, 18, 145-147, 1992.

Mei, R., Lawrence, C.J. and Adrian, R.J., "Unsteady Drag on a Sphere at Finite Reynolds Number with Small Fluctuations in the Free-Stream Velocity", J. Fluid Mech., 233, 613-631, 1991.

Milgram, J. and Erb, P.R., "How Floaters Respond to Subsea Blowouts", Pet. Eng. Intl., 56, No. 7, 64-72, 1984.

Moore, D.W., "The Boundary Layer on a Spherical Gas Bubble", J. Fluid Mech., 16, 161-176, 1962.

Morton, B.R., "Weak Thermal Vortex Rings", J. Fluid Mech., 9, 107-118, 1960.

Morton, B.R., Taylor, G.I. and Turner, J.S., "Turbulent Gravitational Convection from Maintained and Instantaneous Sources", Proc. Roy. Soc. A, 234, 1-23, 1956.

Nakatsuji, K., Tamai, M. and Murota, A., "Dynamic Behaviours of Sand Cloud in Water", Proc. of the Int. ASCE/IAHR Conf. on Phys. Modelling of Transport and Diffusion, M.I.T., 1990.

Namias, J., "On the Dissipation of Tall Cumulus Clouds", Mon. Wea. Rev., 67, 294-296, 1939.

Noh, Y. and Fernando, H.J.S., "The Transition in the Sedimentation Pattern of a Particle Cloud", Phys. Fluids, 3049-3055, 1993.

Norbury, J., "A Family of Steady Vortex Rings", J. Fluid Mech., 57, 417-431, 1973.

Oliver, D.L.R. and Chung, J.N., "Flow about a Fluid Sphere at Low to Moderate Reynolds Numbers", J. Fluid Mech., 177, 1-18, 1987.

Overcamp, T.J., "Interaction of Line Thermal Pairs", Proc. 6th Symposium of Turb. and Diff., Amer. Met. Soc., Boston, Mass., 337-340, 1983.

Poon, J.Y.C., *Modelling of Bubble Plumes*, M. Sc. Thesis, Department of Mechanical Engineering, University of Calgary, Calgary, Alberta, 1985.

Pozrikidis, C., "The Nonlinear Instability of Hill's Vortex", J. Fluid Mech., 168, 337-367, 1986.

Priestley, C.H.B., "Convection from a Large Horizontal Surface", Australian J. Phys., 7, 176-201, 1954.

Reeks, M.W. and McKee, S., "The Dispersive Effects of Basset History Forces on Particle Motion in a Turbulent Flow Field", Phys. Fluids, 27, 1573-1582, 1984.

Reuter, G.W., "A Historical Review of Cumulus Entrainment Studies", Bull. Amer. Met. Soc., 67, No. 2, 151-154, 1986.

Reutsch, G.R. and Meiberg, E., "On the Motion of Small Spherical Bubbles in Two-Dimensional Vortex Flow", Phys. Fluids, 5, 2326-2341, 1993.

Reynolds, O., "On the Resistance Encountered by Vortex Rings, and the Relation Between the Vortex Rings and the Streamlines of a Disc", Nature, 14, 477-479, 1876.

Richards, J.M., "Experiments on the Penetration of an Interface by Buoyant Thermals", J. Fluid Mech., 11, 369-384, 1961.

Rowe, R.D., Poon, J.Y.C. and Laureshen, C.J., "A Simple Method for Predicting Bubble Plume Properties", Proc. 23rd Cong. Intl. Ass. Hydraulic Res. (IAHR), Ottawa, Ontario, Aug. 21-25, D, 23-30, 1989.

Rowe, R.D. and Topham, D.R., "The Application of Reduced Scale Tests for a Subsea Containment System to a Hypothetical Blowout Case", Proc. 2nd Subsea Containment Workshop, Oslo, Norway, 33-77, 1982.

Saffman, P.G., "The Velocity of Viscous Vortex Rings", Studies Appl. Math., 49, 371-380, 1970.

Sánchez, O., Raymond, D.J., Libersky, L. and Petschek, A.G., "The Development of Thermals from Rest", J. Atmos. Sci., 46, No. 14, 2280-2292, 1989.

Saunders, P.M., "Penetrative Convection in Stably Stratified Fluids", Tellus, 14, 177-194, 1962.

Scorer, R.S., "Experiments on Convection of Isolated Masses of Buoyant Fluid", J. Fluid Mech., 2, 583-594, 1957.

Scorer, R.S., *Natural Aerodynamics*, Pergamon Press, London, England, 1958.

Scorer, R.S. and Ludlam, F.H., "Bubble Theory of Penetrative Convection", Quart. J. Roy. Met. Soc., 79, 94-103, 1953.

Scorer, R.S. and Ronne, C., "Experiments with Convection Bubbles", Weather, 11, 151-154, 1956.

Sene, K.J., Hunt, J.C.R. and Thomas, N.H., "The Role of Coherent Structures in Bubble Transport by Turbulent Shear Flows", J. Fluid Mech., 259, 219-240, 1994.

Silberman, E., "Production of Bubbles by the Disintegration of Gas Jets in Liquids", 5th Midwestern Conf. on Fluid Mech., 263-284, 1957.

Simpson, J., "Cumulus Clouds: Early Aircraft Observations and Entrainment Hypotheses", *Mesoscale Meteorology - Theories, Observations and Models*, Ed. Lilly, R.K. and Gal-Chen, T., D. Reidel Publishing Company, 355-373, 1983.

Stommel, H., "Entrainment of Air into a Cumulus Cloud", J. Meteorol., 4, 91-94, 1947.

Taylor, G.I., "The Formation of a Blast Wave by a Very Intense Explosion", Proc. Roy. Soc. A, 201, 159-186, 1950.

Tekeli, S. and Maxwell, W.H.C., "Behaviour of Air Bubble Screens", Report No. 33, Department of Civil Engineering, University of Illinois, 1978.

Telford, J.W., "The Convective Mechanism in Clear Air", J. Atmos. Sci., 23, 652-666, 1966.

Thomas, R.M., "Bubble Coalescence in Turbulent Flows", Int. J. Multiphase Flow, 7, No. 6, 709-717, 1981.

Thomson, J.J., *A Treatise on the Motion of Vortex Rings*, Macmillan and Co., London, England, 1883.

Tio, K.K., Linan, A., Lasheras, J.C. and Ganan-Calvo, A.M., "On the Dynamics of Buoyant and Heavy Particles in a Periodic Stuart Vortex Flow", J. Fluid Mech., 254, 671-199, 1993.

Topham, D.R., Institute of Ocean Sciences, Sidney, B.C., Private Communication, 1983.

Topham, D.R., Clements, R.M. and Smy, P.R., "Turbulent Mixing in a Pulsed Plasma-jet Exhaust", J. Fluid Mech., 148, 207-224, 1984.

Topham, D.R., Laureshen, C.J., Lee, Y.G. and Rowe, R.D., "The Dynamics of Solid Particle and Bubble Groups", Paper No. 14-TP-24, *Heat Transfer 1994*, Proc. of The Tenth International Heat Transfer Conference, Brighton, UK, Vol. 6, G.F. Hewitt, Ed., 283-288, 1994.

Tritton, D.J., *Physical Fluid Dynamics*, 2nd Ed., Oxford University Press, New York, USA, 1988.

Tsang, G., "Modelling Criteria for Bubble Plumes - A Theoretical Approach", Can. J. Civil Eng., 11, 293-298, 1984.

Turner, J.S., "Buoyant Vortex Rings", Proc. Roy. Soc. A, 239, 61-75, 1957.

Turner, J.S., "A Comparison Between Buoyant Vortex Rings and Vortex Pairs", J. Fluid Mech., 7, 419-432, 1960a.

Turner, J.S., "On the Intermittent Release of Smoke from Chimneys", J. Mech. Eng. Sci., 2, No. 2, 97-100, 1960b.

Turner, J.S., "Model Experiments Relating to Thermals with Increasing Buoyancy", Quart. J. Roy. Met. Soc., 89, 62-74, 1963a.

Turner, J.S., "The Motion of Buoyant Elements in Turbulent Surroundings", J. Fluid Mech., 16, 1-16, 1963b.

Turner, J.S., "The Flow into an Expanding Spherical Vortex", J. Fluid Mech., 18, 195-208. 1964a.

Turner, J.S., "The Dynamics of Spheroidal Masses of Buoyant Fluid", J. Fluid Mech., 19, 481-490, 1964b.

Turner, J.S., "Buoyant Plumes and Thermals", Ann. Rev. Fluid Mech., 1, 29-44, 1969.

Turner, J.S., *Buoyancy Effects in Fluids*, Cambridge University Press, Cambridge, UK, 1973.

Turner, J.S., "Turbulent Entrainment: the Development of the Entrainment Assumption, and its Application to Geophysical Flows", J. Fluid Mech., 173, 431-471, 1986.

Wallis, G.B., *One-Dimensional Two-Phase Flow*, McGraw Hill, New York, 1969.

Wallis, G.B., "The Terminal Speed of Single Drops or Bubbles in an Infinite Medium", Int. J. Multiphase Flow, 1, 491-511, 1974.

Walters, J.K. and Davidson, J.F., "The Initial Motion of a Gas Bubble Formed in an Inviscid Liquid", J. Fluid Mech., 12, 408-416, 1962.

Wang, C.P., "Motion of an Isolated Buoyant Thermal", Phys. Fluids, 14, 1643-1647, 1971.

Wegener, P.P. and Parlange, J.Y., "Spherical-Cap Bubbles", Ann. Rev. Fluid Mech., 11, 79-100, 1973.

Widnall, S.E. and Sullivan, J.P., "On the Stability of Vortex Rings", Proc. Roy. Soc. A, 332, 335-353, 1973.

Wilkinson, D.L., "Two-Dimensional Bubble Plumes", ASCE J. of the Hydraulics Div., 105, HY2, 139-154, 1979.

Woodward, B., "The Motion In and Around Isolated Thermals", Quart. J. Roy. Met. Soc., 85, 144-151, 1959.

Yamada, H. and Matsui, T., "Mutual Slip-through of a Pair of Vortex Rings", Phys. Fluids, 22, 1245-1249, 1979.

Yeomans, M., *Modelling of Solid Particle Thermals*, M.Sc. Thesis, Department of Mechanical Engineering, University of Calgary, Calgary, Alberta, 1997.

Yip, K.C., *The Motion of Small Air Bubbles Rising in Stagnant and Flowing Water*, M.Sc. Thesis, Department of Mechanical Engineering, University of Calgary, Alberta, 1966.

APPENDIX A

CALIBRATION AND ERROR ANALYSIS FOR LABORATORY AIR INJECTION SYSTEM

The air injection system used in the small and large tank laboratory tests was shown in Figure 4.1. The volume of air injected in each bubble group was calculated using the pressure change in the control volume, which was the portion of the pressurized air system between the solenoid and shutoff valves and the mercury manometer. A necessary requirement to this calculation was a knowledge of the size of the control volume.

A calibrated volume V_c was determined using the difference between the weight of a steel sample cylinder and a length of tygon tubing when empty, and that when the same items were full of water. The volume included portions of the valves which were used to seal either end of the system. The volume was calibrated by dividing the weight of the water by its density at room temperature. The calibrated volume was then attached to the control volume, as is shown in Figure A.1.

Because the height of the mercury in the manometer changed with pressure, the size of the control volume was determined to the zero-mark on the manometer. The actual volume of air in the control volume before and after the air injection could then be calculated knowing the height of the mercury column from zero (Δh_B). The actual calculation of the control volume size required an iterative procedure, since the system could not be filled with water and weighed without ruining the manometer. Initially, with Valves V1, V2 and V3 open and Valves V4 and V5 shut, both the calibrated and control volumes were pressurized

to the calibration pressure p_c. Then, with Valves V1 and V3 shut, p_c (the difference between the left- and right-hand sides of the manometer) was measured. Valve V5 was opened to equalize the manometer, and then closed. Opening Valve V3 repressurized the control volume and a new reading was taken after the pressure equalized and Valve V3 was closed. Valve V5 was again opened to equalize the manometer, and then closed. These two steps were repeated until the calibrated volume was depleted, with the previous pressure reading becoming the new p_c.

The following equation was used to solve for the control volume V_s and the area of the manometer A:

$$p_c V_c + p_{at} (V_s + A \Delta h_{B1}) = p_2 (V_c + V_s + A \Delta h_{B2}) \qquad \textbf{(A.1)}$$

where p_{at} is the atmospheric pressure. Because of the length of this calculation, the procedure was repeated with Valve V5 hooked up to a vacuum pump so that the second term on the left-hand side of Equation (A.1) could be eliminated. Finally, after five repetitions of the entire procedure to ensure accurate results, the control volume was determined to be 5.138×10^{-5} m^3 and the manometer area to be 2.2×10^{-5} m^2.

Knowing these values, the volume of air injected per burst could then be determined so long as the atmospheric pressure p_{at} (mm Hg), the room temperature T_{rm} (°C), and the initial and final pressures in the control volume were known. The pressures could be calculated using the heights of the mercury columns in the manometer before and after injection: Δh_{A1} and Δh_{B1} ("Hg), and Δh_{A2} and Δh_{B2} ("Hg). The final form of the equation

used to calculate the air volume in cubic metres at standard atmospheric conditions, including all of the appropriate conversion factors, was:

$$V_T = \frac{273.15}{(T_{rm} - 273.15)} \cdot \frac{1}{101.325} \left([133.3\, p_{at} - 3386.5\, (\Delta h_A - \Delta h_B)_1\,] \cdot [0.6\Delta h_{A1} - 51.4] - [133.3 p_{at} - 3386.5(\Delta h_A - \Delta h_B)_2\,] \cdot [0.6\Delta h_{A2} - 51.4\,] \right) \times 10^{-6} \qquad \textbf{(A.2)}$$

The resolution of the mercury manometer of the control volume was 0.1" Hg, the atmospheric pressure was read from a barometer with a resolution of 1.0 mm Hg, and the room temperature from a thermometer which could be read to the nearest degree Celsius.

An error analysis conducted on Equation (A.2) using a test run in the large tank with a water height of 1.20 m gave an accuracy of ± 0.3 percent on the volume calculation. In other words, the injected air volume for that particular run was $1.40 \times 10^{-5} \pm 4.0 \times 10^{-8}$ m³ with a 95 percent confidence level. An average of similar analyses for a sample of 25 large and small tank volume calculations yielded the same result. Thus, all of the volumes given in the data sets may safely be assumed to be within a range of ± 1.0 percent accuracy.

It should be noted that Equation (A.2) is independent of water depth in the tank. Although there is a pressure at the injector which is the sum of the atmospheric pressure plus the hydrostatic head for a given water depth, the desired air volume to be injected could always be achieved by increasing or decreasing the pressure on the air supply side using the regulator (see Figure 4.1) to account for increased or decreased hydrostatic pressure due to a difference in water depth. As long as the correct height differences in the mercury columns were achieved, the injected air volumes were correct.

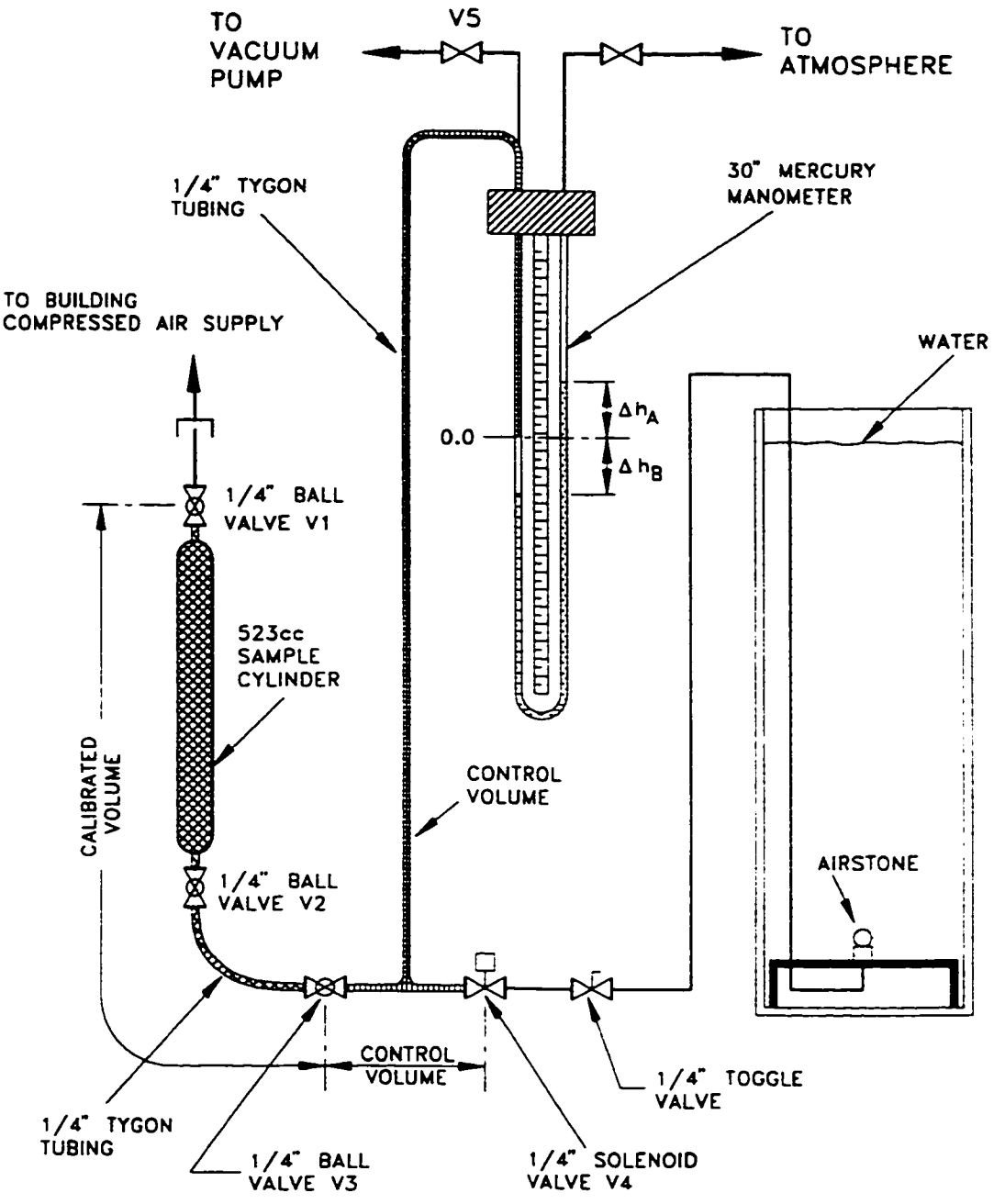

FIGURE A.1 - Schematic of Control Volume Calibration Apparatus

APPENDIX B

TESTING AND ERROR ANALYSIS FOR KC-135 AIR INJECTION SYSTEM

The pressure test and leak check on the pressurized air system of the KC-135 apparatus, which included all components between feed quick connector QC8 and toggle valve V1 as shown on Figure 4.7, were performed simultaneously using helium gas as the pressurizing medium. The system was pressurized with helium and the fittings were checked for leaks using a Varian Model 938-41 "Porta-Test" helium mass spectrometer leak detector which was operated in the "sniffing mode". Leak checks were performed at 46.4, 76.7 and 129.4 psia (measured on the Endevco 8531-100 pressure transducer PT3 which had a range of 0 to 100 psia operating on factory calibration) and the system was found to be free of leaks. Helium was vented to reduce the pressure to the normal operating range and the system remained pressurized overnight. As the pressure remained constant, the integrity of the system was confirmed.

Helium was then bled from the system and the apparatus was recharged with compressed air. The system was left charged for three days and a small pressure drop of 0.4 psia was recorded. This drop was attributed to a temperature change in the laboratory over the period of the test.

The entire contents of the pressurized air system was then discharged through valve V1 so as to pressurize the bubble chamber and air plenum. The pressure readings for the bubble chamber plenum were recorded on pressure gauge PC11 (a Marsh W0274 pressure

gauge with a range of 0 to 3 psig), and a drop of 0.21 psig was observed over a four-hour time period. This was due to air being dissolved in the water. The pressure level selected for testing the bubble chamber and plenum was based on the highly unlikely condition of a total discharge of the entire gas volume from the pressurized air system, thus representing the highest pressure which could develop in the plenum chamber due to the accumulation of free gas.

Because it was recognized that the chamber windows could be exposed to a higher effective pressure if the above condition was combined with the design requirement of a 2.5 **g** acceleration at pull-up and pull-out, one further test was performed. Since it was not possible to generate the exact force distribution which the window would experience during the high-gravity period, the test procedure adopted was to set the plenum pressure at the maximum pressure which would be experienced at the midpoint of the tank. The plenum gauge PG11 and relief valve PRV12 were removed and a calibrated pressure transducer installed on the plenum. Air was injected into the plenum to develop a pressure of 3.85 psig and the chamber was allowed to stand for 15 minutes under this condition. A pressure rise of 0.07 psig was observed over the test period, but the system was not otherwise affected.

The two pressure gauges and the pressure transducer used in the pressurized air system were calibrated to confirm the factory calibrations. The tests were performed using a compressed air bottle, a 60 psig regulator and a 30" mercury manometer which was part of the pressurized air system in the laboratory 1.0 **g** experimental apparatus. The Marsh W'0274 pressure gauge PG11 was found to be accurate within +0.10 psig at the top end of its range, and within +0.01 psig in the usual working range of the instrument. The 3D

Instruments 25544-22B25 pressure gauge (PG10) tested accurately within +0.05 psig in its normal working range of 0 to 30 psig (the gauge had a total range of 0 to 60 psig).

The factory calibration on the Endevco 8531-100 pressure transducer PT3 was 3.55 mV/psi. The calibration was checked with the manometer in the range from 0 to 30 psig, and with the 3D pressure gauge in the range from 0 to 60 psig, by spanning the entire range and calibrating using trial and error. The result obtained in this manner was 3.544 mV/psi, which was very close to the factory calibration. The discrepancy may be accounted for because of the differences in the local conditions (the transducer was factory-calibrated in California) and in the prime calibration device.

The size of the control volume was determined directly by removing it from the pressurized air system, weighing it empty and then weighing it full of water. The volume was calibrated by dividing the weight of the water by its density at room temperature, which resulted in a value of 5.244×10^{-5} m³.

The volume of air injected per burst could then be determined using the following equation so long as the pressure before injection p_1 (psia), the pressure after the release of the bubble group p_2 (psia) and the ambient temperature T_{rm} (°C) were known:

$$V_T = \frac{(p_1 - p_2)}{14.696} \cdot \frac{273.15}{T_{rm} + 273.15} \cdot 52.44 \times 10^{-6} \qquad \textbf{(B.1)}$$

Equation (B.1) gives the injected air volume in m³ at standard atmospheric conditions. This expression is basically the same as Equation (A.1), but is simpler due to the fact that the control volume was a constant size and was not changing with the pressure change on the

manometer. The pressure data was read from the control volume pressure transducer, which had a resolution of 0.1 psia, and the temperature data was determined from readings taken in the aircraft cabin by NRC Space Division. Figure B.1 is typical of the readouts supplied by NRC, and it has been assumed that the values calculated from these graphs are accurate to approximately 0.3 °C.

An error analysis conducted on the above equation using the data from Parabola 1 on the March 14, 1989 KC-135 flight gave an accuracy of ± 2.4% on the volume calculation. In other words, the injected air volume for that parabola was $1.00 \times 10^{-5} \pm 2.4 \times 10^{-7}$ m³ with a 95% confidence level. Similar calculations for the 8.00×10^{-6} m³ runs from that day gave an accuracy of ± 2.9% on average. For all of the data sets actually used from the KC-135 tests, the volumes given can be taken to be accurate within ± 3.0%.

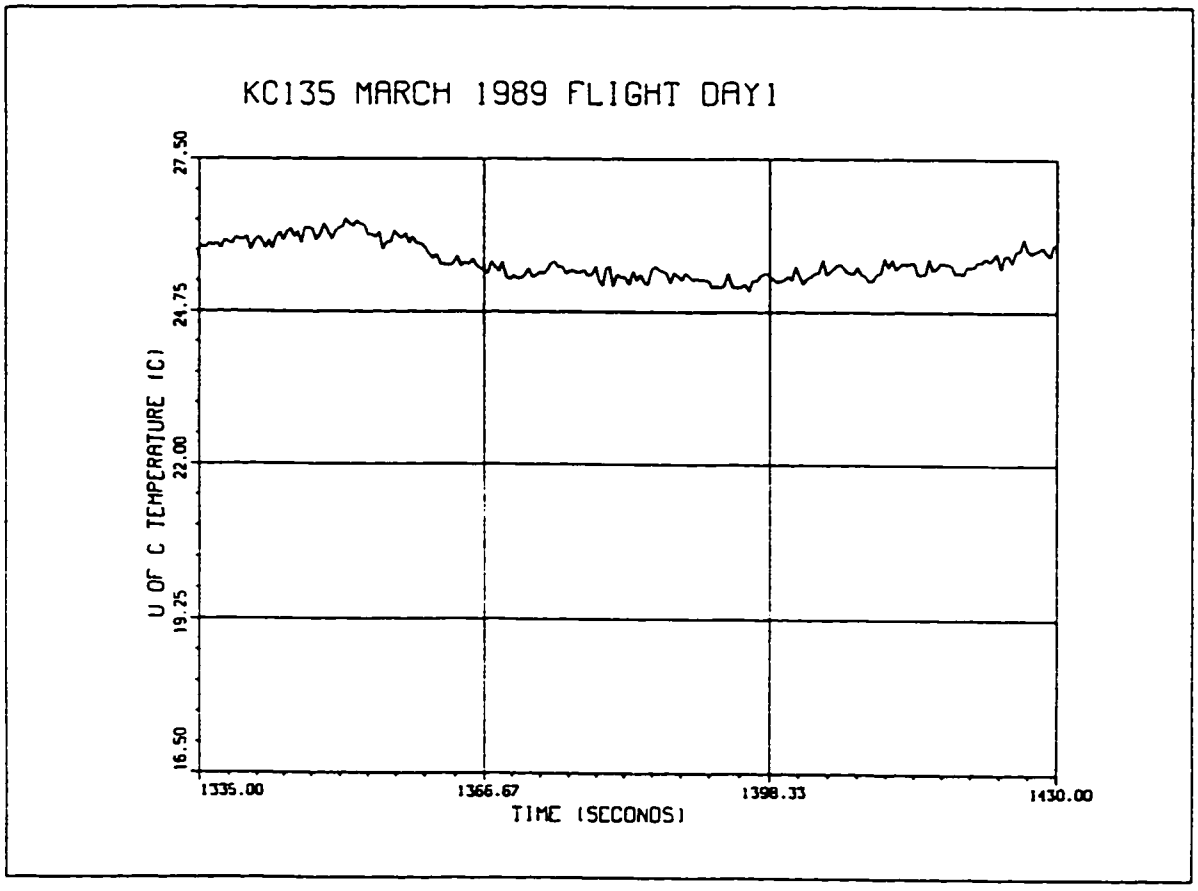

FIGURE B.1 - Typical Temperature Data (KC-135 Experiments)

APPENDIX C

SAMPLES OF SCIENTIST COMPUTER CODE

C.1 Uniform Speed Bubble Model Using Topham *et al.* Equations and Variable α

```
// Uniform Speed Original Bubble Model
IndVars: T
DepVars: A, B, R, Z, BETA, GAM, UFR, UFZ, UBR, UBZ, FD, REB
Params: ALPHA1, ALPHA2, U, VIS, RB, G, RHOF, RHOG
//
//Simplifying Equations
//
MF=RHOF*(4./3)*PI*RB^3
MB=RHOG*(4.3)*PI*RB^3
C1=1./(MB+0.5*MF)
C2=(MB-MF)*G
C3=6.*PI*VIS*RB
C4=1.5*MF
//
A=ABS(ALPHA1*U*T)
EPS=SQRT(R^2+Z^2)
FLAG=UNIT(A-EPS)
TAU=IFGTZERO(FLAG,T,0)
B=ABS(ALPHA2*U*(T-TAU))
//
//Fluid Vortex Equations
//
//Radial Equations:  UFR1 is Internal, UFR2 is External to Fluid Vortex
UFR1=(3.*U*R*(Z))/(2*A^2)
UFR2=(3.*U*R*Z*(ALPHA1*U*TAU)^3)/(2.*(Z^2+R^2)^(5./2.))+(3.*U*R*Z*B^3)/
(2*(Z^2+R^2)^(5./2.))
UFR=UFR2*(1-FLAG)+UFR1*FLAG
//
//Height Equations: UFZ1 is Internal, UFZ2 is External to Fluid Vortex
UFZ1=((-3.*U)/(2.*A^2))*(2.*R^2+(Z)^2-A^2)
UFZ2=(-U*((ALPHA1*U*TAU)^3*(R^2-2*Z^2))/(2*(Z^2+R^2)^(5/2)))+
(-U*(1+(B^3*(R^2-2*Z^2))/(2*(Z^2+R^2)^(5/2))))
UFZ=UFZ2*(1-FLAG)+UFZ1*FLAG
//
//Bubble Reynolds Number
```

```
REB=(RHOF*2.*RB*ABS(U-SQRT(UBZ^2+UBR^2)))/VIS
//
//Drag Force Correction
FD=1.+0.1315*REB^(0.82-0.05*LOG10(REB))
//
//Bubble Equations
//
//Radial Direction
UBR'=C1*(C3*FD*(UFR-UBR)+C4*(DERIV(UFR,T)+UFR*DERIV(UFR,R)))
R'=UBR
//
//Height Direction (z-direction)
UBZ'=C1*(C2+C3*FD*(UFZ-UBZ)+C4*(DERIV(UFZ,T)+UFZ*DERIV(UFZ,Z)))
Z'=UBZ
//
//Dimensionless Variables
//
BETA1=R/A
BETA2=R/(B-ALPHA1*U*TAU)
BETA=BETA2*(1-FLAG)+BETA1*FLAG
GAM=Z/A
//
//Parameter Values and Constraints
U=12.3
ALPHA1=0.36
ALPHA2=0.073
G=-981
VIS=0.01
RB=0.13
RHOF=0.99829
RHOG=0.00122
//
//Initial Conditions
R=1.3
Z=0
UBR=12.3
UBZ=0
0.5<T<1
***
```

C.2 Uniform Speed Bubble Model , Revised Substantive Derivative, Variable α

```
// Uniform Speed Bubble Model with Revised Substantive Derivative Term
IndVars: T
DepVars: A, B, R, Z, BETA, GAM, UFR, UFZ, UBR, UBZ, FD, REB
Params: ALPHA1, ALPHA2, U, VIS, RB, G, RHOF, RHOG
//
//Simplifying Equations
//
MF=RHOF*(4./3)*PI*RB^3
MB=RHOG*(4.3)*PI*RB^3
C1=1./(MB+0.5*MF)
C2=(MB-MF)*G
C3=6.*PI*VIS*RB
C4=1.5*MF
//
A=ABS(ALPHA1*U*T)
EPS=SQRT(R^2+Z^2)
FLAG=UNIT(A-EPS)
TAU=IFGTZERO(FLAG,T,0)
B=ABS(ALPHA2*U*(T-TAU))
//
//Fluid Vortex Equations
//
//Radial Equations:  UFR1 is Internal, UFR2 is External to Fluid Vortex
UFR1=(3.*U*R*(Z))/(2*A^2)
UFR2=(3.*U*R*Z*(ALPHA1*U*TAU)^3)/(2.*(Z^2+R^2)^(5./2.))+(3.*U*R*Z*B^3)/
(2*(Z^2+R^2)^(5/2))
UFR=UFR2*(1-FLAG)+UFR1*FLAG
//
//Height Equations: UFZ1 is Internal, UFZ2 is External to Fluid Vortex
UFZ1=((-3.*U)/(2.*A^2))*(2.*R^2+(Z)^2-A^2)
UFZ2=(-U*((ALPHA1*U*TAU)^3*(R^2-2*Z^2))/(2*(Z^2+R^2)^(5/2)))+
(-U*(1+(B^3*(R^2-2*Z^2))/(2*(Z^2+R^2)^(5/2))))
UFZ=UFZ2*(1-FLAG)+UFZ1*FLAG
//
//Bubble Reynolds Number
REB=(RHOF*2.*RB*ABS(U-SQRT(UBZ^2+UBR^2)))/VIS
//
//Drag Force Correction
FD=1.+0.1315*REB^(0.82-0.05*LOG10(REB))
//
//Bubble Equations
```

```
//
//Radial Direction
UBR'=C1*(C3*FD*(UFR-UBR)
+C4*(DERIV(UFR,T)+UFR*DERIV(UFR,R)+UFZ*DERIV(UFR,Z)))
R'=UBR
//
//Height Direction (z-direction)
UBZ'=C1*(C2+C3*FD*(UFZ-UBZ)
+C4*(DERIV(UFZ,T)+UFZ*DERIV(UFZ,Z)+UFR*DERIV(UFZ,R)))
Z'=UBZ
//
//Dimensionless Variables
//
BETA1=R/A
BETA2=R/(B-ALPHA1*U*TAU)
BETA=BETA2*(1-FLAG)+BETA1*FLAG
GAM=Z/A
//
//Parameter Values and Constraints
U=12.3
ALPHA1=0.36
ALPHA2=0.073
G=-981
VIS=0.01
RB=0.13
RHOF=0.99829
RHOG=0.00122
//
Initial Conditions
R=1.3
Z=0
UBR=12.3
UBZ=0
0.5<T<1
...
```

C.3 Revised Uniform Speed Bubble Model with Lift Term and Variable α

```
// Uniform Speed Bubble Model with Lift Term and Variable ALPHA
IndVars: T
DepVars: A, B, R, Z, BETA, GAM, UFR, UFZ, UBR, UBZ
```

```
Params: ALPHA1, ALPHA2, U, VIS, RB, G, RHOF, RHOG
//
//Simplifying Equations
//
MF=RHOF*(4./3)*PI*RB^3
MB=RHOG*(4.3)*PI*RB^3
C1=1./(MB+0.5*MF)
C2=(MB-MF)*G
C3=6.*PI*VIS*RB
C4=1.5*MF
C5=0.5*MF
//
A=ABS(ALPHA1*U*T)
EPS=SQRT(R^2+Z^2)
FLAG=UNIT(A-EPS)
TAU=IFGTZERO(FLAG,T,0)
B=ABS(ALPHA2*U*(T-TAU))
//
//Fluid Vortex Equations
//
//Radial Equations:  UFR1 is Internal, UFR2 is External to Fluid Vortex
UFR1=(3.*U*R*(Z))/(2*A^2)
UFR2=(3.*U*R*Z*(ALPHA1*U*TAU)^3)/(2.*(Z^2+R^2)^(5./2.))+(3.*U*R*Z*B^3)/
(2*(Z^2+R^2)^(5/2))
UFR=UFR2*(1-FLAG)+UFR1*FLAG
//
//Height Equations: UFZ1 is Internal, UFZ2 is External to Fluid Vortex
UFZ1=((-3.*U)/(2.*A^2))*(2.*R^2+(Z)^2-A^2)
UFZ2=(-U*((ALPHA1*U*TAU)^3*(R^2-2*Z^2))/(2*(Z^2+R^2)^(5/2)))+
(-U*(1+(B^3*(R^2-2*Z^2))/(2*(Z^2+R^2)^(5/2))))
UFZ=UFZ2*(1-FLAG)+UFZ1*FLAG
//
//Bubble Reynolds Number
REB=(RHOF*2.*RB*ABS(U-SQRT(UBZ^2+UBR^2)))/VIS
//
//Drag Force Correction
FD=1.+0.1315*REB^(0.82-0.05*LOG10(REB))
//
//Bubble Equations
//
//Lift Term
LF=DERIV(UFR,Z)-DERIV(UFZ,R)
//
```

```
//Radial Direction
UBR'=C1*(C3*FD*(UFR-UBR)+C4*(DERIV(UFR,T)
+UFR*DERIV(UFR,R)+UFZ*DERIV(UFR,Z))-C5*(UFZ-UBZ)*LF)
R'=UBR
//
//Height Direction (z-direction)
UBZ'=C1*(C2+C3*FD*(UFZ-UBZ)+C4*(DERIV(UFZ,T)
+UFZ*DERIV(UFZ,Z)+UFR*DERIV(UFZ,R))-C5*(UFR-UBR)*LF)
Z'=UBZ
//
//Dimensionless Variables
//
BETA1=R/A
BETA2=(R*(1-ALPHA2/ALPHA1)/A)/(B-ALPHA1*U*TAU)
BETA=BETA2*(1-FLAG)+BETA1*FLAG
GAM=Z/A
//
//Parameter Values and Constraints
U=16.1
ALPHA1=0.511
ALPHA2=0.152
G=-981
VIS=0.01
RB=0.13
RHOF=0.99829
RHOG=0.00122
//
//Initial Conditions
R=1.49
Z=0.16
UBR=16.01
UBZ=1.68
0.5<T<4.5
***
```

C.4 Revised Uniform Speed Bubble Model with Lift Term and Constant α

```
// Uniform Speed Bubble Model with Lift Term and Constant ALPHA1
IndVars: T
DepVars: A, R, Z, BETA, GAM, UFR, UFZ, UBR, UBZ
Params: ALPHA, U, VIS, RB, G, RHOF, RHOG
```

```
//
//Simplifying Equations
//
MF=RHOF*(4./3)*PI*RB^3
MB=RHOG*(4.3)*PI*RB^3
C1=1./(MB+0.5*MF)
C2=(MB-MF)*G
C3=6.*PI*VIS*RB
C4=1.5*MF
C5=0.5*MF
//
A=ABS(ALPHA*U*T)
EPS=SQRT(R^2+Z^2)
FLAG=UNIT(A-EPS)
//
//Fluid Vortex Equations
//
//Radial Equations:  UFR1 is Internal, UFR2 is External to Fluid Vortex
UFR1=(3.*U*R*(Z))/(2*A^2)
UFR2=(3.*U*R*Z*A^3)/(2.*(Z^2+R^2)^(5/2))+(3*U*R*Z*A^3)/(2*(Z^2+R^2)^(5/2))
UFR=UFR2*(1-FLAG)+UFR1*FLAG
//
//Height Equations: UFZ1 is Internal, UFZ2 is External to Fluid Vortex
UFZ1=((-3.*U)/(2.*A^2))*(2.*R^2+Z^2-A^2)
UFZ2=(-U*(A^3*(R^2-2*Z^2))/(2*(Z^2+R^2)^(5/2)))+(-U*(1+(A^3*(R^2-2*Z^2))/
(2*(Z^2+R^2)^(5/2))))
UFZ=UFZ2*(1-FLAG)+UFZ1*FLAG
//
//Bubble Reynolds Number
REB=(RHOF*2.*RB*ABS(U-SQRT(UBZ^2+UBR^2)))/VIS
//
//Drag Force Correction
FD=1.+0.1315*REB^(0.82-0.05*LOG10(REB))
//
//Bubble Equations
//
//Lift Term
LF=DERIV(UFR,Z)-DERIV(UFZ,R)
//
//Radial Direction
UBR'=C1*(C3*FD*(UFR-UBR)+C4*(DERIV(UFR,T)
+UFR*DERIV(UFR,R)+UFZ*DERIV(UFR,Z))-C5*(UFZ-UBZ)*LF)
R'=UBR
```

```
//
//Height Direction (z-direction)
UBZ'=C1*(C2+C3*FD*(UFZ-UBZ)+C4*(DERIV(UFZ,T)
+UFZ*DERIV(UFZ,Z)+UFR*DERIV(UFZ,R))-C5*(UFR-UBR)*LF)
Z'=UBZ
//
//Dimensionless Variables
//
BETA=R/A
GAM=Z/A
//
//Parameter Values and Constraints
U=16.1
ALPHA1=0.511
G=-981
VIS=0.01
RB=0.13
RHOF=0.99829
RHOG=0.00122
//
//Initial Conditions
R=1.49
Z=0.16
UBR=16.01
UBZ=1.68
0.5<T<4.5
***
```

C.5 Uniform Speed Bubble Model with Lift Term, Constant α and CL=1.0

```
// Uniform Speed Bubble Model with Lift Term, Constant ALPHA1 and CL=1.0
IndVars: T
DepVars: A, R, Z, BETA, GAM, UFR, UFZ, UBR, UBZ
Params: ALPHA, U, VIS, RB, G, RHOF, RHOG
//
//Simplifying Equations
//
MF=RHOF*(4./3)*PI*RB^3
MB=RHOG*(4.3)*PI*RB^3
C1=1./(MB+0.5*MF)
C2=(MB-MF)*G
```

```
C3=6.*PI*VIS*RB
C4=1.5*MF
C5=1*MF
//
A=ABS(ALPHA*U*T)
EPS=SQRT(R^2+Z^2)
FLAG=UNIT(A-EPS)
//
//Fluid Vortex Equations
//
//Radial Equations:  UFR1 is Internal, UFR2 is External to Fluid Vortex
UFR1=(3.*U*R*(Z))/(2*A^2)
UFR2=(3.*U*R*Z*A^3)/(2.*(Z^2+R^2)^(5./2.))+(3*U*R*Z*A^3)/(2*(Z^2+R^2)^(5/2))
UFR=UFR2*(1-FLAG)+UFR1*FLAG
//
//Height Equations: UFZ1 is Internal, UFZ2 is External to Fluid Vortex
UFZ1=((-3.*U)/(2.*A^2))*(2.*R^2+Z^2-A^2)
UFZ2=(-U*(A^3*(R^2-2*Z^2))/(2*(Z^2+R^2)^(5/2)))+(-U*(1+(A^3*(R^2-2*Z^2))/
(2*(Z^2+R^2)^(5/2))))
UFZ=UFZ2*(1-FLAG)+UFZ1*FLAG
//
//Bubble Reynolds Number
REB=(RHOF*2.*RB*ABS(U-SQRT(UBZ^2+UBR^2)))/VIS
//
//Drag Force Correction
FD=1.+0.1315*REB^(0.82-0.05*LOG10(REB))
//
//Bubble Equations
//
//Lift Term
LF=DERIV(UFR,Z)-DERIV(UFZ,R)
//
//Radial Direction
UBR'=C1*(C3*FD*(UFR-UBR)+C4*(DERIV(UFR,T)
+UFR*DERIV(UFR,R)+UFZ*DERIV(UFR,Z))-C5*(UFZ-UBZ)*LF)
R'=UBR
//
//Height Direction (z-direction)
UBZ'=C1*(C2+C3*FD*(UFZ-UBZ)+C4*(DERIV(UFZ,T)
+UFZ*DERIV(UFZ,Z)+UFR*DERIV(UFZ,R))-C5*(UFR-UBR)*LF)
Z'=UBZ
//
//Dimensionless Variables
```

```
//
BETA=R/A
GAM=Z/A
//
//Parameter Values and Constraints
U=16.1
ALPHA1=0.511
G=-981
VIS=0.01
RB=0.13
RHOF=0.99829
RHOG=0.00122
//
//Initial Conditions
R=1.49
Z=0.16
UBR=16.01
UBZ=1.68
0.5<T<4.5
***
```

IMAGE EVALUATION
TEST TARGET (QA-3)

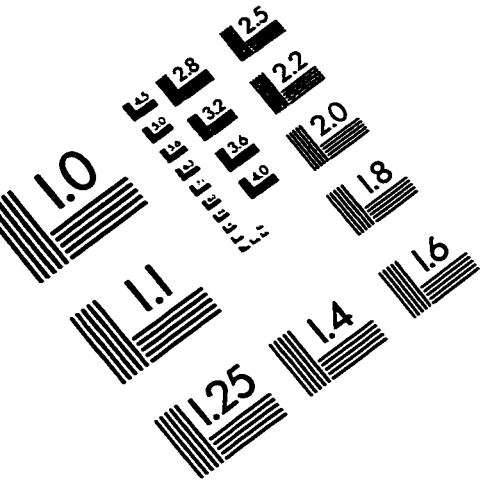

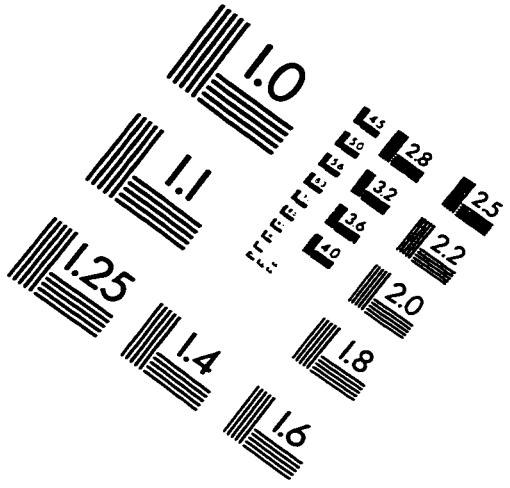

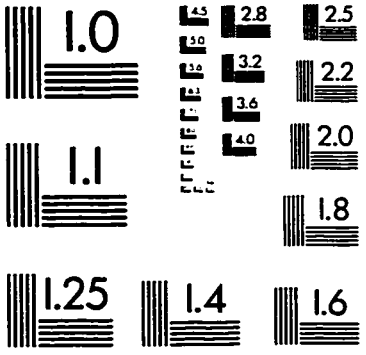

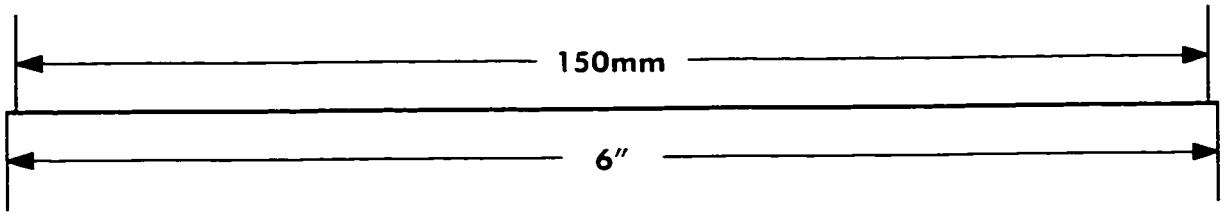

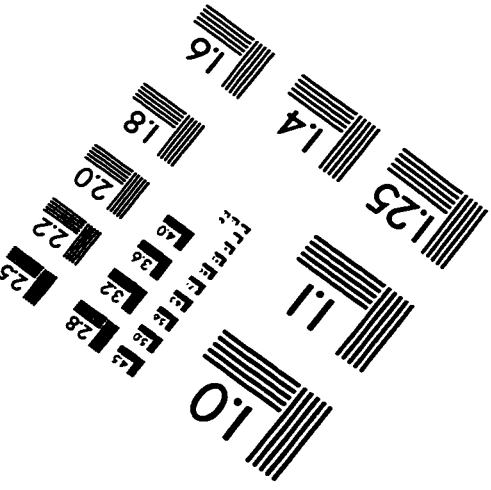

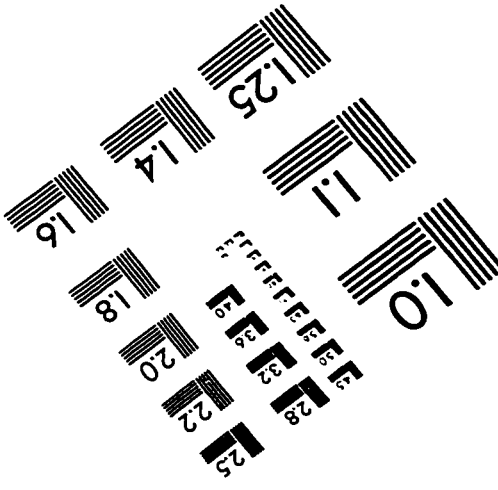

APPLIED IMAGE . Inc
1653 East Main Street
Rochester, NY 14609 USA
Phone: 716/482-0300
Fax: 716/288-5989

© 1993, Applied Image, Inc., All Rights Reserved